



UNIVERSITAT DE
BARCELONA

Mineralogy and geochemistry of the platinum group elements (PGE), rare earth elements (REE) and scandium in nickel laterites

Thomas Hans Aiglsperger

ADVERTIMENT. La consulta d'aquesta tesi queda condicionada a l'acceptació de les següents condicions d'ús: La difusió d'aquesta tesi per mitjà del servei TDX (www.tdx.cat) i a través del Dipòsit Digital de la UB (diposit.ub.edu) ha estat autoritzada pels titulars dels drets de propietat intel·lectual únicament per a usos privats emmarcats en activitats d'investigació i docència. No s'autoritza la seva reproducció amb finalitats de lucre ni la seva difusió i posada a disposició des d'un lloc aliè al servei TDX ni al Dipòsit Digital de la UB. No s'autoritza la presentació del seu contingut en una finestra o marc aliè a TDX o al Dipòsit Digital de la UB (framing). Aquesta reserva de drets afecta tant al resum de presentació de la tesi com als seus continguts. En la utilització o cita de parts de la tesi és obligat indicar el nom de la persona autora.

ADVERTENCIA. La consulta de esta tesis queda condicionada a la aceptación de las siguientes condiciones de uso: La difusión de esta tesis por medio del servicio TDR (www.tdx.cat) y a través del Repositorio Digital de la UB (diposit.ub.edu) ha sido autorizada por los titulares de los derechos de propiedad intelectual únicamente para usos privados enmarcados en actividades de investigación y docencia. No se autoriza su reproducción con finalidades de lucro ni su difusión y puesta a disposición desde un sitio ajeno al servicio TDR o al Repositorio Digital de la UB. No se autoriza la presentación de su contenido en una ventana o marco ajeno a TDR o al Repositorio Digital de la UB (framing). Esta reserva de derechos afecta tanto al resumen de presentación de la tesis como a sus contenidos. En la utilización o cita de partes de la tesis es obligado indicar el nombre de la persona autora.

WARNING. On having consulted this thesis you're accepting the following use conditions: Spreading this thesis by the TDX (www.tdx.cat) service and by the UB Digital Repository (diposit.ub.edu) has been authorized by the titular of the intellectual property rights only for private uses placed in investigation and teaching activities. Reproduction with lucrative aims is not authorized nor its spreading and availability from a site foreign to the TDX service or to the UB Digital Repository. Introducing its content in a window or frame foreign to the TDX service or to the UB Digital Repository is not authorized (framing). Those rights affect to the presentation summary of the thesis as well as to its contents. In the using or citation of parts of the thesis it's obliged to indicate the name of the author.

“Mineralogy and geochemistry of the platinum group elements (PGE), rare earth elements (REE) and scandium in nickel laterites”

Thomas Hans Aiglsperger

PhD Thesis 2015



UNIVERSITAT DE
BARCELONA

Departament de Cristal·lografia, Mineralogia i Dipòsits Minerals

Facultat de Geologia

Departament de Cristal·lografia, Mineralogia i Dipòsits Minerals
Facultat de Geologia

**“Mineralogy and geochemistry of the platinum
group elements (PGE), rare earth elements
(REE) and scandium in nickel laterites”**

Tesi doctoral presentada per:
Thomas Hans Aiglsperger

Per a aspirar a l’obtenció del títol de doctor per la Universitat de
Barcelona amb Menció Internacional

Tesi realitzada dintre del Programa de Doctorat de Ciències de la
Terra, sota la direcció del Dr. Joaquín A. Proenza Fernández

Thomas Hans Aiglsperger

El Doctorand

Dr. Joaquín A. Proenza
Dep. Cristal·lografia, Mineralogia
i Dipòsits Minerals
Universitat de Barcelona

Barcelona, Octubre, 2015



UNIVERSITAT DE
BARCELONA

LE
RU

B:KC Barcelona
Knowledge
Campus
Campus of International Excellence

To every age its science. To every science its freedom.

To Ida, Irma and Kathi

Acknowledgements

This research has been financially supported by FEDER funds, the Spanish projects CGL2009-10924 and CGL2012-36263 and the Catalan project 2014-SGR-1661 as well as by a PhD grant and two travel grants to Leoben and Prague (estancia breve FPI 2012 and 2013, respectively), sponsored by the Ministerio de Economía y Competitividad (Spain).

In particular I want to say thank you to the following persons who were essential for the development of this investigation:

- Dr. Joaquín A. Proenza Fernández (Professor at the University of Barcelona) – a simple *thanks for everything* (it would fill another thesis...)!!
- Dr. John F. Lewis (retired professor at the George Washington University, Washington, USA) – it was a wonderful experience to meet you in the Caribbean during field work. Thank you so much for all your help during all these years!
- Francisco Longo (best mine geologist ever at the Falcondo mining area) - without your help this thesis wouldn't exist. Samples tracked by you changed everything!
- Dr. Xavier Llovet (Director of the EMP laboratory at the Serveis Científics i Tecnològics, University of Barcelona) – your excellent technical support during EPMA sessions is highly appreciated and obtained results thanks to you marked milestones of this investigation!
- Eva Prats (Serveis Científics i Tecnològics, University of Barcelona) – you introduced me to the technique of FE-SEM and shifted PGM investigation from “interpretation of tiny, white spots” to “exploring different planets” – thanks!
- Dr. José María González-Jiménez (Professor at the University of Chile) – many thanks for helping me to obtain Re-Os isotope analyses and to interpret them!
- Dr. William L. Griffin (Professor at the Macquarie University, Australia) - giving me the possibility to apply Re-Os isotope analyses is highly appreciated!
- Dr. Louis J. Cabri (Cabri Consulting Inc.) – it is a privilege to share results with you, your critical comments are invariably constructive and your standards a guideline for every scientist!
- Dr. Vladimir Rudashevsky (CNT-MS) – your help during installation of the HS-11 laboratory in Barcelona and subsequent training are highly appreciated!
- Dr. Federica Zaccarini (Eugen F. Stumpfl EMP laboratory at the Monatanuniversitaet Leoben, Austria) – I will always be grateful that you introduced me to Joa, opening me the door to this magical experience, grazie mille!
- Dr. Dolors Barsó Romeu (Director of the Tècnic Servei Làmina Prima, University of Barcelona) – your patience and professionalism in problem solving during countless sessions were outstanding! Thanks!
- Montserrat Sibila, Fadoua Zoura Oumada and Vicenç Planella (Tècnic Servei Làmina Prima, University of Barcelona) – from the very first deplorable attempt of producing a monolayer polished section to high quality endproducts – you were always there to guide and support me!

- Dr. Salvador Gali (Professor at the University of Barcelona) – all your private lessons regarding crystallography is highly appreciated!
- Dr. Jordi Rius (Institut de Ciència de Materials de Barcelona) – measurements at the ALBA synchrotron with your μ XRD technique were a unique experience and results obtained explain a lot! Many thanks!
- Dr. Mont. Amir Morteza Azimzadeh (Professor at the University of Zanjan, Iran) – knowing you formed me during the last 13 years! Thanks for sharing, Freund der Berge!!
- Dr. Manel Labrador (retired professor at the University of Barcelona) – thanks dear Manel for all the interesting work during these years!
- Dr. Anna Vymazalova (Geological Survey of Prague, Czech Republic) – every visit to Prague and any time we met during SGA conferences resulted always in scientific and private talks of highest quality! Many thanks!
- Dr. Jan Pašava (Geological Survey of Prague, Czech Republic) – thank you for all your time during my stay in Prague, I enjoyed every minute!
- Martin Svojtka and Jana Ďurišová (Institute of Geology, Academy of Sciences, Praha, Czech Republic) – thanks for LA-ICP-MS measurements and interpretation of data!
- Dolors Rodriguez Lopez (Secretary at the CMDM, University of Barcelona) – I don't know how you did it, but all problems just disappeared after talking with you, magic!
- Montserrat Errea (Secretary at the CMDM, University of Barcelona) – any time I felt stressed or needed someone to talk I knew I can count on you, thanks for this and all the other nice moments!
- Manel (retired head of the workshop at the University of Barcelona) and his entire team – you always had the practical answers to my drawn questions!
- Dr. Josep Roque Rosell (Professor at the University of Barcelona) – thanks for the great time we spent during these years, even just via skype... great to have you back!
- Cristina Villanova-de-Benavent (PhD student colleague at the CMDM, University of Barcelona) – someone might think it is not easy to sit face to face for five years in one office...with you it was the easiest exercise! Thanks for all your help right from the beginning, without you I wouldn't even have managed to matriculate...!
- Montgarri Castillo i Oliver (PhD student colleague at the CMDM, University of Barcelona) – thank you so much dear Montgarri for everything you did for me and especially for never having given up to invite me to join activities! I hope that soon we can continue to explore your wonderful Catalunya!
- Lidia Butjosa Molines, Sandra Amores Casals, Marc Campeny and Lisard Torró i Abat (PhD student colleagues at the CMDM, University of Barcelona) – important distractions during coffee/tea breaks, funny moments during lunch and interesting conversations at any occasion were important ingredients for a productive working environment. Thanks!
- The entire stuff of the CMDM, University of Barcelona – *merci* for making this department the best working place I could ever have dreamed off!
- The stuff off the Falcondo mining area – many thanks for help and hospitality during field work!
- My family – thanks for all your support, anywhere and anytime - I love you!!

Abstract

Ni laterites are considered worthy targets for critical metals (CM) exploration as rare earth elements (REE), Sc and platinum group elements (PGE) can be concentrated during weathering as a result of residual and secondary enrichment. In this investigation geochemical and mineralogical data of CM from two different nickel laterite types (i) from the Moa Bay mining area in Cuba (oxide type) and (ii) from the Falcondo mining area in the Dominican Republic (hydrous Mg silicate type) are presented. Emphasis is given on examining their potential to accumulate CM and on processes involved. Results show that CM are concentrated towards the surface in specific zones: (i) REE in clay minerals rich horizons and within zones composed of secondary Mn oxide(s) (ii) Sc within zones rich in secondary Fe and Mn bearing oxide(s) and (iii) PGE in zones with high concentrations of residual chromian spinel and secondary Fe and Mn bearing oxide(s) at upper levels of the Ni laterite profiles. Concentration factors involve (i) residual enrichment by intense weathering (ii) mobilization of CM during changing Eh and pH conditions with subsequent reprecipitation at favourable geochemical barriers (iii) interactions between biosphere and limonitic soils at highest levels of the profile (critical zone) with involved neoformation processes. Total contents of CM in both Ni laterite types are low when compared with conventional CM ore deposits but are of economic significance as CM have to be seen as cost inexpensive by-products during the Ni (+Co) production. Innovative extraction methods currently under development are believed to boost the significance of Ni laterites as future unconventional CM ore deposits.

Two Ni laterite profiles from the Falcondo mining area have been compared for their platinum group element (PGE) geochemistry and mineralogy. One profile (Loma Peguera) is characterized by PGE-enriched (up to 3.5 ppm total PGE) chromitite bodies incorporated within the saprolite, whereas the second profile is chromitite-free (Loma Caribe). Total PGE contents of both profiles slightly increase from parent rocks (36 and 30 ppb, respectively) to saprolite (~50 ppb) and reach highest levels within the limonite zone (640 and 264 ppb, respectively). Chondrite-normalized PGE patterns of saprolite and limonite reveal rather flat shapes with positive peaks of Ru and Pd. Three types of platinum group minerals (PGM) were found by using an innovative hydroseparation technique: (i) primary PGM inclusions in fresh Cr-spinel (laurite and bowieite), (ii) secondary PGM (e.g., Ru-Fe-Os-Ir compounds) from weathering of preexisting PGM (e.g., serpentinization and/or laterization), and (iii) PGM precipitated after PGE mobilization within the laterite (neoformation). Results provide evidence that (i) PGM occurrence and PGE enrichment in the laterite profiles is independent of chromitite incorporation; (ii) PGE enrichment is residual on the profile scale; and (iii) PGE are mobile on a local scale leading to *in situ* growth of PGM within limonite, probably by bioreduction and/or electrochemical metal accretion.

Free grains of PGM with delicate morphologies were discovered in limonite hosted chromitite samples (“floating chromitites”) from highest levels in the Falcondo Ni laterite deposit (Dominican Republic). Textural and chemical evidence obtained via SEM and EMP analysis points to a multistage formation: (i) primary PGM formation at magmatic stage; (ii) transformation to highly porous secondary Os-Ru PGM during serpentinization; (iii) neoformation of Ir-Fe-Ni-(Pt) mineral phases during early stages of lateritization; (iv) neoformation of Pt-(Ir) mineral phases within the critical zone of the profile resulting in nugget shaped accumulation of rounded particulates during late stages of lateritization. The observation of accumulations of most likely biogenic mediated *in situ* growth of Pt rich nanoparticles in supergene environments could help to explain (i) why Pt bearing nuggets are the most abundant PGM found in surface environments, (ii) why Pt nuggets from placer deposits generally surpass the grain sizes of Pt grains found in parent rocks by several orders of magnitude (few micrometers vs. several millimeters) and (iii) how anthropogenic PGE contamination may affect our biosphere.

Osmium isotope characteristics from primary and secondary PGM, separated from chromitite, saprolite and limonite (Falcondo mining area), suggest that serpentinization of the Loma Caribe peridotite has not significantly affected the Re-Os system in Os-rich PGM. This is noted by the fact, that primary PGM formed at magmatic stage and secondary Ru-Os-Mg-Si PGM formed due desulphurization of primary PGM with significant incorporation of Mg silicates, have almost identical Os isotope characteristics, typical of the mantle. However, the Re-Os system can be significantly disturbed during stages of lateritization when porous secondary PGM react with Fe-rich fluids, thus forming hexaferrum and magnetite in the interstices of secondary PGM. Here presented data indicate that more radiogenic $^{187}\text{Os}/^{188}\text{Os}$ ratios in higher levels of the weathering profile are linked to steady mobilization of PGE within secondary PGM resulting in subsequent loss of Os counterbalanced by the incorporation of Fe.

In this investigation presented data clearly states that PGE are neither noble nor inert in surface environments, at least in those related to tropical Ni laterites from the Northern Caribbean.

TABLE OF CONTENTS

Chapter 1. Introduction

1.1. An overview of the Ni-Co laterite deposits.....	1
1.1.1. Oxide type	2
1.1.2. Hydrous Mg silicate type	3
1.1.3. Clay silicate type	3
1.2. Lateritization processes: platinum group element (PGE) enrichment and the enigma of supergene formation of platinum group minerals (PGM)	3
1.3. Lateritization processes: rare earth elements (REE) and scandium enrichment	4
1.4. Goals of this study.....	4
1.5. Outline of this thesis.....	5

Chapter 2. Geological setting

2.1. The Moa Bay mining area.....	7
2.1.1. The Ni laterite profile at Moa Bay	8
2.2. The Falcondo mining area	8
2.2.1. The Ni laterite profile at Falcondo	9

Chapter 3. Materials and Methods

3.1. Sample selection.....	15
3.1.1. Moa Bay mining area (Cuba)	15
3.1.2. Falcondo mining area (Dominican Republic)	15
3.2. Whole rock geochemical analyses	15
3.2.1. Major, minor and lithophile trace elements	15
3.2.2. PGE	16
3.3. Mass balance calculations	16
3.4. X-ray diffraction analyses	16
3.5. Mineralogical methodology: challenge and uncertainty	17
3.5.1. The HS laboratory Barcelona	17
3.5.1.1. Sample preparation	18
3.5.1.2. Hydroseparation	19

3.6. Scanning Electron Microscopy (SEM and FE-SEM).....	19
3.7. Electron Microprobe analyses (EMPA)	19
3.8. Micro-Raman spectroscopy	19
3.9. Laser ablation-inductively coupled plasma-mass spectrometry (LA ICP-MS).....	20
3.10. Synchrotron through-the-substrate X-ray microdiffraction (tts- μ XRD)	20
3.11. Osmium isotopes	21

Chapter 4. Abundance and distribution of critical metals (REE, Sc, PGE) in Ni laterites from Cuba and the Dominican Republic

4.1. Introduction	23
4.2. Geochemistry	25
4.2.1. Moa Bay	25
4.2.2. Falcondo	28
4.3. Isocon analysis and element transfer	30
4.3.1. Moa Bay	30
4.3.2. Falcondo	31
4.4. Profile mineralogy	34
4.4.1. Moa Bay	35
4.4.2. Falcondo	36
4.5. Critical metal bearing mineral phases	36
4.6. The ultramafic index of alteration (UMIA).....	42
4.7. Discussion	42
4.7.1. Rare Earth Elements	43
4.7.2. Scandium	44
4.7.3. Platinum Group Elements	45
4.8. Concluding remarks	47

Chapter 5. Chromian spinel composition and PGE geochemistry of chromitite bodies from the Loma Caribe peridotite, Dominican Republic

5.1. Introduction	49
5.2. Field characteristics of the chromitite bodies.....	49
5.3. Compositions of the chromian spinels	50
5.4. PGE geochemistry.....	49
5.5. Discussion	54
5.5.1. Chromitites hosted in the Loma Caribe peridotite: from exotic to atypical	54
5.6. Concluding remarks	54

Chapter 6. Platinum group minerals (PGM) in the Falcondo Ni laterite deposit, Loma Caribe peridotite (Dominican Republic)

6.1. Introduction	55
6.2. PGE geochemistry of the investigated laterite profiles	56
6.2.1. Loma Peguera.....	56
6.2.2. Loma Caribe	58
6.3. Mineralogy of PGM	59
6.3.1. PGM in chromitites	59
6.3.2. PGM in the saprolite	65
6.3.3. PGM in the limonite	65
6.4. Electron microprobe composition of PGM found in saprolite and limonite	68
6.5. Mineralogical characterization of Ru-Os-Fe compounds.....	71
6.5.1. EMP analysis.....	71
6.5.2. Synchrotron tps- μ XRD	74
6.5.3. Micro-raman spectroscopy	74
6.6. The mystery of fibrous PGM – alteration, neoformation or both?.....	77
6.7. Discussion	80
6.7.1. PGE enrichment in Ni laterites and the role of chromitites.....	80
6.7.2. Origin of platinum group minerals in Ni laterites	82
6.7.2.1. Magmatic origin of primary PGM.....	82
6.7.2.2. Secondary PGM from alteration of pre-existing PGM.....	82
6.7.2.3. Some thoughts about the origin of Ru-Os-Fe grains: Ru-Os oxides? Ru-Os alloys + magnetite? Ru rich hexaferrum + Fe oxide(s)?	83
6.7.2.4. Neoformation of PGM in limonite	86
6.8. Concluding remarks	89

Chapter 7. PGM neof ormation in Ni laterites – “multistage PGE grains” hold the key to explain nugget formation in supergene environments

7.1. Introduction 91
7.2. Sample provenance and PGE geochemistry..... 91
7.3. PGE mineralogy of “floating chromitites” and the observation of “multistage PGE grains”
..... 93
7.4. Discussion 95
7.5. Final remarks..... 101

Chapter 8. Osmium isotope characteristics of primary and secondary PGM in Ni laterites from Falcondo

8.1. Introduction 103
8.2. Samples and analytical methods 103
8.3. Results 105
8.4. Discussion 107
8.5. Final remarks..... 108

Chapter 9. Summary of conclusions 109

References 111

Chapter 1

Introduction

1.1. Overview of Ni±Co laterite deposits

Ni±Co laterite deposits can be defined as regolith derived from ultramafic rocks containing economically exploitable concentrations of Ni±Co (e.g. Norton, 1973; Golightly, 1981, 2010; Gleeson et al., 2003; Freyssinet et al., 2005; Kalatha and Economou-Eliopoulos, 2015). These authors recognized that close interactions between the composition of the protolith,

tectonic setting, geomorphology and topography, drainage, chemistry of ground water and organic matter, climate and weathering rates mainly control enrichment processes within lateritic weathering profiles. Excluding a few exceptions, most of Ni±Co laterite deposits are observed within 26 degrees of the equator, thus indicating a close relationship to tropical climate conditions (Fig. 1.1).

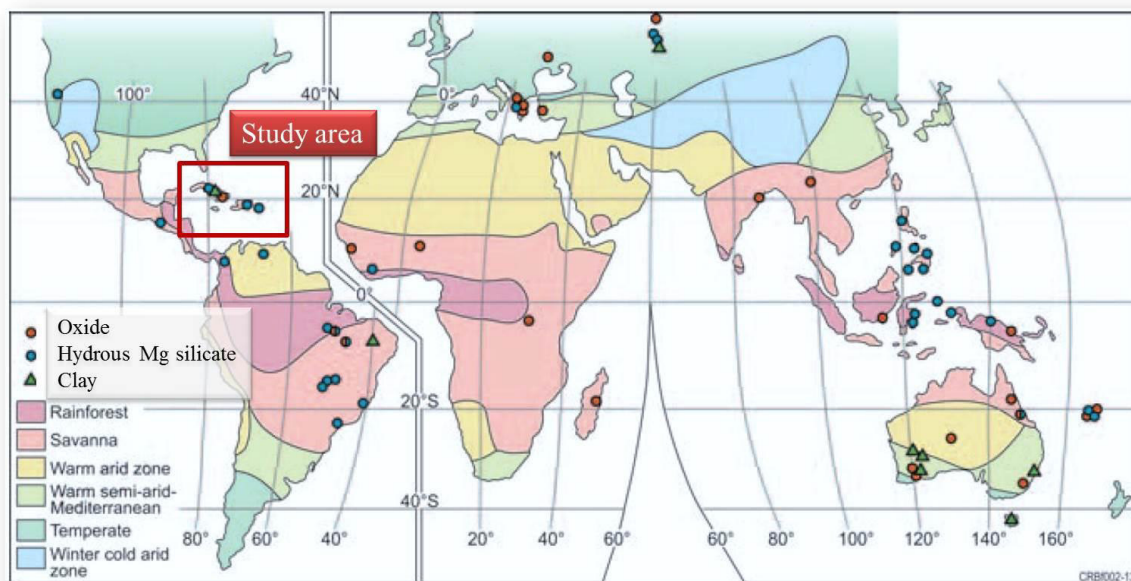


Fig. 1.1. Distribution of different Ni laterite subtypes around the world. Modified after Butt and Cluzel (2013).

It is widely accepted, that extreme weathering conditions lead to a general break down of primary minerals in Ni enriched parent rocks (e.g. ophiolite, komatiite, layered intrusions; all ± serpentinized) and that chemical

components such as Ni and Co are released to the groundwater where they can (i) reprecipitate as or (ii) incorporate in new, stable minerals. This redistribution (gain and loss) of main element components (i.e. Si, Mg, Al and Fe) during

stages of weathering explains the often observed, typical large scale structure of Ni±Co laterites from bottom to top: (i) parent rock (protolith), characterized by unweathered minerals (ii) saprolite, dominated by secondary Si and Mg bearing minerals and (iii) limonite, dominated by residual, Fe and Al bearing mineral phases (Fig. 1.2). As a consequence, saprolitic horizons can generally be discriminated from subsequent limonite by the so called “Mg-discontinuity” (decrease in MgO content

from more than ~20% to less than ~2%) (Butt and Cluzel, 2013) (Fig. 1.2).

However, three subtypes of Ni±Co laterites can be distinguished according to their main laterite architecture as well as by their dominant Ni-bearing mineralogy: (i) oxide, (ii) hydrous Mg silicate and (iii) clay subtype (Samama, 1986; Brand et al., 1998; Gleeson et al., 2003; Freyssinet et al., 2005; Golightly, 2010; Butt and Cluzel, 2013; Proenza et al., 2015 and references therein) (Fig. 1.2).

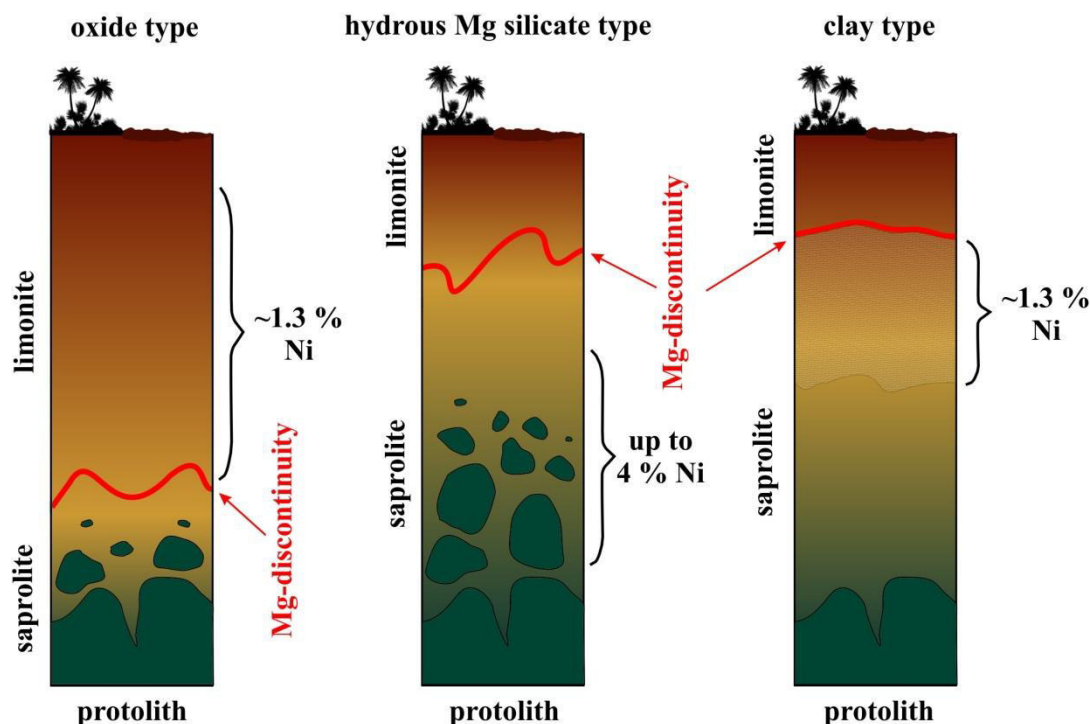


Fig. 1.2. Subtypes of Ni laterites developed on serpentinized ultramafic protolith with indicated main Ni ore zones and grades.

1.1.1. Oxide type

Ni laterites of the oxide type (also known as limonite deposits), are characterized by a dominate limonite horizon. Important saprolitic horizons are generally absent. Main mineral assemblages are Fe oxide(s) with goethite as the economically most important Ni ore mineral. Mean grades of

such ore deposits range from 1.0 to 1.6 wt% Ni and they represent about 60% of the current total Ni laterite resources (Butt and Cluzel, 2013).

1.1.2. Hydrous Mg silicate type

Hydrous Mg silicate Ni laterites are dominated by the saprolite horizon overlying the ultramafic protolith and reveal only a minor contribution of limonite. Ore minerals are hosted within the saprolite and mainly consist of Ni bearing serpentine, talc, sepiolite and chlorite, a group of hydrous Mg-Ni phyllosilicates informally known as “garnierites” (Butt and Cluzel, 2013; Villanova de Benavent et al., 2014). Due to the strong ability of these minerals to store Ni (up to 33% Ni), Ni laterites of this subtype are of the highest grades (up to 4% Ni), however average grade is 1.44 wt%. Today, about 32% of total Ni laterite resources are found within Ni laterites of the hydrous Mg silicate subtype (Butt and Cluzel, 2013).

1.1.3. Clay silicate type

Ni laterites of the clay silicate type, which has been recognized and exploited as an ore type only recently (Butt and Cluzel, 2013), are characterized by a Ni rich horizon of Ni-rich saponite and smectite located in the mid to upper saprolite and subsequent ferruginous zone (Butt and Cluzel, 2013; Gleeson et al., 2003). Highest concentrations between 1.0 and 1.5 wt% Ni are generally found right beneath the Mg-discontinuity. About 8% of the total Ni laterite resources are bound to this subtype (Butt and Cluzel, 2013).

1.2. Lateritization processes: platinum group element (PGE) enrichment and the enigma of supergene formation of platinum group minerals (PGM)

Hypotheses about lateritic weathering processes favouring chemical mobilization of PGE were first raised by Wagner (1929). However, almost a half century later E. F. Stumpfl and M. Tarkian (1976) stated in their survey of platinum genesis that “*Regarding future developments, it is hoped that the findings reported and the concepts discussed may generate interest in a field which, although of paramount importance for the understanding of platinum deposits, has been sadly neglected so far, i.e., the experimental geochemistry of platinum metals*”. Today, another 40 years later, we can look back on an impressive number of laboratory studies dealing with the behaviour of PGE in a great variety of environments (e.g. Wood, 1996; Fleet et al., 1999; Ballhaus et al., 2006; Foustoukos et al., 2015; and reference therein). Although some of these studies have changed our view on formerly considered “noble and inert” PGE, results obtained by experiments have also caused controversy as observations gained on laboratory scale could not be proofed in field or vice versa. Thus, the influence of lateritization processes on PGE enrichment and PGM appearance is still matter of debate (e.g. Augé et al., 1995; Traoré et al., 2008 a,b) and enigmatic PGE nugget occurrence in surface environments (e.g. placer deposits, soils, laterites) have attracted highest attention since decades. Hypogene vs. supergene formation models have been debated in detail: one group believes that weathering of PGM bearing rocks is the sole factor for PGM

accumulation in surface environments (e.g. Koen, 1964; Cabri and Harris, 1975; Hattori and Cabri, 1992; Hattori et al., 2004), whereas others propose *in-situ* neoformation of PGM by secondary processes such as PGE remobilization and continual accretion in addition (e.g. Augusthitis, 1965; Ottemann and Augusthitis, 1967; Stumpfl, 1974; Bowles, 1986; Oberthuer et al., 2014; Campbell et al., 2015).

Recently, new approaches such as the investigation of possible bioavailability of Pt and other PGE for microorganism with subsequent reprecipitation in surface environments, have opened an entire new chapter in this ongoing discussion (Reith et al., 2014).

1.3. Lateritization processes: rare earth elements (REE) and scandium enrichment

In 2010 western governments realised the need to find alternatives for the supply of REE when China, being currently the almost unique supplier of these strategic elements, shocked western high tech industries with export quota. However, in contrast to well-studied weathering profiles developed on REE enriched carbonatites, relatively little is known about the potential of REE and Sc enrichment in lateritic profiles developed on ultramafic rocks. Weathering products are generally considered worthy targets for REE and Sc exploration as these elements can be concentrated during weathering as a result of their limited mobility in surface waters. Eliopoulos et al. (2014) reported high values of up to 6440 ppm REE from Greek Ni and bauxitic laterites. Within the last few years exploration activities for Sc

in laterites developed upon Alaskan-type ultramafic complexes in Australia, have revealed their high potential to accumulate Sc (e.g. the Nyngan project) (Scandium International Mining Corp., 2015). On the contrary, the potential for Sc concentration in Ni laterites derived from ophiolitic peridotites has been assessed only in a few cases: Ahmad and Morris (1978) reported elevated Sc values within nickel laterite ores from Guatemala, New Caledonia and Indonesia. More recently, Audet (2009) investigated the Ni laterites overlying the Koniambo ultramafic massif in New Caledonia and discovered significant Sc contents up to 70 ppm within the limonite. However, these discoveries are of economic interest as Sc and REE, could be readily produced as a by-product during Ni (+Co) production. A recently published review on metallurgical processes for Sc recovery proposes nickel laterite ores as “*the most promising scandium resources for its production*” (Wang et al., 2011).

1.4. Goals of this study

This investigation aims to assess the potential of Ni laterites to accumulate PGE, REE and Sc. Special emphasis is given (i) to examine and compare element contents in different Ni laterite subtypes (i.e. oxide type and hydrous Mg silicate type), (ii) to understand where in the weathering profile these elements get enriched, (iii) to figure out which processes are involved and (iv) to define in which mineral phases PGE, REE and Sc get concentrated.

With respect to PGE it is hoped, that this investigation can contribute to ongoing scientific debates dealing with the nature

of these elements in surface environments and, in the best case, provide answers to the following, fundamental questions: (i) is primary PGE enrichment in bedrock responsible for their (residual) supergene enrichment; (ii) is PGE enrichment intrinsically related to lateritization processes; (iii) how do PGE and PGM behave within the laterite profile and what are criteria for PGE mobilization; (iv) is there unequivocal mineralogical evidence for *in-situ* neoformation of PGM within laterites?

1.5. Outline of this thesis

To achieve the goals of this investigation representative samples from Ni laterites were collected and studied in detail via multidisciplinary techniques. In chapter 2 the geological setting of the study area is explained (i.e. Moa Bay in Cuba and Falcondo in the Dominican Republic). Chapter 3 aims to give an overview of the provenance of studied samples and to provide a comprehensive description of applied analytical techniques. In chapter 4

geochemical and mineralogical features of Ni laterites from the oxide type and the hydrous Mg silicate type are discussed with special emphasis regarding critical metals (CM; i.e. REE, Sc and PGE). Geochemical characteristics of PGE enriched chromitites found within Ni laterites from the Dominican Republic are described in chapter 5. Chapter 6 contains a detailed description of the geochemistry and mineralogy of PGE within two different Ni laterites from Falcondo, including data obtained via scanning electron microscopy (SEM), electron microprobe (EMP), micro-raman spectroscopy and synchrotron through the substrate X-ray microdiffraction (tts- μ XRD). In chapter 7 the observation of complex PGM with delicate morphologies, including textural evidence for *in-situ* neoformation, is discussed and a model explaining multistage nugget formation from hypogene to supergene is presented. Chapter 8 provides and discusses first data of the Re-Os isotopic system of Os rich PGM from Ni laterites. Finally, conclusions of this investigation are summarized in chapter 9.

Chapter 2

Geological setting

The studied Ni laterites (i.e. Moa Bay and Falcondo mining areas) are located in the northern Caribbean (Fig. 2.1). They are developed on ophiolite complexes with serpentinized peridotite that crop out as

tectonic belts along the margins of the Caribbean plate (Lewis et al., 2006a). Eastern Cuba and the central Dominican Republic contain the largest Ni ore deposits of the Greater Antilles.

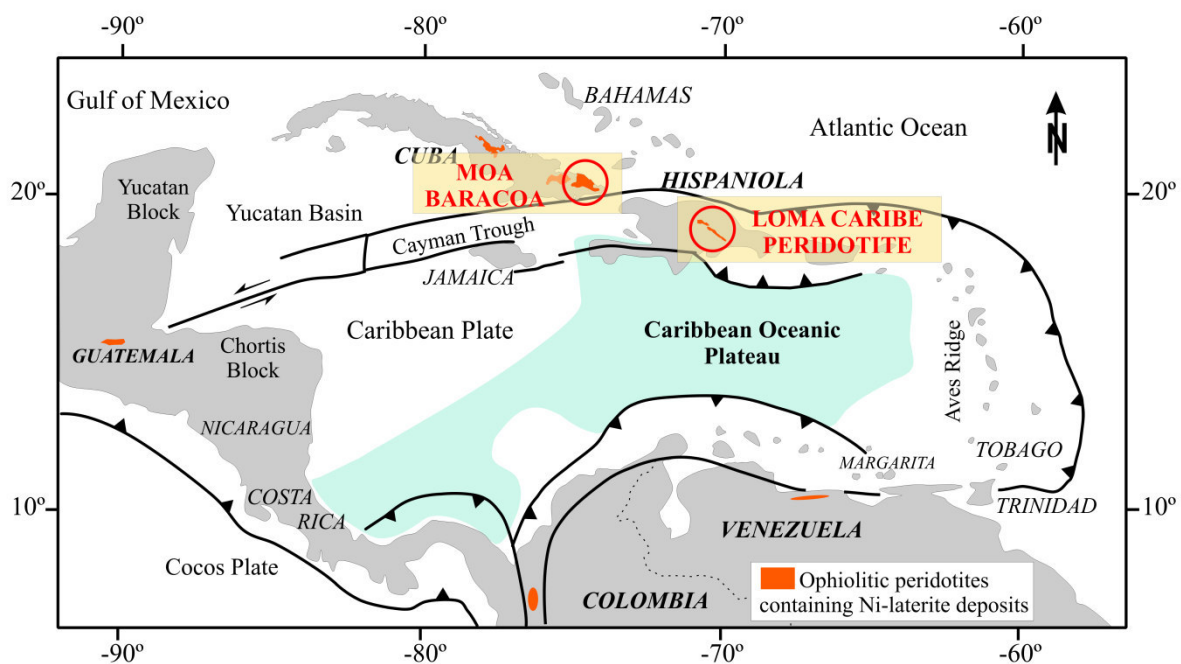


Fig. 2.1. Distribution of ophiolitic peridotites containing Ni laterite deposits around the margins of the Caribbean Plate; Ni laterite deposits from Moa-Baracoa (Cuba) and from the Loma Caribe peridotite (Dominican Republic) are highlighted. Modified from Lewis et al. (2006a).

2.1. The Moa Bay mining area

Ni laterites of the Moa Bay mining area form part of a ~100 km² large Ni laterite province in the northeast of Cuba (Pinares de Mayarí, Nicaro and Moa Bay mining areas), making it one of the largest reserves of nickel and cobalt in the world (Linchenat and Shirokova, 1964; Lavaut,

1998; Lewis et al., 2006a; Fig. 2.2a, b). The Moa Bay Ni laterites have developed from weathering of hydrated ultramafic rocks of the Moa-Baracoa ophiolitic massif. This massif forms the eastern part of the Mayarí-Baracoa ophiolitic belt in northeastern Cuba (Proenza et al., 1999a, b; Marchesi et al., 2006) and consists of mantle tectonites (>2.2 km) followed by a thin (~300 m) crustal section of lower

gabbros and discordant basaltic rocks with back arc basin affinity (Iturralde-Vinent et al., 2006; Marchesi et al., 2006; Proenza et al., 2006). The ultramafic rocks are mainly harzburgites (more than 70%) and lesser amounts of dunites. Concordant and sub-concordant bodies of dunite, sills of gabbro and chromitite bodies within a dunite envelope are also present. The degree of serpentinization is most in shear or fracture zones, where it reaches a maximum value of 95% relative to the whole rock (typical serpentinite). The peridotites are cut by dikes of gabbro, pegmatite gabbro, olivine norite and minor pyroxenite (Proenza et al., 1999a, b; Marchesi et al., 2006). The emplacement of the ophiolite took place in the Maastrichtian to early Danian with weathering, lateritization and subsequent ore deposit formation commencing during the Miocene (Iturralde-Vinent et al., 2006; Lewis et al., 2006a).

The Moa Bay Ni laterite mining area is classified as oxide type (Brand et al., 1998; Gleeson et al., 2003) and is divided into 9 ore deposits: Moa Occidental, Moa Oriental, Punta Gorda, Yagrumaje, Camarioca Norte, Camarioca Sur, La Delta, Cantarrana, and Santa Teresita (e.g. Lavaut, 1998) producing at least 34.263 t of Ni and 3.792 t of Co in 2012 (Sherritt, 2012).

2.1.1. The Ni laterite profile at Moa Bay

The laterite profile at Moa Bay has been divided into various zones and subzones by mine workers and Cuban geologists but the nomenclature of these zones does not follow the recommended classification for Ni laterite deposits (e.g. Lavaut, 1998; Proenza et al., 2007a; Golightly, 2010). In general five horizons can be recognized

from bottom to top that have been described in other Ni laterite deposits of the world: (i) parent rock peridotite, (ii) saprolite, (iii) lower limonite, (iv) upper limonite, (v) duricrust (Fig. 2.2c). Within the profile pale bauxitic zones of weathered gabbro (up to 5 m thick) are abundant. As typical in oxide type Ni laterite deposits the limonite horizons above the magnesium discontinuity (Butt and Cluzel, 2013) are dominant and can reach a total thickness of more than 50 m in the laterite profile. Moa Bay deposits usually lack hydrous Mg silicate rich saprolite horizons beneath the magnesium discontinuity, however, the thicker profiles have saprolite roots (Golightly et al., 2008).

The ore minerals are mainly goethite (~1.4 wt% Ni), minor maghemite (up to ~8 wt% Ni), lithiophorite (~8.1 wt% Ni, ~4.5 wt% Co) and “lithiophorite–asbolane intermediate” (up to 22 wt% Ni), which all occur in the limonite horizon of the profile (Proenza et al., 2007a; Roque-Rosell et al., 2010).

2.2. The Falcondo mining area

Located in the central part of the Dominican Republic the Falcondo mining area contains the largest hydrous Mg silicate type Ni laterite deposits of the Caribbean with measured and indicated Ni resources of 67.8 Mt at a grade of 1.5% Ni plus 4.9 Mt at 1.4% Ni inferred (Redwood, 2014). The Falcondo mining area is divided into 7 ore deposits: Loma Peguera, Loma Larga, Loma Cumpi , Loma Guardarraya, Loma Caribe, Loma Ortega and Loma Miranda (Haldemann et al., 1979; Lithgow, 1993; Lewis et al., 2006a).

2.2.1. The Ni laterite profile at Falcondo

The Ni laterite at Falcondo developed over the so called Loma Caribe peridotite which occurs as a serpentinized belt of ultramafic rocks approximately 4-5 km wide and 95 km long in the NW of Santo Domingo (Fig. 2.3a, b). The Loma Caribe peridotite is accompanied by two major metavolcanic units: 1) the Maimón Formation in the NE representing a primitive island arc tholeiitic unit of Lower Cretaceous age, and 2) the Duarte Complex in the SW representing mantle plume-related oceanic plateau basalts of Late Jurassic or at least Early Cretaceous age (Lewis et al., 2002; Lewis et al., 2006b; Escuder Viruete et al., 2007). Both units are unconformably overlain: the Maimón Formation by the Peralvillo Formation (volcanic arc andesites, diorites, basalts, tuffs, breccias and conglomerates of Late Cretaceous age) and the Duarte Complex by the Siete Cabezas Formation (volcanic arc basalts with minor tuffs and wackes of Cenomanian age) (Haldemann et al., 1979; Lewis et al., 2002; Proenza et al., 2007b). Dolerite and micro gabbro dikes occur within the peridotite belt and diorite bodies outcrop along its faulted margins (Lithgow, 1993; Escuder-Viruete et al., 2006).

According to Lewis and Jiménez (1991) the mineralogy and textural features of the ultramafic rocks indicate that the Loma

Caribe peridotite represents (serpentinized) harzburgitic oceanic mantle as part of a dismembered ophiolite complex. Recent geochemical studies reveal that the ultramafic rocks were formed as an evolving suprasubduction oceanic lithosphere (Lewis et al., 2006a; Marchesi et al., 2012) and have been partially serpentinized by hydrothermal reaction with sea water and by hydrothermal reactions during emplacement. The emplacement of the peridotites is believed to have been due to the collision of an oceanic plateau (Duarte terrane) with the primitive Caribbean island arc (Maimon-Amina-Los Ranchos terrane) resulting in thrusting of the peridotites in a northerly direction as early as late Albian (Draper et al., 1996; Lewis et al., 2002, 2006a).

Starting from early Miocene weathering has formed well-developed Ni laterites in the Dominican Republic showing similar features as other ophiolite-related hydrous Mg silicate Ni deposits found and exploited in the arcs of the West Pacific (Golightly, 2010; Butt and Cluzel, 2013; Villanova de Benavent et al., 2014). Mine geologists of Falcondo have subdivided and named the weathering profile into several zones (A-F) on the basis of Ni, Mg and Fe contents, textures and mineralogy (Fig. 2.4) (Haldemann et al., 1979; Lithgow, 1993; Lewis et al., 2006a; Villanova de Benavent et al., 2014; Aiglsperger et al., 2015).

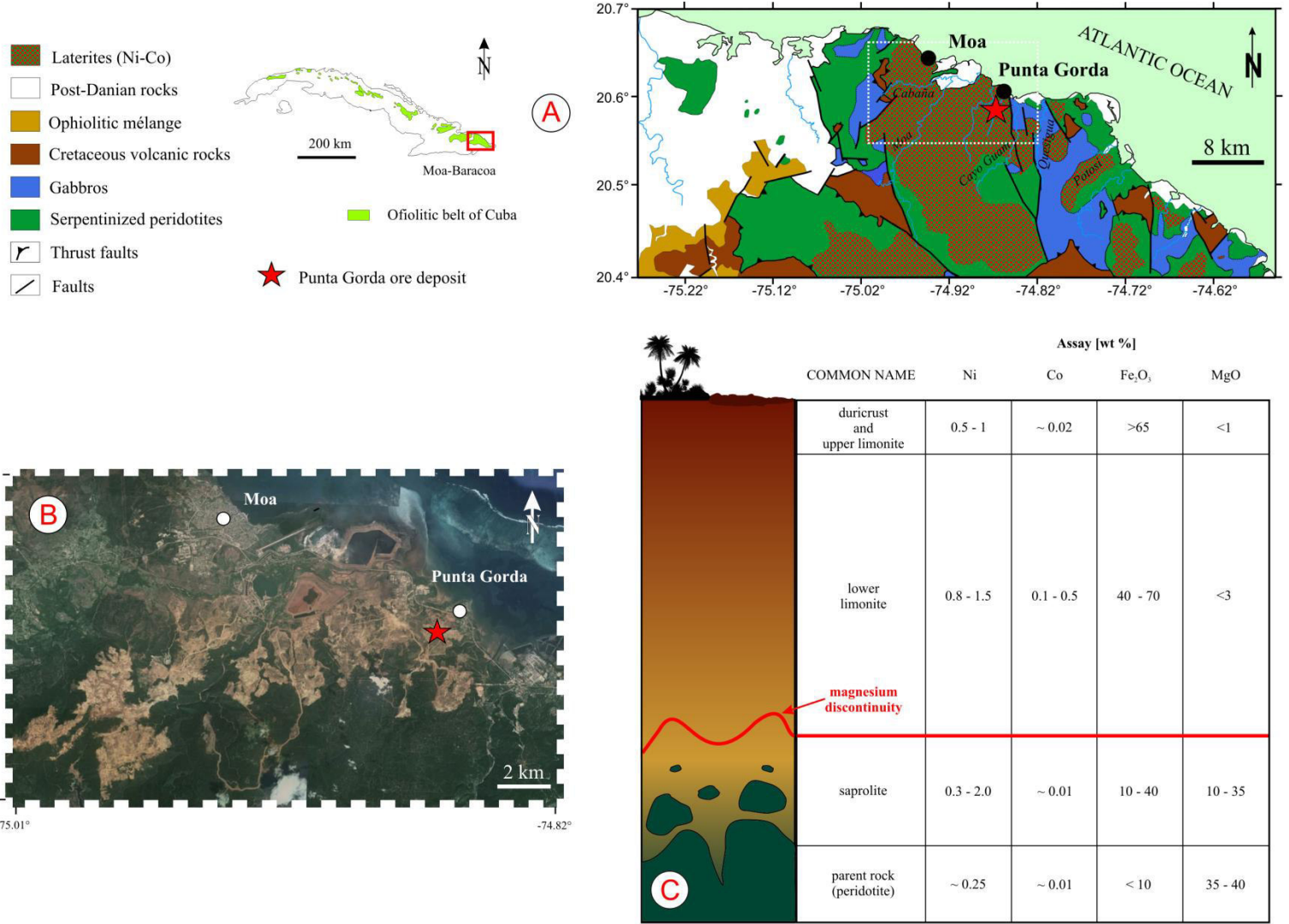


Fig. 2.2. A) Geographic location and simplified geological map of the Cuban study area (Moa-Baracoa) showing the location of the Punta Gorda ore deposit (modified from Marchesi et al., 2006). B) Orthophotograph showing the Moa Bay mining area with the Punta Gorda ore deposit; C) Idealized Ni laterite soil profile from Moa Bay ore deposits with characteristic assay results and in this work used terms (common name)..

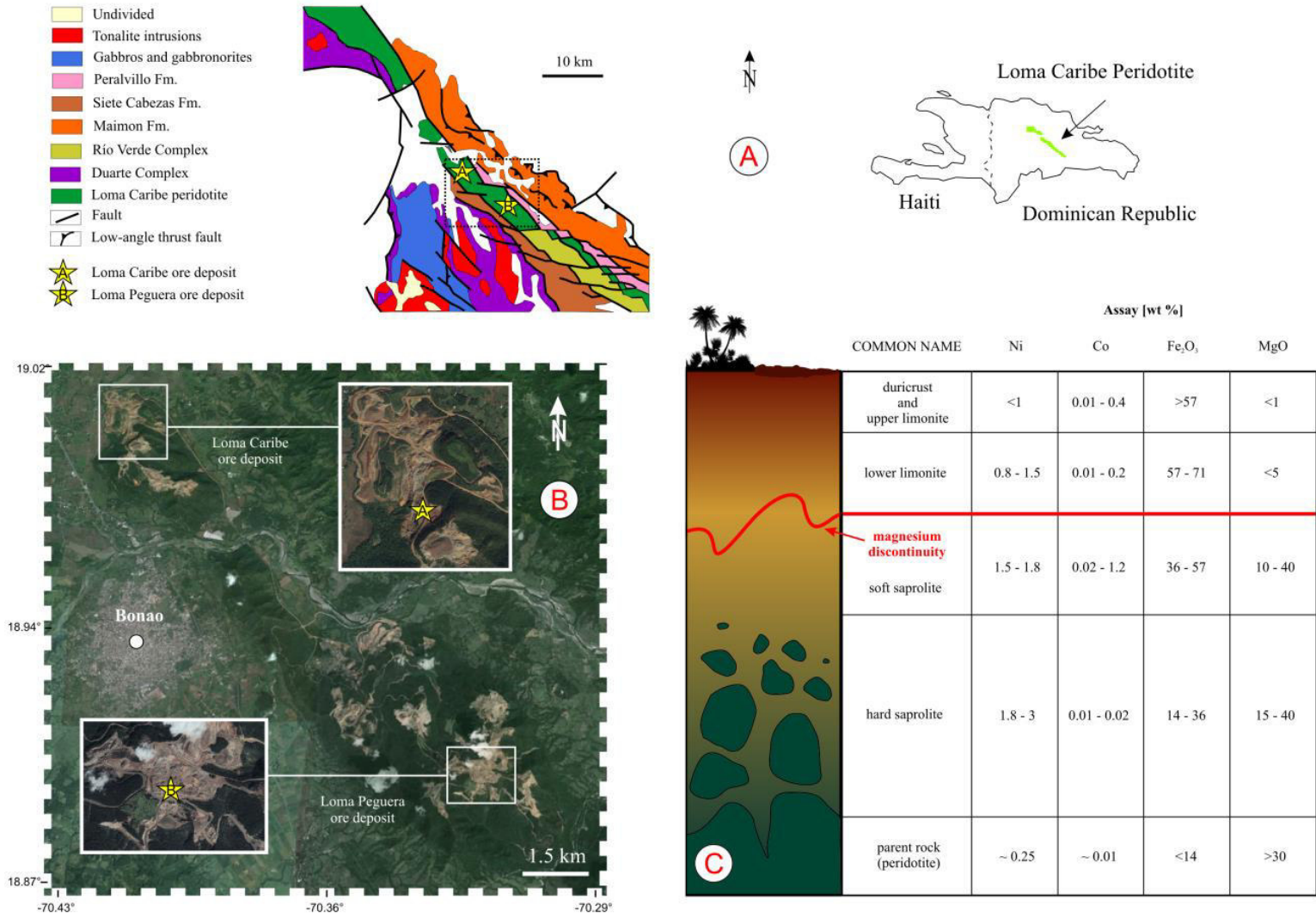


Fig. 2.3. A) Geographic location and simplified geological map of the central section of the Loma Caribe peridotite showing the location of the Loma Caribe and Loma Peguera ore deposits (modified from Bowin, 1966; Escuder-Viruete et al., 2007). B) Orthophotograph showing the Falcondo mining area with Loma Caribe and Loma Peguera ore deposits; C) Idealized Ni laterite soil profile from Falcondo ore deposits with characteristic assay results and in this work used terms.

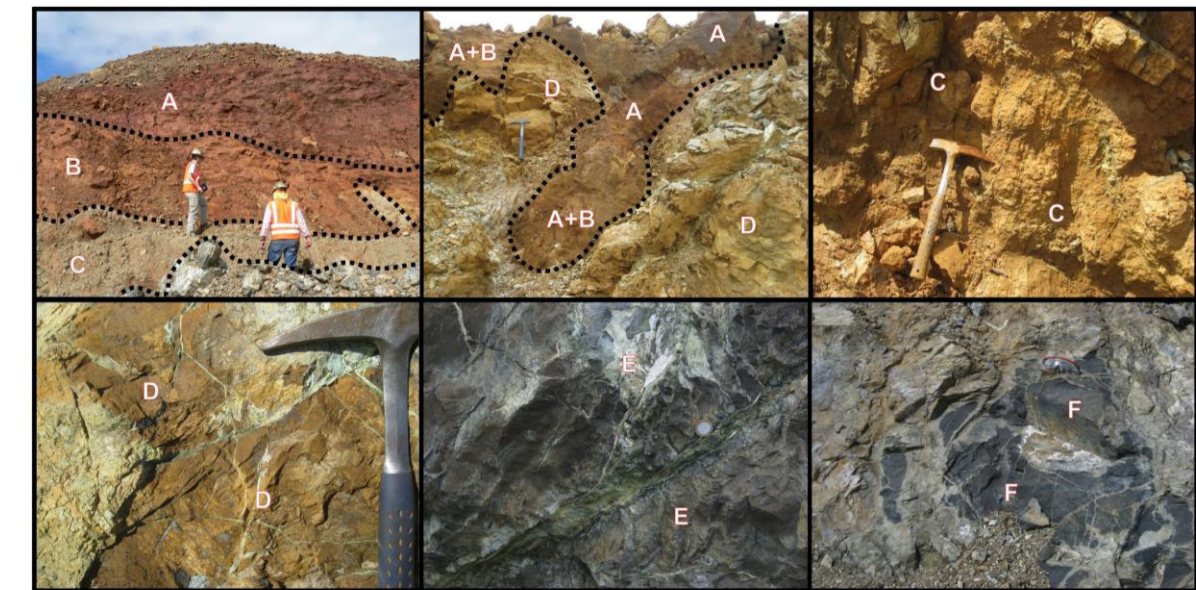
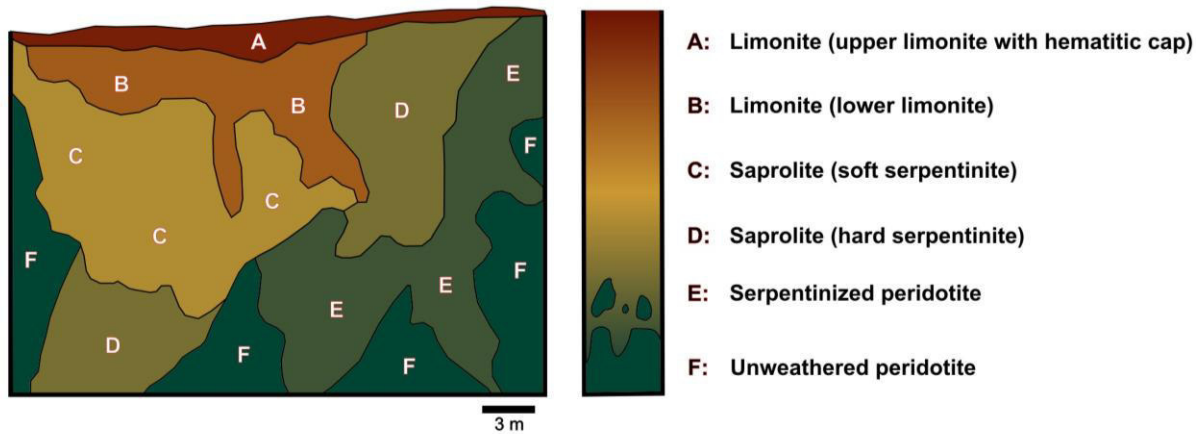


Fig. 2.4. Above: Ni laterite profile from Loma Caribe showing ore zones (A-F) defined by Falcondo mine workers with typical lateral and vertical variation (left) and idealized (right) (modified from Lewis et al., 2006a). **Beneath:** characteristic field observations of different ore zones (A: upper limonite with hematitic cap; B: lower limonite; C: soft serpentinite; D: hard serpentinite; E: serpentinized peridotite; F: unweathered peridotite).

Field observations and analytical studies realized during this work are in good agreement with the following description according to Haldermann (1979) and Lithgow (1993).

Zone A reaches depths of over 20 m on flat areas protected from erosion, but is extremely thin or absent on hill tops and steep slopes. Its typical chocolate brown colour and earthy texture is due to unconsolidated goethite as the main mineralogical component, whereas irregular pockets of gibbsite, scattered

boulders of serpentinized peridotite, traces of concretionary or vein silica and traces of relict chromian spinel, magnetite and Mn-Co-Ni oxyhydroxide (asbolane) are also present. Pisolites of hematite, up to 1 cm in diameter, occasionally occur. Contacts with the underlying zone B are usually sharp.

The volume of **zone B** is approximately twice that of zone A, and shows its greatest development on flat or gently dipping slopes. It is very compact and exhibits a clay-type texture (but without

clay component) with some plasticity, exhibiting reddish to yellowish brown colour. It mainly consists of goethite, with minor amounts of serpentine minerals near the contacts with the underlying zones of the laterite profile.

Zone C is soft displaying some plasticity when fresh and exhibits a large colour range from green to yellow to brown and red. The contact with limonite is usually abrupt, but can be transitional. It commonly shows relict original structures and may contain boulders of hard serpentine. In contrast to the macroscopically structureless limonite zone which has been affected locally by slumping and soil creep, this material is usually formed in place. It contains up to 20% by volume of boulders of hard serpentine, and these increase in proportion through mostly transitional contacts into zones D or E. The mineralogy of soft serpentine is transitional between that of the iron-rich layers of the limonite zones and the underlying Mg-rich zone. Lizardite is the dominant mineral phase, with goethite becoming more abundant at transitional contacts with zone B. Quartz may be abundant locally in the form of silica boxwork, up to 40% of the zone with attendant dilution in nickel grades ranging from 1.5-1.8 % Ni (Lewis et al., 2006a). Other veins of siliceous material consist of nickeliferous cryptocrystalline quartz, often accompanied by bright green garnierite minerals.

Hard serpentine (**zone D**) consists of 20-50 % angular boulder fragments, from 5-25 cm in diameter, set in a matrix of soft serpentine. The rocky fragments are usually of pale yellow ochre or a dark grey colour and often show concentric

alteration zones up to 5 cm in thickness. Most outer skins are enriched in nickel (up to 3% Ni) and there is a gradual inward decrease to a core which assays from 0.3 to 0.6 % Ni. Many of the boulders are transected by serpentine veinlets which are also enriched in nickel. Serpentine mineral content and nickel enrichment in the laterite profile reach their peak in this zone.

Zone E, serpentinized peridotite, is normally found at the bottom of the ore sequence. It is composed of 50-70 % by volume of usually >25 cm diameter massive angular joint fragments with smaller amounts of soft serpentine matrix. Fracture fillings and coatings of garnierite, up to 5 mm wide, enrich the zone to ore grade. Narrow silica boxwork veins also follow along joint planes, often with infillings of serpentine, garnierite and yellowish limonite. Along fault zones, quartz veins or breccia fragments of zone D cemented by quartz may occur up to one-half meter wide. Except for its generally lower nickel content, its major element composition is essentially identical to that of zone D. It has the highest content of primary ferromagnesian minerals (olivine and enstatite) of the ore zones.

Zone F is unweathered peridotite consisting mostly of coarse-grained harzburgite, clinopyroxen-rich harzburgite, lherzolite, fine grained black dunite and sheared greenish black serpentinite. This zone is rarely of ore grade, but can be if sufficiently fractured and penetrated by fracture fillings of garnierite (Tauler et al., 2009; Villanova-de-Benavent et al., 2014). It normally constitutes the barren bedrock below the highly irregular bottom of the

orebody, although some inclusions within zone E may occasionally attain ore grade values. Chemically, it is characterized by very low nickel and iron values ($\sim 0.25\%$ and $<14\%$ wt%, respectively) and moderately high magnesium ($>30\%$).

However, to simplify comparison with the investigated Ni laterite profile of Moa Bay the laterite profile of Falcondo was termed for this study from bottom to top: (i) parent rock peridotite, (ii) hard saprolite, (iii) soft saprolite, (iv) lower limonite, (v) upper limonite and duricrust (Fig. 2.3c).

Ore minerals are mainly Ni-lizardite and poorly defined varieties of Ni containing

serpentine, talc, chlorite and sepiolite, commonly termed as “garnierites” (up to 49 wt% NiO). These are found mainly within the lower part of the saprolite horizon (Villanova de Benavent et al., 2014).

As pointed out earlier, weathering horizons of both Ni laterite mining areas (i.e. Moa Bay and Falcondo) are erratically developed and complete profiles as shown in Fig. 2.2c and Fig. 2.3c are extremely rare. Figure 2.5 shows some additional field impressions.

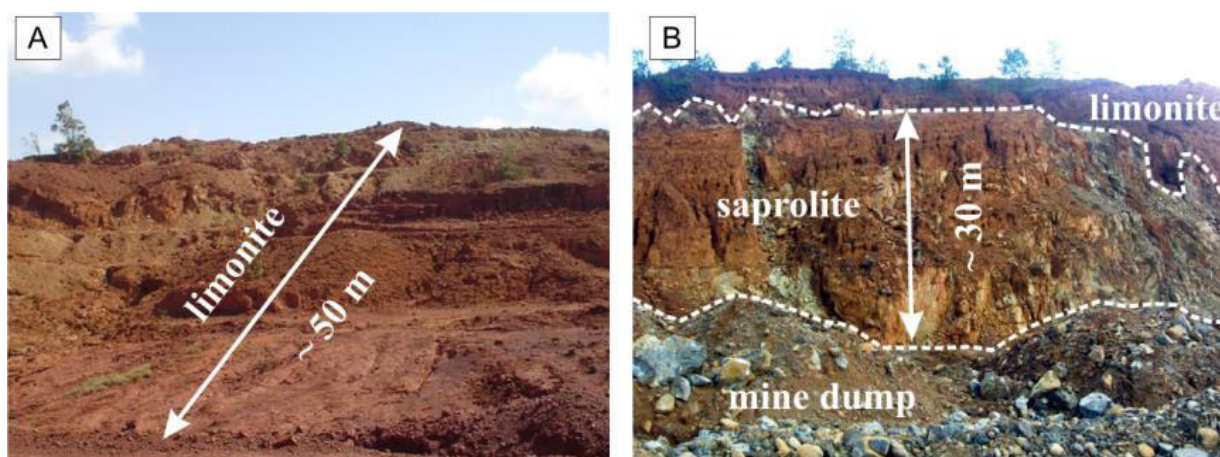


Fig. 2.5. Characteristic field observations of A) limonite horizon dominated ore deposits from the Moa Bay mining area and B) saprolite horizon dominated ore deposits from the Falcondo mining area.

Chapter 3

Materials and Methods

3.1. Sample selection

3.1.1. Moa Bay mining area (Cuba)

Nine samples were selected out of a collection of 21 samples (~1 kg each), representing characteristic levels of one Ni laterite profile approximately 3 km to the south of Punta Gorda (see chapter 2 Fig. 2.2a, b and chapter 4 Fig. 4.2). The profile is ~40 m thick and consists of a 2 m thick layer of duricrust and upper limonite, a 33 m thick package of lower limonite including zones rich in Mn oxide(s) and a 5 m thick zone of soft and hard saprolite overlying serpentinized peridotite (see chapter 4 Fig. 4.2). Parent rocks of Ni laterites from Moa Bay are mainly unweathered harzburgite which have been analysed previously by Marchesi et al. (2006). Average values of unweathered harzburgite from this publication were taken for this investigation.

3.1.2. Falcondo mining area (Dominican Republic)

Two Ni laterite profiles, approximately 13 km apart, were studied, i.e. Loma Caribe and Loma Peguera (see chapter 2 Fig. 2.3a, b).

At Loma Caribe a total of 18 samples (~3 kg each) were collected from different levels of a 16 m thick weathering profile consisting of 2 m upper limonite including an about 10 cm thick layer of clay minerals, 5 m lower limonite, 8 m soft and

hard saprolite, 1 m serpentinized peridotite and underlying unweathered dunite (see chapter 4 Fig. 4.5). A selection of 9 samples from different horizons was chosen for a detailed characterisation of the profile.

At Loma Peguera the 16 m thick weathering profile is characterized by a 2 m thin cover of upper limonite underlain by 13 m of saprolite including rare chromitite bodies a few metres thick, overlying dunites (see chapter 4 Fig. 4.6). In total 19 samples were collected. However, eight characteristic samples (~3 kg each) were chosen from indicated horizons for subsequent detailed investigation (see chapter 4 Fig. 4.6).

3.2. Whole rock geochemical analyses

3.2.1. Major, minor and lithophile trace elements

Major, minor and lithophile trace elements of weathering samples from Moa Bay were determined at the Actlabs Laboratories (Ontario, Canada) by X-ray fluorescence (XRF) and ICP mass spectrometry (ICP-MS), respectively. Weathering samples from Falcondo were analysed by the same methods at the University of Granada (see Lázaro et al., 2013 for details on the applied analytical techniques). Hard rock samples of unweathered peridotite were analysed for major, minor and trace elements at the ISTEEM (Universite'

Montpellier II, Montpellier, France; see Marchesi et al., 2006 for details on the applied analytical techniques).

3.2.2. PGE

All selected samples were analysed at Genalysis Ltd. (Maddington, Western Australia) by ICP-MS after nickel sulfide fire assay collection following the method described by Chan and Finch (2001). In this method, 25 g of homogenised sample is fused with a flux containing borax, soda ash, silica, nickel oxide, and sulphur. Fusion was performed at 1200°C to ensure all chromite grains are completely fused and all PGE are collected by the nickel sulphide. In continuation the nickel sulphide button is dissolved with hydrochloric acid at about 100°C. The undissolved PGE and gold sulphides are then collected on a cellulose nitrate membrane filter and later digested with aqua regia in sealed borosilicate test tubes. The resultant solution is diluted with 10% v/v nitric acid and thoroughly mixed. The final solution is analysed by a Perkin Elmer/Sciex Elan 6000 ICP-MS. Six calibrating standard solutions are used and all standards and samples are spiked with two internal standards for drift monitoring. Internationally certified reference material (South African Reference Material SARM-7) and in-house standards are used in any analysis batch. The PGE isotopes measured are ^{99}Ru , ^{101}Ru , ^{102}Ru , ^{103}Rh , ^{105}Pd , ^{106}Pd , ^{108}Pd , ^{189}Os , ^{193}Ir , ^{195}Pt , and ^{196}Pt . The results are corrected for interferences produced by Ni and Cu argides. Detection limits are 1 ppb for Rh, and 2 ppb for Os, Ir, Ru, Pt, and Pd.

3.3. Mass balance calculations

Mass balance calculations were achieved by using the open source software GCDkit 3.00 (www.gcdkit.org) and its implementation for ISOCON mass balance calculations after Grant (1986, 2005). This method is a graphical approach to the mass transfer equation used by Gresens (1967) which can determine element mobility in a great variety of different rocks. According to this technique, when the compositions of unaltered and altered rocks are plotted as variables, the immobile elements must lie on a straight line (isocon) which passes through the origin. The reciprocal slope gives the total mass change during the alteration process while the deviation of points for mobile elements above and below the isocon gives the gain or loss, respectively, of each component in the altered rock with respect to the original.

3.4. X-ray diffraction analyses

X-ray powder diffraction measurements were performed on homogenised sample aliquots in a Bragg-Brentano $\theta/2\theta$ Siemens D-500 diffractometer (radius = 215.5 mm) with Cu $K\alpha$ radiation, selected by means of a secondary graphite monochromator. The divergence and receiving slits were of 1° and 0.15° respectively. The starting and the final 2θ angles were 4° and 80° respectively. The step size was 0.03° 2θ and the measuring time of 18 seconds per step. The software X'Pert Highscore® was used to subtract the background of the patterns, to detect the peaks and to assign mineral phases and their corresponding d_{hkl} to each peak.

3.5. Mineralogical methodology: challenge and uncertainty

The traditional *in situ* technique is the most used to investigate minute amounts of accessory mineral phases such as PGM. It consists of the study of polished sections by reflected light optical microscopy (OM), scanning electron microscopy (SEM) and by electron microprobe analysis (EMPA) (see beneath). In many studies this technique proved to be an efficient tool to investigate consolidated rocks relatively enriched in PGE, such as chromitite (Garuti et al., 2007, 2012; and references therein). However, the investigation of saprolite and limonite samples requires careful heavy mineral concentration techniques such as in this study applied innovative hydroseparation (HS) techniques (Rudashevsky et al., 1995, 2002; Cabri et al., 2006).

3.5.1. The HS laboratory Barcelona

The HS laboratory (www.hslab-barcelona.com), installed at the University of Barcelona in 2011 (Fig. 3.1), aims to simulate natural beach placer deposits by a combination of laminar water flow at constant pressure with diverse wave impulses. Dense mineral phases (e.g. gold, PGM, zircon) are collected at the bottom of a so called Glass Separation Tube (GST), whereas light particles (e.g. quartz, feldspar, etc.) rise to the top of the GST and leave the system. Using different GSTs, flow rates and impulse regimes the total amount of final heavy mineral concentrates for each size fraction is reduced to about 10 mg. This method has been successfully applied to rock samples previously (e.g. Cabri et al., 2008). However, for this study the method has been adapted for limonite samples and follows Aiglsperger et al. (2011).



Fig. 3.1. Hydroseparation laboratory Barcelona (www.hslab-barcelona.com); 1 water tank; 2 flowmeters; 3 software controlled HS-11 device; 4 Glass Separation Tubes (GST).

3.5.1.1. Sample preparation

Two saprolite samples (LP 4 and LC 8; 3 kg each) and three samples from the exposed limonite horizon (LP-11-007: 2 kg; LP 1: 3.5 kg and LC 2: 0.5 kg) as well as chromitite samples from Loma Peguera 1 (LP6; 0.5 kg) and from Loma Larga (LL, 100 g) were processed.

The chromitite samples were crushed by a jaw crusher and sieved through a 125 μm testing sieve. Subsequently the coarse size fraction was grinded via an agate mill and wet sieved by hand through standard screen series resulting in a size fraction distribution between +125 μm and -53 μm . Soft rock samples were dispersed in water and roughly homogenized by taking out (hand sorting) gravel-sized fragments. For pre-concentration the sample slurries were successively filled into a 250 ml bowl and processed for approximately 10

seconds in a round ultrasonic bath, whereas small, less dense minerals were decanted as tailing. Depending on the initial composition of the slurry this procedure had to be repeated up to five times, with water added after each decantation until the remaining slurry was mainly composed of typically dark coloured, heavy mineral phases. The ultrasonic concentration products were carefully wet sieved by hand through standard screen series resulting in a size fraction distribution between +125 μm and -53 μm . A flow sheet of all necessary steps previous to hydroseparation for limonite samples is given in Fig. 3.2. A CNT Spark-2 Electric Pulse Disaggregation device (CNT Laboratory, St. Petersburg, Russia) was used to crush one hard saprolite sample from zone D (LP-4) and to liberate accessory minerals.

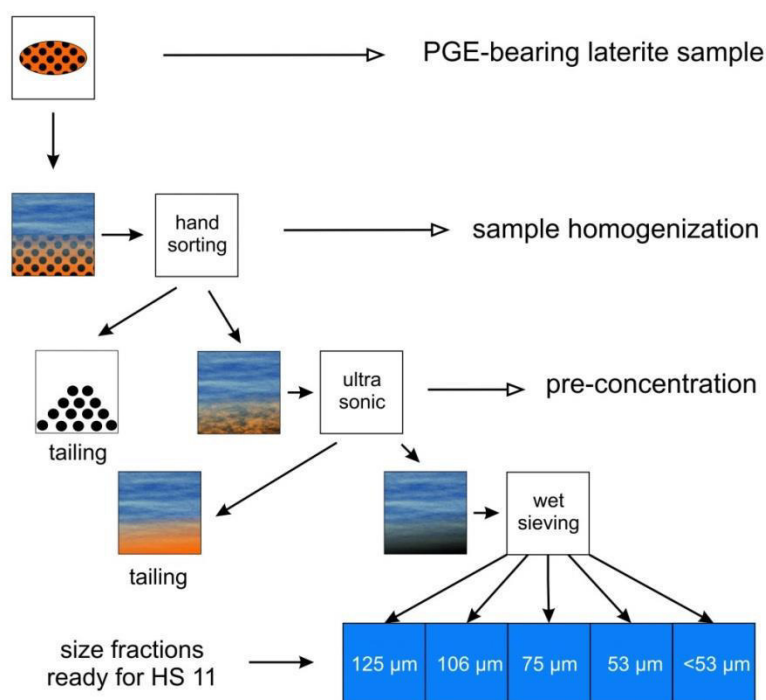


Fig. 3.2. Flowsheet explaining sample preparation of soft rocks before hydroseparation (Aiglsperger et al., 2015).

3.5.1.2. Hydroseparation

Each size fraction was processed by means of the above hydroseparation technique in laboratories in St. Petersburg (saprolite sample) and Barcelona (limonite samples). Heavy mineral concentrates were obtained by using the computer-controlled device CNT HS 11 (Rudashevsky et al., 2001; Rudashevsky and Rudashevsky 2006, 2007; and see <<http://www.cnt-mc.ru/>>). The separation process was accomplished in two steps: (1) preparation of a pre-concentrate by using a 30 cm long glass separation tube (GST) (inner Ø 8 mm); (2) preparation of the final concentrate by using a short (10 cm long) GST (inner Ø 5 mm).

3.6. Scanning Electron Microscopy (SEM and FE-SEM)

Thin sections, in situ polished sections and heavy mineral monolayers were studied with a scanning electron microscope Quanta 200 FEI XTE 325/D8395 and with a field emission scanning electron microscope Jeol JSM-7100 at the Serveis Científics i Tecnològics, University of Barcelona, Spain.

3.7. Electron Microprobe analyses (EMPA)

Quantitative electron-microprobe analyses were obtained in WDS mode, operating with an accelerating voltage of 20 kV, a beam current of 10 nA and a beam diameter of 1 µm with a CAMECA SX50 at the Serveis Científics i Tecnològics, University of Barcelona. Analytical

conditions are summarized in McDonald et al. (2010) and were used for the investigation of PGM found in saprolite. At the same institution PGE grains with complex textures were investigated by element-distribution maps using a JEOL JXA-8230 electron microprobe with an accelerating voltage of 20 kV and a beam current of 128.8 nA. Maps were collected by beam scanning with dwell times of 60 ms/pixel. For each element, the background map was subtracted from the corresponding peak map.

Quantitative electron microprobe analyses of chromian spinels and PGM from the limonite and chromitites were obtained with the same instrument in wavelength-dispersive spectroscopy (WDS) mode, operating with an accelerating voltage of 20 kV, a beam current of 20 nA, and a beam diameter of 1 µm. Pure metals were used as standards for Os, Ir, Ru, Rh, Pt, Pd, Co, Sb and V as well as chromite (Cr, Al, Fe), periclase (Mg), rhodonite (Mn), rutile (Ti), NiO (Ni) and S (S), CuFeS₂ (Cu), GaAs (As) and wollastonite (Si). The proportion of Fe³⁺ in chromian spinel was calculated assuming stoichiometry.

The following interferences RuLβ → RhLα, IrLα → CuKα, RhLβ → PdLα, RuLβ → PdLα, CuKβ → OsLα, and RhLα → PtLα were online corrected.

3.8. Micro-Raman spectroscopy

Micro Raman maps were achieved by using a Thermo Scientific™ DXR™xi Raman imaging microscope. The studied area (35 µm x 17 µm) was mapped at a laser power of 2 mW, the exposure time was 1 sec with 5 scans and the pixel size was 1 µm, thus resulting in 595 spectra collected within 67

min. Obtained raw data were treated with Thermo Scientific OMNIC™xi Raman imaging software.

3.9. Laser ablation-inductively coupled plasma-mass spectrometry (LA ICP-MS)

An Element 2 high resolution mass spectrometer coupled with a 213-nm NdYAG UP-213 laser ablation system placed at the Institute of Geology, Prague (The Czech Academy of Science) was used to acquire the trace element data. The following isotopes were measured at the low mass resolution mode ($m/\Delta m = 300$): ^{45}Sc , ^{57}Fe , ^{89}Y , ^{90}Zr , ^{99}Ru , ^{101}Ru , ^{103}Rh , ^{104}Pd , ^{108}Pd , ^{110}Pd , ^{111}Cd , ^{139}La , ^{140}Ce , ^{141}Pr , ^{146}Nd , ^{147}Sm , ^{151}Eu , ^{159}Tb , ^{160}Gd , ^{161}Dy , ^{165}Ho , ^{166}Er , ^{169}Tm , ^{172}Yb , ^{175}Lu , ^{185}Re , ^{189}Os , ^{193}Ir and ^{195}Pt .

Trace elements, REE and PGE were calibrated against the synthetic silicate standard glass NIST SRM 610 (Jochum et al., 2011). The isotope ^{57}Fe was used as the internal standard. All standards were run before and after each set of 10 unknowns.

Polished resin blocks were used for in situ laser ablation analyses. Both external standards and measured samples were analysed at identical conditions: laser ablation repetition rate of 10 Hz, the laser fluence of 5–7 J/cm² and 55 μm beam spot. Data for the gas blank were acquired for 35 s followed by 35 s of laser ablation signal. The washout time was 120 s between measuring of individual laser spots. Samples were ablated in an in-house small volume ablation cell, a construction which was inspired by conception of Kooijman et al. (2012). The ablated

material was transported by a high purity He gas from the laser ablation cell at a flow rate of 0.4–0.6 l/min.

The time-resolved signal data of spot analyses were processed using the Glitter software (van Achterbergh et al., 2001). The precision of the laser ablation analyses (as relative 1 sigma error – RSD) ranges between 5 and 15 % for most of the detected elements.

3.10. Synchrotron through-the-substrate X-ray microdiffraction (tts-μXRD)

The synchrotron through-the-substrate X-ray microdiffraction (tts- μXRD) is an innovative, new technique which allows the structural characterisation of crystalline mineral phases *in situ* within standard polished sections (Rius et al., 2011; Rius et al., 2015). These authors confirmed that by using synchrotron radiation microvolumes down to 15x15 μm² can be analysed. Basic steps of the procedure are summarized in Rius et al. (2015). Regarding the in this work studied Ru-Os-Fe grain, the grain bearing monolayer polished section was first transformed to a thin section (30 μm thick) attached to an approximately <1 mm thick glass substrate. Subsequently, the X-ray diffraction information was obtained by rotating the thin section with the selected microvolume at the origin (Arndt & Wonacott, 1977) and processed with Bruker software (TOPAS).

The diffraction experiments were performed on the MSPD beamline at the ALBA Synchrotron Facility-CELLS, Cerdanyola del Valle's, Barcelona, 08920, Spain.

3.11. Osmium isotopes

In situ Re-Os isotope analyses on PGM were carried out at GEMOC (Australia) using a LA-MC-ICPMS following the analytical routine described by González-Jiménez et al. (2012):

A New Wave/Merchantek UP 213 laser microprobe with a modified ablation cell was coupled with a Nu Plasma Multicollector ICP-MS. During the analysis of PGM all ion beams were collected in Faraday cups. The laser was fired at a frequency of 4 Hz, with energies of 1–2 mJ/pulse and a spot size of 15 μm . The analyses of BMM used a combination of Faraday cups and ion counters. The laser was fired at a frequency of 5 Hz, with energies of 1–2 mJ/pulse and spot size of 80 μm . During ablation runs, a standard NiS bead (PGE-A) with 199 ppm Os (Lorand and Alard, 2001) and $^{187}\text{Os}/^{188}\text{Os} = 0.1064$ (Pearson et al., 2002) was analysed between samples to monitor and correct any drift in the Faraday cups and ion counters. These variations were much less than 0.1% over a day's analytical session. During both types of analysis, a dry aerosol of Ir was bled into the gas line between the ablation cell and the ICP-MS to provide a mass-bias correction with a precision independent of the abundance of Os in the unknown. The overlap of ^{187}Re on ^{187}Os was corrected by measuring the ^{185}Re peak and using $^{187}\text{Re}/^{185}\text{Re}=1.6742$. All the analysed grains have $^{187}\text{Re}/^{188}\text{Os} < 0.5$, thus ensuring that the isobaric interference of ^{187}Re on ^{187}Os could be precisely corrected (c.f. Nowell et al., 2008). The data were collected using the Nu Plasma time-resolved software, which allows the selection of the most stable

intervals of the signal for integration. The selected interval was divided into 40 replicates to provide a measure of the standard error. An internal precision for $^{187}\text{Os}/^{188}\text{Os}$ typically of $3\text{E}-4$ (2 SE) was obtained for PGM. γOs and model ages have been calculated relative to the Os-isotope evolution of the Enstatite Chondrite Reservoir (ECR, present-day $^{187}\text{Os}/^{188}\text{Os}=0.1281$, $^{187}\text{Re}/^{188}\text{Os}=0.421$, Walker et al., 2002). The ECR has been shown to reproduce the Os isotopic evolution of the convecting mantle and has been used previously as a reference for the Os isotopic composition of PGM in podiform-like chromitites (Marchesi et al., 2011; Shi et al., 2007). The quoted uncertainties on TMA and TRD model ages include the uncertainties in the measured $^{187}\text{Os}/^{188}\text{Os}$ and $^{187}\text{Re}/^{188}\text{Os}$, calculated using the equation of Sambridge and Lambert (1997).

Chapter 4

Abundance and distribution of critical metals (REE, Sc, PGE) in Ni laterites from Cuba and the Dominican Republic

4.1. Introduction

The Rare Earth Elements (REE), Platinum Group Elements (PGE) and scandium (the so-called “High Tech metals”) are elements with special chemical and physical properties needed for sophisticated technical applications associated with renewable energy, reduction of greenhouse gases and energy efficiency (green technologies). The rapidly growing market in this sector (e.g. production of permanent magnets, cell phones, electric cars, wind turbines) led to an increasing demand of these metals over the last few years (e.g. Chakmouradian and Wall, 2012; Hein et al., 2013). In 2014, the EU Commission assessed 54 materials (metallic ore, biotic material and industrial minerals) on their criticality for Europe’s industry on the basis of their high economic importance and their high relative supply risk (EC, 2014). 20 raw materials were identified as critical including REE and PGE (Fig. 4.1).

In 2010, the unexpected drastic reduction of export quotas for REE by the Chinese government revealed the vulnerability of western high tech industries. As a consequence, new exploration projects have been initiated worldwide. However, to be competitive these deposits must be large in scale, easily accessible (open pit mining) with favourable ore mineralogy

from a metallurgical point of view and tolerable environmental impact.

With respect to PGE, being essential for gasoline-engine catalytic converters in the car industry and in other high tech applications, an estimated 82% of the currently mined PGE come from only two major ore deposits in South Africa (Bushveld complex) and Russia (Norilsk) (USGS, 2013). Supply risks and price instabilities can occur when producers suffer full-scale mine shutdowns as seen during several strikes held by mining workers in South Africa 2013 (USGS, 2013), or when political environments change in times of crisis (e.g. 2015 EU – Russia sanctions during Ukraine crisis).

Ore deposits associated with near-surface modification of ultramafic rocks could help to minimize supply risks of these critical metals (CM) (e.g. Wilde et al., 2003). Ni laterites are considered worthy targets for CM exploration as REE, Sc and PGE can be concentrated during weathering as a result of residual and secondary enrichment (e.g. Maksimovic´ and Pantó, 1996; Economou-Eliopoulos et al., 1997; Eliopoulos and Economou-Eliopoulos, 2000; Audet, 2009; Ndjigui and Bilong, 2010; Wang et al., 2011; Eliopoulos et al., 2014). In addition, changing Eh-pH conditions at higher levels of the laterite profile and subsequent interactions within the biosphere can favour mobility, reprecipitation and

concentration of these elements (Aiglsperger et al., 2015).

Ni (\pm Co) laterite deposits account for about 60% of the current world's annual Ni production and host 60 to 70% of the world land-based Ni resources (Butt and Cluzel, 2013). In this context Cuba and the Dominican Republic host some of the world's most important Ni laterite deposits. They formed by weathering of ophiolitic serpentized peridotites in the Tertiary as a result of tropical climate conditions (e.g. Linchenat and Shirokova, 1964; Haldemann et al., 1979; Lithgow, 1993; Lavaut, 1998; Lewis et al., 2006a). They have been mined since 1943 when the Nicaro processing plant (eastern Cuba) went into production (Nelson et al., 2011). The Ni laterite deposits currently being mined are located in eastern Cuba (Moa

Bay mining area) and the central Dominican Republic (Falcondo mining area). According to the mineralogy of principal ore-bearing phases, the Moa Bay ore deposits are classified as oxide type, and Falcondo ore deposits as hydrous Mg silicate type (Brand et al., 1998; Lewis et al., 2006a). In this study, geochemical and mineralogical data from two different nickel laterite types (i) from the Moa Bay mining area (eastern Cuba) and (ii) from the Falcondo mining area (Dominican Republic) is presented, with emphasis on their potential to accumulate CM and on processes involved. The underlying idea of this investigation is that these elements could be produced as by-products additionally to approximately 130 000 tons of Ni annually produced in active plants in the Caribbean (Nelson et al., 2011).

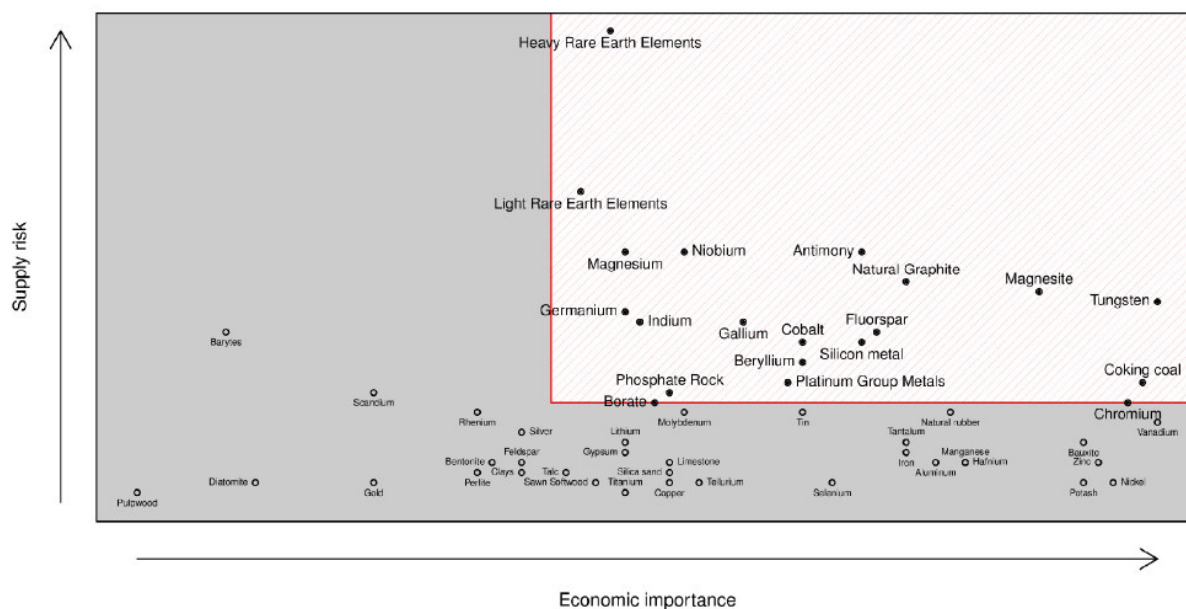


Fig. 4.1. Criticality assessment at EU level on raw materials carried out by the European Commission in 2013 (EC, 2014). REE and PGE plot within the red criticality field.

4.2. Geochemistry

4.2.1. Moa Bay

Figure 4.2 shows the general geochemical trend within the oxide type laterite from Moa Bay with respect to the distribution of major elements (Fe, Al, Si and Mg), relevant minor elements (Ni, Co and Mn) and CM (REE = La + Ce + Nd + Sm + Eu + Tb + Yb + Lu, Sc and PGE = Os, Ir, Ru, Rh, Pt, Pd). Mg and Si are main components in the saprolite (~40 wt%) but extremely depleted in the limonite where Fe and Al prevail (~65 wt% and ~10 wt% respectively) (Fig. 4.2).

Ni shows significant enrichment (2.3 wt%) at the transition zone between saprolite (~0.5 wt%) and lower limonite (~1 wt%) (Fig. 4.2). Co enrichment up to 0.65 wt% is observed within zones of significant Mn oxide(s) accumulation (up to 4.2 wt% MnO) (Fig. 4.2).

Critical elements are enriched in the limonite, especially within zones with elevated concentrations of Mn oxide(s) as well as towards the surface (Fig. 4.2). Total REE concentrations are low in the unweathered harzburgite (~0.1 ppm) and vary from 1 to 3 ppm in the saprolite and from 15 to 68 ppm in the limonite (Table 4.1).

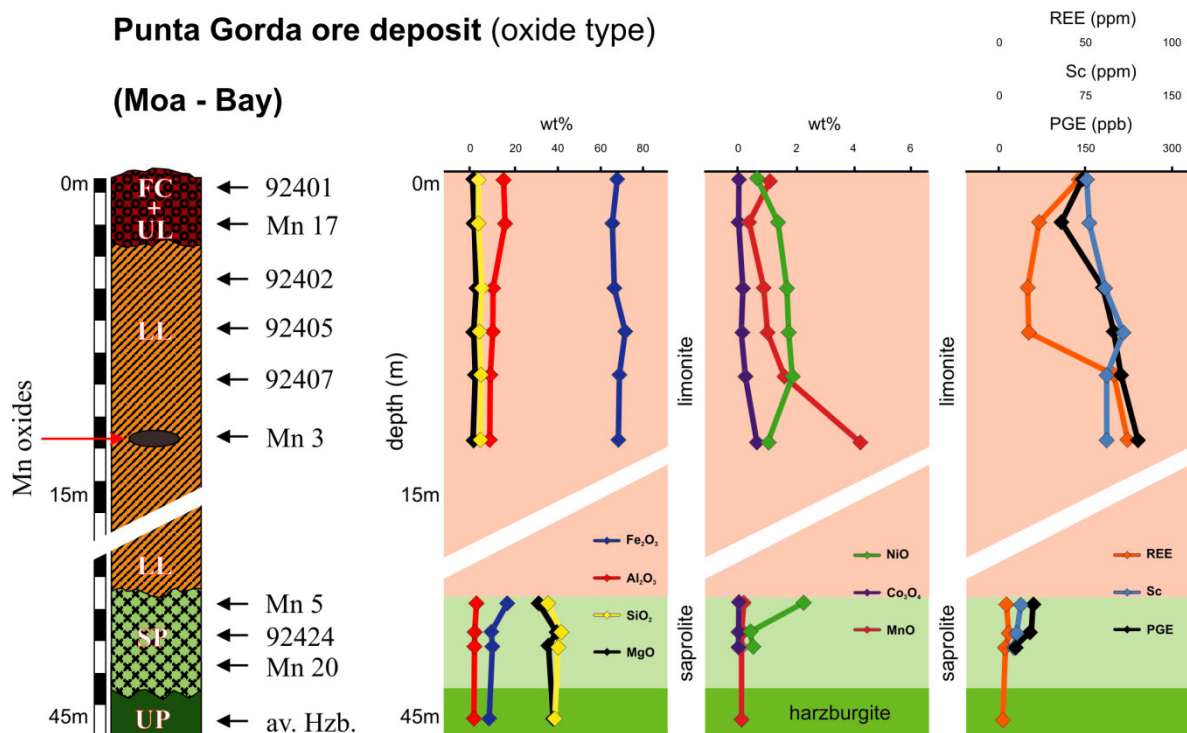


Fig. 4.2. Ni laterite profile from the Punta Gorda ore deposit (Moa Bay) showing location of samples with major, relevant minor and CM contents. Values for the parent rock (harzburgite) *av. Hzb.* are taken from Marchesi et al. (2006).

	Punta Gorda ore deposit, oxide type (Moa Bay)										Loma Caribe ore deposit, hydrous Mg silicate type (Falcondo)										Loma Peguera ore deposit, hydrous Mg silicate type (Falcondo)									
	92401 DC + UL	Mn 17 DC + UL	92402 LL	92405 LL	92407 LL	Mn 3 LL	Mn 5 SP	92424 SP	Mn 20 SP	av. Hzb. UP	LC-11-001 DC + UL	LC-1 UL	LC-2 UL	LC-5 UL	LC-6 LL	LC-7 LL-SS	LC-8 HS	LC-9 HS	C-629 UP	LP-11-007 A DC + UL	LP-11-008 B UL	LP-3 HS	LP-2 HS	LP-5 HS	LP-4 HS	LP-7 HS	LP-101 UP			
wt%																														
SiO ₂	2.72	2.69	4.35	3.18	3.92	3.58	35.17	41.36	39.43	38.59	6.46	14.60	6.64	9.79	3.82	2.16	41.27	45.67	43.03	17.21	11.15	44.37	40.07	41.19	44.04	39.98	39.84			
Al ₂ O ₃	14.52	15.00	9.59	9.16	8.26	7.98	1.84	1.04	0.94	0.64	31.82	14.16	9.72	23.37	9.39	17.67	1.19	1.15	1.76	26.27	3.50	1.86	0.07	0.58	0.26	5.67	0.84			
Fe ₂ O ₃	68.03	65.81	66.75	71.83	69.13	68.66	16.17	9.22	9.28	7.81	40.10	55.97	65.55	42.59	67.31	50.60	13.24	12.14	8.59	35.71	72.24	16.86	9.41	14.10	14.59	7.80	8.44			
MnO	1.07	0.38	0.83	1.02	1.60	4.24	0.18	0.12	0.12	0.11	0.26	0.38	2.24	0.67	1.36	8.42	0.26	0.25	0.14	0.73	1.28	0.19	0.17	0.23	0.26	0.11	0.13			
MgO	0.56	0.72	1.73	0.28	1.19	0.49	30.81	39.16	35.69	38.27	0.11	1.05	0.57	0.08	0.56	0.01	28.80	28.65	41.05	0.19	1.04	24.72	35.93	30.55	27.43	33.29	41.23			
CaO	0.03	0.04	0.03	0.04	0.05	0.05	0.03	0.27	0.06	0.32	0.02	0.06	0.01	<dl	0.01	0.05	0.26	0.34	1.90	0.01	0.02	0.28	0.03	0.02	0.01	0.13	1.06			
Na ₂ O	0.07	0.11	0.12	0.13	0.17	0.15	0.07	0.05	0.06	<dl	0.06	0.08	<dl	<dl	<dl	0.18	0.05	<dl	<dl	<dl	0.08	<dl	<dl	<dl	<dl	<dl	<dl			
K ₂ O	0.08	0.06	0.06	0.07	0.09	0.13	0.03	0.03	0.03	<dl	0.04	0.10	<dl	<dl	<dl	0.03	0.03	<dl	<dl	<dl	0.04	0.05	<dl	<dl	<dl	<dl	<dl			
TiO ₂	0.48	0.51	0.06	0.08	0.05	0.06	0.01	0.01	0.01	0.01	3.33	0.78	0.26	7.86	0.11	0.34	0.02	0.01	0.06	1.31	0.03	0.01	0.01	0.06	0.01	0.33	0.03			
P ₂ O ₅	0.05	0.03	0.02	0.02	0.01	0.02	0.01	0.01	0.01	n.a.	0.07	0.05	0.02	0.27	0.04	0.04	0.01	0.01	0.01	0.01	0.13	0.03	0.01	0.01	0.01	0.01	0.01	0.01		
Cr ₂ O ₃	2.40	4.05	3.34	2.78	4.13	2.13	0.81	0.32	0.34	n.a.	0.49	1.70	1.82	0.57	2.41	3.18	0.63	0.32	0.38	0.63	3.12	0.40	0.04	0.17	0.08	0.20	0.35			
Co ₃ O ₄	0.03	0.01	0.16	0.14	0.25	0.65	0.03	0.02	0.02	n.a.	0.02	0.05	0.55	0.09	0.23	1.68	0.03	0.03	0.02	0.11	0.21	0.02	0.02	0.03	0.03	0.01	0.02			
NiO	0.65	1.38	1.69	1.75	1.89	1.06	2.28	0.40	0.52	n.a.	0.63	0.89	1.42	0.27	1.87	1.64	2.34	2.31	0.27	0.26	1.14	1.82	1.08	1.80	2.00	1.81	0.27			
LOI	8.90	10.55	10.50	9.13	8.07	10.46	13.09	8.74	13.91	14.29	16.34	9.47	9.54	15.00	11.96	14.30	12.07	10.59	2.78	16.22	5.05	10.21	13.19	12.31	11.68	11.94	7.62			
ppm																														
Rb	3.0	0.4	3.0	4.0	4.0	<dl	<dl	<dl	<dl	0.0	<dl	6.0	<dl	<dl	<dl	<dl	<dl	<dl	<dl	<dl	<dl	<dl	<dl	<dl	<dl	<dl	<dl			
Cs	0.6	0.1	<dl	<dl	<dl	<dl	<dl	<dl	<dl	0.4	<dl	1.2	<dl	<dl	<dl	<dl	<dl	<dl	<dl	<dl	<dl	<dl	<dl	<dl	<dl	<dl	<dl			
Be	<dl	0.5	<dl	<dl	<dl	<dl	<dl	<dl	<dl	0.0	<dl	<dl	1.4	1.5	<dl	<dl	<dl	<dl	n.a.	2.0	5.0	<dl	<dl	<dl	<dl	<dl	n.a.			
Sr	16.0	6.9	3.0	3.0	4.0	4.0	<dl	3.0	0.7	5.0	17.0	<dl	17.3	<dl	2.0	2.0	<dl	<dl	<dl	<dl	3.0	<dl	<dl	<dl	<dl	<dl	<dl			
Ba	48.0	6.3	25.0	26.0	122.0	1269.0	17.0	5.0	12.0	n.a.	<dl	22.0	20.4	221.1	21.0	78.0	34.0	20.3	<dl	9.0	48.0	13.8	6.2	7.0	6.8	6.7	<dl			
Sc	70.0	72.0	85.0	98.0	86.0	85.0	17.0	12.0	8.0	n.a.	87.0	58.0	55.6	122.7	82.1	41.0	14.0	13.3	10.5	121.0	70.0	21.1	4.9	11.5	6.6	10.6	8.3			
V	387.0	195.2	339.0	361.0	364.0	362.0	65.0	45.0	33.0	38.2	822.0	306.0	202.9	<dl	413.9	234.0	54.0	45.3	60.6	445.0	362.0	72.3	13.9	29.5	13.6	65.2	38.6			
Cr	16438.4	27760.8	22876.7	19041.1	28287.7	14589.0	5670.0	2150.0	2230.0	2669.2	3260.0	6986.2	12496.7	3894.2	16492.9	21780.8	4170.0	2204.5	2596.9	3420.0	21369.9	2731.4	241.2	1174.5	518.6	1349.1	2426.9			
Co	203.0	106.0	1205.9	949.0	1838.2	4750.0	241.0	90.0	112.0	96.4	100.0	309.0	4008.1	651.7	1724.8	12352.9	228.0	207.6	137.0	682.0	1536.8	153.5	137.3	204.0	230.3	96.6	151.1			
Ni	4610.0	10851.8	13312.4	13776.0	14844.8	8322.2	17878.2	2620.0	3610.0	2265.4	4600.0	6670.0	11189.8	2109.6	14714.6	12895.9	18389.0	18192.0	2099.6	1780.0	9680.0	14300.7	8465.1	14179.0	15701.5	14213.6	2094.9			
Cu	90.0	140.8	150.0	150.0	170.0	190.0	30.0	<dl	20.0	n.a.	80.0	60.0	75.4	72.3	31.6	650.0	30.0	29.7	<dl	260.0	220.0	35.6	<dl	<dl	<dl	<dl	<dl			
Zn	230.0	129.8	490.0	280.0	520.0	460.0	110.0	<dl	50.0	n.a.	<dl	230.0	262.6	185.9	82.4	960.0	<dl	57.5	46.5	110.0	340.0	62.4	36.5	61.8	48.2	49.2	44.0			
Ga	17.0	9.7	10.0	10.0	10.0	9.0	2.0	1.0	1.0	n.a.	33.0	20.0	12.1	29.2	14.7	27.0	1.0	1.6	2.1	27.0	7.0	2.1	<dl	1.3	<dl	5.5	1.1			
Y	2.0	3.3	<dl	<dl	6.0	5.0	<dl	<dl	<dl	n.a.	6.0	3.0	7.8	39.2	8.1	15.0	<dl	<dl	<dl	9.5	16.0	3.9	<dl	<dl	<dl	<dl	4.0			
Nb	8.0	5.3	<dl	<dl	<dl	<dl	<dl	<dl	0.0	<dl	1.0	11.0	<dl	5.4	<dl	<dl	<dl	<dl	3.1	4.3	<dl	<dl	<dl	<dl	<dl	<dl	<dl			
Zr	85.0	36.0	23.0	32.0	29.0	7.0	5.0	<dl	<dl	0.1	114.0	115.0	24.3	267.1	6.5	14.0	5.0	6.0	6.1	63.0	<dl	<dl	7.8	7.1	6.8	22.2	5.6			
Hf	1.8	1.8	<dl	<dl	<dl	<dl	<dl	<dl	0.0	<dl	3.2	3.0	0.4	5.0	<dl	0.4	<dl	<dl	4.7	1.8	<dl	<dl	<dl	<dl	<dl	<dl	<dl			
Pb	12.0	5.1	<dl	<dl	<dl	7.0	<dl	<dl	<dl	n.a.	<dl	11.0	<dl	<dl	7.6	<dl	<dl	<dl	<dl	15.0	<dl	<dl	<dl	<dl	<dl	<dl	<dl			
U	2.3	2.0	0.2	0.3	0.1	0.5	<dl	<dl	<dl	0.0	0.4	2.3	<dl	0.2	0.1	<dl	<dl	<dl	<dl	1.3	<dl	<dl	<dl	<dl	<dl	<dl	<dl			
Th	7.3	3.3	0.2	0.4	0.1	0.5	<dl	<dl	<dl	0.0	0.4	8.8	0.3	0.4	<dl	<dl	<dl	<dl	<dl	2.3	<dl	<dl	<dl	<dl	<dl	<dl	<dl			
La	8.6	3.9	2.6	2.5	11.6	12.5	1.2	2.2	0.5	<dl	8.5	10.7	3.7	99.8	2.0	4.1	0.2	0.2	0.0	4.2	16.1	0.4	0.1	0.1	0.1	0.5	0.0			
Ce	24.8	9.1	6.5	8.1	1.7	34.6	0.4	0.2	0.3	0.0	53.4	24.6	68.3	80.0	23.1	66.4	0.4	0.8	0.0	150.0	0.6	0.5	0.2	0.1	0.2	1.4	0.0			
Pr	1.7	1.0	0.6	0.5	3.7	2.6	0.1	0.2	0.1	<dl	2.0	2.1	1.9	20.3	0.8	2.3	0.1	0.0	0.0	1.2	6.9	0.2	0.0	0.0	0.0	0.2	0.0			
Nd	6.2	3.7	2.8	2.0	16.2	9.3	0.2	0.5	0.2	0.0	8.6	7.4	8.9	74.7	3.9	9.7	0.2	0.2	0.0	5.0	35.4	1.2	0.1	0.1	0.1	0.9	0.0			
Sm	1.2	0.8	0.8	0.5	6.5	1.8	<dl	<dl	<dl	n.a.	2.2	1.4	3.4	15.8	1.2	3.6	<dl	0.1	0.0	1.7	17.4	0.4	0.0	0.0	0.0	0.4	0.0			
Eu	0.2	0.2	0.2	0.1	1.5	0.5	<dl	<dl	<dl	0.0	0.6	0.3	1.1	4.8	0.5	1.1	<dl	0.0	0.0	0.5	4.8	0.2	0.0	0.0	0.0	0.1	0.0			
Gd	1.0	0.7	0.6	0.4	3.8	1.7	<dl	<dl	<dl	0.0	2.1	1.1	2.3	12.9	1.2	3.9	<dl	0.1	0.0	2.0	8.1	0.5	0.0	0.0	0.0	0.5	0.0			
Tb	0.2	0.1	0.1	<dl	0.8	0.3	<dl	<dl	<dl	0.0	0.3	0.2	0.5	2.0	0.2	0.8	<dl	0.0	0.0	0.4	1.8	0.1	<dl	<dl	<dl	0.1	0.0			
Dy	1.0	0.8	0.7	0.4	4.6	1.6	<dl	<dl	<dl	0.0	2.0	1.2	2.7	11.7	1.4	5.1	<dl	0.1	0.1	2.2	11.2	0.4	0.0	0.0	0.0	0.6	0.0			
Ho	0.2	0.2	0.1	<dl	0.8	0.3	<dl	<dl	<dl	0.0	0.4	0.3	0.5	2.1	0.3	1.1	<dl	0.0	0.0	0.5	1.9	0.1	<dl	0.0	0.0	0.1	0.0			
Er	0.7	0.5	0.4	0.3	2.7	0.9	<dl	<dl	<dl	0.0	1.3	0.8	1.5	5.3	0.9	3.2	<dl	0.0	0.1	1.4	5.6	0.2	0.0	0.0	0.0	0.3	0.0			
Tm	0.1	0.1	0.1	<dl	0.6	0.2	<dl	<dl	<dl	0.0	0.2	0.1	0.3	0.7	0.2	0.6	<dl	0.0	0.0	0.2	1.2	0.0	<dl	0.0						

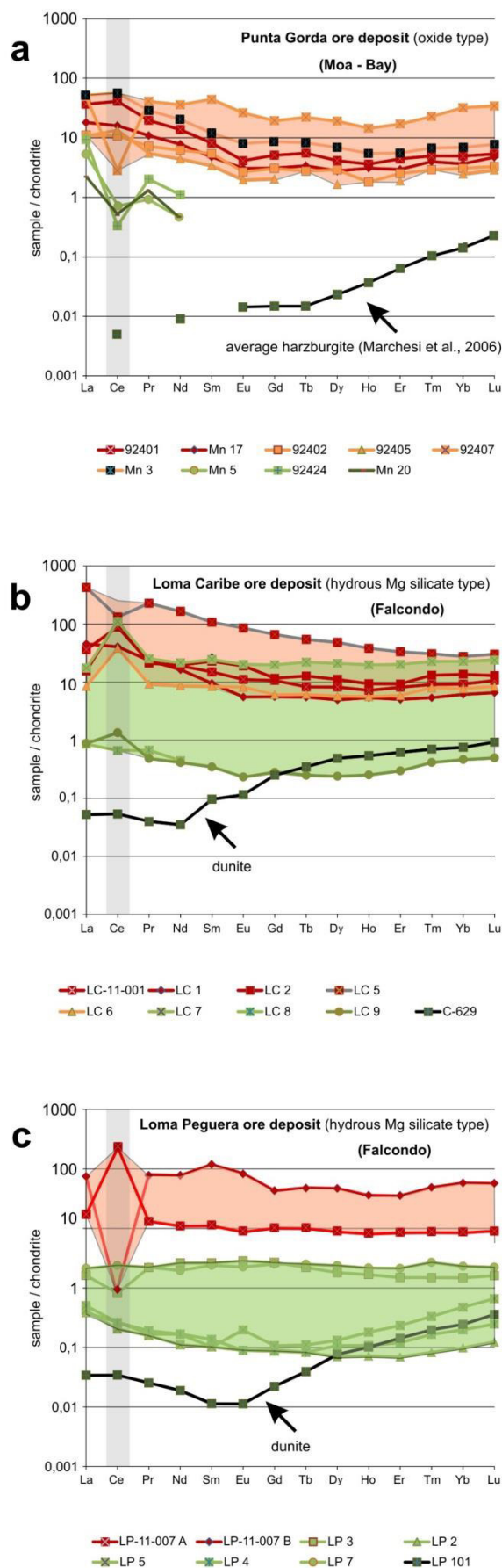
REE chondrite normalized patterns for weathering products show in general rather flat trends with slight negative slopes from La-Eu and slight positive slopes from Ho-Lu (Fig. 4.3). The parent rock (harzburgite) shows a pronounced positive slope from Tb-Lu (Fig. 4.3). Cerium anomalies are observed in the saprolite (negative) and in the limonite (positive and negative) (Fig. 4.3).

Scandium and PGE contents of the unweathered harzburgites were not analysed in Marchesi et al. (2006). However Sc contents range from 8 to 17 ppm in the saprolite and from 70 to 98 ppm in the limonite whereas PGE concentrations vary from 27 to 61 ppb in the saprolite and from 109 to 239 ppb in the limonite (Table 4.1, Fig. 4.3).

In general saprolite and limonite samples have similar flat PGE chondrite normalized patterns with slight peaks of Ru and Pd as previously observed in Ni laterites from Falcondo (Fig. 4.4) (Aiglsperger et al., 2015).

However, one sample from the Mn oxide(s) rich limonite horizon (i.e. Mn 3) shows a clear positive Pt anomaly and duricrust samples (i.e. 92401 and Mn 17) have slightly negative patterns from Pt to Pd (Fig. 4.4).

Fig. 4.3. Chondrite normalized REE patterns with highlighted Ce-anomalies and indicated fields of limonite (red) and saprolite (green) of samples from A) Punta Gorda ore deposit (Moa Bay); B) Loma Caribe ore deposit (Falcondo); C) Loma Peguera ore deposit (Falcondo). Normalization values from Anders and Grevesse (1989). Parent rock (harzburgite) *av. Hzb.* are taken from Marchesi et al. (2006).



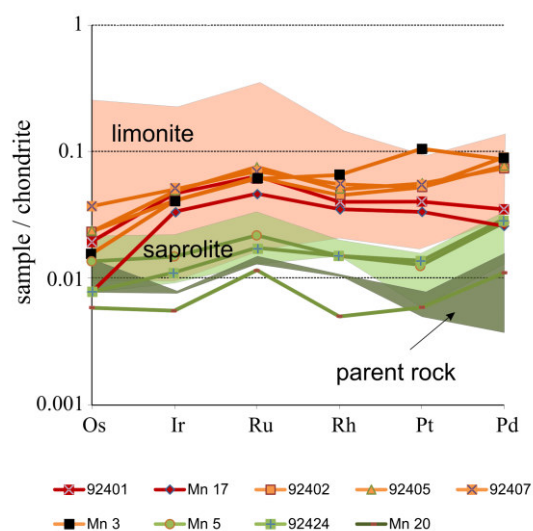


Fig. 4.4. Chondrite normalized PGE patterns of samples from the Punta Gorda ore deposit (Moa Bay) with indicated fields of limonite, saprolite and parent rock from samples from the Loma Caribe and Loma Peguera ore deposits (Falcondo) (Aiglsperger et al., 2015). Note the positive Pt anomaly in the Mn-oxide rich sample Mn 3. Normalization values from Naldrett and Duke (1980).

4.2.2. Falcondo

Major elements in Ni laterites from Loma Caribe and Loma Peguera (Fig. 4.5, 4.6, respectively) follow the general trend for Ni laterites with characteristic enrichment of Fe + Al towards the surface and Si + Mg depletion within the limonite. Close to the surface Al shows a significant peak of up to ~30 wt% in both Ni laterite locations, whereas Fe decreases from ~60 to ~40 wt% (Loma Caribe) and from ~70 to ~35 wt% (Loma Peguera) (Table 4.1, Fig. 4.5, 4.6). Within the Ni laterite profile of Loma Caribe two Mn rich levels are observed: one at the transition zone between saprolite and limonite (8.4 wt%) and one in the lower part of the upper limonite (2.2 wt%) (Fig. 4.5). Co enrichment (1.68 wt% at the transition zone and 0.6 wt% in the upper limonite) correlates with Mn enrichment.

CM are constantly enriched from parent rock to limonite: the parent rock from Loma Caribe contains 0.6 ppm REE, 11 ppm Sc and 30 ppb PGE, slightly enriched saprolite contains 0.9 to 1.6 ppm REE, ~14 ppm Sc and ~50 ppb PGE whereas the limonite concentrates 37 to 335 ppm REE, 41 to 123 ppm Sc and 35 to 264 ppb PGE (Table 4.1, Fig. 4.5).

Highest REE and Sc contents are observed within a clay minerals rich layer in the lower part of the upper limonite whereas the highest PGE contents occur at the top of the profile (Fig. 4.5). In general REE chondrite normalized patterns of weathering products from Loma Caribe are slightly negative from La-Eu and flat from Eu-Lu (Fig. 4.3b). Ce positive anomalies in saprolite and limonite samples as well as a clear Ce negative anomaly in one clay minerals rich limonite sample (i.e. LC 5) are evident (Fig. 4.3b).

The Ni laterite profile at Loma Peguera shows, similar to Loma Caribe, Mn and Co enrichment (1.3 wt% and 0.2 wt% respectively) close to the transition zone between saprolite and limonite (Fig. 4.6). Slight enrichment trends of CM occur from parent rock (0.2 ppm REE, 8 ppm Sc and 36 ppb PGE) to saprolite (0.5 to 6 ppm REE, 5 to 21 ppm Sc and 37 to 62 ppb PGE) whereas a more significant enrichment is observed within the limonite towards the surface: values reach 122 to 171 ppm REE, 70 to 121 ppm Sc and 331 to 412 ppb PGE (Table 4.1, Fig. 4.6). Values of up to 640 ppb total PGE were reported from highest levels in the same Ni laterite profile (Aiglsperger et al., 2015). In general, saprolite and limonite exhibit flat REE chondrite normalized patterns in contrast to HREE enriched patterns in the parent rock (dunite) (Fig. 4.3c).

A distinctive Eu positive peak is observed in one sample from the central part of the saprolite (LP 5) as well as pronounced

positive and negative Ce trends in the highest limonite sample and underlying limonite sample, respectively (Fig. 4.3c).

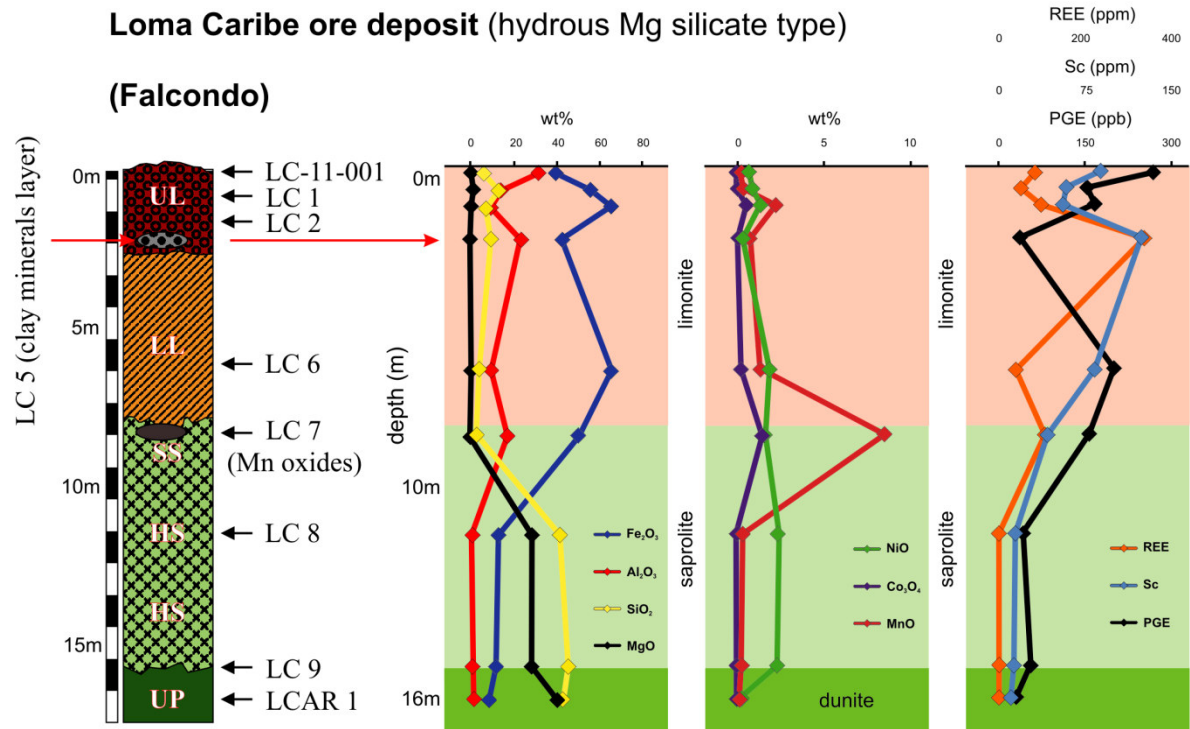


Fig. 4.5. Ni laterite profile from the Loma Caribe ore deposit (Falcondo) showing location of samples with major, relevant minor and CM contents.

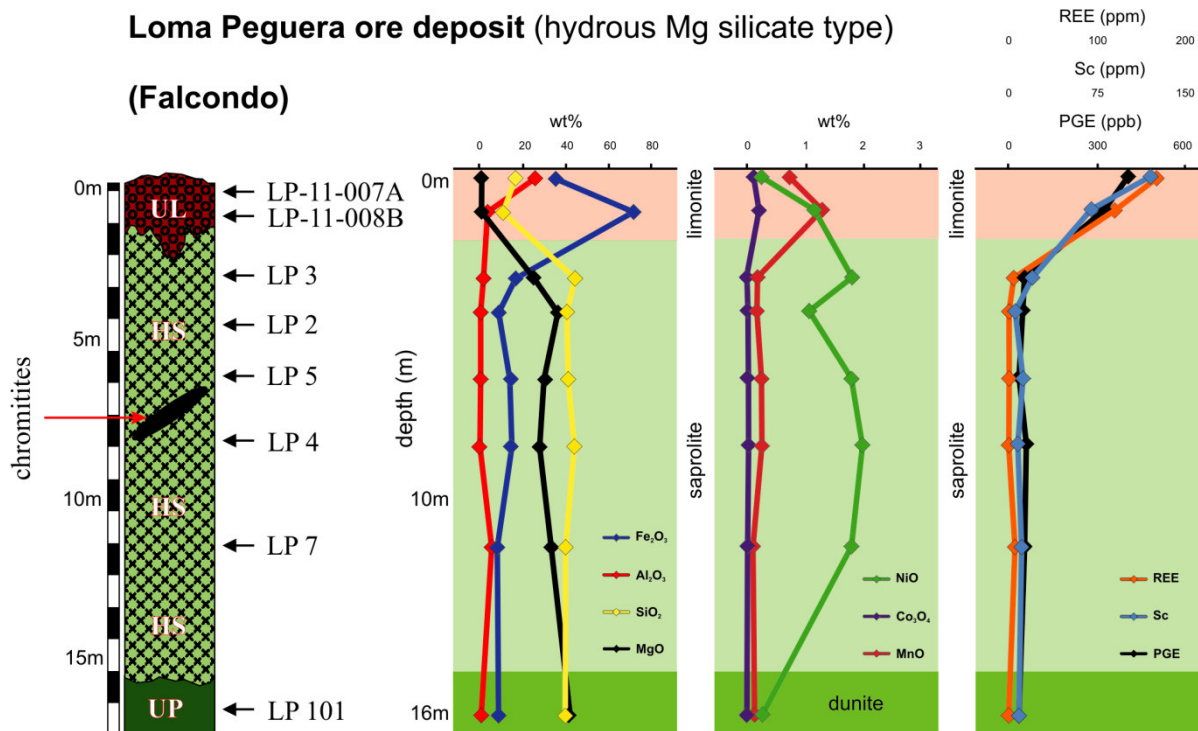


Fig. 4.6. Ni laterite profile from the Loma Peguera ore deposit (Falcondo) showing location of samples with major, relevant minor and CM contents.

4.3. Isocon analysis and element transfer

The isocon method described by Grant (1986) was applied to evaluate the potential redistribution of major, minor and critical elements from parent rock to surface during serpentinisation and lateritization. This method is a graphical approach to the mass balance equation used by Gresens (1967) and was previously used to determine element mobility in various rock types (e.g. Meyer et al., 2002; Medaris et al., 2003; Tsikouras et al., 2009; Frost et al., 2013; Liivamägi et al., 2014; Trincal et al., 2014; Chu et al., 2015).

Choosing immobile elements for mass balance calculations is a challenging task. However, sample/bedrock comparisons of all measured elements suggest that Ti and Zr are relatively immobile within investigated Ni laterites. In the case of the Ni laterite from Moa Bay only Ti could be used for mass balance calculations as the Zr content in the protolith is very low (55 ppb; Marchesi et al., 2006) and Zr concentrations for subsequent saprolite samples are below detection limits (Table 4.1). Because Sc and PGE were not analysed in the average harzburgite of Moa Bay (Marchesi et al., 2006), concentrations of these elements in the less weathered sample (Mn 20) were taken for mass balance calculations.

4.3.1. Moa Bay

Figure 4.7 shows gains and losses in wt%, ppm or ppb relative to the parent rock. During the weathering of peridotite Mg and Si are continuously lost and up to -20

% (-7.46 wt%) of the initial Mg content and approximately -10 % (-3.82 wt%) of the initial Si content have been removed in the higher levels of the saprolite. In contrast Fe gain doubles (+8.36 wt%) and Al reaches gains of up to +190 % (+1.2 wt%) relative to unweathered peridotite. Within the investigated limonite of Moa Bay mass balance calculations reveal that nearly all Mg (-38 wt%) and Si (-38 wt%) are lost. Fe and Al show gains in the lower limonite (up to +6.5 wt%, +84 % and +1.2 wt%, +188 % respectively) but are subsequently lost within the duricrust on top of the profile (-6.5 wt%, -84 % and -0.3 wt%, -54 % respectively).

With respect to the mass balance of Ni, Co and CM, Fig. 4.7 indicates important gains of Ni (up to +15 000 ppm) together with Co (up to +145 ppm), Sc (up to +9 ppm), LREE (up to +3 ppm) as well as PGE (up to +34 ppb) in the saprolite. HREE were all below detection limit in samples in the saprolite and could not be balanced (Table 4.1). Within the lower limonite Ni reaches gains of up to +700 ppm (+31 %), Co up to +700 ppm (+721 %), Sc between +6 ppm (+65 %) and +12 ppm (+130 %), LREE up to +11 ppm (1000 fold), HREE up to +3 ppm (6 fold) and PGE up to 14 ppb (+53 %). In contrast, duricrust is characterized by significant loss of Ni (down to -2169 ppm, -96 %), Co (down to -94 ppm, -98 %), Sc (down to -6.6 ppm, -73 %) and PGE (down to -24.9 ppb, -92 %), whereas LREE show strong gains (up to +1 ppm, 90 fold). A general observation with respect to the oxide type Ni laterite of Moa Bay is that enrichment trends of Ni, Sc and PGE strongly correlate with the enrichment trend of Fe (Fig. 4.7).

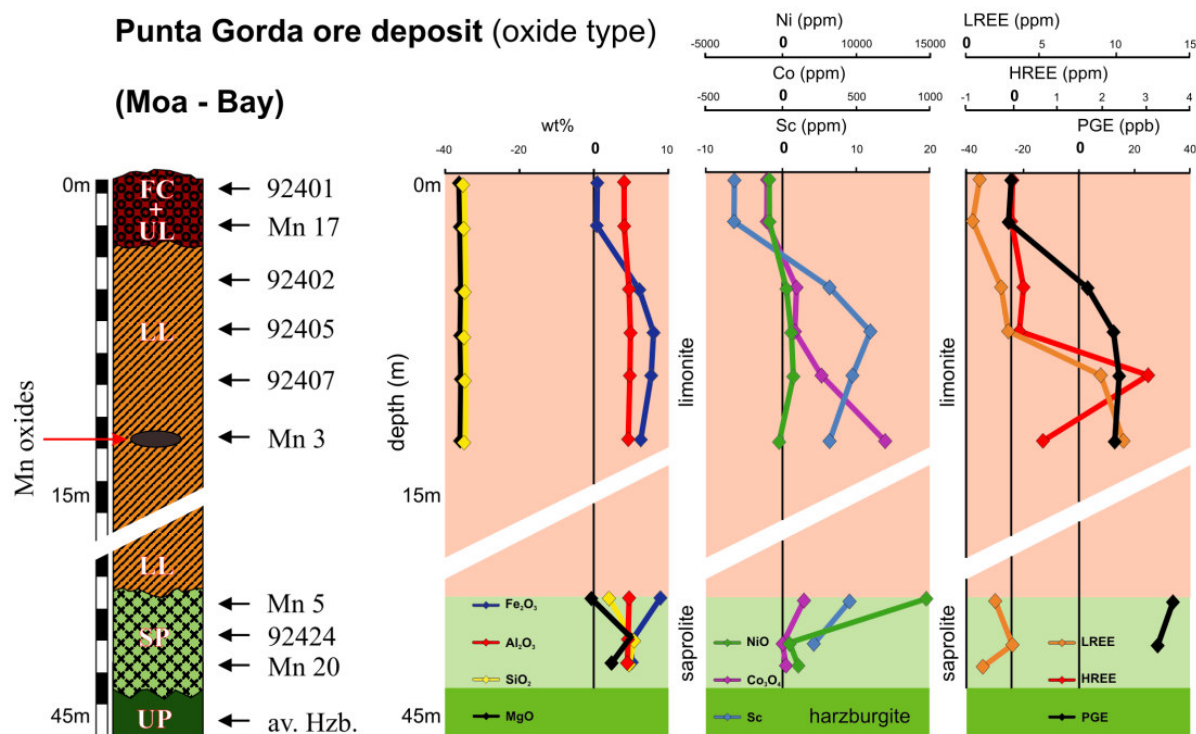


Fig. 4.7. Isocon analysis of relevant elements in the Ni laterite profile from the Punta Gorda ore deposit (Moa Bay). Vertical lines mark the 0 positions with respect to mass balance calculations.

4.3.2. Falcondo

In general the saprolite of the Ni laterite profile at Loma Caribe is characterized by gains of major elements: Mg (+9 wt%), Si (up to +36 wt%), Fe (up to +13 wt%) and Al (up to +0.3 wt%) (Fig. 4.8). A sudden change is observed at the transition zone between saprolite and limonite when Mg and Si drops down to approximately -40 wt% with minor gains of Fe (+4 wt%) and Al (+3 wt%). However, Mg and Si remain lost in the subsequent limonite in contrast to gains of Fe (+38 wt%) and Al (+5 wt%). Within the limonite a clay-minerals rich layer shows losses of all four major elements (-41 wt% Mg, -43 wt% Si, -8 wt% Fe, -2 wt% Al). In the lower part of

the upper limonite Fe and Al are gained (+7 wt% and +0.6 wt%, respectively) whereas at highest levels of the profile significant losses of Fe (down to -7.51 wt%) and Al (down to -0.9 wt%) are observed.

In general minor elements as well as CM are gained in the saprolite of Loma Caribe: Ni (up to +30 000 ppm, 14 fold), Co (up to +259 ppm, +189 %), Sc (up to +14 ppm, +131 %), LREE (up to +2 ppm, 17 fold) and PGE (up to +66 ppb, +219 %). In contrast HREE are either lost or measurements of HREE were below detection limit and therefore unsuitable for mass balance calculations (Table 4.1).

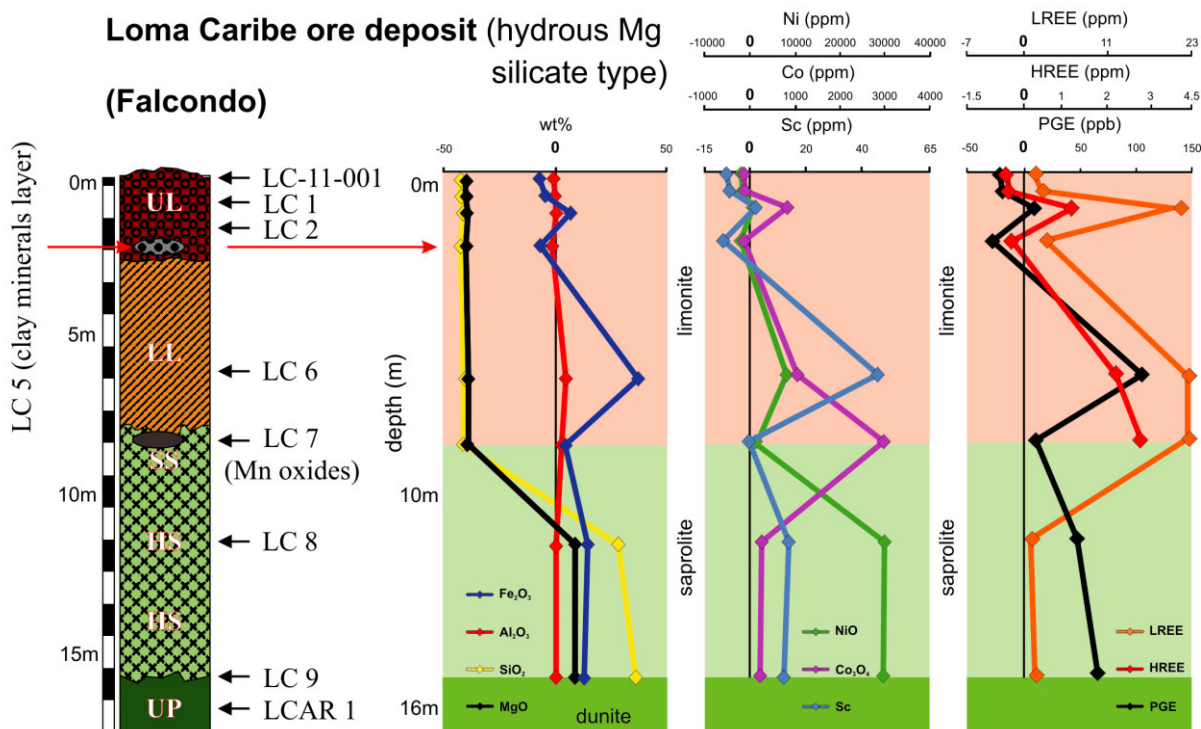


Fig. 4.8. Isocon analysis of relevant elements in the Ni laterite profile from the Loma Caribe ore deposit (Falcondo). Vertical lines mark the 0 positions with respect to mass balance calculations.

However, a gain of HREE (+3 ppm) is observed at the transition zone between saprolite and limonite together with gains of LREE (+23 ppm, 170 fold), Co (+3000 ppm, 22 fold), Ni (+1140 ppm, +54 %) and PGE (+10 ppb, +32 %). Lower levels of the limonite are generally characterized by gains of Ni (up to +8052 ppm, +384 %), Co (up to +1053 ppm, +769 %), Sc (up to +46 ppm, +439 %), LREE (up to +22 ppm, 168 fold), HREE (up to +3 ppm, +643 %) and PGE (up to +107 ppb, +355 %). In a clay-minerals rich horizon within the limonite, mass balance calculations reveal a general loss of Ni (-2075 ppm, -99 %), Co (-132 ppm, -95 %), Sc (-10 ppm, -87 %), HREE (-0.2 ppm, -26 %) and PGE (-30 ppb, -99 %) but a little gain of LREE (+2 ppm, 25 fold). With respect to highest levels of the upper limonite the following elements are lost: Ni (down to -2017 ppm, -94 %), Co (down to -135 ppm, -98 %), Sc

(down to -9 ppm, -78 %), HREE (down to -0.3 ppm, -62 %) and PGE (down to -25 ppb, -76 %). Gains are only observed for LREE (up to +4 ppm, 21 fold).

Gains and losses of major elements in the saprolite of Loma Peguera vary from -37 wt% to +33 wt% (Mg), from -35 wt% to +93 wt% (Si), from -8 wt% to +42 wt% (Fe) and from -1 wt% to +5 wt% (Al) (Fig. 4.9). Within the thin limonite horizon of Loma Peguera Mg and Si are almost entirely lost (approximately -40 wt% for both elements), whereas Fe (+64 wt%) and Al (+3 wt%) are gained in the lower part of the upper limonite. However, at the upper limonite exposed to the surface Fe is lost (-8 wt%).

Concerning mass balances of Ni, Co and CM in the Loma Peguera Ni laterite profile a continuous gain trend is observed within the saprolite: Ni reaches values of up to +40 000 ppm (+1948 %), Co up to +300 ppm (+205 %), Sc up to +55 ppm (+663 %), LREE up to +10 ppm (100 fold), HREE up to +3 ppm (68 fold) and PGE up to +130 ppb (+358 %) relative to underlying dunite. Highest gains in the profile, with exception of Ni (+7600 ppm, +362 %), are observed in the lower part of the upper limonite: Co up to +1400 ppm (+917 %), Sc up to +62 ppm (+742 %), LREE up to +87 ppm (870 fold), HREE up

to +55 ppm (1100 fold) and PGE up to +300 ppb (+819 %). However, at highest levels of the limonite Ni (-2000 ppm, -97 %), Co (-130 ppm, -84 %), Sc (-4 ppm, -47 %) and PGE (-20 ppb, -58 %) are lost, whereas LREE and HREE are slightly gained (approximately +2 ppm for both elements, 30 fold).

Both Ni laterite profiles from the hydrous Mg silicate type at Falcondo reveal rather similar features with respect to mass balance calculations: Ni correlates with Mg and Si, Sc and PGE show a general correlation with Fe (Fig. 4.8 and 4.9).

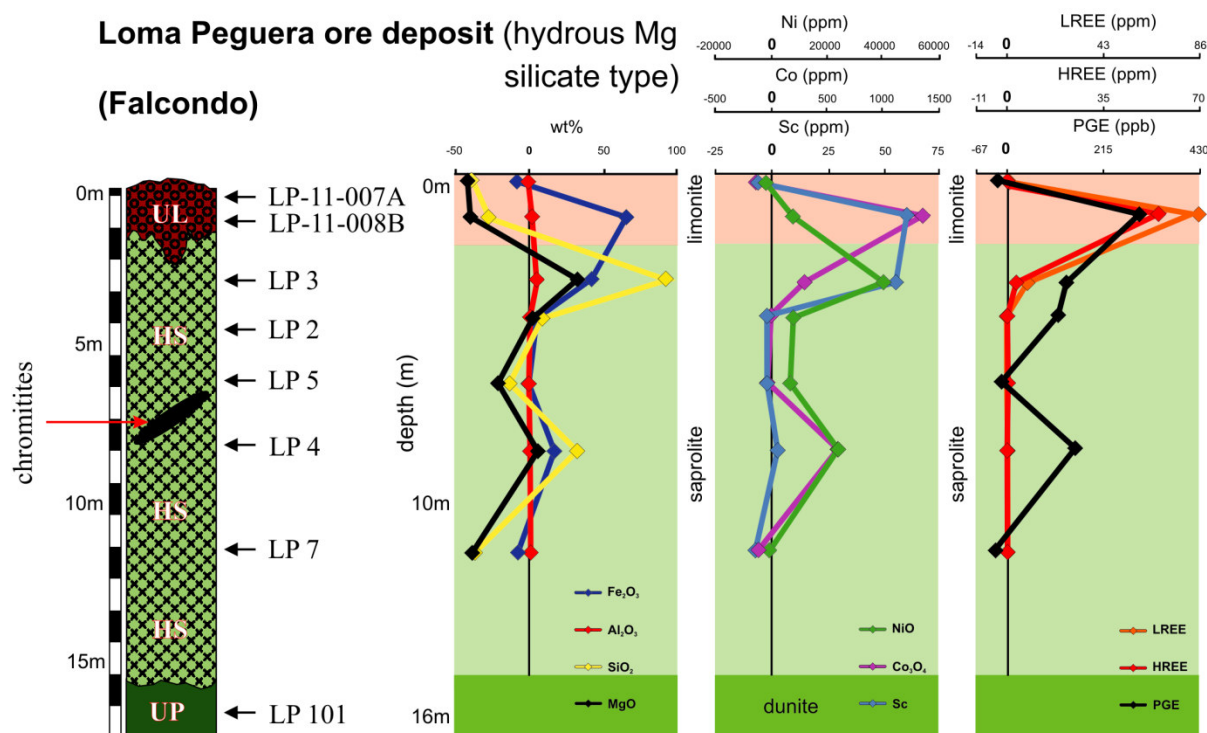


Fig. 4.9. Isocon analysis of relevant elements in the Ni laterite profile from the Loma Peguera ore deposit (Falcondo). Vertical lines mark the 0 positions with respect to mass balance calculations.

4.4. Profile mineralogy

Fig. 4.10 gives an overview of the general appearance of alteration products.

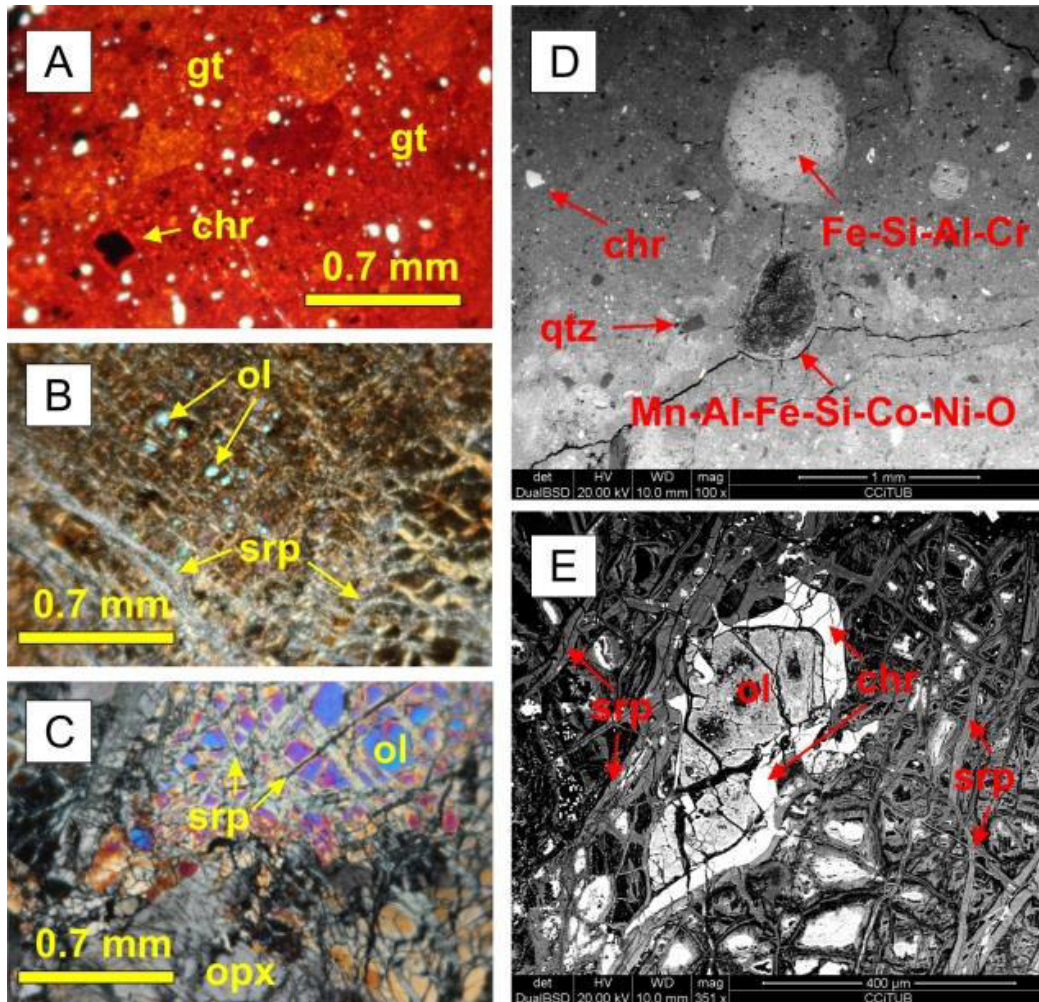


Fig. 4.10. Cross-polarized photomicrographs (A-C) and BSE images (D and E). A) sample from the limonite horizon mainly consisting of goethite (gt) and minor amounts of chromian spinel (chr); B) sample from the hard saprolite horizon composed of serpentine minerals (srp) with only small remnants of olivine (ol); C) serpentinized peridotite sample with olivine (ol) and orthopyroxene (opx) crosscut by serpentine minerals (srp); D) sample from the limonite horizon containing chromian spinel (chr), quartz (qtz) and unidentified secondary mineral compounds with indicated chemistry; E) sample from the hard saprolite showing a characteristic network of serpentine minerals (srp), olivine (ol) and chromian spinel (chr).

4.4.1. Moa Bay

Main minerals found in the serpentinized peridotite are olivine and orthopyroxene (enstatite) crosscut by serpentine minerals (mainly lizardite). Chromian spinel and magnetite occur as minor mineral phases. The saprolite horizon is dominated by lizardite replacing primary olivine grains with goethite and chromian spinel as minor mineral phases. The oxide ore consists mainly of goethite (>50 wt%) with minor maghemite, hematite and gibbsite. Original textures of the parent rock are not preserved and locally some goethite grains show replacement by hematite. Maghemite is slightly more abundant towards the lowest part of the limonite horizon, whereas hematite is

dominant in its upper part. Accumulations of Mn-Co-Ni oxide(s), mainly lithiophorite, Al-rich asbolane and lithiophorite-asbolane intermediate minerals, are present as veins and coatings or concretions along fractures, at certain levels within the lower part of the limonite horizon. Gibbsite is believed to be a less soluble alteration product of plagioclase from the gabbro bodies in the parent rock (Galí et al., 2007). It is more abundant towards the top of the profile (i.e. duricrust). Chromian spinel is an abundant minor mineral phase in the upper limonite. A summary of the observed profile mineralogy from Moa Bay, determined by means of XRD, optical microscopy and SEM, is given in Fig. 4.11a.

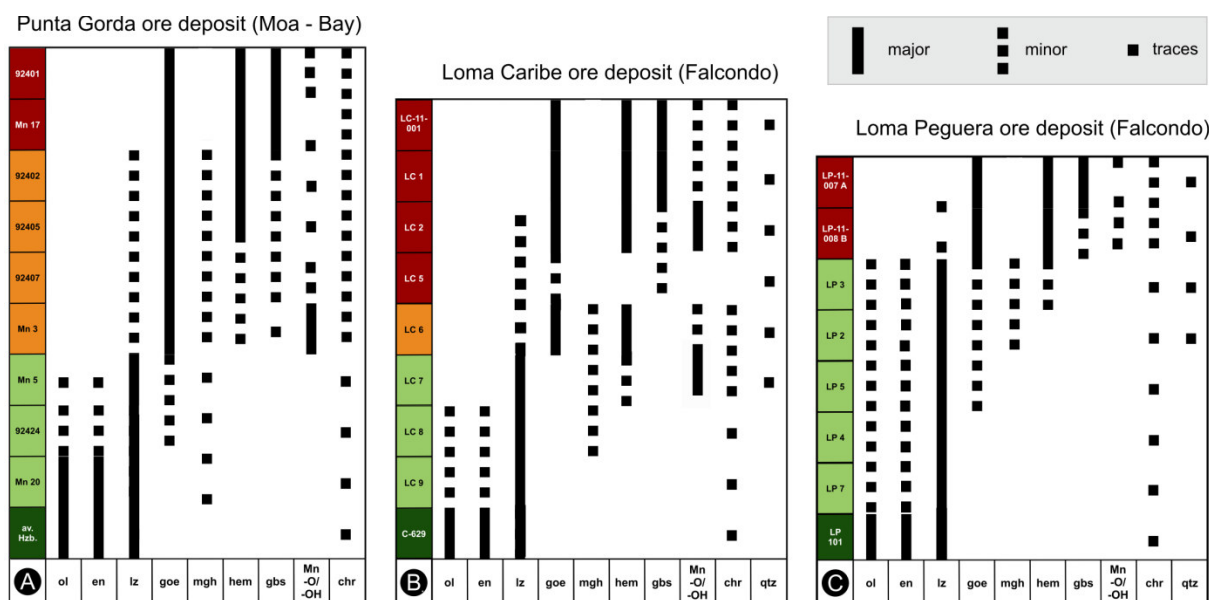


Fig. 4.11. Summary of identified, characteristic mineral compounds of Ni laterites from A) Punta Gorda ore deposit, B) Loma Caribe ore deposit and C) Loma Peguera ore deposit.

4.4.2. Falcondo

Parent rocks of Ni laterites at Loma Caribe and Loma Peguera are serpentized dunite and harzburgite, respectively. Olivine and orthopyroxene (enstatite) are major minerals crosscut by abundant serpentine minerals (lizardite). Chromian spinel occurs occasionally as an accessory mineral. The general saprolitic horizon is dominated by Ni-rich lizardite and relicts of olivine and enstatite. Minor clinocllore, goethite, maghemite and/or hematite also occur depending on the individual sample. Chromian spinel and quartz appear only in trace amounts. Major minerals in the limonite horizon are goethite, hematite and gibbsite, whereas lizardite, maghemite and chromian spinel are minor components. Accumulations of Co-bearing Mn oxide(s), mainly heterogenite, Ni-rich asbolane and minor, lithophorite-asbolane intermediate minerals, are found in the transition zone between saprolite and limonite as well as in the central upper limonite. They occur as veinlets, coatings along joints and cracks. In this study observed mineral abundances on the profile scale for Ni laterites from Loma Caribe and Loma Peguera are given in Fig. 4.11b and c, respectively.

4.5. Critical metal bearing mineral phases

Cerium oxide mineral compounds were detected in heavy mineral concentrates from limonite samples close to the surface at Falcondo. They are always associated with Mn bearing oxide(s) and occur either as rings with diameters of approx. 5 μm (Fig. 4.12a), as similar sized spheres or as larger aggregates (to 30 μm) of submicron

sized flakes (Fig. 4.12b and c). Cerium oxide in the form of submicrometre to micrometre grains of cerianite with similar shapes has been reported from other lateritic soils around the world (e.g. Braun et al., 1990; Mongelli, 1997; Janots et al., 2015 and reference therein). In the same horizon one small grain (5 μm) of an unidentified La-F mineral phase was found included in secondary Fe oxide(s) (Fig. 4.12d). REE bearing phosphates were detected in HS concentrates of the upper limonite from Loma Caribe. They are generally associated with secondary Mn oxide(s), one large (~50 μm) free grain with clear crystal faces was also observed (Fig. 4.12e and f, respectively). Due to the small grain sizes of described REE minerals X-ray diffraction of single crystals for subsequent mineralogical identification was not possible. However, bastnäsite and monazite have been described in Greek laterites by Eliopoulos et al. (2014).

Chromian spinel was observed to contain platinum group minerals (PGM) as small scaled inclusions (<10 μm) and therefore is considered to be the main PGE host at Falcondo (see chapter 6; Aiglsperger et al., 2015). However, one Pt-Fe-Ni bearing mineral phase with neof ormation features found in secondary Fe oxide(s) from highest levels of the lateritic profile was reported by these authors as well. In general PGM grains found in limonite are small in size (<1 μm to 15 μm) and sometimes occur as very irregular and/or compositionally complex inclusions in secondary Fe oxide(s) (Fig. 4.13a-c) or awaruite (Fig. 4.13d). PGM found in the underlying saprolite are different in size and occurrence (Aiglsperger et al., 2015).

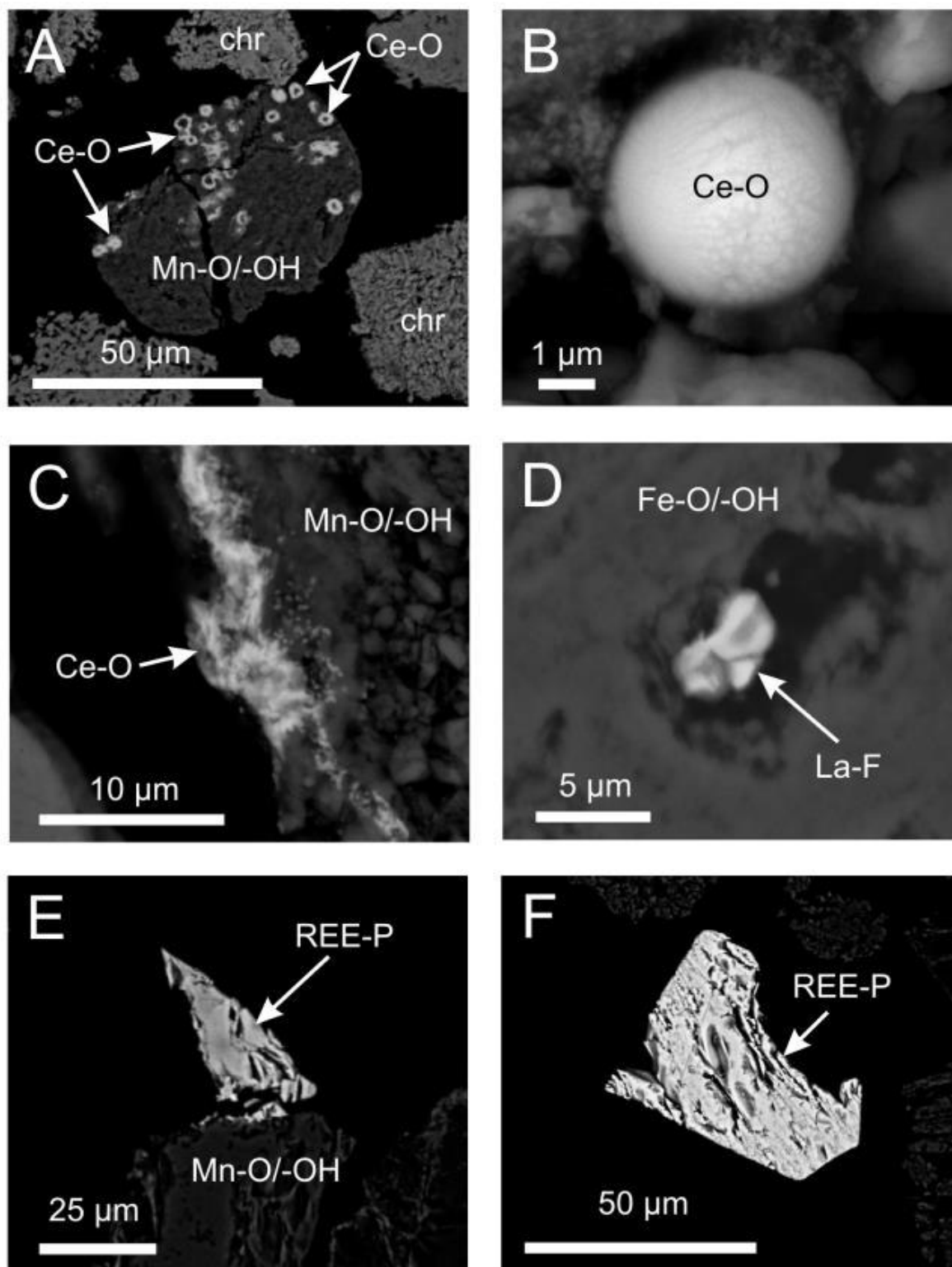


Fig. 4.12. Selection of BSE images with REE bearing mineral compounds detected in heavy mineral concentrates from the upper limonites. A) free grain of secondary Mn oxide(s) containing numerous rings of Ce-O; B) close up of one perfectly round Ce-O sphere; C) accumulation of Ce-O nano-flakes at the border of one free Mn-oxide(s) grain; D) unidentified La-F grain included in a grain of secondary Fe oxide(s); E) REE-P grain attached to a free grain of Mn oxide(s); F) free crystal of REE-P.

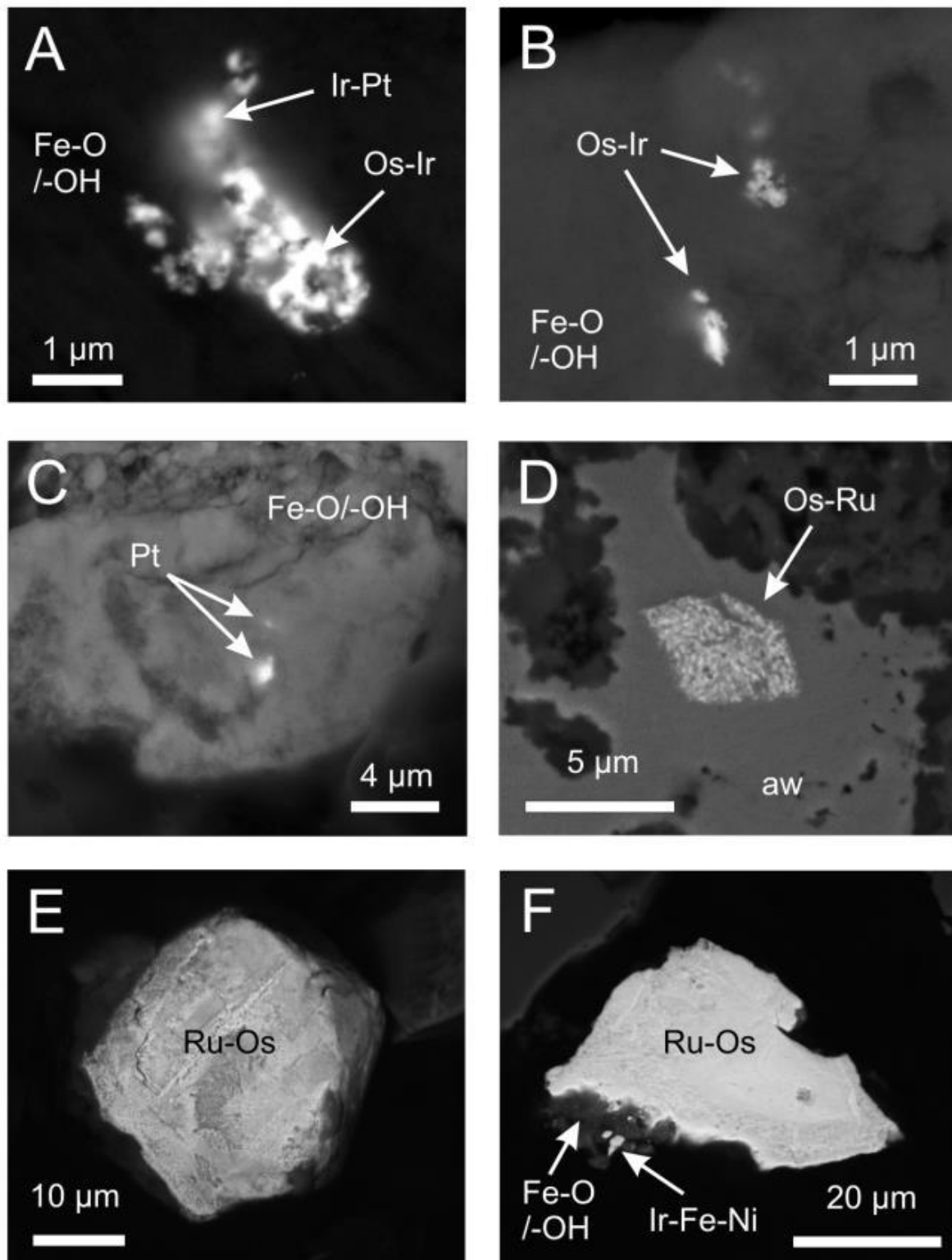


Fig. 4.13. Selection of BSE images with PGE bearing mineral compounds detected in heavy mineral concentrates from the upper limonites. A) Complex aggregates of nano-particulates consisting of Ir-Pt and Os-Ir included in secondary Fe-oxide(s); B) Accumulation of Os-Ir bearing nano-particulates at the border of a secondary Fe oxide(s) grain; C) Pt particles at the border of a secondary Fe oxide(s) grain; D) Accumulation of Os-Ru bearing nano-particulates at the border of an awaruite (aw) grain; E and F) examples of abundantly occurring free grains of Ru-Os mineral compounds found in chromitite samples from the Loma Peguera ore deposit (Falcondo).

Examples of free grains of altered primary PGM detected in HS concentrates of PGE enriched (~2 ppm total PGE) chromitites from Loma Peguera (Proenza et al., 2007b) are shown in Fig. 4.13e and f.

Element mapping was applied to one complex PGM found within the upper limonite (Fig. 4.14). The PGE grain (~15 μm) occurs at the Fe, Ni and Si rich border of a weathered chromian spinel grain and shows aggregate features of submicron particulates. A clear zonation in PGE can be observed at grain scale: Os, Ir and Ru (IPGE) are mainly concentrated in central parts of the grain area, whereas Rh, Pt and Pd (PPGE) are either found in the innermost part (Pt) or at the outside border of the grain (Fig. 4.14). In addition the element mapping reveals a visual correlation of Ru with As, Rh and Pd with Sb as well as Pt with Ni for zones of highest concentrations. Medium concentrations of Ru in the lower left

corner of the image are not detected via back scattered electrons imaging. However, these Ru concentrations correlate visually also with Al, Fe and Si.

Sc vs. Fe_2O_3 discrimination diagrams show two clusters, one for saprolite samples (beneath the Mg discontinuity) and one for limonite and duricrust samples (above the Mg discontinuity), thus suggesting a positive correlation between these elements similar to observations from Ni laterites from New Caledonia (Audet, 2009) (Fig. 4.15).

This indicates that secondary Fe oxide(s) most likely represent the main Sc host in Ni laterites.

LA-ICP-MS analyses on secondary Mn oxide(s) phases from Moa Bay and Falcondo were applied to assess their capacity to host CM and show clear signals for all REE (mainly Ce, La, Pr and Nd), Sc and Pt (Fig. 4.16).

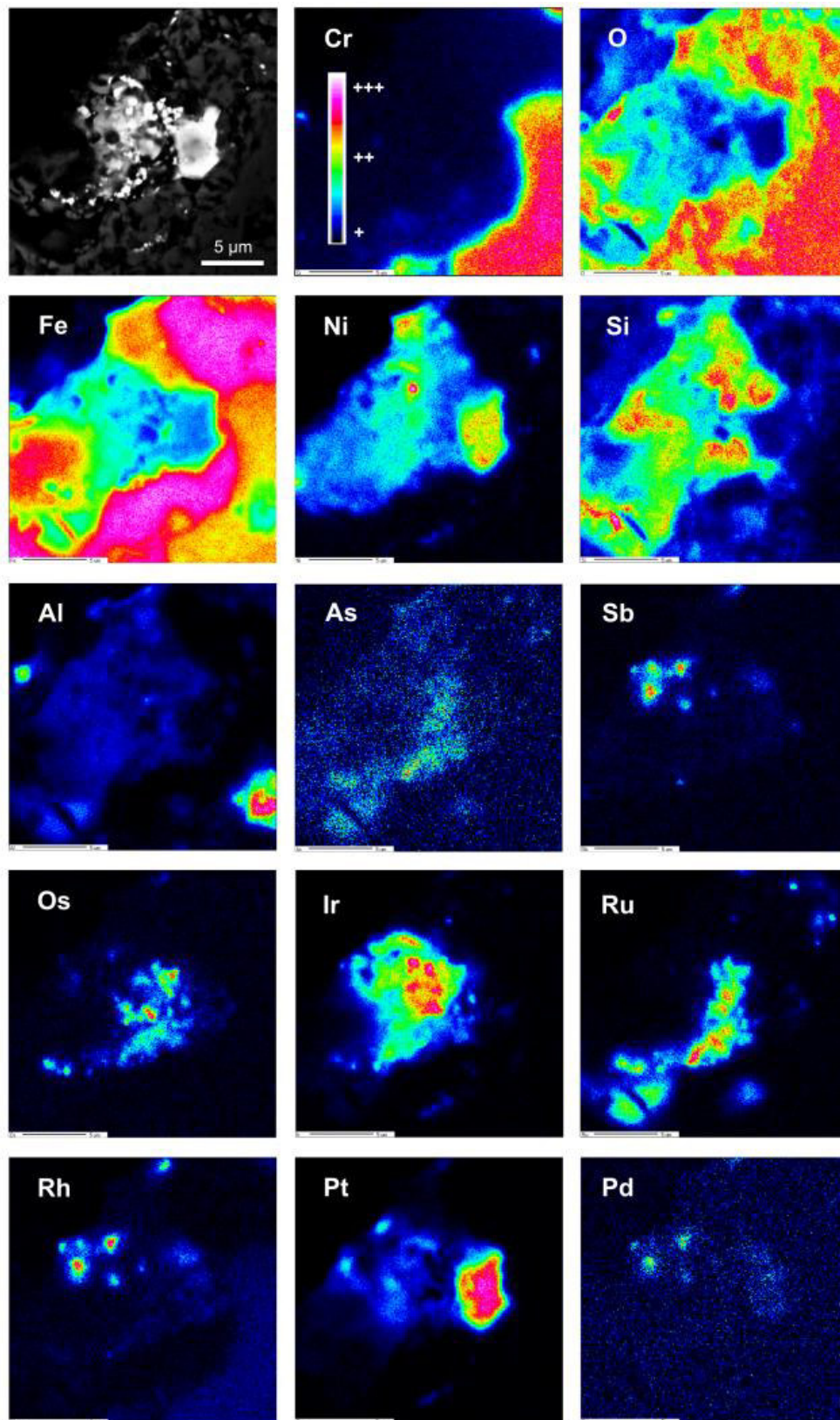


Fig. 4.14. BSE image and element distribution maps (background corrected) showing the distribution of all PGE and Cr, O, Fe, Ni, Si, Al, As and Sb in a complex PGM grain located at the border of a weathered chromian spinel from the upper limonite of the Loma Caribe ore deposit (Falcondo). Interestingly, Ru contents in the lower left corner of the element distribution map are not observed in the BSE image (dark area).

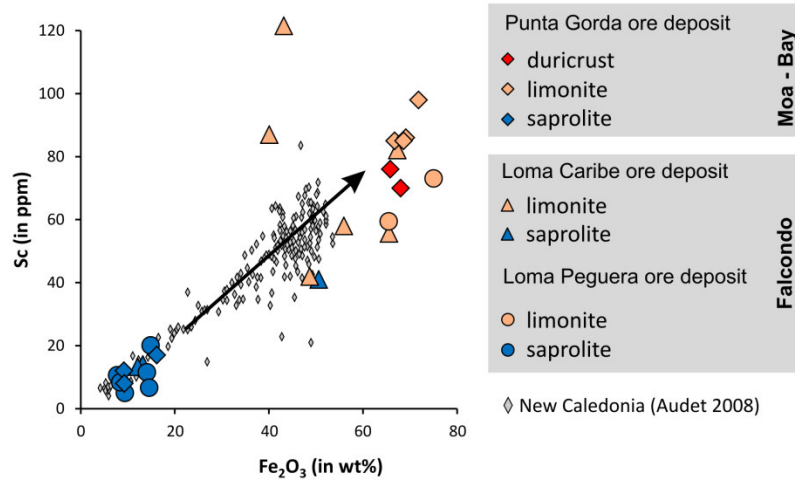


Fig. 4.15. Sc vs. Fe₂O₃ contents in saprolite, limonite and duricrust showing two clusters indicating a positive correlation as previously observed by Audet (2009) in Ni laterites from New Caledonia.

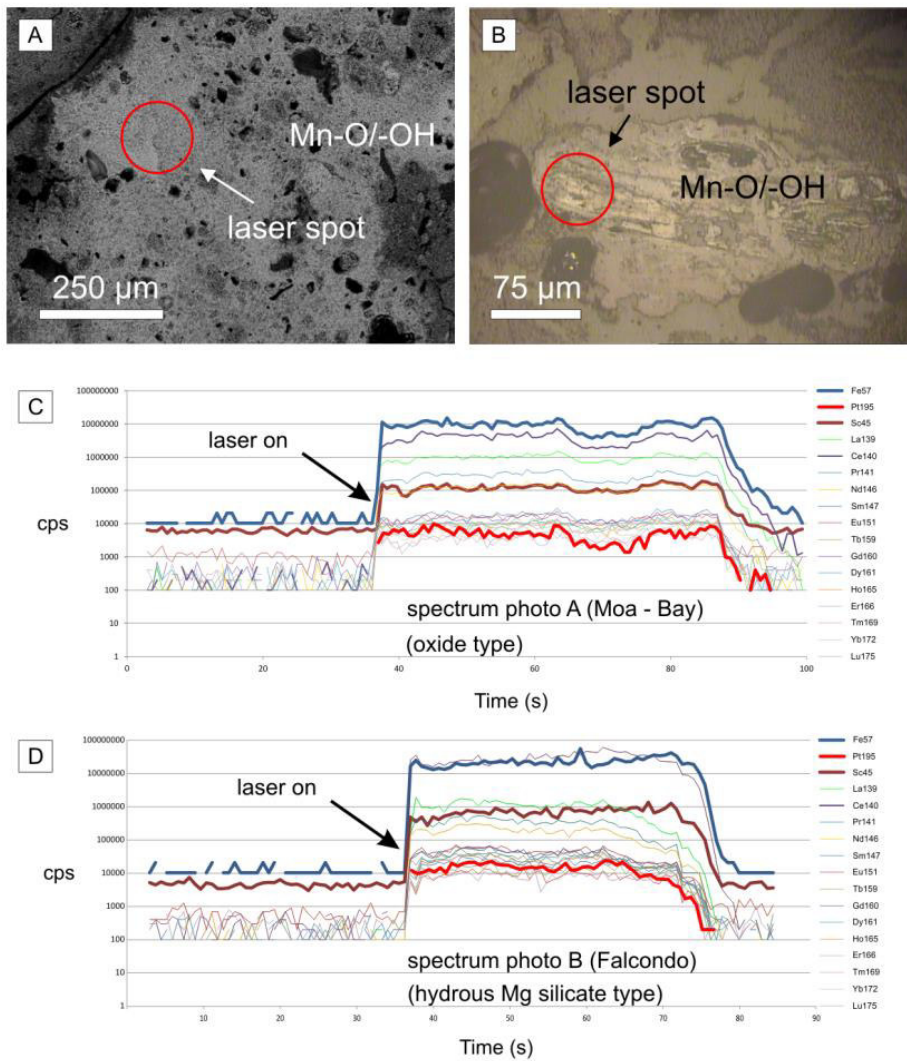


Fig. 4.16. LA-ICP-MS scans of two spots in secondary Mn oxide(s) from limonite samples from Moa Bay (A and C) and Falcondo (B and D) showing the presence of CM (REE, Sc and Pt) in both cases.

4.6. The ultramafic index of alteration (UMIA)

In an attempt to quantify and visualize the geochemical changes in Ni laterites developed above ultramafic rocks (e.g. peridotites) an ultramafic index of alteration (UMIA) was defined as:

$$\text{UMIA} = 100 \times \left[\frac{(\text{Al}_2\text{O}_3 + \text{Fe}_2\text{O}_{3(\text{T})})}{(\text{SiO}_2 + \text{MgO} + \text{Al}_2\text{O}_3 + \text{Fe}_2\text{O}_{3(\text{T})})} \right] \quad (1)$$

This chemical weathering index is based on previous work done by Babechuk et al. (2014) and references therein and considers the dominance of MgO and SiO₂ compared to negligible contents of CaO, Na₂O and K₂O in parent rocks as well as the widely observed depletion of MgO and SiO₂ with concomitant enrichment of Fe₂O₃ and Al₂O₃ towards the surface in most Ni laterites.

As other chemical weathering indices the UMIA is calculated using molar ratios of the major element oxides by converting wt% concentrations of whole rock analysis into moles (Duzgoren-Aydin et al., 2002). Unweathered peridotites of this study have UMIA values generally around 3, saprolite samples have UMIA values in the range of 4 to 8 and limonite and duricrust samples reach UMIA values between 60 and >90 (Table 4.1, Fig. 4.17).

The proposed UMIA aims to give a general weathering trend for ultramafic rocks. Calculated UMIA values have to be verified by observed mineralogy. For instance locally occurring formation of amorphous silica within highly altered limonite will result in low UMIA values. However, the UMIA can be directly combined with an AF-S-M ternary plot used to illustrate the weathering trend for

peridotite samples from investigated Ni laterites (Fig. 4.17a).

Continuous weathering of pyroxene and olivine leads to a loss of Mg and Si whereas redox dependent elements such as Fe are constantly enriched by formation of secondary oxide(s). Trends for either Fe-enrichment or bauxitisation (Al-enrichment) are visualized by an A-F-SM ternary plot (Fig. 4.17b). Ni laterite samples from Moa Bay are characterized by constantly high Fe/Al ratios, whereas limonite samples from Falcondo are more dispersed and show some tendency to bauxitisation (Fig. 4.17b).

4.7. Discussion

Ultramafic rocks exposed to the surface undergo intense chemical and mechanical weathering processes which are mainly controlled by climatic and topographic conditions (Golightly, 1981, 2010; Freyssinet et al., 2005).

Supergene processes leach main elements (i.e. Mg and Si) from ferromagnesian minerals in parent rocks whereas other elements (e.g. Ni, Mn, Co) can be enriched up to economic values. Redox dependent elements such as Fe as well as immobile elements such as Zr and Ti can be residually concentrated towards the surface. Ni laterites are the resulting product and can be classified according to their dominant Ni-bearing mineralogy (Marsh and Anderson, 2011 and references therein). 60% to 70% of the world land-based Ni resources are hosted by Ni laterites (Butt and Cluzel, 2013) and approximately 10% of these Ni resources are located in the northern Caribbean (Dalvi et al., 2004; Lewis et al., 2006a; Nelson et al., 2011).

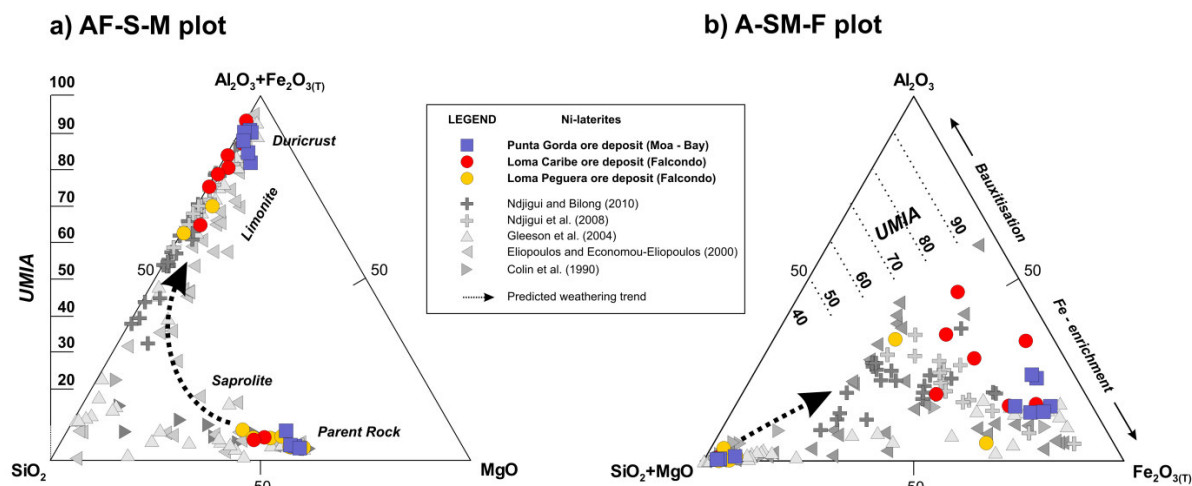


Fig. 4.17. Molar ternary plots in the Al-Fe-Mg-Si space showing weathering trends of ultramafic rocks and relationships with the in this work defined ultramafic index of alteration (UMIA) with data from the literature and studied samples. A) AF-S-M ternary plot illustrating the general weathering trend of peridotites with initial loss of MgO followed by loss of SiO₂ and concomitant enrichment of Al₂O₃ and Fe₂O₃. B) A-SM-F ternary plot illustrating the weathering trend with respect to Al₂O₃ enrichment (bauxitisation) or Fe₂O₃ enrichment.

4.7.1. Rare Earth Elements

It is clear that overall REE contents in investigated Ni laterites are very low when compared with conventional REE ore deposits (Chakhmouradian and Wall, 2012). However, concentrations of up to 335 ppm total REE are reached within clay rich zones in the limonite zone of Loma Caribe (Fig. 4.5). These values, which always have to be seen in the context of possible additional by-products in operating Ni (+Co) laterite mines, are approximately 10 times less as low grade ion adsorption clay-containing REE deposits. These ores are considered economic under favourable conditions as they are easy to mine and process (Simandl, 2014). Additionally an important advantage of lateritic REE ores is their very low content of radioactive elements.

The observation of REE minerals as phosphates or as Ce-rings and Ce-accumulations in association with REE enriched secondary Mn oxide(s) reveals

that REE are mobilized during the weathering process and can precipitate as newly formed minerals within the limonite (Fig. 4.12). As a consequence, enrichment peaks of REE are observed at zones with higher MnO accumulations (Fig. 4.2, 4.5 and 4.6). Mass balance calculations of both Ni laterite types reveal that LREE are preferably gained in these horizons compared to minor gains of HREE (Fig. 4.7, 4.8 and 4.9). This observation is supported by LA-ICP-MS analyses on secondary Mn oxide(s) (Fig. 4.16). However, within the hydrous Mg silicate type Ni laterites at Loma Caribe (Falcondo) the highest concentrations in REE of 335 ppm were found within a clay-minerals rich layer in the limonite (Fig. 4.5). Mass balance calculations indicate that only LREE are gained (25 fold) in this horizon, which is characterized by a general massive loss of elements relativizing the observed HREE loss of -26% (Fig. 4.8). Because MnO contents are negligible in this horizon (<0.7 wt%) a close relationship between clay-minerals

and REE (e.g. REE adsorbed on clay-minerals) is suspected.

Within the well-developed duricrust of Moa Bay (UMIA ~90) REE are the only measured elements showing gains in mass balance calculations (Fig. 4.7). This observation is linked to positive Ce anomalies observed in chondrite normalized patterns of all samples located close to the surface (Fig. 4.3). Cerium anomalies in lateritic profiles have been interpreted previously by REE leaching in a reducing environment with subsequent oxidation of Ce^{3+} to Ce^{4+} in an oxidizing environment and formation of cerianite (Braun et al., 1990; Janots et al., 2015 and references therein). These authors explained frequently occurring ring structures of cerianite as fillings of pores in a matrix of clay minerals (see Fig. 7c in Braun et al., 1990). However, recent studies on heterogeneous near surface environments, which are characterized by complex interactions involving rock, soil, water, air and (micro-)organisms, have shown that heavy-metals mobility in these environments is most likely controlled by biogeochemical processes (e.g. Chorover et al., 2007). In this context, the shape of observed cerianite ring structures could alternatively be explained by metal-depositing bacteria as described from experimental studies on bacteria-mineral spatial relationships (Little et al., 1997 and reference therein). The role of microorganisms in the mineralogical and chemical composition of laterite ores has been emphasized by Laskou and Economou-Eliopoulos (2007) and Kalatha and Economou-Eliopoulos (2015) who concluded, due detection of bacteria fossils, that bacterial communities can drive the formation of minerals in these

environments. It is widely accepted, that microorganisms favour accumulation of lanthanides in biogenic bodies such as Fe-Mn nodules and Fe-ochre (e.g. Vodyanitskii, 2010). Recently, lanthanides even have been proved to be essential for bacterial life in the case of volcanic mudpots (Pol et al., 2014). In addition, metal depositing microorganisms possibly act as subsequent nucleation sites for the precipitation of secondary minerals as likely observed in the case of REE phosphate formation on secondary Mn oxide(s) (Fig. 4.12e).

4.7.2. Scandium

Although Sc is a high tech element with wide application potential the global scandium consumption is currently estimated in the range of only 10 t (USGS, 2013). This is mainly explained due to high prices in combination with the absence of a reliable long term production for Sc. However, the yearly demand is constantly growing making scandium a worthy exploration target. To date scandium is mainly recovered as by-product from residues, tailings and waste liquors in the production of other metals (Wang et al., 2011). On the other hand, residual nickel ores in Australia containing average grades of 76 ppm and up to 370 ppm have recently been reported as important scandium resources and industrialized plants for scandium recovery from nickel laterites are expected to produce scandium oxides in large amount (Wang et al., 2011 and reference therein). In fact highly encouraging extraction results of up to 87% for scandium have been reported very recently from the Owendale laterite ore (Australia)

via high Pressure Acid Leach (“HPAL”) tests (Platina Resources, 2015).

Sc contents of ~120 ppm, with average contents of approximately 70 – 80 ppm Sc, were found in the upper limonite in the Ni laterites examined in this study (Fig. 4.2, 4.5 and 4.6). These values are slightly higher than those reported from similar Ni laterites located in New Caledonia (Fig. 4.15; Audet, 2009). It is believed, that Sc is predominantly present in pyroxene minerals of the peridotite as a substitute for ferrous iron. The strong positive correlation with Fe throughout the studied Ni laterite profiles in mass balance calculations (Fig. 4.7, 4.8 and 4.9) indicates that Sc is mainly concentrated in the final weathering products containing ferric iron (Fig. 4.15). Clear Sc signals in laser ablation ICP-MS analyses on Fe bearing secondary Mn oxide(s) from both Ni laterite types support this assumption (Fig. 4.16).

4.7.3. Platinum Group Elements

Large oxidized deposits associated with near surface modification of ultramafic rocks have been considered worthy exploration targets for unconventional Pt and Pd deposits (e.g. Wilde et al., 2003). The Owendale platinum - scandium project in New South Wales (Australia), which has estimated mineral resources of 520 000 oz Pt and 9 100 t Sc, represents such an exploration target (Platina Resources, 2015). In general, total PGE concentrations found in Ni laterites around the world are in the range of less than 100 ppb to up to a few hundred ppb (e.g. Augé and Legendre, 1994; Eliopoulos and Economou-Eliopoulos, 2000; Ndjigui and Bilong, 2010). However, lateritic crust

with 2 ppm PGE over the Ora Banda Sill, Western Australia, was reported from Gray et al. (1996) as well as more than 4 ppm PGE from Burundi (Maier et al., 2008).

Total PGE concentrations of investigated Ni laterites from the northern Caribbean are systematically enriched in the limonite and reach values of up to a few hundred ppb (Fig. 4.2, 4.5 and 4.6). Mass balance calculations reveal that PGE show similar enrichment trends as Fe, Ni and Sc within both Ni laterite types. PGE are importantly gained within the saprolite as well as within the lower part of the limonite (e.g. up to +358% and +819%, respectively in the case of Loma Peguera) (Fig. 4.7, 4.8 and 4.9). It is believed that PGE are enriched on the profile scale in the residue as PGM inclusions are protected in relatively resistant chromian spinel. However, recent studies also have provided evidence of neoformation processes close to the surface on the local scale (Aiglsperger et al., 2015). The assumption of common PGE redistribution in high levels of tropical Ni laterites is supported by detection of Pt within in-situ formed Mn oxide(s) (Fig. 4.16). Thus, chondrite normalized PGE patterns of one Mn oxide(s) rich sample (Mn 3) are characterized by a clear positive Pt anomaly (Fig. 4.4).

To assess an economic significance of observed PGE enrichment in Ni laterites the final product of Falcondo (i.e. ferronickel-cone after pyrometallurgical extraction from hydrous Mg silicates found in saprolite) was sent to Genalysis for PGE determination. The results show a PGE concentration of more than 2 ppm total PGE characterized by similar chondrite normalized patterns as for the laterite bulk; however, slightly more positive trends for Ir and Pt are evident (Fig. 4.18).

In addition, Lazarenkov et al. (2005) reported Pt and Pd contents of approximately 3 ppm each from final products from Moa Bay (i.e. sulphide concentrates after high pressure acid leach “HPAL” of oxide(s)) (Fig. 4.18). Considering the higher values measured in

final products from Moa Bay, these are probably likely linked to the exclusive mineral processing of oxidized limonite ores. A similar treatment of limonite ore from Falcondo would likely result in an important increase of total PGE within the final products of Falcondo.

Innovative direct extraction technologies such as the carbonyl process recently introduced by Terekhov and Emmanuel (2013), tested by the authors to be capable to produce 1.7 t PGE from a standard 1 000 000 t limonite Ni ore, as well as ongoing improvements in the metal extraction from oxidized ores by biomining (Johnson and du Plessis, 2015) will probably lead to a more diverse supply chain for these CM in the near future.

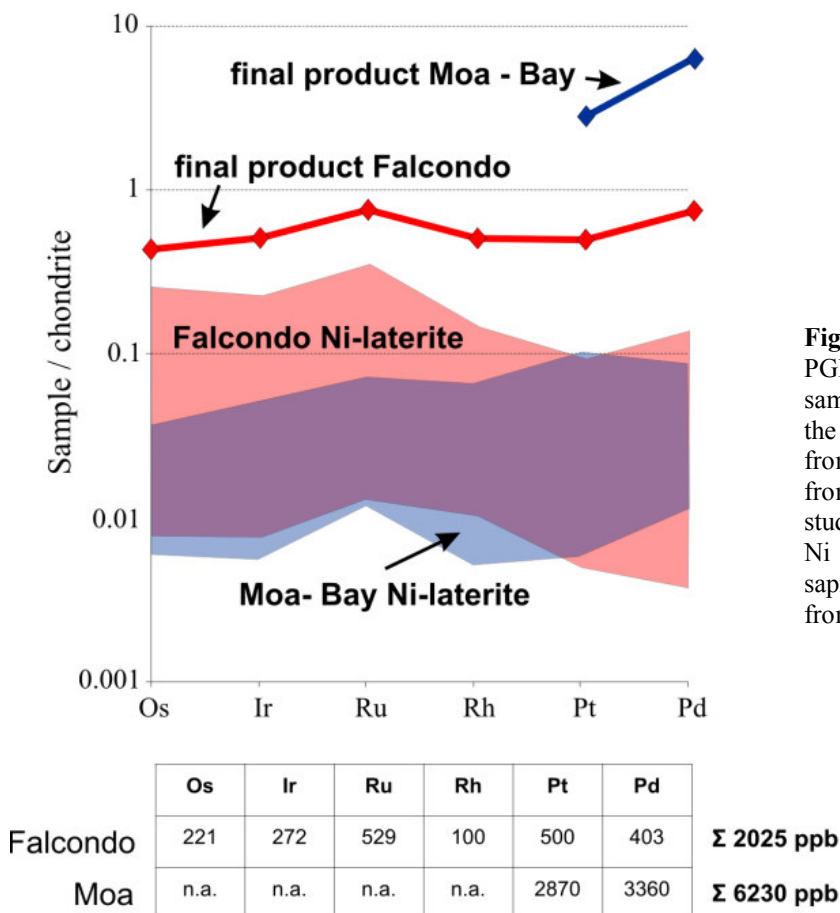


Fig. 4.18. Chondrite normalized PGE patterns and PGE contents of samples from final products from the Moa Bay mining area (values from Lazarenkov et al., 2005) and from the Falcondo mining area (this study) with indicated fields for both Ni laterite mining areas (limonite + saprolite). Normalization values from Naldrett and Duke (1980).

4.8. Concluding remarks

1. CM (REE, Sc, PGE) are concentrated in Ni laterites towards the surface in specific zones: (i) REE in clay minerals rich horizons and within zones composed of secondary Mn oxide(s) (ii) Sc within zones rich in secondary Fe and Mn bearing oxide(s) and (iii) PGE in zones with high concentrations of residual chromian spinel and secondary Fe and Mn bearing oxide(s) at upper levels of the Ni laterite profile.
2. Concentration factors involve (i) residual enrichment by intense weathering (ii) mobilization of CM during changing Eh and pH conditions with subsequent reprecipitation at favourable geochemical barriers (iii) interactions between biosphere and limonitic soils at highest levels of the profile with involved neoformation processes.
3. Total contents of CM in investigated Ni laterites are low when compared with conventional ore deposits but are of economic significance as CM should be seen as cost inexpensive by-products during the Ni (+Co) production. Innovative extraction methods currently under development will boost the significance of Ni laterites as future unconventional CM ore deposits.

Chapter 5

Chromian spinel composition and PGE geochemistry of chromitite bodies from the Loma Caribe peridotite, Dominican Republic

5.1. Introduction

In general ophiolitic chromitite deposits found around the world are characterized by wide spread compositional ranges and various morphologies. However, by determination of their chromian spinel composition two main groups of occurring chromitites can be defined: Cr-rich chromitites with Cr# $[\text{Cr}/(\text{Cr} + \text{Al})] > 0.6$ and Al-rich chromitites with Cr# values < 0.6 (González-Jiménez et al., 2014a and reference therein). TiO_2 concentrations for Cr-rich chromitites are normally < 0.25 wt% (Leblanc and Nicolas, 1992) whereas Al-rich chromitites reveal slightly higher values up to a maximum of ~ 0.5 wt% (Proenza et al., 1999a). These geochemical data is important as it can subsequently be used for petrogenetic indications. Proenza et al. (2007b) reported the discovery of chromitites from the Loma Caribe peridotite belt (Dominican Republic) with rather unusual characteristics: high Cr# (~ 0.75) and systematically high concentrations of TiO_2 (0.52-1.15 wt%). In addition elevated concentrations of platinum group elements (PGE; Os, Ir, Ru, Rh, Pt, Pd) up to 2.04 ppm total PGE were reported. However, these first findings were limited to a single, small scaled occurrence of chromitite bodies at Loma Peguera (Fig. 5.1) and concerns, if these atypical chromitites described by Proenza

et al. (2007b) are representative for a larger scale, remained.

Four recently discovered chromitite bodies from different locations along the Loma Caribe peridotite belt are examined in this chapter. All investigated chromitites reveal high PGE concentrations (up to 17.5 ppm total PGE).

Aim of this investigation is to characterize chromitite occurrences within the study area to better understand their role as possible sources for observed PGE enrichment (see chapter 6).

5.2. Field characteristics of the chromitite bodies

Chromitites show typical massive textures (95 vol.% chromian spinel) and were defined as:

- I. Loma Peguera 1; chromitites occur as small pods (approx. 5 m in diameter) included in serpentized peridotite (for details see Proenza et al., 2001, 2007b; Lewis et al., 2003) (Fig. 5.2)
- II. Loma Peguera 2; chromitites occur as veins (approx.. 2 cm in diameter) crosscutting serpentized peridotite (Fig. 5.3)
- III. Loma Caribe; chromitites occur as small pods (approx. 5 m in

- diameter) included in serpentinized peridotite
- IV. Loma Cumpié; chromitites occur as small pods (approx. 5 m in diameter) included in serpentinized peridotite; chromitites are crosscut by veins of uvaruite
- V. Loma Larga; chromitites occur as small pods (approx. 2 m in diameter) of highly decomposed chromitite within a matrix of limonite close to the surface (“floating chromitites”; see chapter 6 for additional information)

Primary silicate minerals were not observed in the matrix of studied chromitite samples but interstitial minerals such as chlorite and to a lesser extent serpentine as well as accessory pentlandite and awaruite are present.

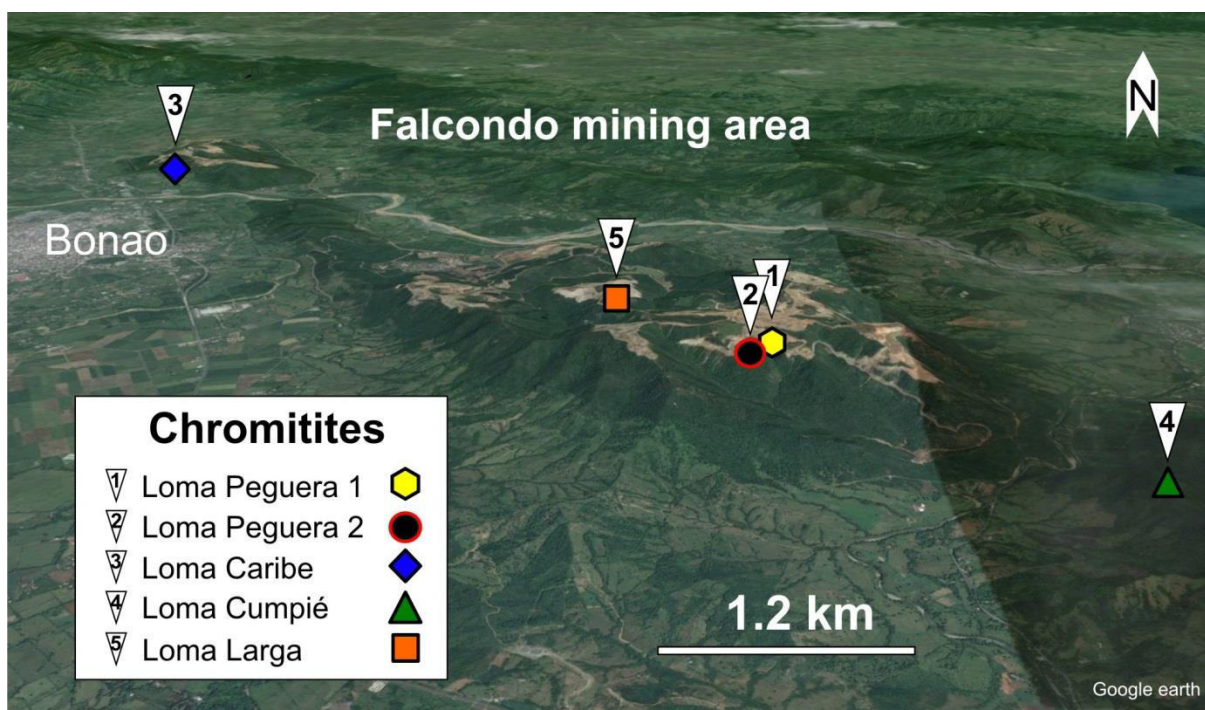


Fig. 5.1. Geographic overview and occurrence of investigated chromitites. Loma Peguera 1 localization is taken from Proenza et al. (2007b).

5.3. Compositions of the chromian spinels

Only chromian spinels in the cores of grains were analyzed and considered for petrogenetic indications. In general the composition of all investigated chromitite bodies is homogeneous in terms of Cr# [Cr/(Cr + Al)] and Mg# [Mg/(Mg + Fe²⁺)] within each sample location, thus they plot

in separate fields in a discrimination diagram (Fig. 5.4). However, in this work analyzed chromian spinels reveal systematically high average Cr#: 0.73 (Loma Peguera 2), 0.76 (Loma Caribe), 0.78 (Loma Larga) and 0.81 (Loma Cumpié) (Fig. 5.4).

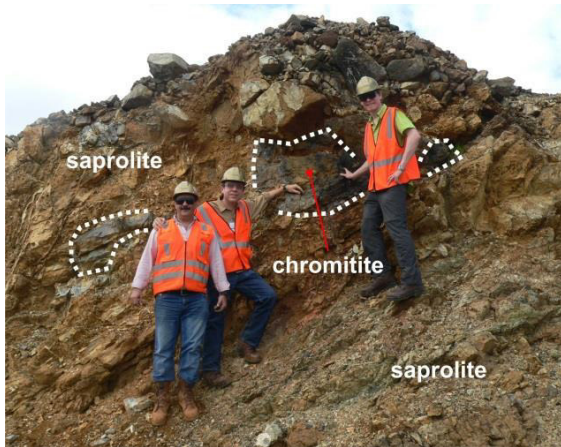


Fig. 5.2. Loma Peguera 1 chromitite.

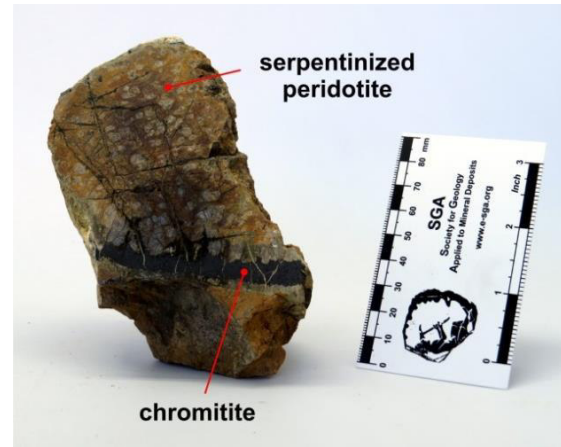


Fig. 5.3. Loma Peguera 2 chromitite.

TiO₂ contents are heterogeneous in analyzed chromian spinels and vary in Loma Caribe from 0.31-0.82 wt%, in Loma Larga from 0.14-0.56 wt%, in Loma Cumpié from 0.07-0.44 wt% and in Loma Peguera 2 from 0.44-1.25 wt% (Table 5.1; Fig. 5.5). In addition, NiO contents are relatively high reaching values between 0.13-0.23 wt% (Loma Larga), 0.16-0.25 wt% (Loma Caribe), 0.14-0.41 wt% (Loma Cumpié) and 0.19-0.55 wt% (Loma Peguera 2).

Furthermore average concentrations of heterogeneous V₂O₃, MnO and ZnO are 0.09 wt%, 0.26 wt%, 0.08 wt% (Loma Larga), 0.13 wt%, 0.30 wt%, 0.12 wt% (Loma Caribe), 0.19 wt%, 0.36 wt%, 0.13 wt% (Loma Peguera 2) and 0.05 wt%, 0.32 wt%, 0.09 wt% (Loma Cumpié), respectively (Table 5.1).

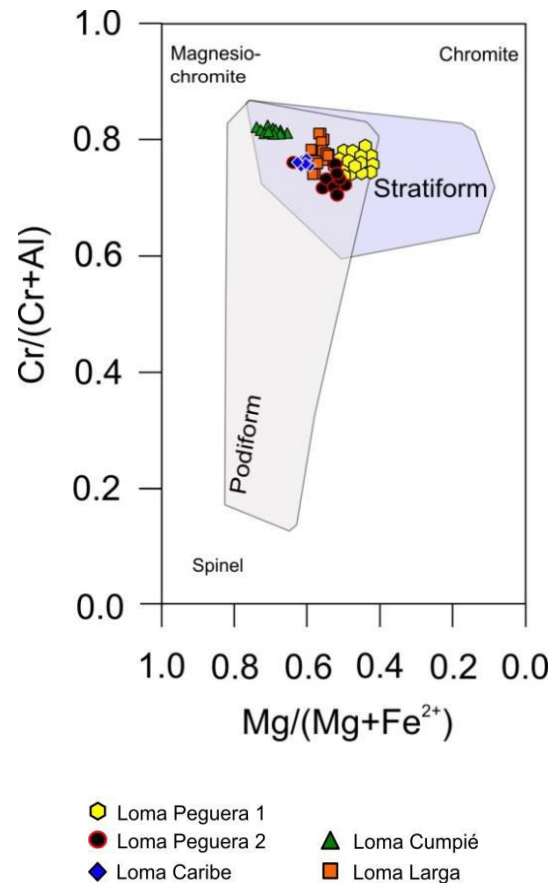


Fig. 5.4. Cr# [Cr/(Cr + Al)] versus Mg# [Mg/(Mg + Fe²⁺)] content for chromian spinels in chromitites from the Loma Caribe peridotite. Fields labeled “podiform” and “stratiform” are after Irvine (1967) and Leblanc and Nicolas (1992), respectively.

wt%	Loma Peguera 2			Loma Caribe			Loma Cumpié			Loma Larga		
	max	min	avg	max	min	avg	max	min	avg	max	min	avg
SiO ₂	3.81	0.00	0.16	1.24	0.00	0.05	0.64	0.00	0.04	0.13	0.00	0.02
TiO ₂	1.25	0.44	0.96	0.82	0.31	0.55	0.44	0.07	0.20	0.56	0.14	0.32
V ₂ O ₃	0.23	0.15	0.19	0.15	0.11	0.13	0.07	0.02	0.05	0.11	0.07	0.09
Al ₂ O ₃	13.35	9.79	12.17	12.28	11.30	11.69	9.36	8.02	9.10	13.26	9.98	11.73
Cr ₂ O ₃	50.66	43.66	48.61	57.01	53.38	55.72	60.20	59.31	59.83	61.19	54.17	58.62
FeO	18.16	8.73	17.06	16.05	13.85	14.81	13.65	9.88	11.22	14.97	13.16	14.27
Fe ₂ O ₃	12.94	6.46	7.96	4.93	3.09	4.03	6.16	1.80	4.51	0.00	0.00	0.00
MnO	0.41	0.30	0.35	0.42	0.25	0.30	0.36	0.27	0.32	0.31	0.22	0.26
MgO	14.19	10.26	10.79	12.84	11.60	12.41	15.10	11.48	14.18	11.56	9.85	10.65
NiO	0.55	0.19	0.31	0.25	0.16	0.20	0.41	0.14	0.26	0.23	0.13	0.19
ZnO	0.19	0.08	0.13	0.17	0.06	0.12	0.13	0.04	0.09	0.12	0.02	0.08
Total	99.81	93.10	98.68	100.84	99.41	100.01	100.84	95.66	99.80	97.92	89.56	96.23
Mg#	0.74	0.50	0.53	0.62	0.56	0.60	0.73	0.60	0.69	0.61	0.55	0.57
Cr#	0.76	0.71	0.73	0.77	0.75	0.76	0.83	0.81	0.82	0.80	0.75	0.77

Table 5.1. Maximum, minimum and average results of electron microprobe analyses of chromian spinel from recently discovered chromitites occurrences (n=50 each).

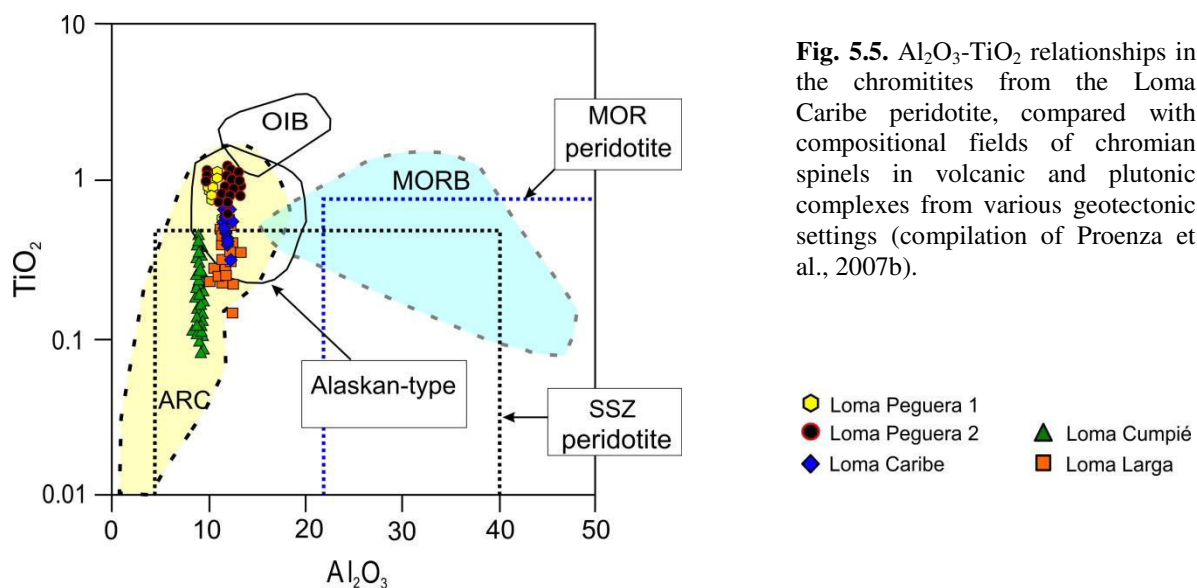


Fig. 5.5. Al₂O₃-TiO₂ relationships in the chromitites from the Loma Caribe peridotite, compared with compositional fields of chromian spinels in volcanic and plutonic complexes from various geotectonic settings (compilation of Proenza et al., 2007b).

5.4. PGE geochemistry

Whole rock analyses of PGE reveal that chromitites from the Loma Caribe peridotite are systematically characterized by high contents of total PGE, i.e. 17.5 ppm (Loma Larga), 6.54 ppm (Loma Cumpié), 4.55 ppm (Loma Caribe), 2.04

ppm (Loma Peguera 1) (Proenza et al., 2007b) and 1.19 ppm (Loma Peguera 2) with high IPGE (Os+Ir+Ru)/PPGE (Rh+Pt+Pd) ratios (Table 5.2).

In general chondrite normalized patterns of all studied chromitite bodies show similar shapes characterized by rather flat slopes from Os to Ru and subsequent negative slopes from Rh to Pd (Fig. 5.6). However,

Ir reveals in general a clear negative slope and Pt displays heterogeneous anomalies ranging from slightly negative slopes (Loma Peguera 2) to pronounced enrichment (Loma Larga; explained in chapter 7) (Fig. 5.6).

chromitites are in good agreement with chondrite normalized patterns from Loma Peguera 1 chromitites (Proenza et al., 2007b) (Fig 5.6).

Excluding variations of Pt these observations from recently discovered

Sample	Os	Ir	Ru	Rh	Pt	Pd	total PGE
Loma Peguera 1	432	461	778	90	269	6	2036
Loma Peguera 2	262	229	446	47	194	11	1189
Loma Caribe	1084	787	1388	178	1096	15	4548
Loma Cumpié	1732	1174	2141	198	1282	11	6538
Loma Larga	4945	3455	6536	281	2282	14	17513

Table 5.2. Concentrations (in ppb) of PGE in chromitites from the Loma Caribe peridotite.

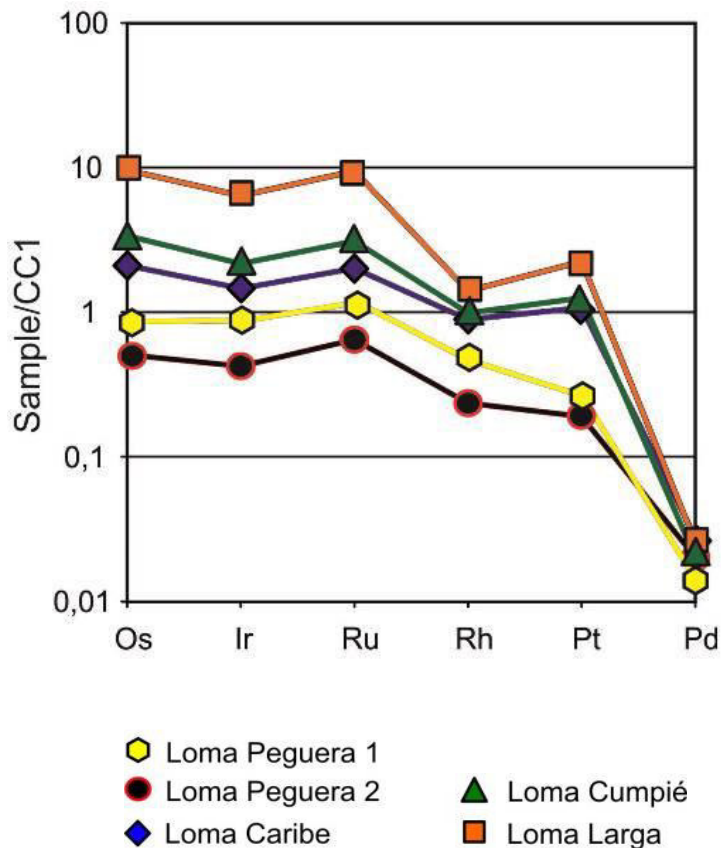


Fig. 5.6. Chondrite normalized patterns (Naldrett and Duke, 1980) of chromitites from the Loma Caribe peridotite.

5.5. Discussion

5.5.1. Chromitites hosted in the Loma Caribe peridotite: from exotic to atypical

Several genetic models have been proposed for the origin of Cr-rich ophiolitic chromitites (see González-Jiménez et al., 2014 and reference therein). However, the genesis of chromitites hosted by the Loma Caribe peridotite is still a matter of debate (Proenza et al., 2007b). Compositions of chromian spinels from Loma Caribe chromitites are atypical compared to those of ordinary ophiolitic chromitites, as they show systematically high values of Cr# (up to 0.82) together with high concentrations of TiO₂ (up to 1.25 wt%). To the best of the authors' knowledge such high TiO₂ contents have not been reported from ophiolitic chromitites.

It is widely accepted that Ti and Al concentrations in chromian spinel reflect the composition of the parent melt from which it had crystallized (Kamenetsky et al., 2001). Estimated parental melt compositions, with the exception of Loma Cumpié chromitites, are not boninitic as generally accepted for high-Cr ophiolitic chromitites (González-Jiménez et al., 2014 and reference therein). High TiO₂ contents in chromian spinel from ophiolitic chromitites are systematically associated with Al-rich chromitite.

In addition atypical PGE enrichments are observed in all investigated chromitites (up to 17.5 ppm total PGE). Positive Pt anomalies in chondrite normalized patterns are normally not observed in usual ophiolitic chromitites around the world but

are abundant in Alaskan-type chromitites (Garuti et al., 2003).

5.6. Concluding remarks

Overall chromitites hosted within the Loma Caribe peridotite are distinct to ordinary ophiolitic chromitites. Their geochemical fingerprint with high Cr#, high TiO₂ and extraordinary high PGE concentrations, including conspicuous Pt anomalies, point to two possible formation processes previously suggested by Proenza et al. (2007b):

- (i) due to an interaction between a heterogeneous oceanic mantle (Loma Caribe peridotite) and Cretaceous island-arc-derived melts.
- (ii) due to a mantle plume percolating through suboceanic upper mantle (Loma Caribe peridotite).

Chapter 6

Platinum group minerals (PGM) in the Falcondo Ni laterite deposit, Loma Caribe peridotite (Dominican Republic)

6.1. Introduction

As discussed in chapter 4, Ni laterites have to be considered worthy targets for PGE exploration. However, scientific work on the PGE mineralogy of unconventional PGE deposits is rare. In 1986 Bowles reported the occurrence of well-preserved crystals of laurite-erlichmanite and Os-Ir alloys found in laterites from the Freetown Complex in Sierra Leone. These Platinum Group Minerals (PGM) were not present within the underlying anorthosite and did not show abrasion features. In addition, some of the laurite-erlichmanite crystals showed platelike overgrowth of (Os,Ru)S₂. Bowles concluded that these PGM have most likely been formed *in situ* in the lateritic environment after remobilization of PGE under very acid, chloride-rich conditions with high Eh.

However, the influence of lateritization processes on PGE enrichment and PGM appearance is still matter of debate (e.g. Augé et al., 1995; Traoré et al., 2008 a,b). The model of PGM *in situ* growth within laterite profiles, as proposed by Bowles (1986), faces the possibility of residual enrichment due to intense weathering of primary PGM bearing rocks. Most of the available data, based on experiments and studies of natural occurrences, concern only the behaviour of Pd and Pt (Fuchs

and Rose, 1974; Pan and Wood, 1994; Azaroual et al., 2001; Talovina and Lazarenkov, 2001) but little is known about the mobility of the refractory IPGE (Os, Ir and Ru). Based on mineralogical observation, several authors recognized that also IPGE can be mobilised under hydrothermal or lateritic weathering conditions, occasionally producing secondary PGE alloys, sulfides, sulfarsenides or oxides by alteration of magmatic PGM precursors (Stockman and Hlava, 1984; Garuti and Zaccarini, 1997; Zaccarini et al., 2005; Garuti et al., 2007, 2012). A supergene origin of PGM has previously been reported from the platinumiferous Au-Pd belt of Minas Gerais, Brazil (e.g. Cabral et al., 2009, 2011) and was speculated for Pt-Fe alloys found in the alluvium of the Bushveld complex, South Africa (Oberthuer et al., 2014).

Fundamental questions still have to be solved for a better understanding of PGE mobility in supergene environments: (i) is primary PGE enrichment in the bedrock required for (residual) supergene enrichment; (ii) is PGE enrichment intrinsically related to lateritization processes; (iii) how do PGE and PGM behave within laterite profiles and what are criteria for PGE mobilization; (iv) is there unequivocal mineralogical evidence for neof ormation of PGM within laterites?

6.2. PGE geochemistry of the investigated laterite profiles

Eight samples (~3 kg each) from different horizons of two differing profiles (one chromitite bearing, i.e. Loma Peguera; one chromitite free, i.e. Loma Caribe) were selected. Table 6.1 gives an overview of concentrations of mayor and minor elements as well as PGE in whole rock analyses. Chondrite-normalized PGE patterns reveal rather similar, flat PGE trends for parent rocks, saprolite and limonite from both profiles (Fig. 6.1). However, saprolite and limonite patterns are shifted up, the latter by about one order of magnitude, in the case of Loma Peguera. As observed in chapter 5 the PGE-enriched chromitites of Loma Peguera displays a high $(Os+Ir+Ru)/(Rh+Pt+Pd)$ ratio with a particularly strong Pd negative spike (Fig. 6.1).

6.2.1. Loma Peguera

The sample from the parent rock (harzburgite) reveals total PGE contents of 36 ppb. Excluding the PGE-enriched chromitite sample in horizon D, the total PGE contents vary between 37 ppb (saprolite) and 640 ppb (limonite) (Table 6.1). The maximum concentration of PGE is observed near the exposed limonite (zone A), whereas the minimum value occurs right above the chromitite bodies in the central part of the saprolitic horizon (zone D) (Fig. 6.2). In general, ruthenium has the highest values among all PGE, ranging from 9 ppb (zone D) to 236 ppb (zone A) (Fig. 6.2; Table 6.1). Ruthenium peaks can be observed in saprolite underlying the chromitite bodies and within the generally PGE-enriched exposed limonite (Fig. 6.2). The IPGE and PPGE trends are similar within the laterite profile and IPGE/PPGE ratios of the weathering products vary from 0.77 (saprolite) to 3.08 (limonite) (Fig. 6.2; Table 6.1).

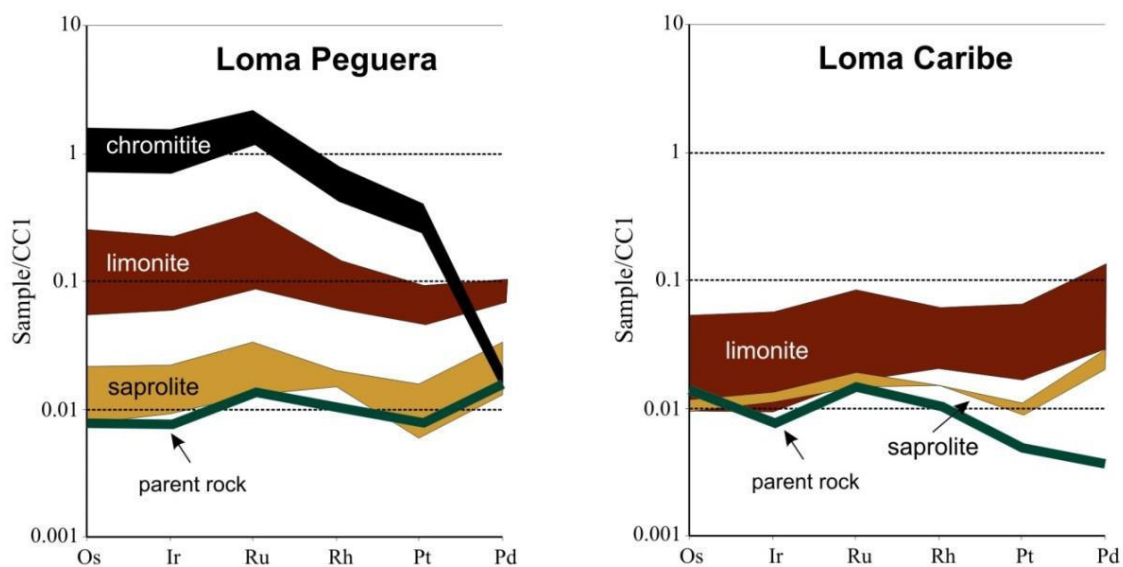


Fig. 6.1. Characteristic chondrite-normalized PGE patterns of samples from Loma Peguera and Loma Caribe Ni laterite profiles. Normalization values from Naldrett and Duke (1980).

Table 6.1. Concentrations of relevant major and minor elements (in wt%) as well as PGE contents (in ppb) in parent rocks and weathering products of the studied Ni laterite samples

Code	Loma Peguera										Loma Caribe							
	LP-11-007 limonite	LP-1 limonite	LP-3 saprolite	LP-2 saprolite	LP-5 saprolite	LP-6 chromitite	LP-4 saprolite	LP-7 saprolite	LP-101 harzburgite		LC-11-001 limonite	LC-1 limonite	LC-2 limonite	LC-6 limonite	LC-7 saprolite	LC-8 saprolite	LC-9 saprolite	LCAR-1 dunite
Zone	A	A	D	D	D	D	D	D	F		A	A	A	B-C	C	D	E+F	F
SiO ₂	7.25	11.07	44.37	40.07	41.19	n.a.	44.04	39.98	39.84		6.46	13.75	6.64	3.82	1.00	45.28	45.67	36.96
Al ₂ O ₃	3.64	3.77	1.86	0.07	0.58	n.a.	0.26	5.67	0.84		31.82	15.33	9.72	9.39	19.42	0.76	1.15	0.01
Fe ₂ O ₃	75.03	65.49	16.86	9.41	14.10	n.a.	14.59	7.80	8.44		40.10	55.80	65.55	67.31	44.64	10.60	12.14	8.00
MnO	1.28	1.07	0.19	0.17	0.23	n.a.	0.26	0.11	0.13		0.26	0.25	2.24	1.36	10.21	0.18	0.25	0.12
MgO	1.23	2.37	24.72	35.93	30.55	n.a.	27.43	33.29	41.23		0.11	0.55	0.57	0.56	0.28	29.85	28.65	43.85
NiO	1.20	1.95	1.82	1.08	1.80	n.a.	2.00	1.81	0.27		0.63	0.81	1.42	1.87	1.69	1.97	2.31	0.29
Co ₃ O ₄	0.20	0.12	0.02	0.02	0.03	n.a.	0.03	0.01	0.02		0.02	0.02	0.55	0.23	0.00	0.02	0.03	0.02
Cr ₂ O ₃	4.02	1.79	0.40	0.04	0.17	n.a.	0.08	0.20	0.35		0.49	1.08	1.82	2.41	1.39	0.26	0.32	0.26
Ir	118	32	7	5	5	802	12	6	4		30	24	23	27	24	6	7	4
Os	129	28	6	6	4	812	11	6	4		27	19	15	20	25	5	6	7
Pd	37	35	18	8	7	8	7	11	9		71	26	32	25	16	11	15	2
Pt	91	46	10	12	8	408	6	16	8		66	33	38	66	39	9	11	5
Rh	29	12	3	4	4	152	3	4	2		12	8	10	11	9	3	3	2
Ru	236	59	11	13	9	1396	23	13	9		58	42	47	49	45	10	13	10
ΣPGE	640	212	55	48	37	3578	62	56	36		264	152	165	198	158	44	55	30
Pt/Pd	2.46	1.31	0.56	1.50	1.14	51.00	0.86	1.45	0.89		0.93	1.27	1.19	2.64	2.44	0.82	0.73	2.50
Pt/Ir	0.77	1.44	1.43	2.40	1.60	0.51	0.50	2.67	2.00		2.20	1.38	1.65	2.44	1.63	1.50	1.57	1.25
Pt/Rh	3.14	3.83	3.33	3.00	2.00	2.68	2.00	4.00	4.00		5.50	4.13	3.80	6.00	4.33	3.00	3.67	2.50
Pt/Ru	0.39	0.78	0.91	0.92	0.89	0.29	0.26	1.23	0.89		1.14	0.79	0.81	1.35	0.87	0.90	0.85	0.50
IPGE	483	119	24	24	18	3010	46	25	17		115	85	85	96	94	21	26	21
PPGE	157	93	31	24	19	568	16	31	19		149	67	80	102	64	23	29	9
a	3.08	1.28	0.77	1.00	0.95	5.30	2.88	0.81	0.89		0.77	1.27	1.06	0.94	1.47	0.91	0.90	2.33

IPGE Os+Ir+Ru, PPGE Pt+Pd+Rh, a IPGE/PPGE, n.a. not analyzed

6.2.2. Loma Caribe

The unweathered dunite sample from Loma Caribe has a total PGE content of 30 ppb. Within the laterite profile total PGE values range between 44 ppb (saprolite) and 264 ppb (limonite) (Table 6.1). The highest PGE contents of the laterite profile are found within the highest level of zone A as well as within the transition zone between saprolite (zone C) and limonite (zone B) (Fig. 6.2; Table 6.1). Ruthenium and Pt are generally the most abundant PGE in the profile, reaching maximum values of 58 ppb Ru and 66 ppb Pt within

the limonite zone; however, in sample LC-11-001 Pd reaches a higher concentration (71 ppb) (Fig. 6.2; Table 6.1). Disregarding the highest levels of the laterite profile Pd does not correlate with the general trend of the other PGE (Fig. 6.2). IPGE and PPGE follow a similar trend with notable variations at the highest levels of the limonite zone (IPGE < PPGE), at the transition zone from zone B to zone C (IPGE < PPGE) and within zone C (IPGE > PPGE) (Fig. 6.2; Table 6.1).

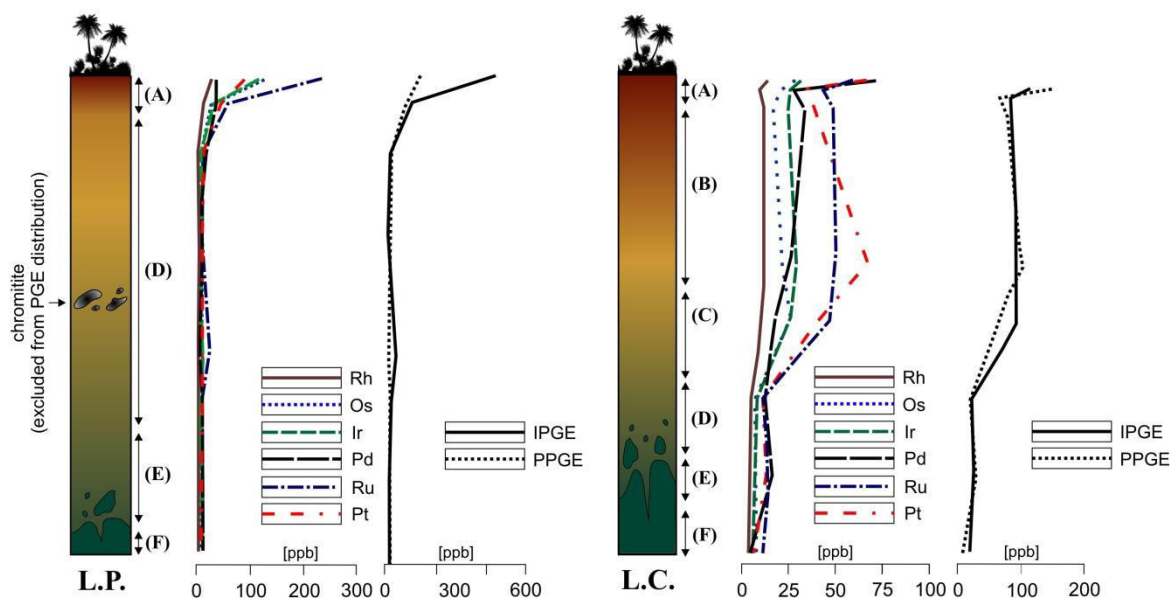


Fig. 6.2. Idealized Ni laterite profile from Loma Peguera (L.P.) and Loma Caribe (L.C.) with PGE contents and comparison of IPGE (Os+Ir+Ru) and PPGE (Pt+Pd+Rh) contents (in ppb): A, B limonite; C, D saprolite; E serpentinized peridotite; F unweathered peridotite.

6.3. Mineralogy of PGM

6.3.1. PGM in chromitites

A total of several hundreds of platinum-group minerals (PGM) were detected within recently discovered chromitites (see chapter 5), in thin and polished sections as well as in heavy mineral concentrates. Because of the great number of PGM and their in general very complex nature, only a small portion of these PGM has been investigated in detail at time of writing.

PGM phases range from 10 μm to more than a 100 μm in size and can be classified as: (i) primary PGM included in chromian spinel and believed to have formed at magmatic stage (ii) secondary, postmagmatic PGM, believed to have (trans-)formed during alteration processes (e.g. serpentinization) (iii) PGM with different features compared to (i) and (ii), suggestive for neof ormation processes.

In general, the most abundant PGM within chromitites from the Loma Caribe peridotite are primary laurite and to a lesser extent erlichmanite as well as secondary, highly porous Ru-Os-Fe alloys. These observations are in good agreement with the clear IPGE dominated whole rock geochemistry (see chapter 5). However, Rh-Ni arsenides, Ir-Fe-Ni alloys (frequently attached to porous Ru-Os-Fe alloys; discussed in chapter 7) and Pt bearing mineral compounds of unknown mineralogy occur in addition. Pd bearing mineral phases are either absent or

negligible. It is important to note, that two PGM detected within chromitites from Loma Peguera 1 have been described and accepted as new minerals recently (Garutiite, McDonald et al., 2010; Zaccarinite, Vymazalová et al., 2012). In addition a number of potentially new mineral species of PGM has been discovered (Zaccarini et al., 2009).

Examples of different PGM groups found in chromitites from the Loma Caribe peridotite are given in Fig. 6.3 and 6.4. Figure 6.5 aims to give an overview of main PGM groups found in chromitites of the Loma Caribe peridotite. Figures 6.6 and 6.7 show compositional variations for different groups in ternary diagrams. Table 6.2 reveals average, minimum and maximum EMP analysis in wt% and at% for different PGM groups. Some compositions of PGM are undescribed in the literature and therefore could represent new (undescribed) minerals. For example, Ir-Ni-Fe compounds (Fig. 6.3d) displayed in the ternary plot of Fig. 6.6a (Loma Peguera 1) may represent the hexagonal polymorph of native Ir. The Ni rich analogue (garutiite), found in the Loma Peguera 1 chromitite, has recently been accepted by the IMA as a new mineral (McDonald et al., 2010). In addition Pt rich Ni-Fe varieties are observed (Fig. 6.6b), thus leading to the assumption of a solid solution amongst the following endmembers: hexaferrum, Ir-Fe-Ni, Pt-Fe-Ni and garutiite.

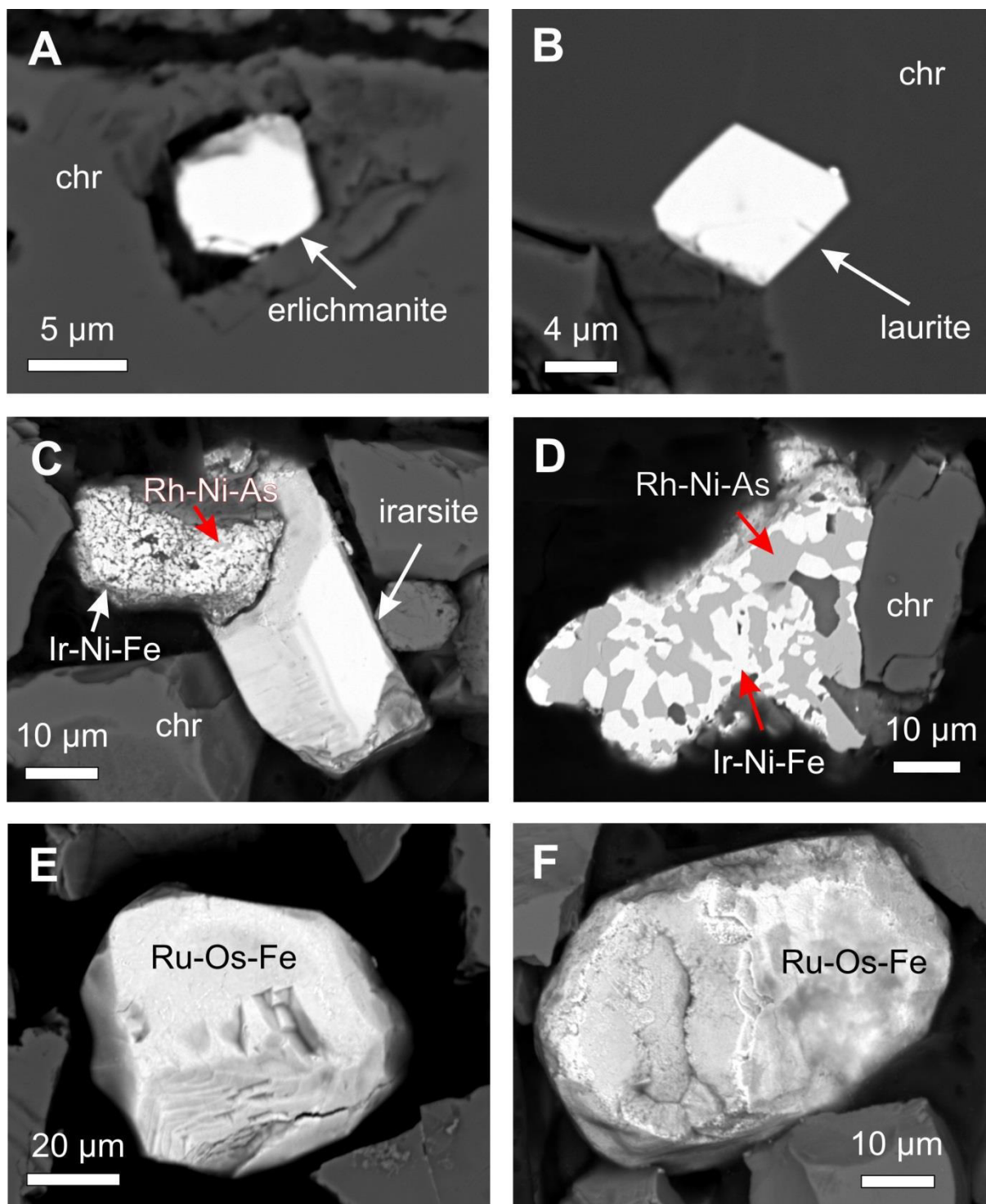


Fig. 6.3. Examples of most common PGM found in chromitites from the Loma Caribe peridotite. Fresh erlichmanite and laurite included in chromian spinel (A and B); Fresh crystals of irarsite (C) and Rh-Ni-As intergrown with Ir-Ni-Fe (C and D); porous Ru-Os-Fe grains with enigmatic layers architecture found in chromitites from Loma Larga.

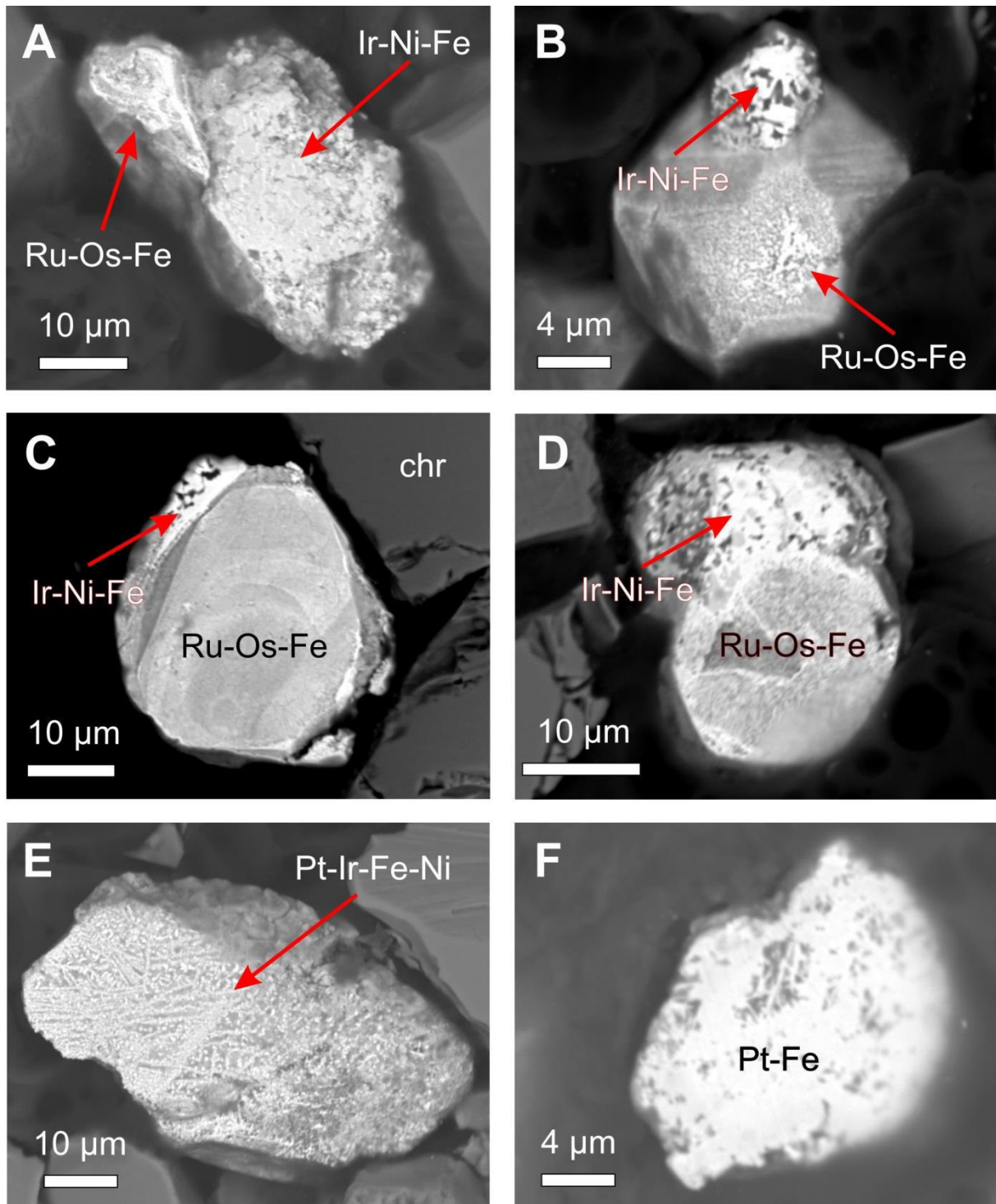


Fig. 6.4. Examples of most common PGM found in chromitites from the Loma Caribe peridotite. Note: frequent observation of Ir-Ni-Fe overgrowth on porous Ru-Os-Fe alloys (A-D), complex Pt bearing compounds of string forming nanoparticulates in Fe oxide(s) (E) and free grains of Pt-Fe alloys (F).

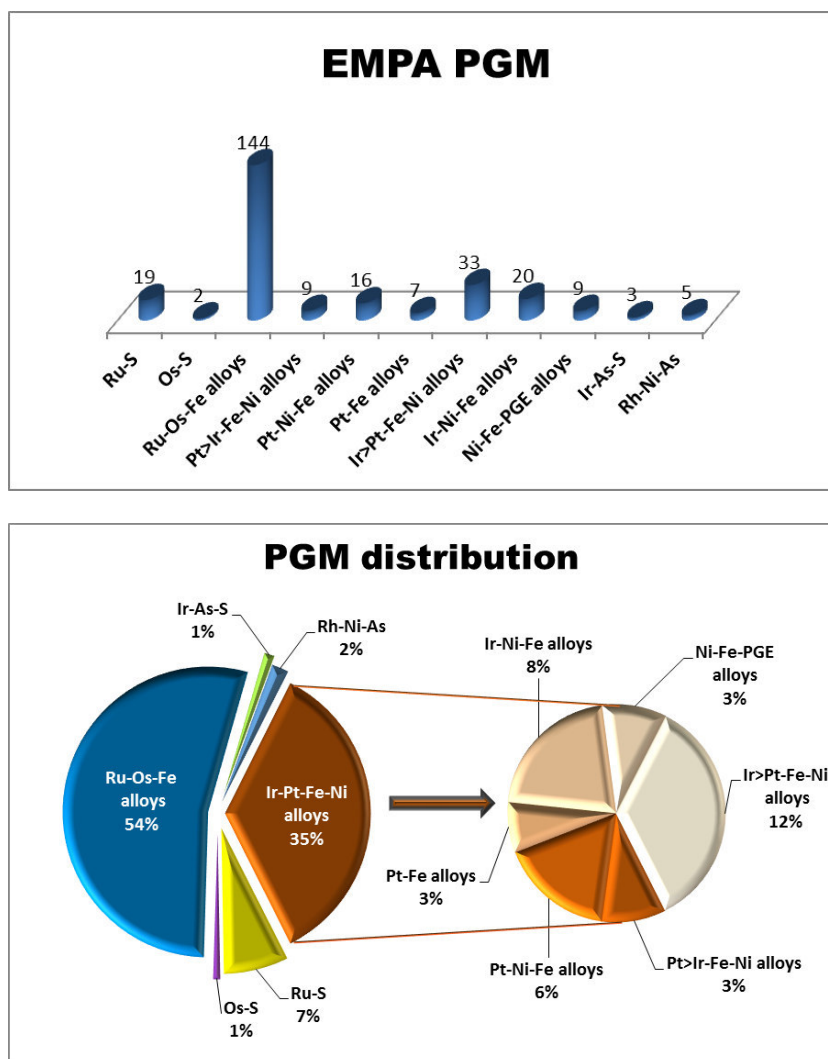


Fig. 6.5. Overview of detected PGM groups present in chromitites from the Loma Caribe peridotite. Note: proportion represents current number of quantitative EMP analysis and not the expected PGM distribution.

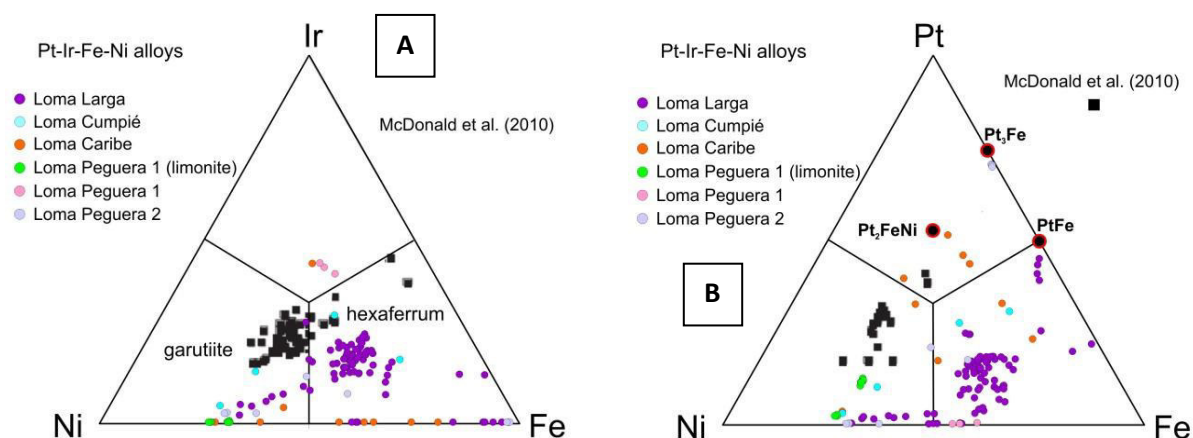


Fig. 6.6. Compositions of Pt-Ir-Fe-Ni alloys (in at. %) plotted in the ternaries: (a) Ni-Fe-Ir and (b) Ni-Fe-Pt. Comparison data of McDonald et al. (2010) represents composition of garutiite.

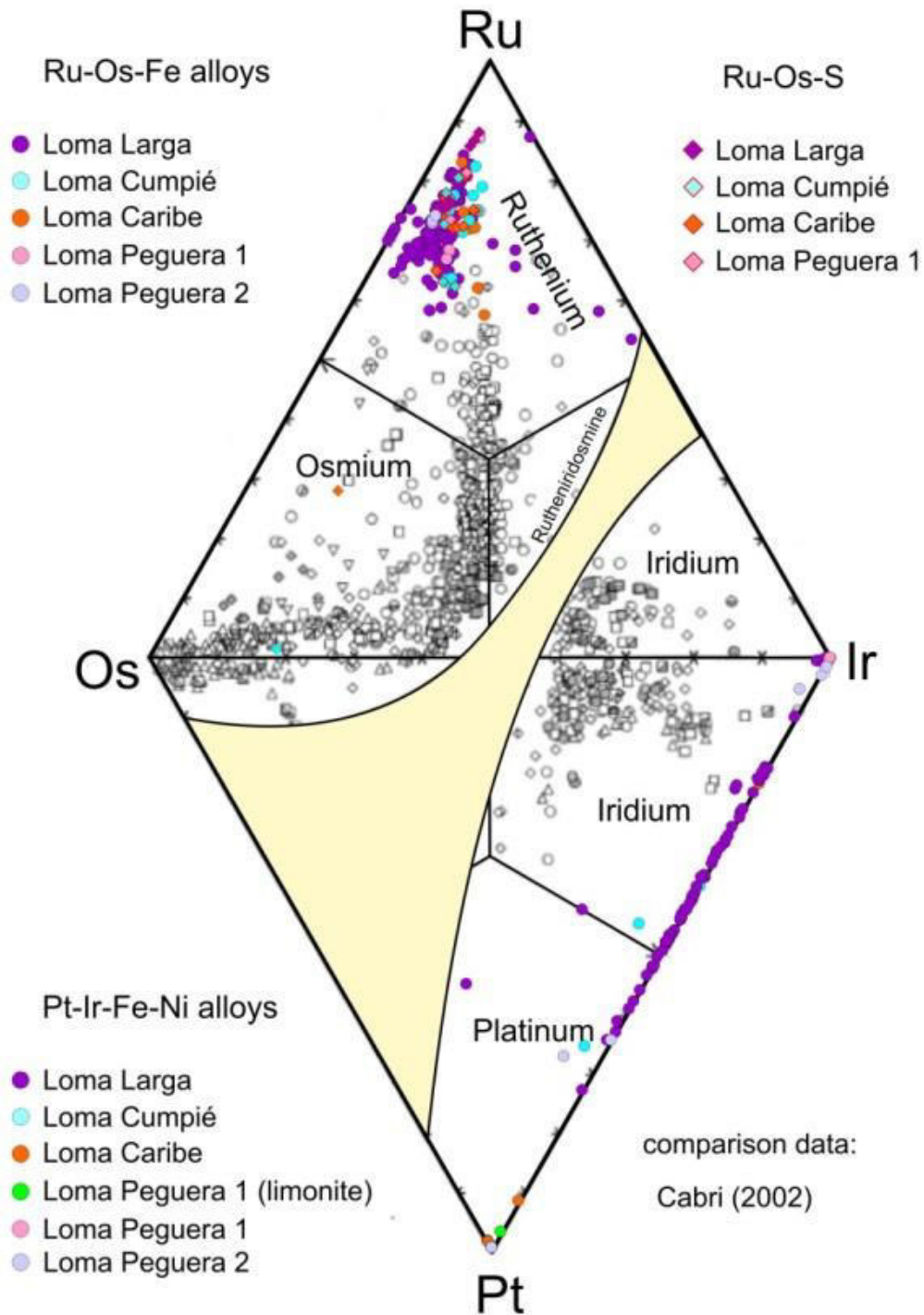


Fig. 6.7. Plot of analyses of Os-Ir-Ru-Pt compounds found in chromitites from Loma Caribe peridotite. Comparison data with alloys from deposits around the world were taken from Cabri et al. (2002).

	n	wt%	Os	Ir	Ru	Rh	Pt	Pd	Cu	Fe	Co	Ni	Sb	S	As	Si	Mg	Al	Total
Ru-S	19	Avg.	15.96	6.47	39.39	0.88	0.42	1.48	0.14	0.60	0.02	0.12	0.04	33.55	0.91	0.02	0.18	0.17	100.34
		Max.	23.54	11.00	48.95	3.17	6.91	2.04	2.49	1.29	0.05	0.92	0.11	35.18	1.15	0.31	1.02	0.43	103.38
		Min.	7.43	4.13	26.95	0.03	0.00	0.95	0.00	0.27	0.00	0.00	0.00	31.04	0.60	0.00	0.00	0.06	95.58
Os-S	2	Avg.	51.43	12.06	5.84	0.14	0.03	0.19	0.00	1.05	0.01	0.06	0.00	26.62	0.43	0.00	0.17	0.51	98.53
		Max.	58.28	13.38	11.30	0.22	0.04	0.35	0.00	1.50	0.02	0.11	0.00	26.72	0.52	0.00	0.33	0.62	100.06
		Min.	44.58	10.74	0.38	0.06	0.01	0.03	0.00	0.60	0.00	0.01	0.00	26.52	0.34	0.00	0.00	0.40	97.01
Ru-Os-Fe alloys	144	Avg.	22.09	6.90	39.53	0.22	0.11	0.40	0.01	17.41	0.11	0.83	0.01	0.09	0.66	0.29	0.27	0.58	89.51
		Max.	32.13	18.79	53.02	3.10	2.27	1.92	0.14	29.58	0.68	4.80	0.11	0.95	1.37	3.61	5.76	1.50	101.33
		Min.	11.00	0.00	24.33	0.00	0.00	0.00	0.00	2.07	0.00	0.18	0.00	0.00	0.16	0.00	0.00	0.00	79.97
Pt>Ir-Fe-Ni alloys	9	Avg.	0.04	19.97	0.08	0.78	26.50	0.10	0.60	24.93	0.15	14.09	0.03	0.01	0.01	0.26	0.02	0.14	87.47
		Max.	0.14	23.85	0.14	1.39	30.49	0.19	0.83	28.56	0.26	19.22	0.09	0.04	0.05	0.62	0.04	0.49	90.50
		Min.	0.00	10.93	0.01	0.28	23.50	0.03	0.39	21.69	0.06	11.48	0.00	0.00	0.00	0.05	0.00	0.00	82.67
Pt-Ni-Fe alloys	16	Avg.	0.18	1.35	0.12	0.71	43.13	0.23	1.75	18.75	0.29	24.64	0.05	0.29	0.08	0.19	0.10	0.01	91.00
		Max.	1.78	16.44	1.14	2.21	71.83	1.35	5.46	32.90	0.87	47.80	0.24	3.64	0.87	0.91	1.28	0.19	98.81
		Min.	0.00	0.00	0.00	0.13	26.60	0.00	0.44	9.84	0.00	5.79	0.00	0.00	0.00	0.00	0.00	0.00	84.87
Pt-Fe alloys	7	Avg.	0.00	0.00	0.04	0.32	73.51	0.31	0.50	17.63	0.11	1.16	0.05	0.00	0.01	0.03	0.07	0.00	93.75
		Max.	0.00	0.00	0.10	0.39	86.79	0.52	0.70	24.58	0.24	2.43	0.10	0.02	0.04	0.07	0.20	0.01	98.19
		Min.	0.00	0.00	0.00	0.25	60.72	0.16	0.34	9.89	0.02	0.24	0.00	0.00	0.00	0.00	0.00	0.00	89.70
Ir>Pt-Fe-Ni alloys	33	Avg.	0.08	27.49	0.27	0.88	19.79	0.07	0.64	22.34	0.11	14.07	0.01	0.03	0.02	0.35	0.02	0.23	86.01
		Max.	0.28	32.80	2.48	2.03	24.70	0.41	1.47	27.35	0.32	21.73	0.08	0.13	0.12	0.94	0.04	0.65	91.48
		Min.	0.00	22.14	0.00	0.25	11.26	0.00	0.33	18.77	0.00	9.52	0.00	0.00	0.00	0.15	0.00	0.03	80.95
Ir-Ni-Fe alloys	20	Avg.	0.24	32.99	0.65	0.56	3.27	0.10	1.44	24.96	0.33	28.60	0.02	0.03	0.05	0.12	0.04	0.10	92.77
		Max.	0.76	69.72	1.76	1.63	7.42	0.33	8.37	30.02	0.72	52.71	0.10	0.16	0.16	0.41	0.64	0.67	98.94
		Min.	0.00	10.29	0.07	0.10	0.00	0.00	0.36	14.24	0.05	11.94	0.00	0.00	0.00	0.00	0.03	0.00	81.80
Ir-As-S	3	Avg.	0.23	63.38	0.57	0.45	0.28	0.00	0.00	0.32	0.00	0.01	0.19	12.99	21.64	0.07	0.00	0.00	100.12
		Max.	0.32	63.65	0.69	0.51	0.38	0.00	0.00	0.35	0.01	0.01	0.31	13.18	22.27	0.08	0.00	0.00	100.30
		Min.	0.14	63.11	0.40	0.39	0.18	0.00	0.00	0.29	0.00	0.00	0.07	12.70	21.27	0.06	0.00	0.00	99.79
Rh-Ni-As	5	Avg.	0.05	1.44	0.98	41.51	0.21	0.10	0.23	0.81	0.06	24.33	0.00	0.01	26.79	0.32	0.15	0.10	96.91
		Max.	0.12	4.42	1.10	44.01	0.98	0.23	0.23	2.80	0.18	25.03	0.02	0.02	29.40	1.49	0.76	0.52	100.42
		Min.	0.00	0.47	0.71	33.08	0.00	0.02	0.23	0.26	0.00	21.96	0.00	0.00	18.54	0.01	0.00	0.00	86.26
Ni-Fe-PGE alloys	9	Avg.	0.05	2.49	0.16	3.68	3.97	0.10	0.46	23.57	0.41	60.48	0.01	0.01	0.05	0.11	0.06	0.00	95.39
		Max.	0.26	7.12	1.25	10.51	9.89	0.18	0.59	27.54	0.70	65.88	0.04	0.05	0.16	0.22	0.24	0.01	98.36
		Min.	0.00	0.00	0.00	0.14	0.09	0.03	0.19	22.03	0.00	45.67	0.00	0.00	0.00	0.00	0.04	0.00	89.18

	n	at%	Os	Ir	Ru	Rh	Pt	Pd	Cu	Fe	Co	Ni	Sb	S	As	Si	Mg	Al
Ru-S	19	Avg.	5.20	2.09	24.00	0.53	0.14	0.85	0.14	0.66	0.02	0.13	0.02	64.58	0.75	0.04	0.46	0.39
		Max.	7.82	3.62	28.59	2.00	2.30	1.15	2.54	1.51	0.05	1.00	0.06	65.38	0.93	0.67	2.57	1.05
		Min.	2.31	1.29	17.28	0.02	0.00	0.58	0.00	0.29	0.00	0.00	0.00	62.53	0.52	0.00	0.00	0.13
Os-S	2	Avg.	21.29	4.94	4.41	0.11	0.01	0.14	0.00	1.45	0.01	0.08	0.00	65.12	0.45	0.00	0.53	1.47
		Max.	24.74	5.62	8.51	0.17	0.02	0.25	0.00	2.05	0.02	0.14	0.00	66.78	0.53	0.00	1.05	1.76
		Min.	17.84	4.25	0.30	0.05	0.00	0.03	0.00	0.86	0.00	0.02	0.00	63.45	0.37	0.00	0.01	1.19
Ru-Os-Fe alloys	144	Avg.	12.60	3.88	42.04	0.23	0.06	0.41	0.01	33.21	0.19	1.54	0.01	0.30	0.94	1.10	1.12	2.35
		Max.	19.56	9.90	56.06	3.53	1.28	1.89	0.24	51.17	1.23	9.08	0.09	2.83	1.95	12.70	23.41	6.22
		Min.	5.99	0.00	25.24	0.00	0.00	0.00	0.00	3.82	0.00	0.34	0.00	0.01	0.21	0.00	0.00	0.00
Pt>Ir-Fe-Ni alloys	9	Avg.	0.02	10.81	0.09	0.80	14.18	0.10	0.54	46.47	0.27	25.00	0.03	0.05	0.02	0.99	0.07	0.56
		Max.	0.07	12.66	0.15	1.40	16.66	0.20	1.33	51.96	0.47	31.92	0.08	0.12	0.07	2.45	0.16	2.01
		Min.	0.00	6.06	0.01	0.27	11.74	0.04	0.00	41.55	0.09	19.95	0.00	0.00	0.00	0.20	0.00	0.00
Pt-Ni-Fe alloys	16	Avg.	0.12	0.82	0.15	0.78	23.48	0.27	1.55	33.01	0.45	36.89	0.04	1.00	0.12	0.77	0.50	0.06
		Max.	1.11	10.13	1.34	2.54	44.97	1.73	10.49	60.72	1.53	61.21	0.27	11.85	1.37	3.84	6.24	0.84
		Min.	0.00	0.00	0.00	0.13	10.25	0.00	0.00	18.39	0.01	11.36	0.00	0.00	0.00	0.00	0.00	0.00
Pt-Fe alloys	7	Avg.	0.00	0.00	0.05	0.42	52.88	0.39	1.07	41.75	0.23	2.51	0.05	0.02	0.02	0.14	0.45	0.01
		Max.	0.00	0.00	0.12	0.50	68.98	0.59	1.43	53.70	0.49	5.05	0.11	0.07	0.09	0.30	1.26	0.04
		Min.	0.00	0.00	0.00	0.31	37.98	0.23	0.65	27.39	0.04	0.64	0.00	0.00	0.00	0.00	0.00	0.00
Ir>Pt-Fe-Ni alloys	33	Avg.	0.04	15.52	0.28	0.91	11.11	0.07	0.45	43.15	0.20	25.75	0.01	0.10	0.03	1.37	0.07	0.93
		Max.	0.16	19.74	2.55	2.10	14.12	0.41	2.64	48.54	0.54	34.31	0.07	0.47	0.18	3.90	0.19	2.78
		Min.	0.00	10.68	0.00	0.23	5.61	0.00	0.00	38.82	0.00	20.13	0.00	0.00	0.00	0.57	0.00	0.13
Ir-Ni-Fe alloys	20	Avg.	0.11	16.39	0.58	0.45	1.39	0.08	0.84	38.65	0.49	40.05	0.01	0.08	0.05	0.38	0.13	0.32
		Max.	0.33	42.48	1.51	1.30	3.54	0.25	9.30	49.79	1.21	62.52	0.07	0.41	0.21	1.36	1.85	2.31
		Min.	0.00	3.78	0.05	0.11	0.00	0.00	0.00	22.21	0.09	23.04	0.00	0.00	0.00	0.09	0.00	0.00
Ir-As-S	3	Avg.	0.12	31.52	0.54	0.42	0.14	0.00	0.00	0.55	0.01	0.01	0.15	38.72	27.61	0.23	0.00	0.00
		Max.	0.16	31.54	0.65	0.48	0.18	0.00	0.00	0.59	0.02	0.02	0.24	39.14	28.56	0.26	0.00	0.00
		Min.	0.07	31.49	0.38	0.36	0.09	0.00	0.00	0.50	0.00	0.00	0.06	38.05	27.03	0.19	0.00	0.00
Rh-Ni-As	5	Avg.	0.02	0.63	0.79	32.63	0.09	0.08	0.06	1.24	0.08	33.60	0.00	0.02	28.87	1.00	0.55	0.34
		Max.	0.05	2.01	0.87	33.84	0.44	0.19	0.32	4.38	0.27	34.16	0.01	0.07	31.05	4.64	2.75	1.69
		Min.	0.00	0.19	0.56	28.08	0.00	0.01	0.00	0.38	0.00	32						

6.3.2. PGM in the saprolite

Sixteen PGM grains were found and divided in two groups: occurrence (i) as discrete free grains or (ii) as inclusions in Cr-spinel. Free PGM are restricted to the finest size fraction (<53 μm) and vary in grain size from 10 to 50 μm . Idiomorphic laurite crystals and Ru-Fe-Os-Ir bearing compounds with irregular shape and spongy surface due to high porosity are the most abundant PGM within this group (Fig. 6.8). One Ru-Pt-Fe-Os-Ir phase was observed attached to laurite (Fig. 6.8a) and some PGE compounds display well defined Fe-Si-Mg-O-Ru rims with or without Ni (Fig. 6.8b and c). Dark areas on BSE images are explained by Si- and Mg-rich domains resulting in skeleton textures (Fig. 6.8d). In addition, undetermined Pt-Ir-Fe-Ni and Ru-Os-Ir-Rh compounds have been observed. PGM included in fresh Cr-spinel grains were found within the coarser size fractions (>53 μm) and consist of bowieite and laurite (Fig. 6.8e and f).

6.3.3. PGM in the limonite

A total of 10 PGM was detected in the finest size fractions (<53 μm) of the limonite samples. In sample LC 2 two small-sized PGM (<10 μm) were found: one elongated grain of Ir-Ru-Os-Pt-Fe-Ni included in awaruite (Fig. 6.9a), and one complex grain assemblage of Pt-Fe-Ni with clusters of Ru-Ir and zones of Ir-Fe-Si-Al-Ni included in a strongly weathered Cr-spinel grain (Fig. 6.9b). Both irregularly shaped PGM occur close to the edge of their hosts and element mapping (see Fig. 4.14 of chapter 4) of the complex PGM aggregate shows a heterogeneous

PGE distribution with Pt, Ir and Ru as the most abundant PGE.

Within sample LP-11-007 five 5-20 μm sized PGM were found as inclusions in Fe-oxide(s), derived from weathering of ferrian Cr-spinel. They are either present as well defined, euhedral grains of Os-Ru compounds with primary features or as disperse Pt-Fe particles with occasionally elongated shapes. One elongated Pt-Fe-Ni grain (20 μm) is characterized by delicate botryoidal textures similar to Pt-Pd aggregates interpreted as *in situ* growth at surface conditions (Fig. 6.9c) (Cabral et al., 2011). Three PGM were detected within sample LP 1 which can be divided into two groups: two PGM occur as small (<10 μm) inclusions within awaruite and within the contact zone of awaruite with altered Cr-spinel (Fig. 6.9d and e), whereas one PGM occurs as a significantly bigger (40 μm), irregularly shaped free grain (Fig. 6.9f) (Table 6.3). The included PGM show similarities with included PGM from Loma Caribe in terms of occurrence and shape, however, their composition is dominated by Os-Ru-Ir-S-Ni-Fe and Os-Ir-Ru-Fe-Ni, respectively. The irregularly zoned free PGM grain is characterized by an oxidation rim with minor Ru and a heterogeneous composition of mainly Ni-Fe-Pt-Ir-Co with very scarce Pd, Rh and Os. Element mapping reveals the complexity of this grain with zones composed of Pt-Ir-Ni-Fe (center), Ru-Ni-Fe (oxidized rim) and Ni-Fe-Co braiding crosscutting the grain (Fig. 6.10). Besides PGM, one elongated 50 μm gold grain (99 wt% Au) was detected.

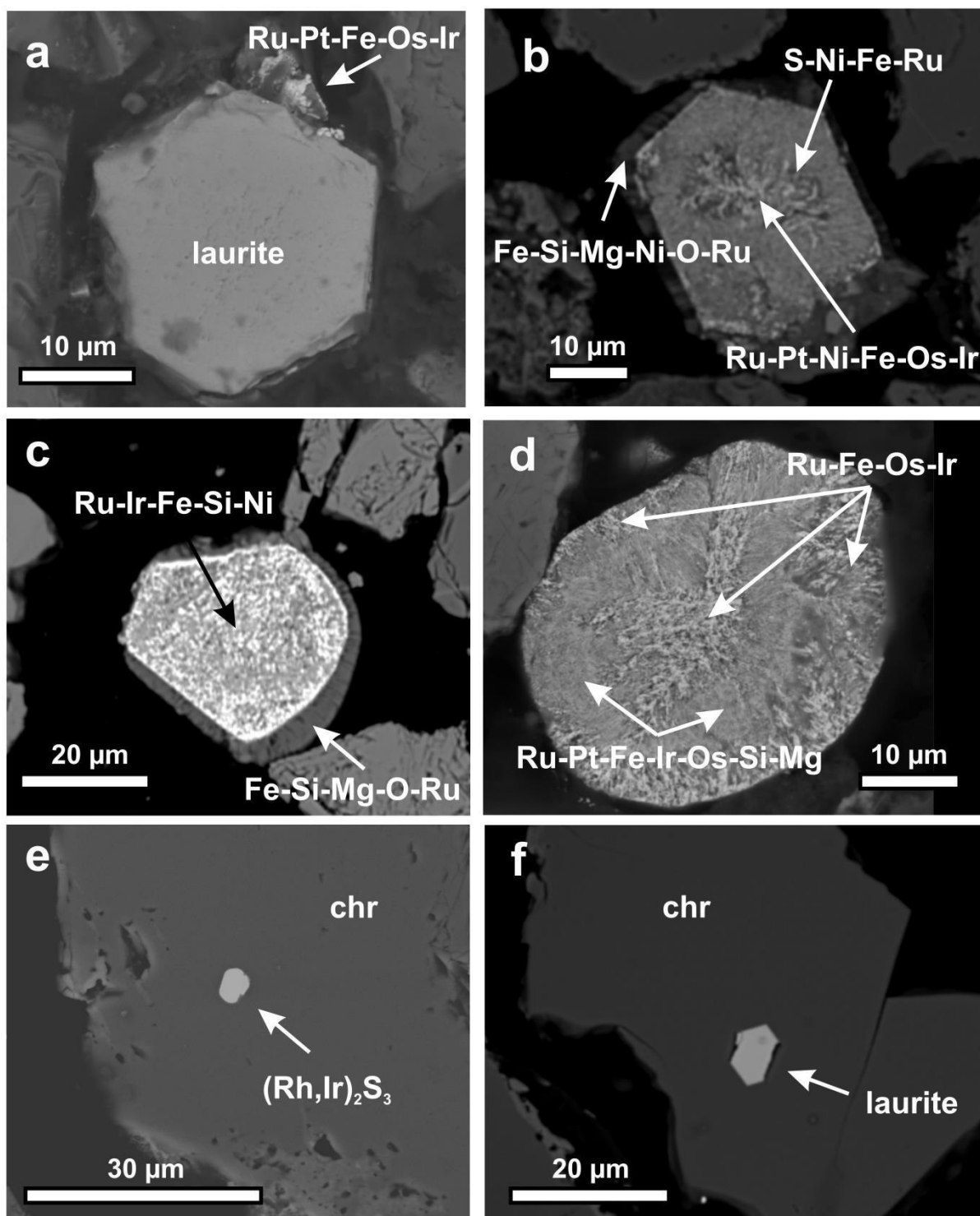


Fig. 6.8. BSE images of PGM found within saprolite from Loma Peguera: (a) euhedral crystal of laurite with attached Ru-Pt-Fe- Os-Ir phase, (b–d) examples of porous PGE compounds, (e–f) PGM included in Cr-spinel.

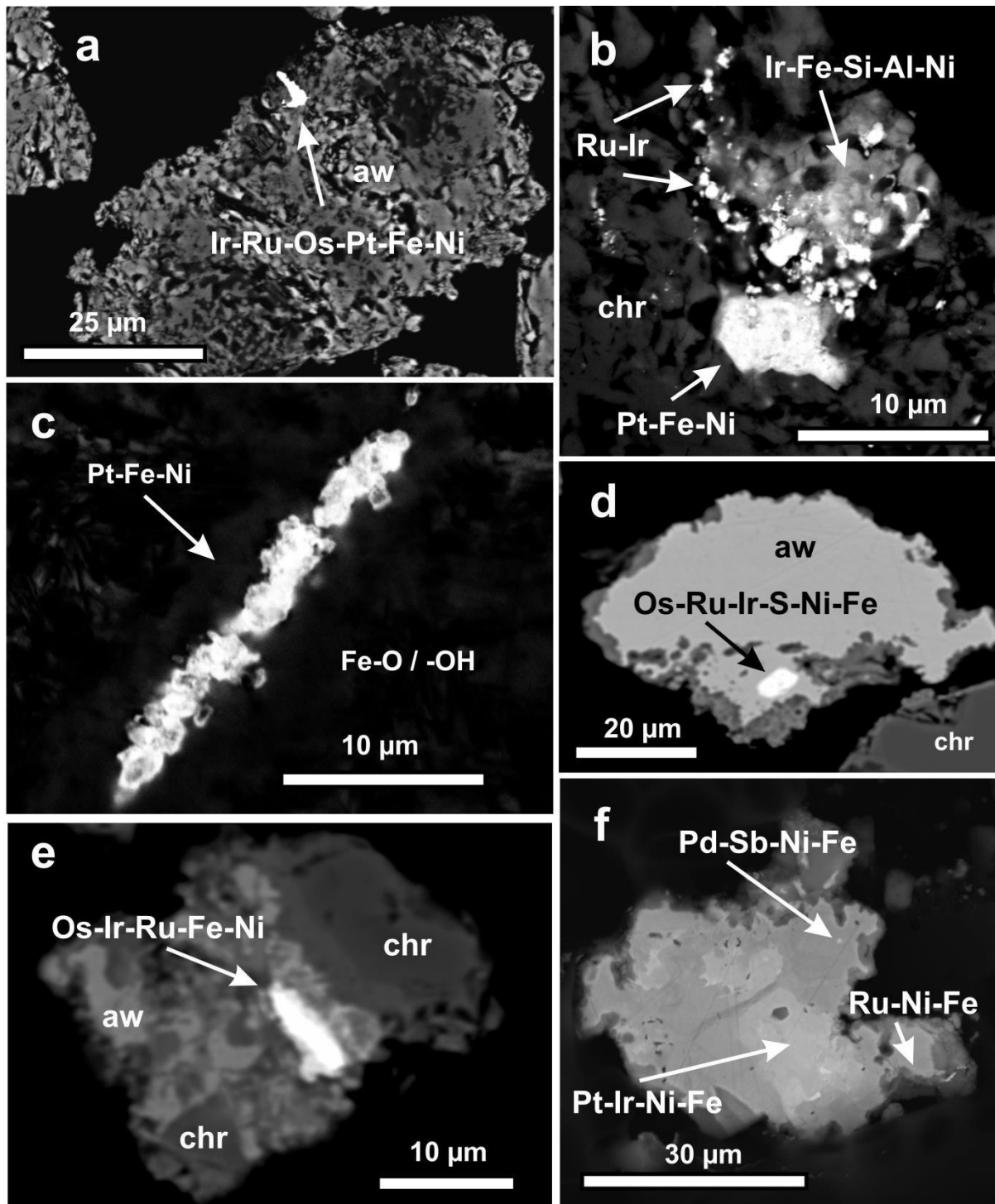


Fig. 6.9. BSE images of PGM found within limonite from Loma Caribe (a, b) and Loma Peguera (c–f); aw awaruite; chr Cr-spinel.

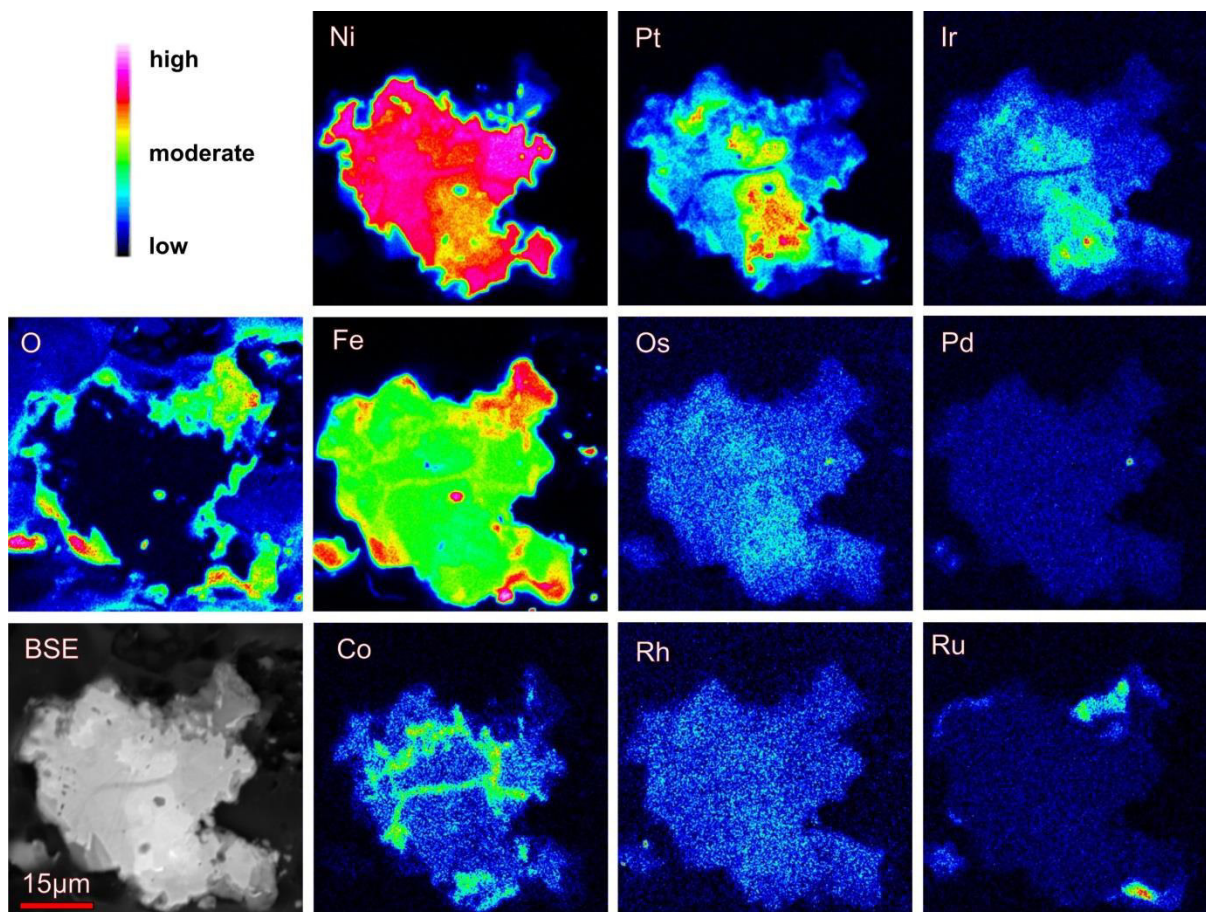


Fig. 6.10. Element distribution map of a free PGM found in limonite from Loma Peguera.

6.4. Electron microprobe composition of PGM found in saprolite and limonite

A summary of quantitative analyses obtained by electron microprobe for representative laurite, bowieite, PGE compounds and two PGM from the limonite zone is given in Table 6.4. Compositions of PGM are shown in Fig. 6.11 together with literature data for comparison. Ru-Os-Ir-Fe oxides (?) found in chromitite bodies from Loma Peguera (Proenza et al., 2007b; Zaccarini et al., 2009) have in general significant lower Ru contents than Ru-Os-Ir-Fe compounds from the underlying saprolite. Quantitative analyses of two PGM in the limonite zone

show generally higher Os contents; low totals are due to very small grain sizes, high porosities and Mg-Si impurities. PGE compositions of magmatic and partially desulphurized laurite from chromitite display rather variable Ru and Os contents when compared with laurite found in saprolite (Fig. 6.11).

Small bowieite inclusions in Cr-spinel are characterized by compositions along the kashinite – bowieite solid solutions line, close to $\text{Rh}_{1.5}\text{Ir}_{0.5}\text{S}_3$ (Fig. 6.12). Bowieite with similar composition, normally associated with Alaskan-Uralian type intrusions, was found in Pt nuggets from Goodnews Bay, Alaska (Desborough et al., 1984).

	Loma Peguera		Loma Caribe
	saprolite	limonite	limonite
laurite	O; +		
bowieite	+		
Ru-Fe-Os-Ir	O		
Ru-Ir-Fe-Si-Ni	O		
Ru-Os-Ir-Rh	O		
Ru-Pt-Fe-Os-Ir	O		
Ru-Pt-Ni-Fe-Os-Ir	O		
Ru-Pt-Fe-Ir-Os-Si-Mg	O		
Pt-Ir-Fe-Ni	O		
Fe-Si-Mg-Ni-O-Ru	O		
Fe-Si-Mg-O-Ru	O		
S-Ni-Fe-Ru	O		
Ir-Ru-Os-Pt-Fe-Ni			x
Ir-Fe-Si-Al-Ni			+
Ru-Ir			+
Pt-Fe-Ni		#	+
Pt-Fe-Ni-Cu		#	
Os-Ru-Fe		#	
Os-Ru-Ir-S-Ni-Fe		x	
Os-Ir-Ru-Fe-Ni		+/x	
Ni-Fe-Pt-Ir-Co-Ru-Pd-Sb		O	

Table 6.3. PGM found in the investigated laterite samples. + included in Cr-spinel, x included in awaruite, +/x included in Cr-spinel-awaruite transition zone, # included in Fe-oxide(s), O free grains.

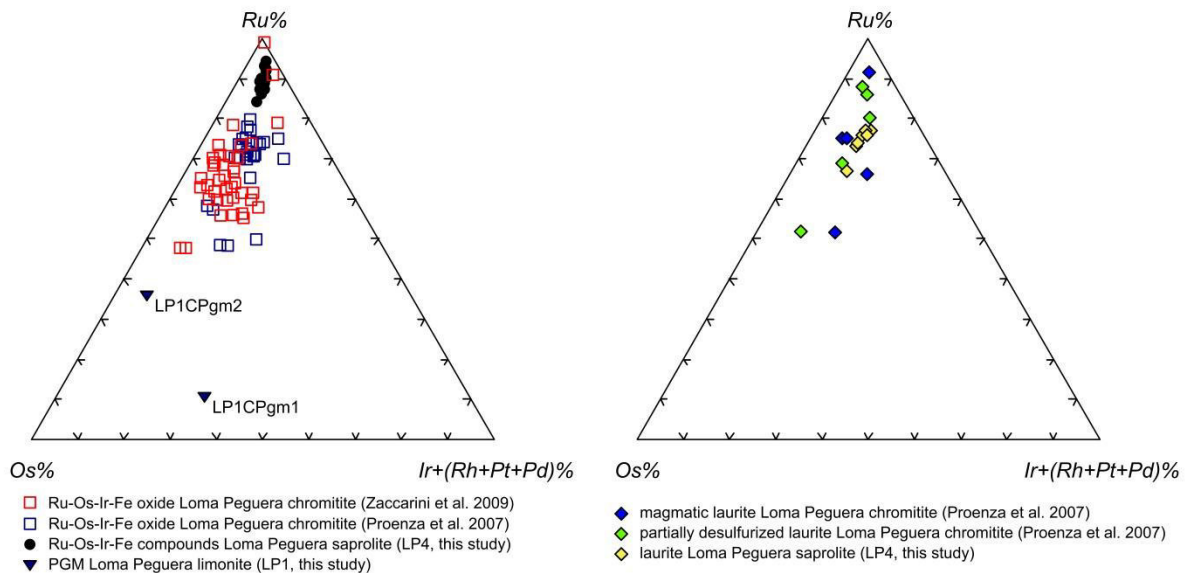


Fig. 6.11. Left composition (at%) of Ru-Os-Ir-Fe compounds found in chromitite and saprolite (Loma Peguera) and of two PGM found in limonite (Loma Peguera) in terms of Ru-Os-Ir(Rh+Pt+Pd). Right composition (at%) of laurite occurring in chromitite and saprolite (Loma Peguera).

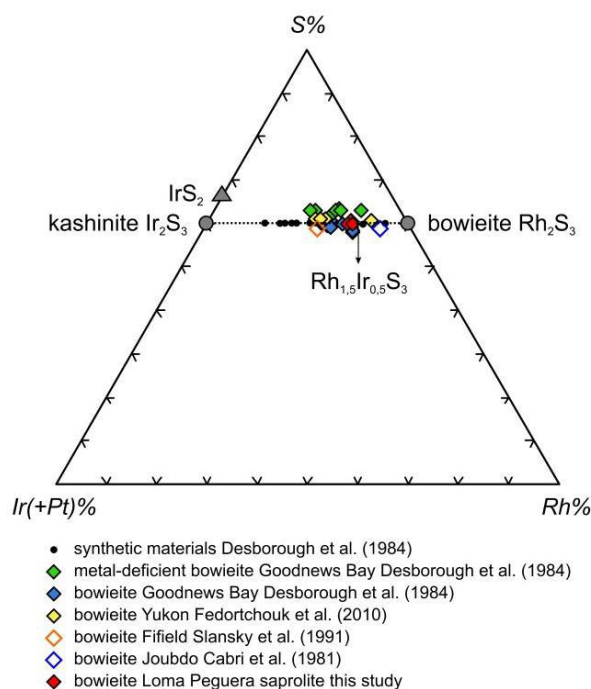
Composition of PGM (found in saprolite) analysed by Electron Microprobe

Grain	wt%														Total
	S	Os	Ir	Ru	Rh	Pt	Pd	Fe	Ni	Cu	Co	Cr	As		
laurite															
LP4-40-1-3	34.34	13.34	9.37	42.04	1.20	n.d.	n.d.	0.43	0.04	n.d.	n.d.	0.58	n.d.	101.34	
LP4-40-7-2	34.86	12.39	9.30	43.16	1.19	n.d.	n.d.	0.40	0.03	0.07	0.04	0.50	0.01	101.95	
LP4-40-7-3	33.93	11.81	9.52	42.42	1.34	n.d.	n.d.	0.35	0.04	0.01	n.d.	0.48	n.d.	99.90	
LP4-40-7-4	34.09	13.60	9.00	42.01	1.18	n.d.	n.d.	0.35	0.04	n.d.	0.05	0.49	n.d.	100.81	
LP4-40-7-5	33.04	16.38	8.67	39.12	1.25	0.09	n.d.	0.45	n.d.	n.d.	0.02	0.59	n.d.	99.61	
LP4-40-7-7	33.70	14.95	9.33	40.06	1.15	0.25	n.d.	0.44	0.07	0.02	0.05	0.53	n.d.	100.55	
LP4-40-7-8	34.19	13.12	9.78	41.69	1.07	0.07	n.d.	0.45	0.07	0.03	0.02	0.52	n.d.	101.01	
LP4-40-7-9	34.18	12.56	9.11	42.89	1.20	n.d.	n.d.	0.38	0.04	0.04	n.d.	0.51	n.d.	100.91	
LP4-64/2-x3-2	32.50	12.15	8.26	39.83	2.02	n.d.	n.d.	0.87	0.05	n.d.	0.05	1.32	n.d.	97.05	
LP4-64/2-x3-4	32.48	12.13	7.92	40.06	1.94	0.03	n.d.	0.84	0.05	0.02	0.04	1.35	n.d.	96.86	
bowieite in chr															
LP4-80-x2	25.98	0.37	29.58	0.27	40.15	n.d.	0.39	1.05	0.06	0.01	0.01	1.90	n.d.	99.77	
LP4-80-x2-2	26.40	0.12	29.86	0.05	40.27	n.d.	0.50	1.11	0.03	0.02	0.10	1.91	n.d.	100.37	
LP4-80-x2-3	26.21	n.d.	29.40	0.11	39.72	0.06	0.31	1.17	n.d.	0.10	0.04	1.98	n.d.	99.10	
LP4-80-x2-4	25.85	n.d.	29.77	0.02	39.15	0.08	0.49	1.45	0.08	n.d.	0.02	2.73	n.d.	99.64	
LP4-80-x2-6	25.29	0.38	28.40	n.d.	38.73	0.93	0.33	1.63	0.03	0.03	0.04	1.93	n.d.	97.72	
PGE compounds															
LP4-40-4-1	0.02	4.69	5.25	50.25	0.76	0.08	n.d.	8.59	1.12	0.02	1.62	0.36	n.d.	72.76	
LP4-40-4-2	0.03	6.50	5.05	39.46	0.73	n.d.	n.d.	23.03	0.91	n.d.	1.29	0.45	n.d.	77.45	
LP4-40-4-3	0.02	4.80	4.69	41.40	0.59	n.d.	n.d.	16.82	1.12	0.02	2.46	0.34	n.d.	72.26	
LP4-40-4-4	0.04	5.84	5.49	47.74	0.87	n.d.	n.d.	11.23	1.20	n.d.	1.10	0.40	n.d.	73.91	
LP4-40-4-5	0.03	5.56	4.97	42.42	0.66	n.d.	n.d.	15.79	1.02	n.d.	1.00	0.46	n.d.	71.91	
LP4-40-1-1	0.04	8.78	6.31	67.06	1.11	n.d.	n.d.	8.65	0.68	0.03	0.39	0.17	n.d.	93.22	
LP4-40-1-2	0.05	9.93	6.51	65.86	1.06	n.d.	n.d.	9.50	0.68	n.d.	0.36	0.18	n.d.	94.13	
LP4-40-1-3	0.01	8.50	5.84	44.68	0.43	n.d.	n.d.	8.26	0.69	n.d.	0.30	0.29	n.d.	69.00	
LP4-40-1-4	0.02	6.40	5.20	56.76	0.67	0.09	n.d.	5.89	0.60	0.04	0.42	0.15	n.d.	76.24	
LP4-40-1-5	0.04	8.07	6.54	59.22	0.91	n.d.	n.d.	7.18	0.60	n.d.	0.38	0.23	n.d.	83.17	
LP4-40-1-6	0.02	7.37	5.26	59.53	0.80	n.d.	n.d.	5.65	0.59	0.02	0.42	0.22	n.d.	79.88	
LP4-40-1-100-	0.03	4.15	4.09	62.85	0.78	n.d.	n.d.	11.72	0.62	n.d.	0.24	0.18	n.d.	84.66	
LP4-40-1-100-	0.02	4.38	4.33	61.35	0.74	0.01	n.d.	8.52	0.69	n.d.	0.24	0.16	n.d.	80.44	
LP4-40-1-100-	0.02	3.13	4.14	73.45	1.04	n.d.	n.d.	9.04	0.57	0.01	0.26	0.23	n.d.	91.89	
LP4-40-1-100-	0.07	3.28	4.09	56.03	0.63	n.d.	n.d.	11.64	0.72	n.d.	0.22	0.19	n.d.	76.87	

Composition of PGM (found in limonite) analysed by Electron Microprobe

Grain	incl.	wt%											Total
		S	Os	Ir	Ru	Rh	Pt	Pd	Fe	Ni	Cu	As	
LP1CPgm1	in aw	5.09	26.57	1.86	9.05	0.41	n.d.	0.42	22.61	21.89	0.05	0.62	88.57
LP1CPgm2	in aw	0.32	46.99	25.21	4.68	0.26	n.d.	0.30	11.65	1.18	0.23	0.20	91.02

n.d. = not detected

Table 6.4. Selected results of electron-microprobe analyses of PGM found in saprolite and limonite from the Loma Peguera Ni laterite profile**Fig. 6.12.** Composition (at%) of bowieite found as inclusions in dissiminated Cr-spinel from saprolite (Loma Peguera) and comparison with data from literature.

6.5. Mineralogical characterization of Ru-Os-Fe compounds

Low totals of Ru-Os-Ir-Fe compounds obtained by EMP analyses have previously raised the question if they could possibly represent PGE oxides (e.g. Garuti and Zaccarini, 1997; Proenza et al., 2007b, 2008; Uysal et al., 2009). However, recent studies on one Ru-Os-Fe compound, separated from the Loma Peguera 1 chromitite (included in saprolite) by HS techniques at the University of Barcelona, has stated that nanoscale intergrowths of Ru with magnetite is a more likely explanation (Zaccarini et al., 2014). To prove this theory and with the aim to compare results, one Ru-Os-Fe grain (100 x 60 μm in size) from the “floating chromitite” (included in limonite) was investigated by EMP, micro-Raman spectroscopy and synchrotron micro XRD.

6.5.1. EMP analysis

According to the complex zoning visible in BSE images (Fig. 6.13a), quantitative EMP analyses reveal a rather heterogeneous composition of the grain (n=10) (average and minimum- maximum in wt%): Os 20 (16-23), Ir 9 (7-11), Ru 37 (25-46), Rh 0.05 (0-0.2), Pt 0.1 (0-0.4), Pd 0.04 (0-0.1), Fe 26 (23-30), Co 0.3 (0.1-0.4), Ni 0.5 (0.4-0.7), Sb 0.01 (0-0.07), S 0.07 (0.02-0.23), As 0.5 (0.4-0.7), Si 0.2 (0-0.3), Mg 0.03 (0-0.06), Al 0.4 (0.1-0.8), corresponding to an average total of 94 wt% ranging from 89-101 wt% (Table 6.5). Comparison with data in Zaccarini et al. (2014), which unfortunately miss analysis of Pt, S, Co and Si, Mg, Al (to examine possible silicate incorporation during serpentinization), reveal significant

discrepancies: Fe contents are three times higher than in the grain from Loma Peguera, whereas Os concentrations are 27% lower than reported in Zaccarini et al. (2014), Rh and Pd contents are around 0.05 wt% (approximately 3wt% each in the grain from Loma Peguera) and As has an average concentration of 1.5 wt% in the grain from Loma Peguera but only 0.5 wt% in the grain from Loma Larga. However, concentrations of Ru, Ir and Ni are nearly identical in both grains. Surprisingly, totals obtained by EMP analyses from the grain from Loma Larga reach values close to 100 wt% (Table 6.5), whereas EMP analyses published in Zaccarini et al (2014) only reach these values after including oxygen (8 wt% O in average). Reliable determination of O by electron microprobe is still matter of scientific debate. Porosity and complex internal structure of these grains could alternatively be responsible for generally observed low totals. To better understand the complex zoning observed in the grain from Loma Larga, quantitative element mapping was applied. As shown in Fig. 6.13 different element distribution patterns for Ru, Os and Fe are evident: bright zones in BSE images correspond to highest concentrations of Ru which occurs either as batches in the central part of the grain or as enigmatic layers and void infills at the border of the grain (Fig. 6.13b). Os appears mainly homogeneously distributed with deficits in the central part (Fig. 6.13c), whereas Fe shows highest concentrations in zones close to the centre of the grain, resembling a fine-grained braiding (Fig. 6.13d). Fe also contributes to the Ru rich banding at the border of the grain.

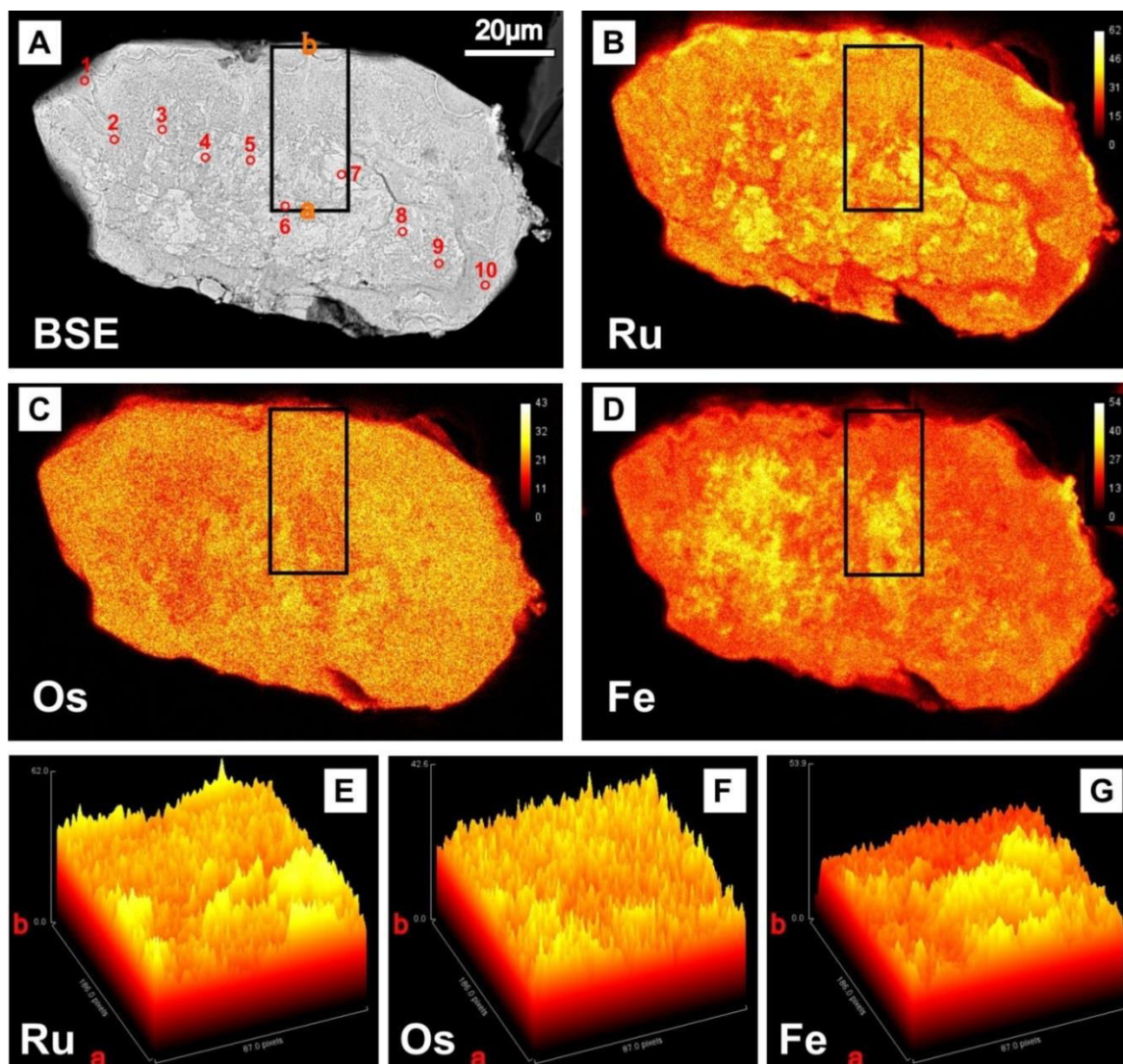


Fig. 6.13. BSE image with indicated points of EMP measurements, zone of surface plots and profile direction *a-b* for column average plots (a); quantitative element mappings for Ru, Os and Fe (b-d); surface plots of marked area in (a) for Ru, Os and Fe with indicated profile direction *a-b* for column average plots (e-g).

wt%	Os	Ir	Ru	Rh	Pt	Pd	Fe	Co	Ni	Sb	S	As	Si	Mg	Al	Total
1	20.23	10.45	34.59	0.07	0.08	0.02	23.03	0.13	0.51	0.07	0.10	0.40	0.20	0.05	0.71	90.64
2	21.74	9.51	32.63	0.03	0.04	0.04	23.50	0.18	0.38	0.00	0.02	0.43	0.29	0.06	0.56	89.41
3	16.51	7.33	43.07	0.19	0.20	0.00	29.58	0.43	0.65	0.00	0.06	0.71	0.01	0.00	0.10	98.85
4	16.08	7.40	45.07	0.02	0.03	0.08	29.10	0.40	0.49	0.01	0.05	0.59	0.03	0.01	0.12	99.49
5	22.13	9.56	37.39	0.08	0.09	0.01	22.99	0.22	0.37	0.00	0.03	0.41	0.20	0.03	0.38	93.89
6	23.15	9.88	31.90	0.01	0.04	0.11	23.76	0.18	0.39	0.01	0.02	0.42	0.29	0.04	0.41	90.60
7	17.70	7.34	45.90	0.09	0.42	0.09	27.73	0.43	0.62	0.04	0.23	0.57	0.03	0.00	0.14	101.33
8	19.22	9.01	37.49	0.00	0.00	0.02	28.31	0.34	0.40	0.00	0.04	0.51	0.19	0.03	0.25	95.82
9	20.72	9.50	32.65	0.00	0.08	0.00	27.44	0.23	0.42	0.00	0.07	0.43	0.22	0.05	0.32	92.12
10	22.47	11.14	25.48	0.03	0.01	0.03	28.54	0.11	0.50	0.00	0.04	0.36	0.29	0.04	0.82	89.87
Avg.	20.00	9.11	36.62	0.05	0.10	0.04	26.40	0.27	0.47	0.01	0.07	0.48	0.17	0.03	0.38	94.20
Max.	23.15	11.14	45.90	0.19	0.42	0.11	29.58	0.43	0.65	0.07	0.23	0.71	0.29	0.06	0.82	101.33
Min.	16.08	7.33	25.48	0.00	0.00	0.00	22.99	0.11	0.37	0.00	0.02	0.36	0.01	0.00	0.10	89.41

Table 6.5. Electron microprobe analyses of points indicated in Fig. 6.13a.

A more accurate comparison of Os with Fe mappings suggests that zones rich in Fe are depleted in Os (Fig. 6.13c and d). By using the open source image processing program *imageJ* (www.imagej.net) quantitative surface plots were obtained

for the zone indicated in Fig. 6.13e-g. In continuation, raw data were exported and used for element profiles obtained by column average plots. As seen in Fig. 6.14 a negative correlation trend between Os and Fe is evident (Fig. 6.15).

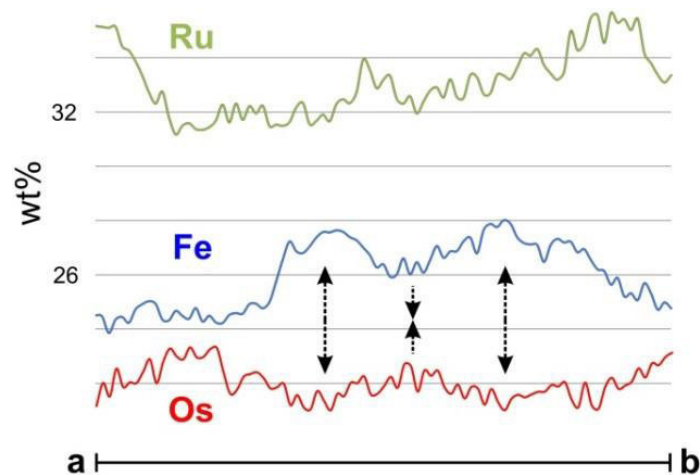


Fig. 6.14. Ru, Fe and Os concentrations of column average plots along the rectangle from *a-b* in Fig. 6.13a.

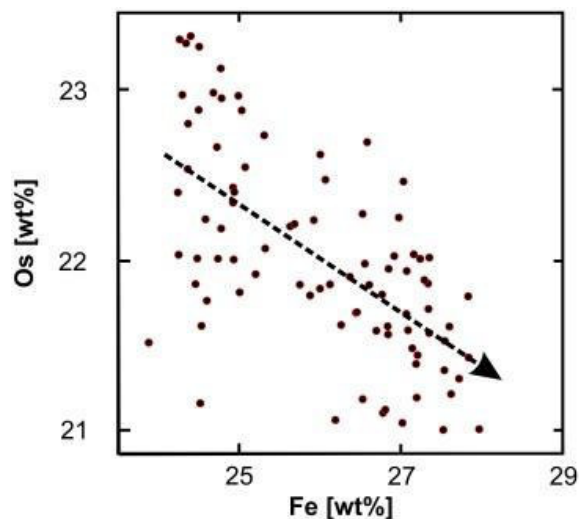


Fig. 6.15. Os vs. Fe diagram with data from column average plots showing a negative correlation trend.

6.5.2. Synchrotron tts- μ XRD

Investigation of the Ru-Os-Fe grain by means of synchrotron tts- μ XRD revealed the presence of at least two mineral phases: one alloy belonging to the hexagonal structure (space group $P6_3/mmc$) and one mineral belonging to the isometric (cubic) structure. Assessment of diffraction patterns confirms the presence of oxidized magnetite ($d_{(111)} = 4.76 \text{ \AA}$ and $d_{(220)} = 2.92 \text{ \AA}$) in the Ru-Os-Fe grain. Subsequently, d values and cell parameters of the Ru-Os-Fe alloy were compared to relevant literature data (Table 6.6 and 7). The Ru-Os-Fe alloy points to Ru rich hexaferrum with $d_{(111)} = 2.02 \text{ \AA}$ and with cell parameters of $a = 2.65 \text{ \AA}$ and $c = 4.23 \text{ \AA}$. In addition, calculated and observed XRD spectra for the Ru-Os-Fe alloy are identical, thus confirming the presence of Ru rich hexaferrum (Fig. 6.16).

6.5.3. Micro-Raman spectroscopy

The same area as for quantitative element mappings was chosen for a detailed micro-Raman spectroscopy investigation. Results of the Raman mapping revealed the presence of at least three mineral compounds: (i) one Raman inactive mineral, (ii) one mineral with its main band at 667 cm^{-1} and (iii) one mineral with its main bands at 720 and 1325 cm^{-1} (Fig. 6.17). The Raman inactive mineral is associated with bright areas of the grain, thus with highest Ru concentrations as verified by comparison with EMP analysis (e.g. point 7 in Fig. 6.13a and Table 6.5). Raman active minerals occur in dark appearing areas, corresponding to Fe rich zones (Fig. 6.13c). Comparison with literature data shows that Raman active minerals most likely represent (oxidized) magnetite and maghemite. Notably, shapes of their occurrence resemble micro channels circuiting Raman inactive Ru rich alloys.

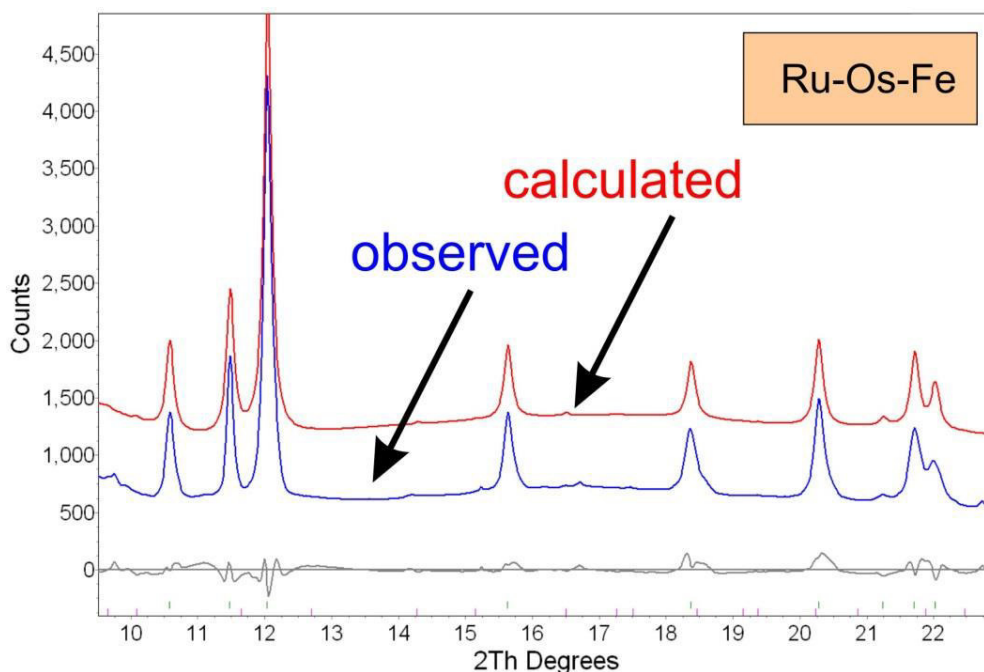


Fig. 6.16. Comparison of observed synchrotron XRD pattern (Ru-Os-Fe alloy) with calculated pattern.

Ru-Os-Fe			Hexaferrum (PDF 54-0704)			Ruthenium (PDF 00-06-0663)			Osmium (PDF 00-041-0601)			Garutiite ^a		
<i>I</i> meas	<i>d</i> meas(Å)	<i>hkl</i>	<i>I</i> meas	<i>d</i> meas(Å)	<i>hkl</i>	<i>I</i> meas	<i>d</i> meas(Å)	<i>hkl</i>	<i>I</i> meas	<i>d</i> meas(Å)	<i>hkl</i>	<i>I</i> meas	<i>d</i> meas(Å)	<i>hkl</i>
20	2.2980	100	50	2.28	100	40	2.343	100	80	2.363	100	50	2.330	100
20	2.1168	002	60	2.10	002	35	2.142	2	30	2.166	002	30	2.136	2
100	2.0197	101	100	2.006	101	100	2.056	101	100	2.071	101	100	2.046	101
25	1.5569	102	30	1.549	102	25	1.5808	102	40	1.594	102	30	1.576	102
40	1.3267	110	30	1.316	110	25	1.3530	110	60	1.364	110	40	1.3470	110
50	1.2025	103	30	1.195	103	25	1.2189	103	20	1.232	103	40	1.2155	103
10	1.1490	200				6	1.1715		10	1.180	200	10	1.1669	200
60	1.1242	112	20	1.118	112	25	1.1434	112	50	1.153	112	20	1.1391	112
40	1.1089	201	20	1.108	201	20	1.1299	201	40	1.039	201	20	1.1256	201
						4	1.0705	4	1	1.080	4	5	1.0680	4
						5	1.0278	202	10	1.035	202	5	1.0239	202
						6	0.9738	104	5	0.9835	104	5	0.9715	104
						16	0.9056		40	0.9135	203			
						6	0.8857		10	0.8929	210			
						25	0.8673		50	0.8737	211			
						18	0.8395		20	0.8472	114			
						10	0.8185		20	0.8252	212			
						16	0.8043		20	0.8123	105			
									5	0.7974	204			
									10	0.7866	300			

Table 6.6. Comparison of X-ray data for Ru-Os-Fe alloy and chemically related phases; ^a McDonald et al. (2010).

	Ru-Os-Fe	Hexaferrum ^a	Ruthenium ^b	Osmium ^c	Garutiite ^d
Chemical Formula	Ru _{0.4} (Os,Ir) _{0.1} Fe _{0.5}	(Fe,Os,Ru,Ir)	(Ru,Ir,Os)	(Os,Ir,Ru)	(Ni,Fe,Ir)
Crystal System	Hexagonal	Hexagonal	Hexagonal	Hexagonal	Hexagonal
Group Unit cell	<i>P6₃/mmc</i>	<i>P6₃/mmc</i>	<i>P6₃/mmc</i>	<i>P6₃/mmc</i>	<i>P6₃/mmc</i>
<i>a</i>	2.65358	2.64(1)	2.726	2.726	2.6939(5)
<i>c</i> (Å)	4.23362	4.20(2)	4.326	4.326	4.2732(6)
<i>V</i> (Å ³)	25.817	25.35	27.84	27.84	26.86(1)
<i>Z</i>	2	2	2	2	2

^a Mochalov et al. (1998) - Ru rich hexaferrum

^b Urashima et al. (1974)

^c Swanson et al. (1955)

^d McDonald et al. (2010)

Table 6.7. Comparative data for Ru-Os-Fe alloy, ruthenium and osmium-group mineral and garutiite.

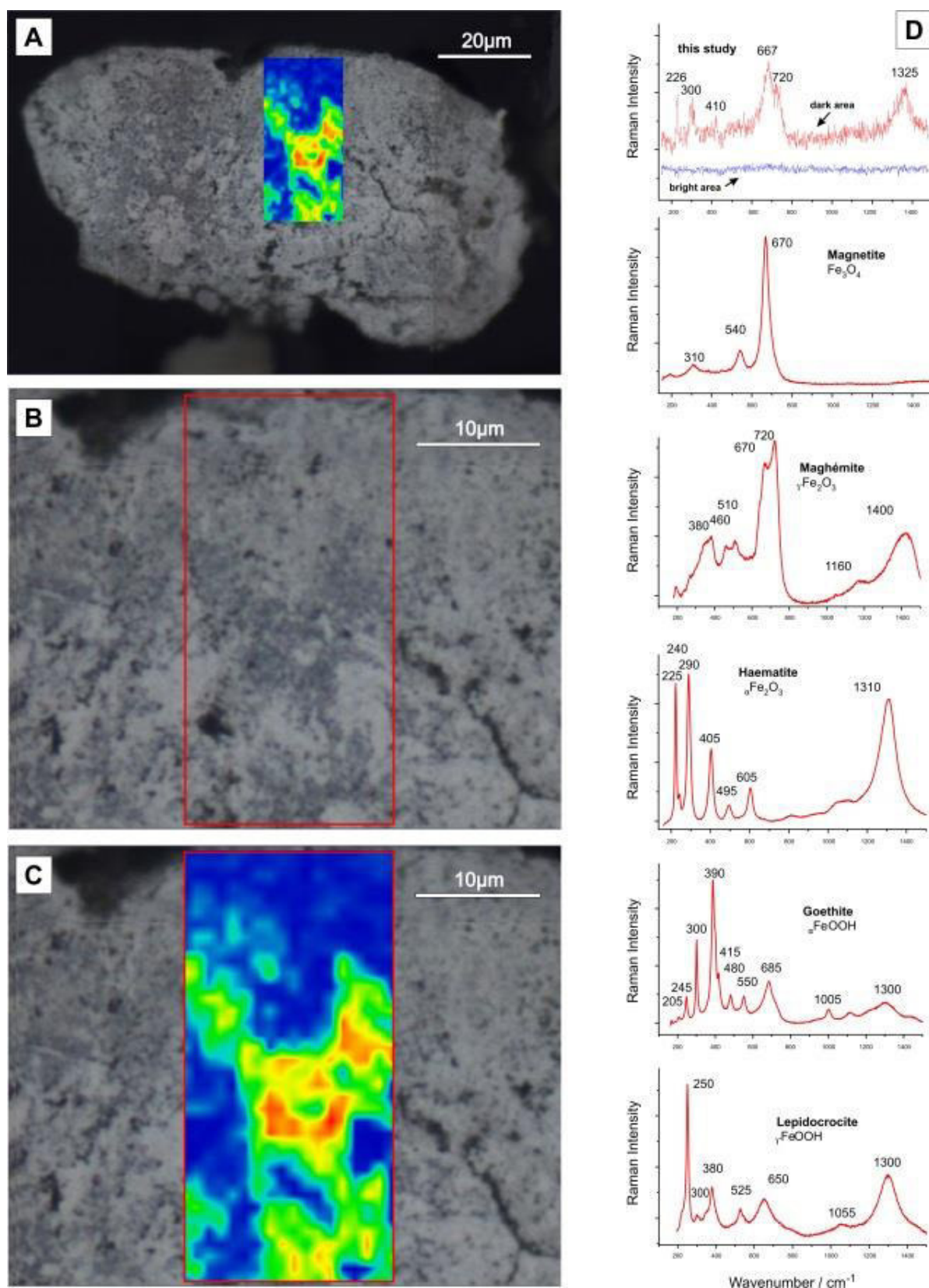


Fig. 6.17. Micro-Raman spectroscopy mapping of the Ru-Os-Fe grain (a-c) with reference spectra for common Fe oxide(s) (modified from Froment et al., 2008) (d).

6.6. *The mystery of fibrous PGM – alteration, neoformation or both?*

An unsolved problem of this investigation is the detection of one fibrous PGM (Ru-Os-Ir-Fe-Si) found as a free grain within the floating chromitite of Loma Larga. The grain is approximately 70 μm big and is characterized by well-preserved crystal shapes (Fig. 6.18a). However, the crystal itself is not perfect as seen by damaged corners and its broken central part. It is not clear if this damage occurred during sample preparation or if it is a consequence of the alteration/(trans-)formation process of the grain. Investigation of this enigmatic PGM monocrystal (without polishing) by means of FE-SEM reveals numerous features which, to the best to the author's knowledge, have not been described for PGM before:

- (i) the crystal shape is explained by a complex symbiosis of PGM nanoparticles and Si rich nanofibers which are perpendicular to crystal faces (Fig. 6.18a);
- (ii) the Si rich nanofibers seem to grow, as layers of different thickness as well as “healing of cracks” are observed (Fig. 6.18b-d);
- (iii) comparison of BSE images and secondary electron images suggests that elements of high atomic number (e.g. PGE) are present in the central part of the nanofibers, whereas the outer part seems to consist of elements with lower atomic

numbers (e.g. Si) (Fig. 6.18e and f);

- (iv) at the end of some nanofibers a thin layer of homogenous film occurs (Fig. 6.18g-j);
- (v) within these films PGM nanoparticles are widespread (Fig. 6.18g-j);
- (vi) within the (broken) centre of the grain a 5 μm big crater of round shape is present with enigmatic accumulations of Ir bearing phases, resembling “smoke” coming out of the crater (Fig. 6.18k);
- (vii) within the crater as well as to its outside complex forms of PGM nanoparticles are observed, resembling spicules remains of fungi. Interestingly, the Si richer crater has smaller PGM nanoparticles than its surrounding area (Fig. 6.18k);
- (viii) on plain walls, representing the backside of nanofibers layers and therefore most likely film material, oval forms with PGM nanoparticles are observed, suggesting remnants of PGE reducing bacteria (Fig. 6.18l).

At time of writing it is not clear whether these textures are explained by weathering of a secondary PGM (e.g. Ru-Os-Fe grains) with incorporation of secondary silicates or by dissolution/reprecipitation processes involving biogenic activity (e.g. biofilms including bacteria and/or fungi). Analyses currently under development such as XRD and Transmission Electron Microscopy (TEM) is hoped to shed some light on the genesis of these enigmatic group of PGM.

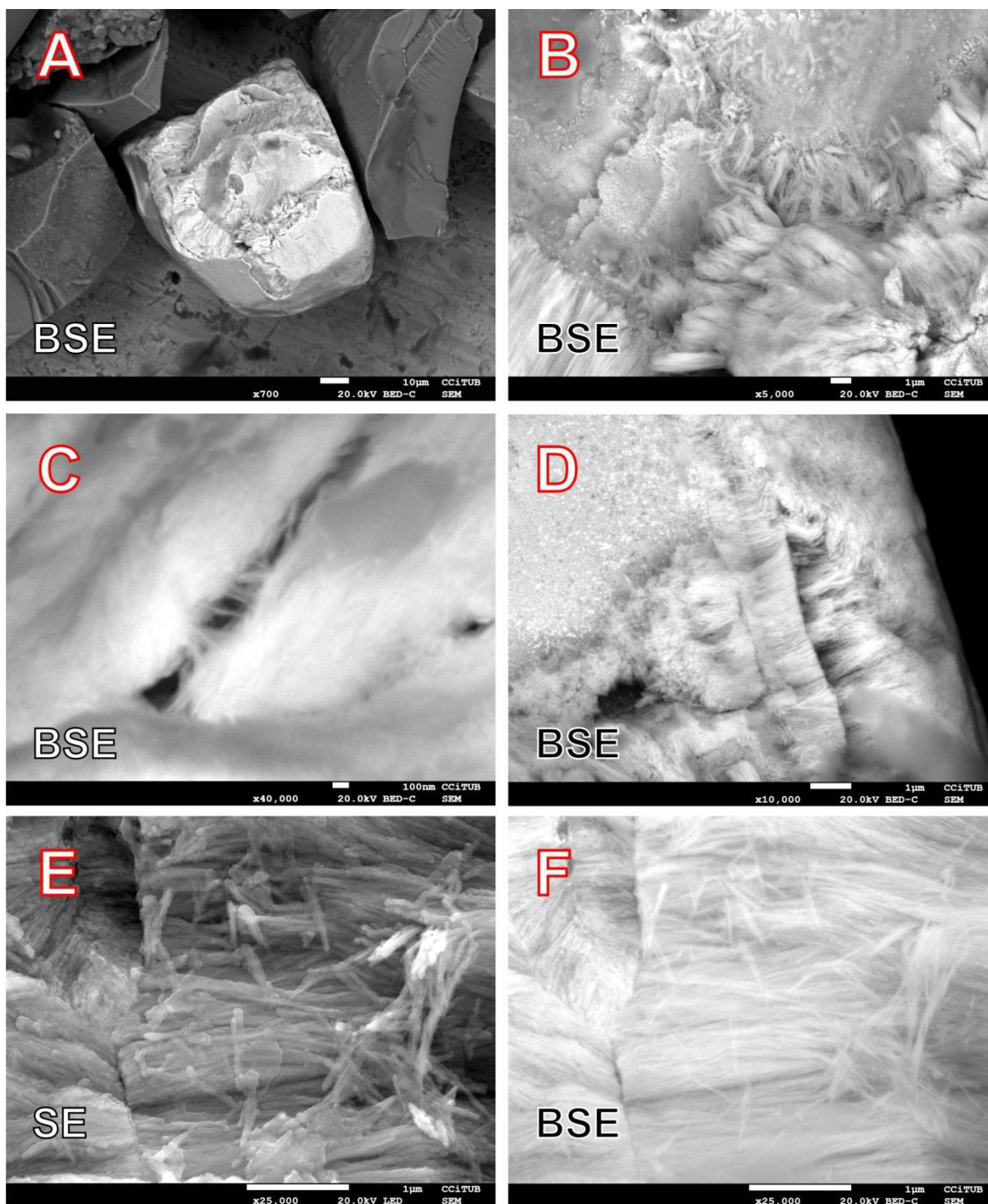


Fig. 6.18. FE-SEM BSE and secondary electron images (SE) of an enigmatic PGM composed of Si rich layers of nanofibers and PGM nanoparticulates. (A) overview; note intact crystal shapes and the dark occurring crater in the centre; (B) close up of nanofibers and subsequent film with PGM nanoparticulates; (C) “healing of cracks” by nanofibers; (D) layers of nanofibers perpendicular oriented to crystal faces; (E) close up of nanofibers (SE); (F) close up of the same area as in (E) with BSE; note the bright occurring centre of the nanofibers suggesting the presence of PGE.

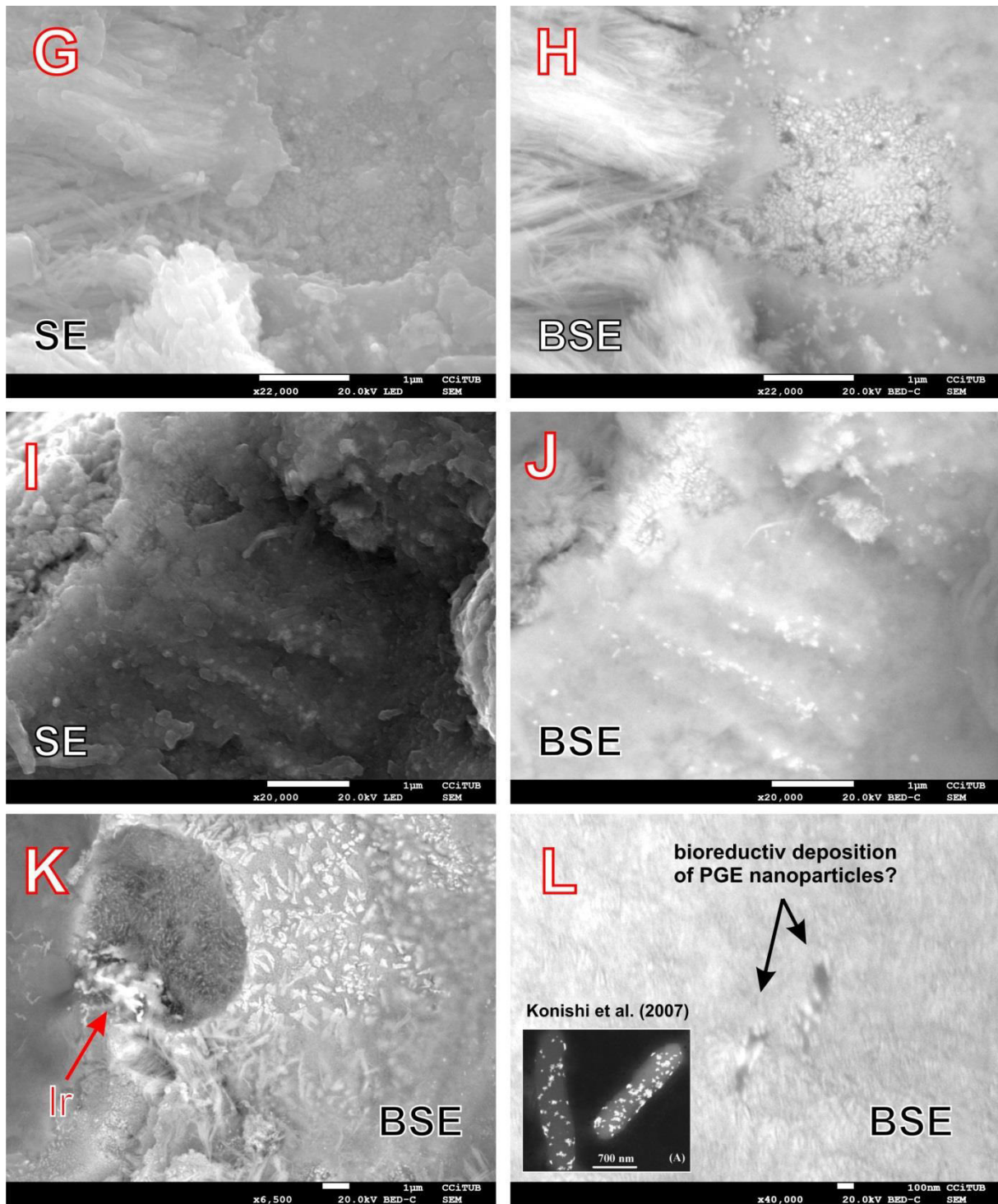


Fig. 6.19. Continuation. Close up of the contact between nanofibers and subsequent film (biofilm?) with PGM nanoparticulates in SE (G) and BSE (H); close up of a film showing layering and numerous PGM nanoparticulates (I) in SE and (J) in BSE; overview of the region around the crater structure with Ir accumulation and complex morphologies of PGM nanoparticulates; note that the dark appearing crater is Si enriched compared to its outer area (K); approximately 500 nm big oval forms with PGE nanoparticles at its inside resembling observations of Pt depositing bacteria (Konishi et al., 2007).

6.7. Discussion

6.7.1. PGE enrichment in Ni laterites and the role of chromitites

A main issue to explain elevated PGE values within supergene environments is the question if high PGE abundances in the parent rock are essential or not. The investigated Ni laterites developed above PGE depleted peridotites (<36 ppb total PGE) but show general PGE enrichments towards the surface. However, PGE distribution differs within both investigated Ni laterite profiles: Loma Caribe shows peaks of Pt and Ru within zone C and very pronounced within the highest levels of zone A. Palladium, nearly absent in the parent rock (2 ppb), reaches maximum values (71 ppb) in the exposed limonite. In contrast, weathering products from Loma Peguera are exclusively enriched in PGE within the limonite. The PGE enriched (up to 640 ppb) exposed limonite is dominated by Ru (236 ppb) and the other IPGE, whereas Pd and Pt contents (37 ppb and 91 ppb, respectively) are relatively low. The enrichment of IPGE over PPGE in total rock analysis, together with the discovery of small scaled chromitite occurrences, presumes a close relation between PGE enrichment and underlying chromitites. However, this hypothesis is not supported by the following observations. PGM with similar composition were found within both limonite horizons, chromitite bearing (Loma Peguera) and chromitite free (Loma Caribe) Ni laterite profiles. In addition, the chemical compositions of fresh Cr-spinel from chromitite (Loma Peguera 1) and unaltered, disseminated Cr-spinel found in saprolite (Loma Peguera and Loma

Caribe) reveals discrepancies as shown in Table 6.8. Cr-spinel within the chromitite free Ni laterite profile of Loma Caribe is characterized by variable Cr# of 0.43 to 0.55, Mg# of 0.54 to 0.61 and low TiO₂ contents in the range of 0.01 to 0.08 wt%. In contrast, Cr# are significantly higher (~0.75) for Cr-spinel associated with chromitites and saprolite from Loma Peguera, whereas Mg# range from ~0.35 (LP 4) to ~0.47 (chromitites) and TiO₂ contents from ~0.2 (LP 4) to ~0.85 (chromitites).

Code	Loma Peguera			Loma Caribe
	chromitite	Cr-spinel	Cr-spinel with laurite	Cr-spinel
SiO ₂	0.16	0.00	0.00	0.07
TiO ₂	0.84	0.18	0.17	0.04
Al ₂ O ₃	10.23	11.10	12.22	27.64
Cr ₂ O ₃	51.42	53.06	51.81	39.81
Fe ₂ O ₃	7.63	4.55	4.57	2.22
FeO	19.88	23.82	23.60	16.67
V ₂ O ₃	0.16	0.17	0.16	0.30
MnO	0.33	0.00	0.00	0.21
MgO	9.08	6.24	6.58	12.55
ZnO	0.17	0.40	0.26	0.32
NiO	0.39	0.15	0.08	0.14
Total	100.29	99.67	99.45	99.97
Si apfu	0.04	0.00	0.00	0.02
Ti	0.17	0.04	0.03	0.01
Al	3.21	3.54	3.87	7.86
Cr	10.82	11.34	11.02	7.60
Fe ³⁺	1.53	0.99	0.99	0.46
Fe ²⁺	4.42	5.42	5.34	3.35
V	0.03	0.04	0.03	0.06
Mn	0.07	0.00	0.00	0.04
Mg	3.60	2.52	2.64	4.52
Zn	0.03	0.08	0.05	0.06
Ni	0.08	0.03	0.02	0.03
Cr#	0.77	0.76	0.74	0.49
Mg#	0.45	0.32	0.33	0.57
Fe ³⁺ #	0.10	0.06	0.06	0.03

Table 6.8. Geochemical comparison of Cr-spinel from chromitite (Loma Peguera 1) with unaltered, disseminated Cr-spinel from saprolite samples (Loma Peguera and Loma Caribe).

Fig. 6.20 summarizes and visualizes chemical variance of analyzed Cr-spinel in the studied Ni laterite profiles in form of discrimination diagrams. It seems evident that Cr-spinel found in saprolite from Loma Caribe and Loma Peguera derived from a different source than from chromitites. The geochemical fingerprint of Cr-spinels from Loma Caribe suggests that they have formed within fertile mantle rocks (e.g. lherzolite), whereas Cr-spinels from Loma Peguera seem to have crystallized within more depleted peridotite (e.g. harzburgite/dunite). Taking into consideration all listed observations we suggest that PGE enrichment within the studied Ni laterites is not intrinsically dependent on incorporation of PGE enriched chromitites. This finding is in good agreement with previous studies of

weathering profiles from the New Caledonia ophiolite (Augé et al., 1995).

The good correlation of Cr with PGE in both profiles and the fact that PGM are observed included in fresh Cr-spinel indicate that disseminated Cr-spinels in peridotites are an important source for PGE within studied Ni laterites at Falcondo. Small amounts of Cr-spinel in mantle rocks (<2-3 vol%) could have accumulated significantly during lateritization due to their resistant nature, leading to residual PGE enrichment within highest levels of the laterite profile. In addition, base-metal sulfides (Fe-Ni-Cu sulfides), believed to form 0.1 vol% of the upper mantle and containing PGE at ppm level, could also have contributed importantly to the PGE budget (Lorand et al., 2008).

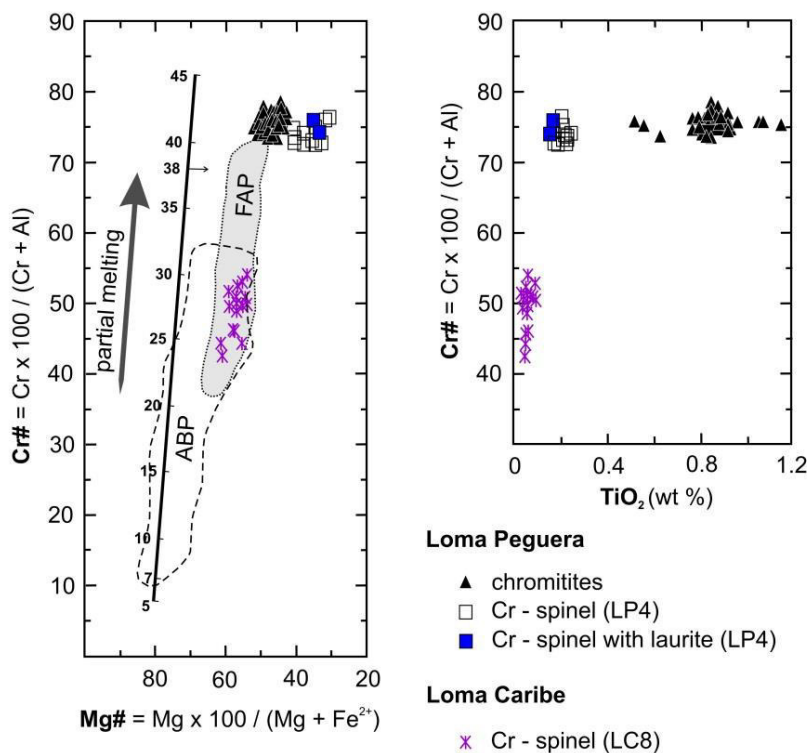


Fig. 6.20. Left: Cr# vs Mg# of Cr-spinel in Loma Peguera chromitites and within saprolites from Loma Peguera (LP4) and Loma Caribe (LC8). Fields for different tectonic environments were compiled from Pagé et al. (2008) and references therein. ABP = abyssal peridotites; FAP = fore-arc peridotites. The line with ticks is the experimental equilibrium-melting curve of Hirose and Kawamoto (1995). Right: Cr# vs TiO₂ of Cr-spinel in Loma Peguera chromitites and within saprolites from Loma Peguera (LP4) and Loma Caribe (LC8).

6.7.2. Origin of platinum group minerals in Ni laterites

6.7.2.1. Magmatic origin of primary PGM

Euhedral crystals of laurite and bowieite included in unaltered Cr-spinel were found in saprolite of Loma Peguera. Their shape, textural position and chemical composition suggest a primary origin. The dominance of Ir, Ru and Rh suggests that these elements were fractionated into accessory Cr-spinel in mantle peridotite during earlier magmatic stages (Capobianco and Drake 1990; Richter et al., 2004; Lorand et al., 2008), thus crystallizing as discrete PGM grains before or concurrently with Cr-spinel. Cr-spinel is more resistant to alteration than silicates, thus magmatic PGM inclusions were protected from serpentinization and lateritization. The chemical composition of Cr-spinels with primary laurite inclusions indicates that there is no obvious relation with nearby chromitite bodies (Fig. 6.20).

6.7.2.2. Secondary PGM from alteration of pre-existing PGM

Free PGM grains in saprolite (Loma Peguera) as well as all PGM grains within the limonite horizons from the studied laterite profiles clearly differ from primary PGM in morphology, optical appearance and chemical composition. Free PGM grains from the saprolite of Loma Peguera are characterized by porous textures and generally S-free compositions. Their more complex nature may be explained by the interaction with serpentinization-related fluids when alteration processes resulted in desulphurization of primary PGM and thus formation of secondary PGM compounds. Incorporation of Si and Mg (clinochlore or

serpentine?) in some PGM grains supports this hypothesis which was previously described for secondary Ru-Fe-Os-Ir oxides found in chromitites (e.g. Garuti and Zaccarini 1997; Uysal et al., 2009).

Elemental mapping of one free Ni-Fe-Co-PGE grain found within the limonite of Loma Peguera shows a complex PGE distribution with Pt in the center and Ru at oxidized rims (Fig. 6.10). Compared with secondary PGM of the underlying saprolite the grain does not show the characteristic porosity apart from a spongy, irregular surface. This difference could be explained by a more stable primary PGM which was not importantly affected by alteration processes during pre-lateritization. However, considering the present Ru-oxide rims and nebulous PGE distribution further compositional modifications by supergene weathering under tropical conditions can be assumed. Generally, it is observed that Pt-rich PGM become more abundant in the highest levels of the investigated Ni laterite profiles. It is important to point out, that PGM detected in limonite of Loma Caribe occur within the porous border of their Fe oxide(s) hosts and that morphological features of the PGM are suggestive of infill of alteration voids (Fig. 6.21 a and b). The porosity of Cr-spinel is mainly explained by hydrolysis processes during lateritization producing $\text{Cr}(\text{OH})_3$ which can result in liberation of PGM (Cooper 2002; Traoré et al., 2008a, b) (Fig. 6.21). Thus, the occurrence of some PGM as free particles in the weathering profile can be interpreted as derived from the supergene dissolution of PGM-bearing Cr-spinel.

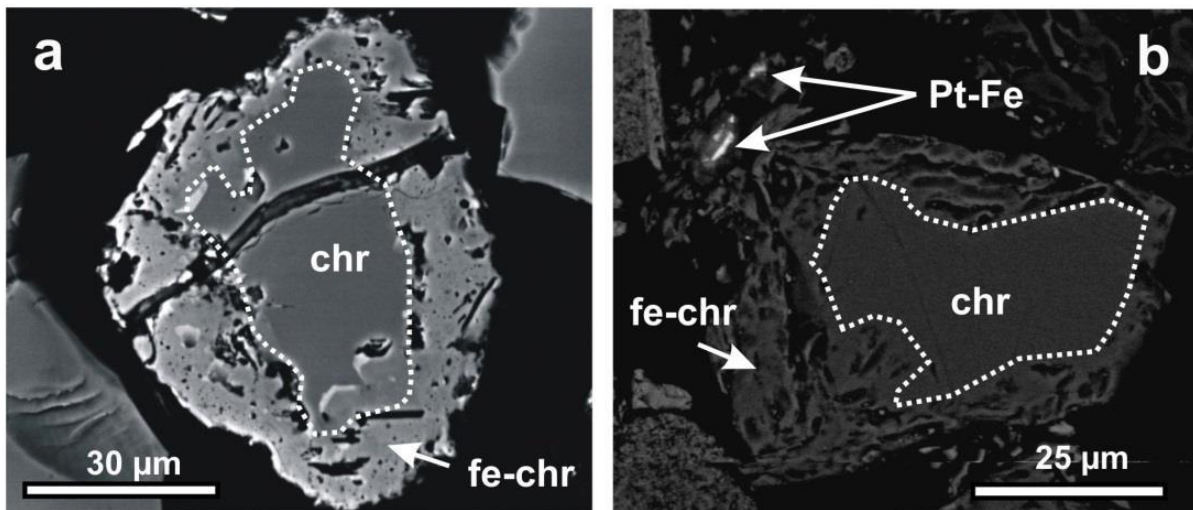


Fig. 6.21. BSE images showing progressive weathering of Cr-spinel (**chr**) (**a**, **b**) and Pt-Fe phases located within the alteration rim (**b**). *fe-chr* ferrian Cr-spinel

Free PGM grains with similar optical and chemical properties as observed in the saprolite of Loma Peguera (Fig. 6.8 b-d) are absent in all investigated limonite samples, indicating that they may not be stable within higher levels of the Ni laterite profile. Their characteristically high porosity could have favoured entire erosion of the grains during lateritization, whereas more stable secondary PGM (e.g. Fig. 6.9f) only suffered PGE redistribution with Fe rich PGE alloys becoming the final phase. If this hypothesis is true the PGM cluster shown in Fig. 6.9b reflects coexistent stages of PGM breakdown and PGM consolidation (e.g. Pt-Fe-Ni compound). Given the experimental and theoretical evidence for PGE solubility under lateritic conditions (e.g. Bowles et al., 1994) we propose that erosion of secondary PGM with subsequent remobilization and reprecipitation of PGE has to be considered for the Ni laterites at Falcondo.

6.7.2.3. Some thoughts about the origin of Ru-Os-Fe grains: Ru-Os oxides or Ru-Os alloys + magnetite? Ru rich hexaferrum + Fe oxide(s)?

Taking into consideration that (i) Ru rich zones analysed by EMP reach values close to 100 wt% without the need of including O and that (ii) these zones contain up to 29 wt% Fe without showing any signals of magnetite nor maghemite in micro-raman analyses, reveal some important new insights regarding the assumption of Zaccarini et al. (2014), that Ru-Os-Fe grains found in the Ni laterites of Falcondo are nanoscale intergrowths of magnetite with Ruthenium. Here presented multidisciplinary data indicate that most of the iron is bound to the Ru-Os alloy, thus suggesting that these grains are mainly composed of accumulations of nanoscaled Ru rich hexaferrum. The fine-grained nature of these grains makes EMP analyses challenging. However, as observed nanoparticles can accumulate to bigger patches (remobilization and reprecipitation during weathering?) which allow EMP analyses close to 100 wt%. These analyses were used to calculate the stoichiometry,

which in addition to synchrotron $tts-\mu$ XRD and micro-raman data clearly points to hexaferrum ($Ru_{0.4}(Os, Ir)_{0.1}Fe_{0.5}$). It can be speculated, that hexaferrum of this composition represents the

endmember of secondary PGM after desulphurization and (trans)formation processes (e.g. Fe incorporation) of primary laurite/erlichmanite within Ni laterites (Fig. 6.22 and Fig.6.23).

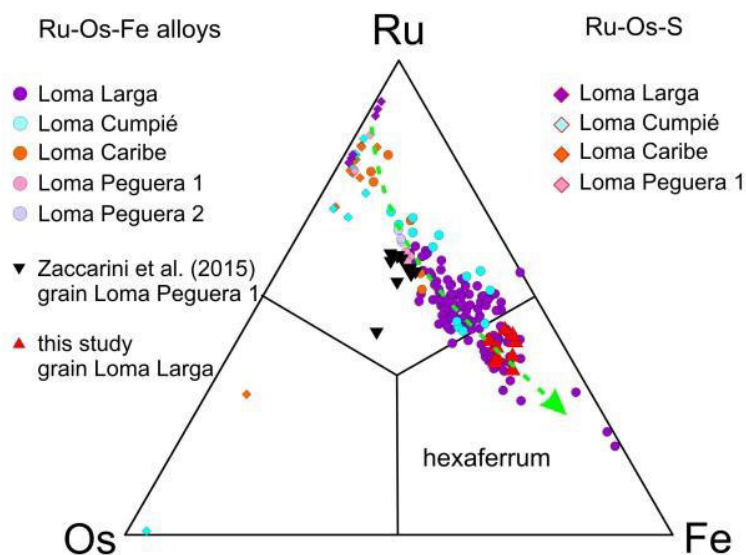


Fig. 6.22. Ternary diagram in the Os-Fe-Ru system showing the transformation trend from primary laurite to hexaferrum. Note: Fe enrichment is mainly explained by formation of hexaferrum.

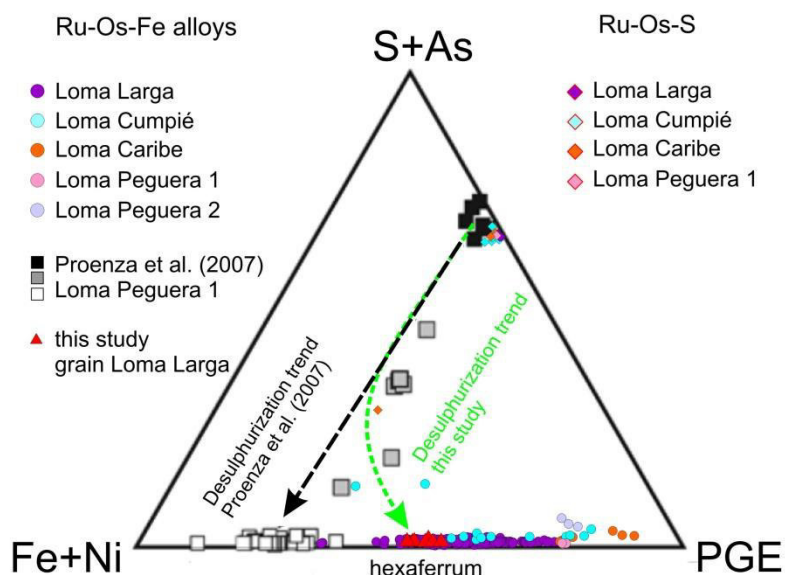


Fig. 6.23. Ternary diagram in the Fe+Ni-PGE-S+As system showing the proposed desulphurization trend from primary laurite to hexaferrum. Note: data from Proenza et al. (2007b) include O+Cu in the Fe+Ni axis.

Previous work has shown, that silicates can be incorporated in PGM at serpentinization stage on a sub-micron

scale (e.g. Uysal et al., 2009; McDonald et al., 2010 and reference therein). FE-SEM BSE images and EDS spectra of Ru-Os

alloys, found included in chromitites from the Loma Caribe peridotite, suggest that silicate incorporation during serpentinization results (i) in desulphurization of the primary PGM and

(ii) in significant redistribution of PGE. Textures appear porous but are explained by nanoscaled Mg-silicates (dark) and PGE alloys (bright) (Fig. 6.24).

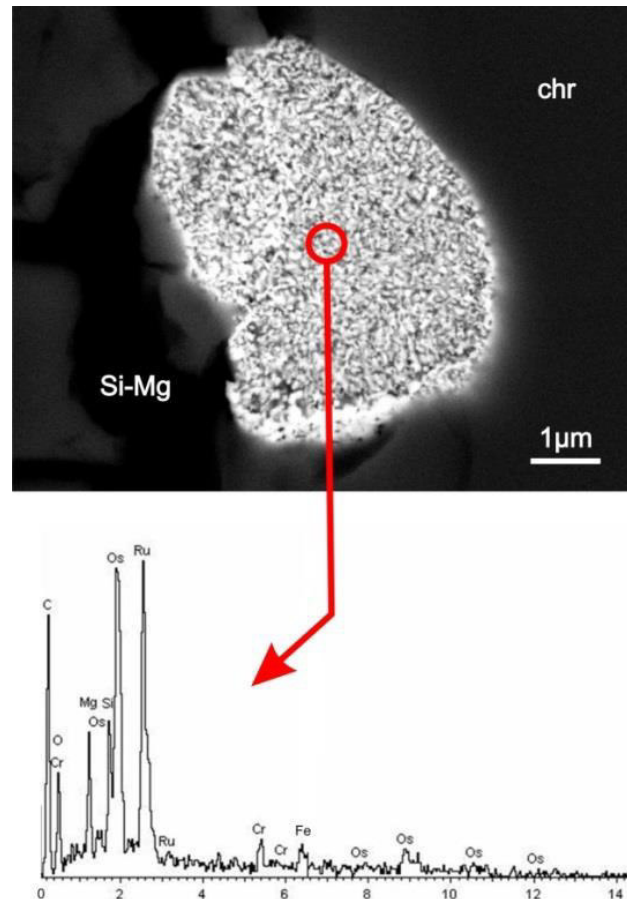


Fig. 6.24. Fine-grained, porous appearing Ru-Os grain included between chromian spinel (right) and a Si-Mg vein (left). Note: no sulphur but traces of Fe and significant amounts of Mg and Si.

However, Mg-silicates are not stable within higher levels of the Ni laterite, thus resulting in weathering of these phases and subsequently in a high porosity and high permeability of the Ru-Os grain. As a consequence oxidized, Fe rich fluids can enter the grain along micro channels with subsequent incorporation of Fe in the Ru-Os alloy (formation of hexaferrum) and minor crystallization of magnetite during early stages of lateritization. Interestingly, Fe oxide(s) filled micro channels from this stage are best observed in the central part

of the studied grain (Fig. 6.13d). They are missing at the outer part of the grain, thus indicating that at latest stages of lateritization (i.e. at highest levels of the Ni laterite profile with high Eh and low pH) remobilization of PGE occur and that enigmatic banding of Ru at the border of the grain may represent the result of such (trans-)formation processes (e.g. detoxifying biofilms). The theory of PGM neoformation in Ni laterites is discussed in continuation (see also chapter 7).

6.7.2.4. Neoformation of PGM in limonite

The possibility of PGM neoformation within laterites has been discussed for more than 40 years (e.g. Ottemann and Augustithis 1967; Cabri and Harris 1975) but unequivocal mineralogical evidence of *in situ* growth of PGM at low temperatures is still missing. One elongated Pt-Fe-Ni grain with botryoidal textures was found within the limonite of Loma Peguera (Fig. 6.9c). FESEM images reveal well-defined, submicron-sized clusters and plate-like textures of Pt-Fe-Ni which are difficult to explain by magmatic processes or alteration (Fig. 6.25). These features rather

indicate a similar process for neoformation of PGM as it has been recently described for Pt-Pd aggregates found in alluvium from Córrego Bom Sucesso in Brazil (Cabral et al., 2009; 2011). These authors suggest that Pt and Pd are transported in aqueous solution in soils and subsequently deposited on organic substrata by microbial activity. Crystal growth up to mm-sized Pt-Pd grains was explained by continuous bioreduction and/or electrochemical accretion. Iodine enrichment within the Pt-Pd nuggets provided evidence for biogenic precious-metal fixation (Cabral et al., 2011).

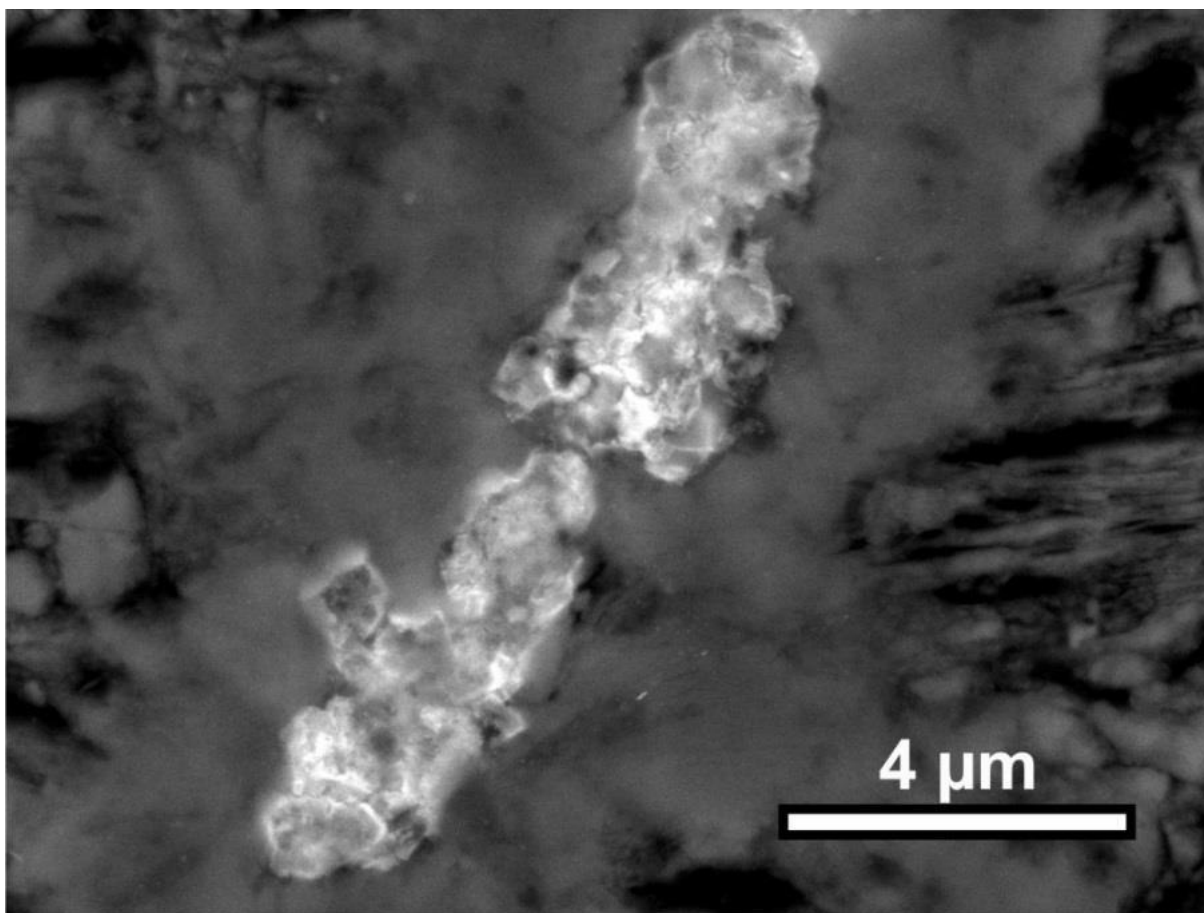


Fig. 6.25. Close-up of BSE image by FESEM from the Pt-Fe-Ni bearing PGM with botryoidal textures of Fig. 6.9c.

We applied electron microprobe element mapping to the Pt-Fe-Ni grain with botryoidal textures and detected trace

amounts of iodine in the grain which was confirmed by WDS spectra (Fig. 6.26).

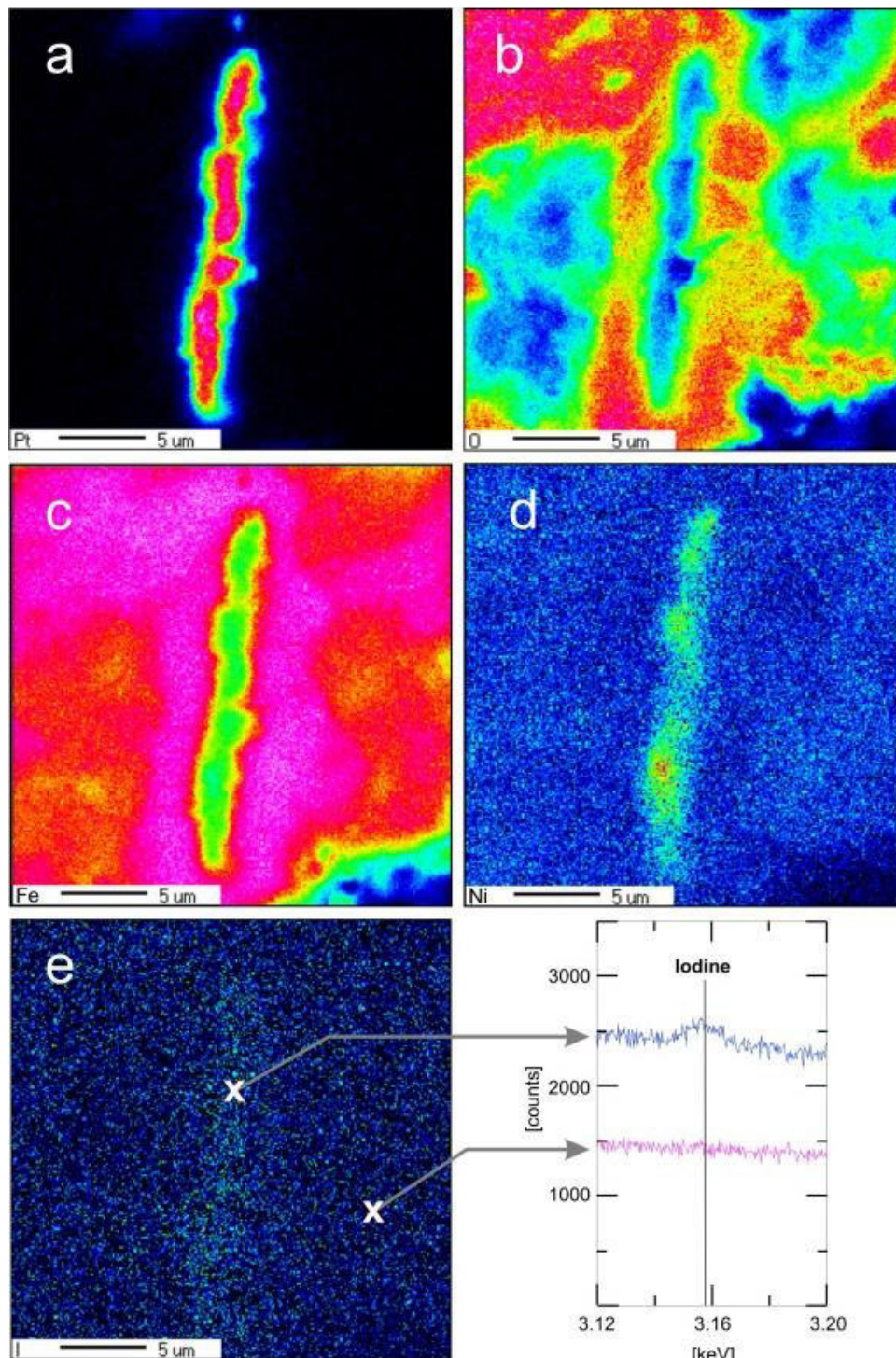


Fig. 6.26. Element distribution maps (background corrected) showing the distribution of Pt, O, Fe, Ni, and I in the botryoidal Pt-Fe-Ni grain of Fig. 6.9c found in the limonite horizon of Loma Peguera (a–e) and WDS spectra obtained at the indicated positions (e) confirming the presence of I in the Pt-Fe-Ni grain (note: no signals of iodine were detected within the matrix). Intensity scale identical with Fig. 6.10.

Recent thermodynamic calculations demonstrate that Pt, Pd and Rh are capable to interact with inorganic ligands to form stable sulfide, hydroxide, ammonia, chloride and mixed-ligand complexes (Colombo et al., 2008). Additionally, Salpeteur et al. (1995) described Pt and Pd mobility in ferralitic soils from Madagascar and found evidence for neoformation of PGE minerals by the presence of accretionary secondary Pt, Pd oxides which were restricted to the upper oxidized layer. In the case of the Ni laterites at Falcondo PGE could have been continuously dissolved due to acidic conditions at the highest levels of the limonite horizon (e.g. humification of plant remains) at high Eh during tropical weathering and transported in solution in

the form of Cl_4^{2-} ions as previously proposed (Bowles et al., 1986, 1994; Azaroual et al., 2001) (Fig. 6.27). Changing water tables due to dry and rainy seasons may have transported Pt_{aq} , Pd_{aq} (and other PGE?) close to the surface where they precipitated on organic matter by bioreduction and/or electrochemical metal accretion as has been suggested by Cabral et al. (2011) (see chapter 7). However, additional incorporation of PGE within secondary Fe-oxide(s) as proposed by Gray et al. (1996), observed and widely accepted in the case of gold (e.g. Mann, 1984; Nahon et al., 1992; Yang et al., 2009), has probably contributed to the significant enrichment of PGE in the exposed limonite at Falcondo.

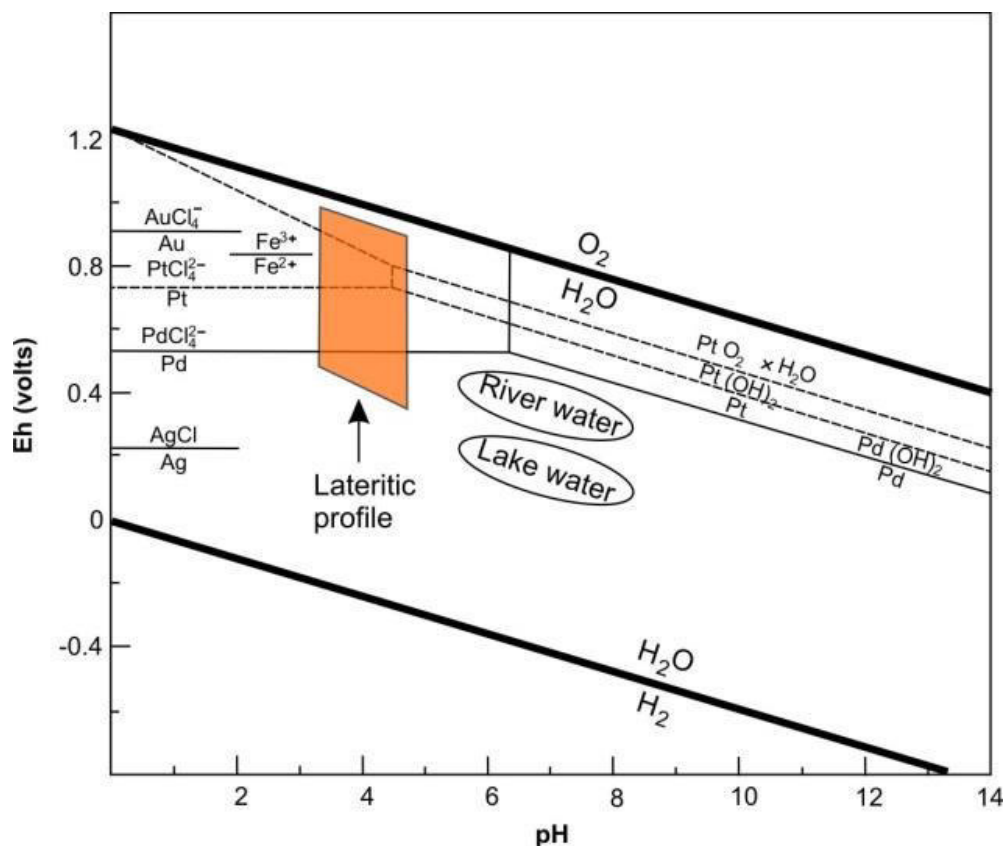


Fig. 6.27. Characteristic Eh-pH conditions for lateritic profiles showing stability field and redox potentials of Au, Pt, Pd and Ag as chlorine complexes (after Baas Becking et al., 1960; Rösler and Lange, 1972; Fuchs and Rose, 1974; Westland, 1981; Mann, 1984; Bowles, 1986).

6.8. Concluding remarks

1. Ni laterites at Falcondo contain up to 640 ppb total PGE and have to be considered potential unconventional PGE deposits. The observed PGE enrichment is independent of PGE-enriched substratum (e.g. chromitites) and mainly explained by residual accumulation of PGE-bearing mineral phases (e.g. disseminated Cr-spinel).
2. Three different types of PGM are present within the lateritic profiles: (i) primary PGM (magmatic stage); (ii) secondary PGM (alteration of pre-existing PGM); (iii) PGM due to *in situ* neoformation after PGE mobilization.
3. Results of this investigation provide morphological and chemical evidence for *in situ* neoformation of PGM within Ni laterites by bioreduction and/or electrochemical accretion.
4. The innovative HS-11 heavy-mineral separation technique has proven to be highly suitable to find minute amounts of PGM within limonite and saprolite samples.

Chapter 7

PGM neoformation in Ni laterites – “multistage PGE grains” hold the key to explain nugget formation in supergene environments

7.1. Introduction

The platinum group elements (PGE) are a group of precious metals consisting of Os, Ir, Ru, Rh, Pt and Pd. Due to their unique physical and chemical properties PGE are essential for a wide range of industries including high tech applications (e.g. pollution control via catalytic converters), medicine (e.g. cancer treatment) and jewellery. Currently >80% of the worldwide demand of PGE is provided by two major magmatic ore deposits: the *Bushveld Complex* in the Republic of South Africa and *Norilsk* located in the Russian Federation (USGS, 2013). Supergene ore deposits such as placers of platinum group minerals (PGM), usually found in the surroundings of Ural-Alaskan type complexes (Garuti et al., 2012), are historically important.

However, the origin of PGE nuggets found in surface environments is still matter of scientific debate and two opposing genesis models exist: (i) PGM crystallize exclusively under hypogene conditions and get liberated at the surface by weathering of the source rock (e.g. Koen, 1964; Cabri and Harris, 1975; Hattori and Cabri, 1992); (ii) PGM form also by secondary processes through PGE mobilization and continual accretion within the supergene environments (e.g. Stumpfl, 1974; Bowles, 1986; Cabral et al., 2011).

Recent work confirms that Pt gets mobilized under surface conditions (Campbell et al., 2015) and including the idea of biogenic PGE cycling has opened new possibilities to explain supergene PGM occurrences (Reith et al., 2014 and reference therein).

In this chapter presented and discussed PGM contribute to the ongoing debate on the genesis of PGM found in the supergene environment. Special emphasis is given to document new insights on low temperature PGE mobility in soils which might be useful in future exploration strategies and studies aiming to evaluate anthropogenic PGE contamination.

7.2. Sample provenance and PGE geochemistry

Study area is the ophiolite related Loma Caribe peridotite located within the central part of the Dominican Republic which currently hosts one of the largest resources of Ni-laterite in the Greater Antilles (Redwood, 2014). The weathering profile developed from underlying serpentized ultramafic rocks and consists of a Fe-oxide/hydroxide dominated limonitic cover at the top and a thick Mg-silicate saprolite horizon beneath (for details see chapter 2 and Lewis et al., 2006a; Villanova de Benavent et al., 2014; Aiglsperger et al., 2015).

Recently, small scaled (approx. 2 m in diameter), highly weathered chromitite bodies were discovered included in limonite (“floating chromitites”), occurring partly exposed to the surface (Fig. 7.1).

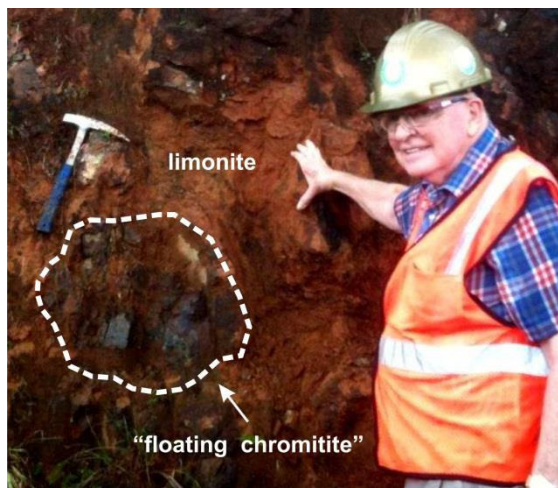


Fig. 7.1. Investigated chromitite pod “floating” within limonite from the Ni laterite deposit Falcondo (Dominican Republic). These chromitites are PGE and PGM rich.

Whole rock PGE analyses provided by ICP-MS after nickel sulphide fire assay collection at the Genalysis Ltd. laboratory (Maddington, Western Australia) revealed abnormally high total PGE concentrations of 17.5 g/t (Table 7.1).

Comparison of chondrite normalized patterns with chromitite samples from underlying saprolite show similar IPGE (Os, Ir and Ru) enrichment relative to PPGE (Rh, Pt and Pd), however a distinct positive Pt anomaly is evident (Fig. 7.2).

Code	LP	LL
Zone	chromitite saprolite	chromitite limonite
Ir	802	3455
Os	812	4945
Pd	8	14
Pt	408	2282
Rh	152	281
Ru	1396	6536
ΣPGE	3578	17513
Pt/Pd	51.00	163.00
Pt/Ir	0.51	0.66
Pt/Rh	2.68	8.12
Pt/Ru	0.29	0.35
IPGE	3010	14936
PPGE	568	2577
IPGE/PPGE	5.30	5.80

Table 7.1. Comparison of the PGE geochemistry (in ppb) of chromitites included in saprolite (LP - Loma Peguera) and chromitites included in limonite (LL - Loma Larga).

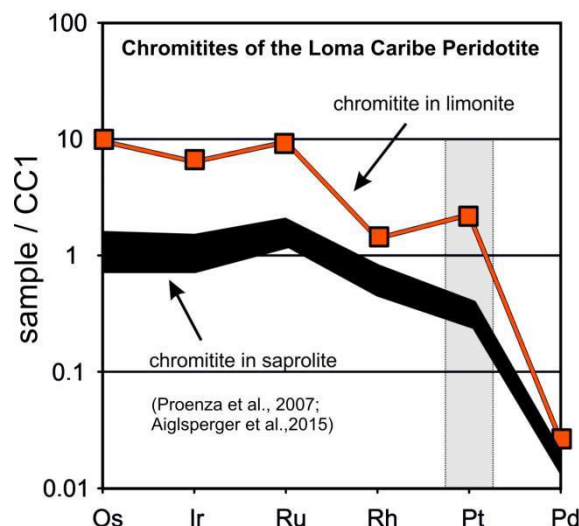


Fig. 7.2. Comparison of PGE chondrite normalized patterns of chromitites included in saprolite and limonite. Note: similar patterns but a clear positive Pt anomaly for chromitites included in limonite. Normalization values from Naldrett and Duke (1980) .

7.3. PGE mineralogy of “floating chromitites” and the observation of “multistage PGE grains”

Hundreds of PGM in the size range of <20 µm to 125 µm were detected and classified into three groups according to their form of appearance:

- (i) primary PGM as inclusions in chromite and with magmatic features
- (ii) secondary PGM after transformation processes due to alteration (e.g. desulphurization during serpentinization)
- (iii) PGM with delicate morphologies and chemical compositions different to (i) and (ii), suggestive for neoformation processes.

Examples of PGM belonging to these groups and found in Ni laterites developed above the Loma Caribe peridotite are shown in chapter 6. The vast majority (>90 %) of detected PGM from the “floating chromitites” of Loma Larga belongs to Ru-Os rich secondary PGM of group (ii). However, several single grains

of PGM show a characteristic PGE zonation by close spatial relationships of individual PGM, thus indicating different stages of PGM formation: highly porous Os-Ru-Fe-(Ir) grains with sometimes intact crystal shapes are overgrown by fine grained Ni-Fe-Ir and Ir-Fe-Ni-(Pt) phases which are subsequently followed by a layer of round shaped Pt-(Ir) bearing mineral phases (Fig. 7.3). It is noteworthy, that complete sequences of this group of “multistage PGE grains” are only observed within chromitite samples from Loma Larga, hence from highest levels of the Ni-laterite profile.

Quantitative EMP analyses reveal a general loss of Ru, Os and As from early to late considered sequences, whereas Fe and Pt, showing a positive correlation, are constantly gained (Fig. 7.4). Relatively high concentrations of Al (2.4 wt%), Si (1.4 wt%) and S (0.3 wt%) are measured within latest considered Pt-(Ir) mineral phases which appear dark grey in reflected light microscopy (Fig. 7.4 and Table 7.2).

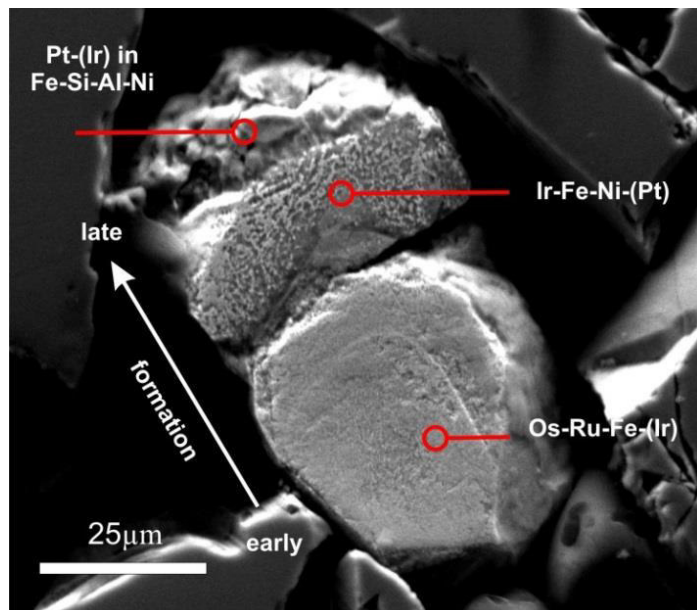


Fig. 7.3. Secondary electrons image of a “multistage PGE grain” from Falcondo with indicated and suggested stages of formation from early (Os, Ru rich) to late (Pt rich).

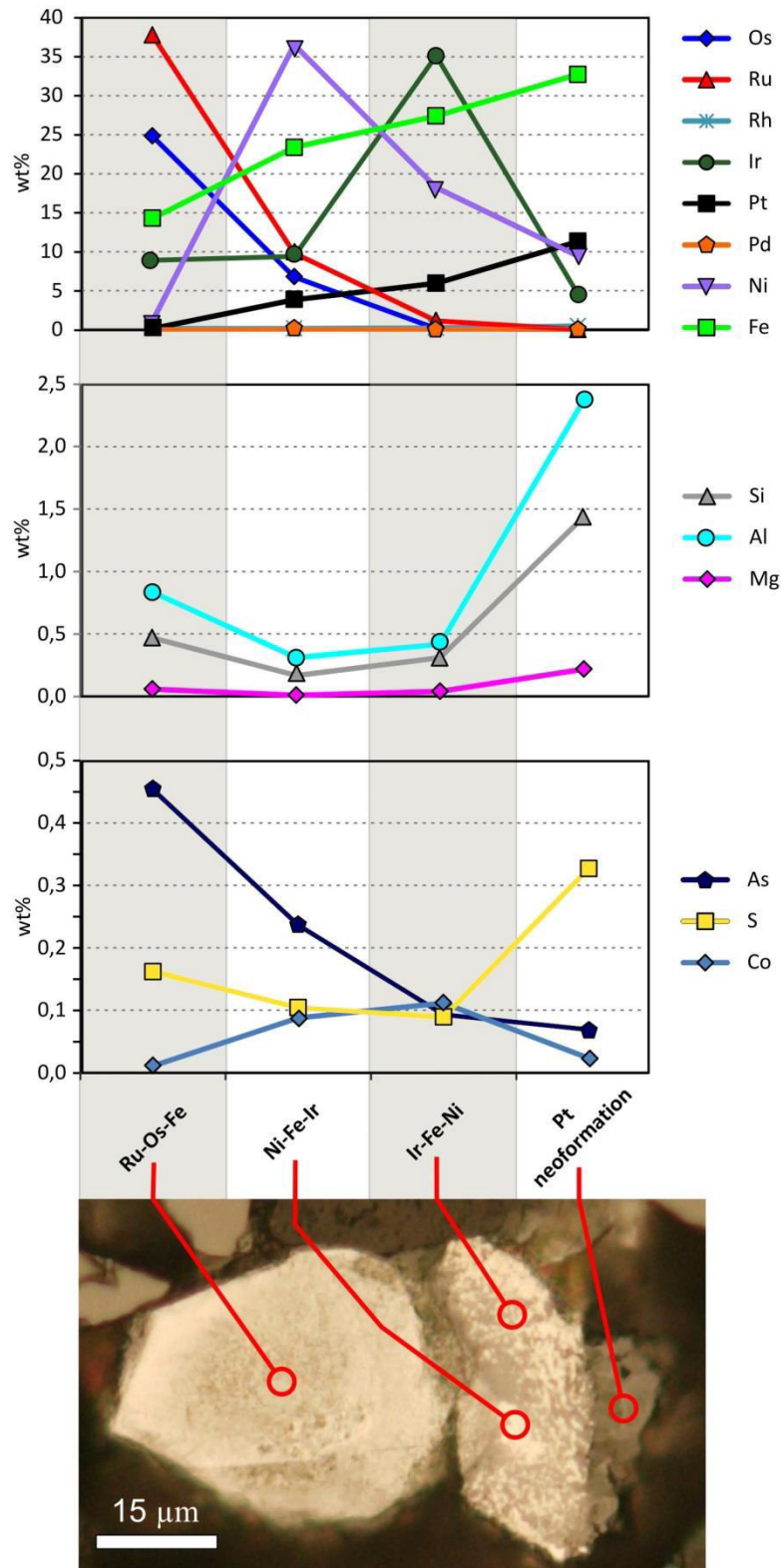


Fig. 7.4. EMP analyses profile of relevant elements through one “multistage PGE grain”. Note the positive correlation of Fe and Pt, as well as the dark appearing Pt rich layer in reflected light microphotographs.

Code	Ru-Os-Fe	Ni-Fe-Ir	Ir-Fe-Ni	Pt neo-formation
Os	24.83	6.81	0.19	0.07
Ru	37.75	9.87	1.17	0.10
Ir	8.94	9.44	35.14	4.62
Rh	0.20	0.18	0.26	0.50
Pt	0.20	3.90	5.99	11.34
Pd	0.00	0.04	0.04	0.00
S	0.16	0.10	0.09	0.33
As	0.45	0.24	0.09	0.07
Fe	14.32	23.39	27.42	32.74
Ni	1.20	36.54	18.25	9.50
Co	0.01	0.09	0.11	0.02
Sb	0.02	0.01	0.00	0.01
Mg	0.06	0.01	0.04	0.22
Si	0.47	0.17	0.31	1.44
Al	0.83	0.31	0.42	2.37
Total	89.44	91.10	89.52	63.31

Table 7.2. EMP analyses of measurement points displayed in Fig. 7.4.

Elemental mapping reveals a clear zonation of Ru, Os, Ir and Pt whereas enigmatic micron Ru phases occur at the boundary of the Ir-Fe-Ni-(Pt) sequence (Fig. 7.5). Highest nickel contents (~37 wt%) are observed precisely at the crystal’s top of the porous Os-Ru-Fe-(Ir) grain (Fig. 7.4 and 7.5).

7.4. Discussion

A constantly growing literature is demonstrating that PGE can be mobilized in the surface environment and numerous experimental studies have shown that biogenic mediated neo-formation of PGM is possible at the laboratory scale (Reith et al., 2014 and reference therein). On the contrary field evidence of such *in-situ* formation of supergene PGE grains is extremely rare (e.g. Cabral et al., 2011; Aiglsperger et al., 2015).

Here described “multistage PGE grains” from Ni laterites are characterized by a close spatial relationship between hypogene and supergene considered formation sequences (Fig. 7.3). Hence, both competing origin models are veritable, an assumption which has been stressed by others earlier (e.g. Oberthuer et al., 2014).

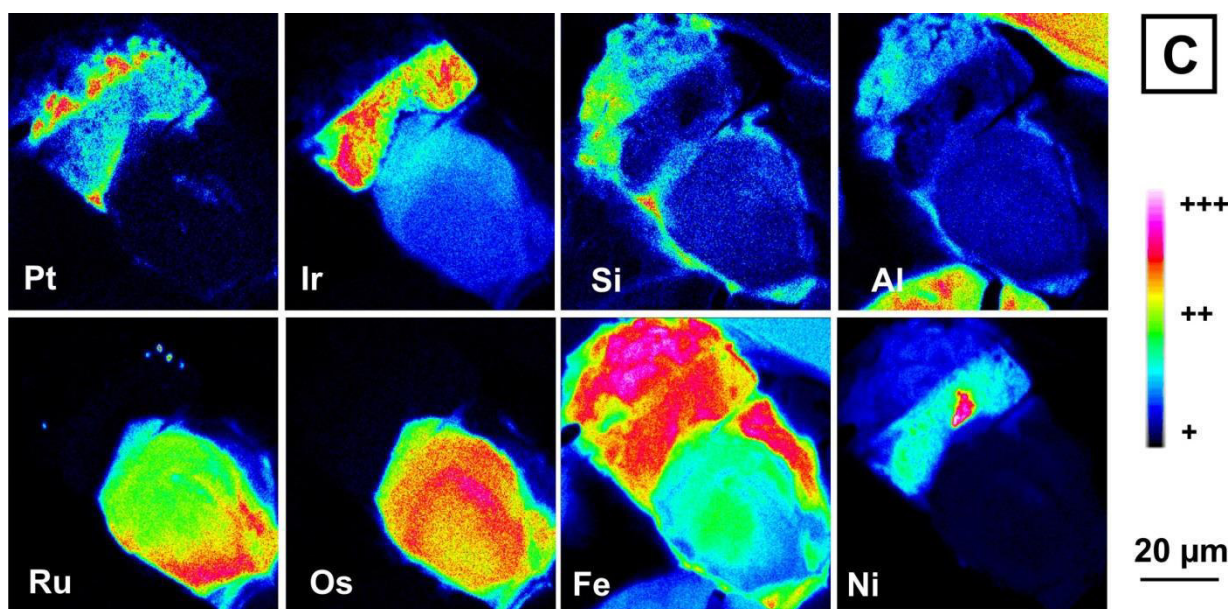


Fig. 7.5. Element mapping of a “multistage PGE grain” from Falcondo. Note the zonation of Ru, Os, Fe and Ir in the lower part of the grain, the visual correlation of Fe and Ni with Pt and Ir enrichment toward the top as well as micron Ru phases at the boundary of the Ir-Fe-Ni-(Pt) zone.

Primary PGM formed during magmatic stage can be affected by alteration processes and subsequent (trans-)formation processes are likely to occur until PGM are finally released to the surface environment. For instance, serpentinization is believed to lead to desulphurization of primary laurite and erlichmanite causing transformation into highly porous Ru-Os mineral phases and frequently reported as “secondary PGM” (e.g. Stockman and Hlava, 1984; Gonzalez-Jiménez et al., 2014b and references therein). Comparison of EMP elemental mappings and quantitative EMP analyses of PGM, considered primary in origin, with PGM, considered secondary in origin, suggests following general PGE mobility trend for Ni laterites from Falcondo: Pd>Pt>Ir>Rh>Ru>Os.

Several in this study detected free grains of secondary PGM show well preserved rims of Mg-Si minerals, thus indicating a close relationship between formation of these PGM and serpentinization. Considering the expected high specific area of these porous PGE grains it can be speculated that their surface probably serves as a natural catalyst promoting formation processes of PGM at favourable conditions. With respect to in this work observed “multistage PGE grains” Ni, Ir and Fe enriched fluids are thought to have been mobilized during serpentinization and/or earlier stages of lateritization and subsequently have crystallized on secondary, porous Ru-Os mineral phases. Our observations are in good agreement with previous work on Ni-Fe-Ir bearing mineral phases found in saprolite hosted chromitites from the Loma Caribe peridotite (McDonald et al., 2010). These authors postulated a low temperature

genesis for studied Ni-Fe-Ir mineral phases and linked their formation to serpentinization and/or lateritization based on morphology, internal texture and associated minerals.

However, the observation of an even more recent overgrowth of Pt dominated mineral phases, which is only present in PGE grains from highest levels of the lateritic profile, leads to the assumption for anew supergene PGE mobilization and re-crystallization. Intense weathering and subsequent erosion of surrounded matrix material led to the exposure of secondary PGM to the surface environment (residual enrichment) and weathering processes within the so called critical zone (Brantley et al., 2006; 2007), characterized by complex interactions involving rock, soil, water, air, plants, (humic-) acids and (micro-)organisms, are believed to have mobilized Pt (+Ir) in form of chloride complexes (e.g. Bowles et al., 1994; Azaroual et al., 2001; Wood et al., 2002). Precious element mobilization in the presence of halides with subsequent Au and Ag crystallization observed in a gossan from the proximity of our study area has recently been reported from Andreu et al. (2015).

In accordance with laboratory experiments demonstrating bioreductive deposition of platinum nanoparticles on bacteria (Konishi et al., 2007), *in situ* Pt mineral neof ormation in highest levels of studied Ni-laterites is believed to be driven by detoxifying biofilms within a porous matrix of secondary Fe oxides.

A simplified model explaining the proposed formation history of “multistage PGE grains” in Ni laterites is given in Fig. 7.6a-d:

- (i) primary laurite included in chromian spinel (Fig. 7.6a) suffers disulphurization during serpentinization which leads to subsequent formation of porous appearing secondary Ru-Os alloy with incorporated Mg silicates in Fig. 7.6b).
- (ii) During weathering the grain gets liberated and Mg silicates disappear because of their lower stability and as a consequence highly porous Ru-Os alloy form. Their expected high specific surface is believed to function as a natural catalysator which favours the precipitation of Ir rich Fe-Ni alloys (Fig. 7.6c). This Ir dominated stage during the

formation of “multistage PGE grains” is first observed within samples from the saprolite (beneath the Mg-discontinuity).

- (iii) A final stage of Pt and Ir dominated nanoparticle neoformation can be observed close to the surface within the limonite (above the Mg-discontinuity) (Fig. 7.6d). An association between aqueous solutions and agglutination processes of PGE bearing nanoparticles is evident in high magnification FE-SEM BSE images from well preserved “multistage PGE grains”: matrix pores are clearly filled by Pt and Ir nanoparticles (“growing of PGE nuggets”) (Fig. 7.7a-c).

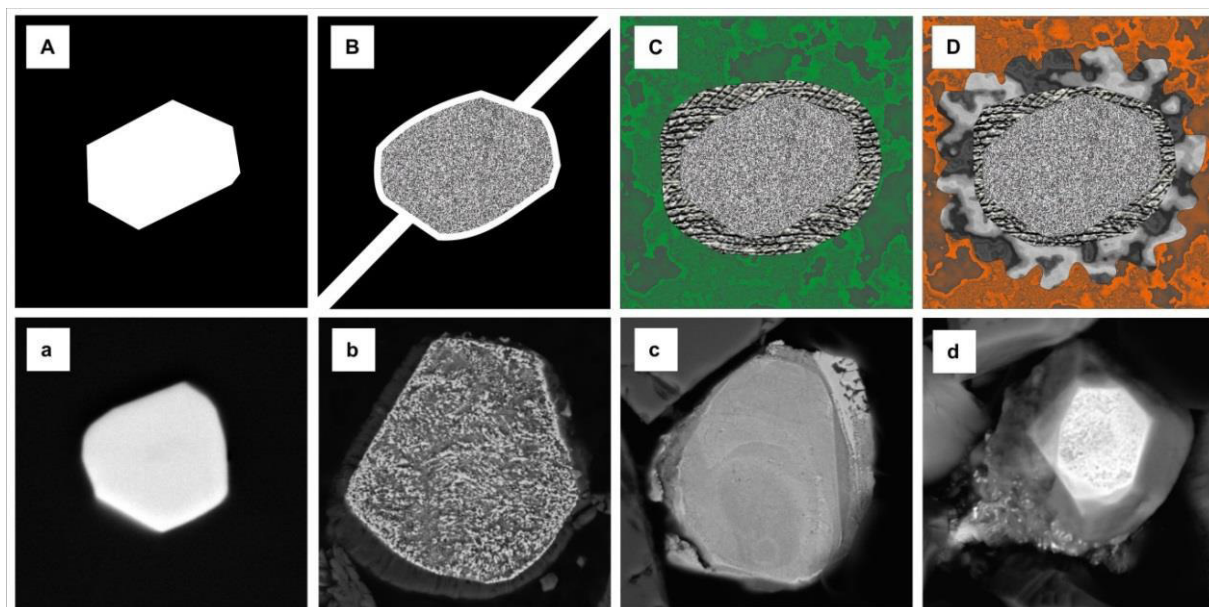


Fig. 7.6. Genesis model for “multistage PGE grains”, capital letters show an idealized cartoon, small letters give examples of detected PGM in the size range of 10-50 μm . (A,a) primary laurite included in chromian spinel; (B,b) serpentinization and subsequent formation of porous appearing secondary Ru-Os alloys with Mg silicates; (C,c) grain liberation during serpentinization and/or within the saprolite and formation of Ir rich Fe-Ni alloys around secondary, highly porous Ru-Os alloys; (D,d) Pt and Ir nanoparticle neoformation *in situ* within limonite close to the surface around secondary Ru-Os alloys and layers of Ir-Fe-Ni.

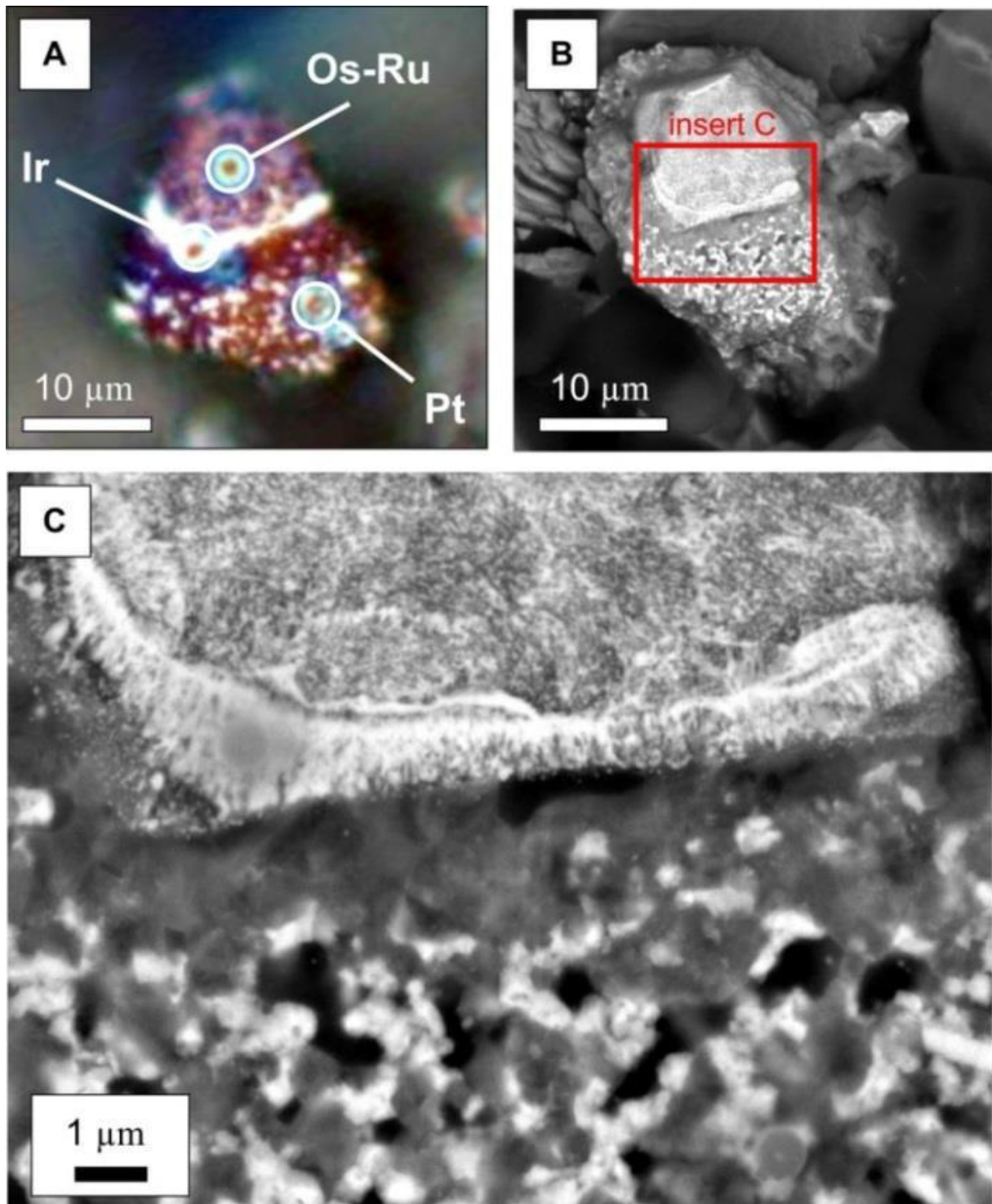


Fig. 7.7. (A) microphotograph of a “multistage PGE grain” obtained by reflected light microscopy (plane polarized light) showing purple appearing Os-Ru rich alloy, white appearing banding of Ir rich alloy and white spots of Pt and Ir rich nanoparticle accumulations within a redish matrix of Fe oxide(s). Note: EDS analyses lead to brownish marks on the grain surface. (B) BSE image of the same grain; note the three dimensional direction of Pt and Ir nanoparticles neoformation around the secondary Os-Ru and Ir alloy. (C) FE-SEM BSE image close up of the transition zone between Os-Ru alloy, Ir rich layer and Pt and Ir neoformation nanoparticles. Note that Pt and Ir nanoparticles are oriented around pores (black) within secondary Fe oxide(s), hence suggesting a close relationship between fluid infill and *in situ* PGE crystallisation.

Observations indicate continuous Pt substitution of secondary PGM within the supergene environment, resulting in porosity reduction and subsequent formation of densely packed, stable Pt-Ir-Fe-Ni alloys (Fig. 7.8 and 7.9). It can be speculated that only these grains are suitable for potential transportation and

deposition in stream sediments. However, detection of spheroidal nano-sized Pt particles at oxidized rims of such grains (Fig. 7.10) suggests continuous PGM modifications via biogenic processes (e.g. biofilms), similar to processes previously reported for gold nuggets (e.g. Reith et al., 2012).

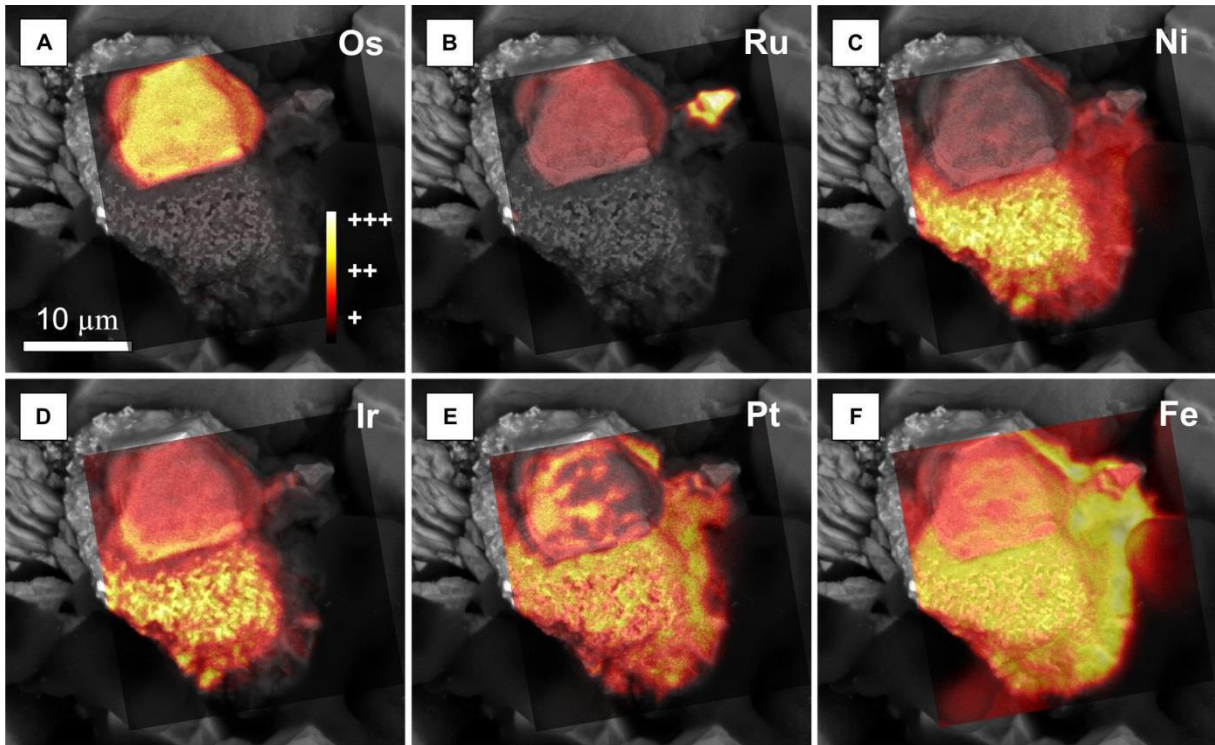


Fig. 7.8. Element mapping of a rather complete “multistage PGE grain” from Falcondo (see also Fig. 7.7). Note the advanced stage of Pt substitution within Os-Ru rich secondary PGM.

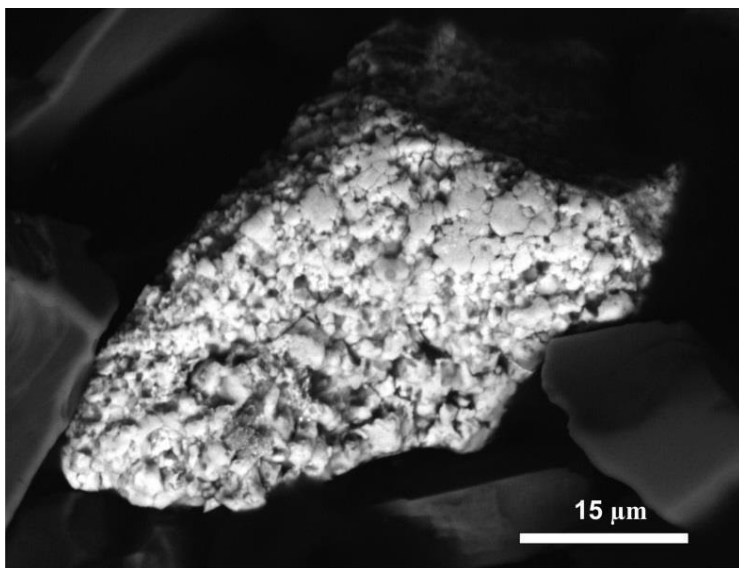


Fig. 7.9. Accumulation of Pt-Ir-Fe-Ni particles forming a nugget shaped grain of approximately 50 x 30 µm. Note: general porosity reduction (e.g. upper right part of the grain). No relicts of secondary Ru and/or Os rich grains are observed.

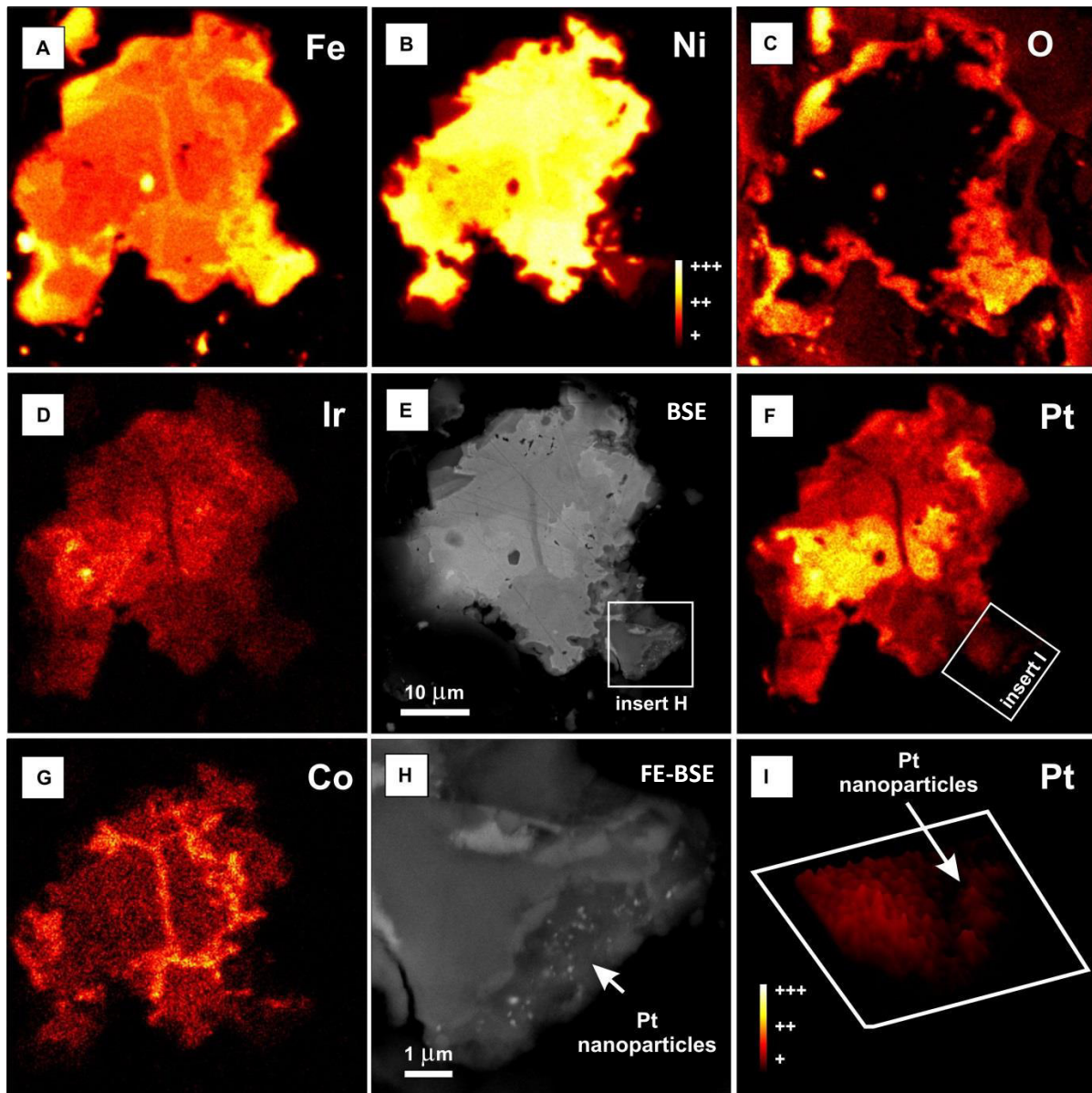


Table 7.10. Element mapping of a dense, nugget shaped, free Pt-Fe-Ni-Fe grain found in limonite. This grain are is believed to represent a product of (trans-)formation processes of a “multistage PGE grain”. Note: continuous Pt crystallisation in form of nanoparticles at Fe oxide(s) rich rims.

However, Brugger et al. (2013) investigated the contrasting behaviour of platinum and gold in surface environments. These authors found, that Au has a higher cell-toxicity compared to Pt-complexes resulting in Au-detoxifying biofilms and subsequent formation of spheroidal nano-particulate. Such features were not observed for Pt and explained by its lower toxicity. In a recent study, Le et

al. (2006) assessed bioleaching of weathered saprolite nickel ore by using heavy metal tolerant fungi (*Aspergillus foetidus*). One remarkable result of this research was that the presence of multi-metals (e.g. Ni, Fe, Co, Al, Cr, Cu, Mg, Mn, Zn) led to greater toxic response to the growth behaviour of the microorganism relative to single metals. With respect to the study area of Falcondo

the presence of multi-metals in the limonitic horizon is verified by geochemical analyses (see chapter 4). Hence, this could explain a sufficient toxicity for the formation of Pt-detoxifying biofilms resulting in subsequent PGM neoformation.

7.5. Final remarks

Considering the constantly growing number of experimental laboratory studies confirming that PGE are mobilized and can re-crystallize at low temperature environments, surprisingly little mineralogical data from field sites is currently available. Thus, here presented “multistage PGE grains” from highest levels of Ni laterites are good objects to investigate PGM (trans-)formations from hypogene to supergene environments.

The observation of accumulations of most likely biogenic mediated *in situ* growth of Pt rich nanoparticles in supergene environments could help to explain (i) why Pt bearing nuggets are the most abundant PGM found in surface environments (Cabri et al., 1996) (ii) why Pt nuggets from placer deposits generally surpass the grain sizes of Pt grains found in parent rocks by several orders of magnitude (few micrometers vs. several millimeters) (Reith et al., 2014 and reference therein) and (iii) how anthropogenic PGE contamination may affect our biosphere.

Finally, here presented evidence clearly states that PGE are neither noble nor inert in surface environments, at least in those related to tropical Ni laterites from the Northern Caribbean.

Chapter 8

Osmium isotope characteristics of primary and secondary PGM in Ni laterites from Falcondo

8.1. Introduction

Osmium-isotope compositions of Os-rich platinum-group minerals (PGM) provide critical insights about timing of melting/infiltration of melts in the upper mantle (e.g. González-Jiménez et al., 2012 and reference therein). Earlier studies have used the $^{187}\text{Os}/^{188}\text{Os}$ and $^{187}\text{Os}/^{186}\text{Os}$ ratios of PGM recovered from sediments in the supergene environment in an attempt to establish the geochemical evolution of the convecting upper mantle (Hattori and Hart, 1991; Walker et al., 2005). These isotopic ratios were used to elucidate whether PGM are supergene or hypogene in origin (Hattori and Cabri, 1992). The latter authors concluded that PGM nuggets from placers around the world were formed in the mantle and transferred to the supergene environment only by mechanical processes without modifying their original Os isotopic compositions.

However, a different view on the origin of PGM in supergene environments discussed in this study (see chapters 6 and 7) suggests that PGM can effectively grow in supergene settings from low-T fluids (Augustithis, 1965; Stumpfl 1974; Bowles, 1986). Ni laterites from the Falcondo mining area in the Dominican Republic provides textural and chemical evidence for the *in situ* neoformation of PGM, presumably with an important role of

biogenic processes (see chapter 7; Aiglsperger et al., 2014; 2015).

The aim of this work is to start with the investigation of characteristics of the Re-Os system in PGM found in Ni laterites. To the best of the author's knowledge this is the first description of Re-Os systematics from PGM found in Ni laterites.

8.2. Samples and analytical methods

Chromitite samples and soil samples were collected from different levels in Ni laterites (limonite and saprolite) from the Falcondo mining area located in the central part of the Dominican Republic. As explained in chapter 2 the Falcondo mining area is the largest hydrous Mg silicate type Ni laterite deposit in the Greater Antilles. The weathering profile is developed on serpentinized ophiolite-related ultramafic rocks (mainly harzburgite) and consists of a Fe oxide(s) - dominated limonitic cover at the top and a thick silicate saprolite horizon beneath (Lewis et al., 2006a; Villanova de Benavent et al., 2014; Aiglsperger et al., 2015a).

Recently, small-scale chromitite pods (2 - 5 m in diameter) were discovered during mining activities (see chapter 5). These chromitites are systematically enriched in total PGE (up to 17 ppm) and show Ru-

dominated PGM mineralogy (e.g. laurite – erlichmanite and Ru-Os-Fe compounds). In addition to PGM in chromitites, PGM also occur to a much lesser extent, within the limonite and saprolite (Aiglsperger et al., 2015, see chapter 6). Numerous PGM grains were discovered in polished and thin sections as well as in heavy mineral concentrates after applying innovative hydroseparation techniques (www.hslab-barcelona.com). 26 Os-rich PGM from different horizons and lithologies (i.e. chromitite, saprolite and limonite) of the Ni laterite profiles were selected and different types of PGM were considered: (i) high temperature PGM formed during magmatic stages, (ii) intermediate

temperature PGM produced by reworking of the formers during stages of serpentinization and (iii) very low temperature PGM derived from the alteration of the two formers during stages of lateritization. PGM of group (i) are considered primary in origin, whereas PGM of group (ii) and (iii) are classified as secondary in origin (Fig. 8.1). Examples of analysed PGM are given in Fig. 8.2. A detailed mineralogical investigation of one Ru-Os-Fe grain of group (ii) allows us to identify that these grains are composed of Ru rich hexaferrum with microchannels filled with oxidized magnetite (see chapter 6).

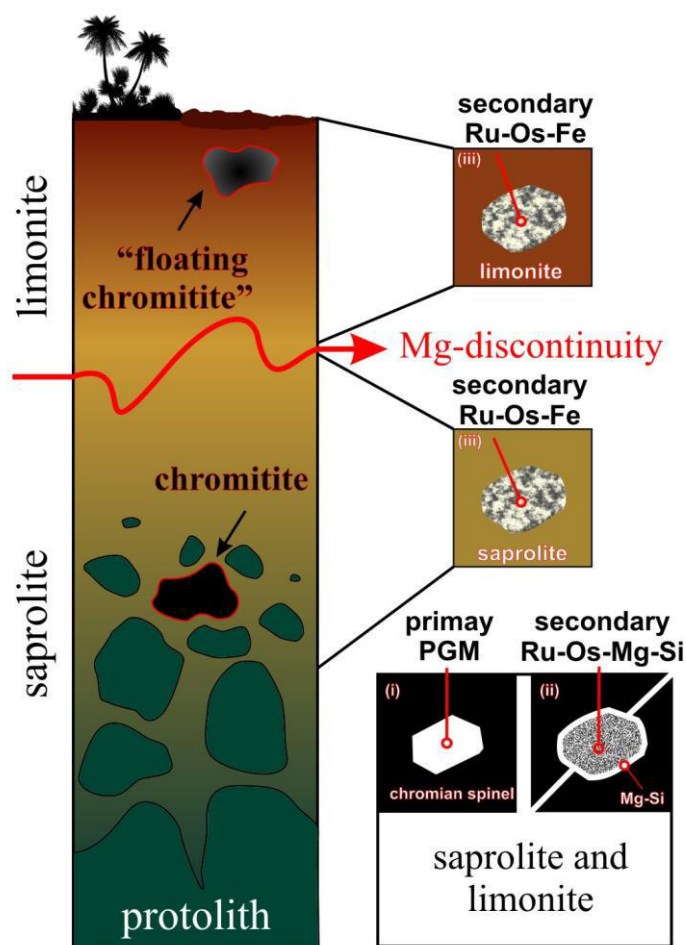


Fig.8.1. Schematic Ni laterite profile with indicated location of analysed primary PGM (i) (formed during magmatic stage), secondary Ru-Os-Mg-Si compounds (ii) (formed during stages of serpentinization) and secondary Ru-Os-Fe grains (iii) (formed during stages of lateritization).

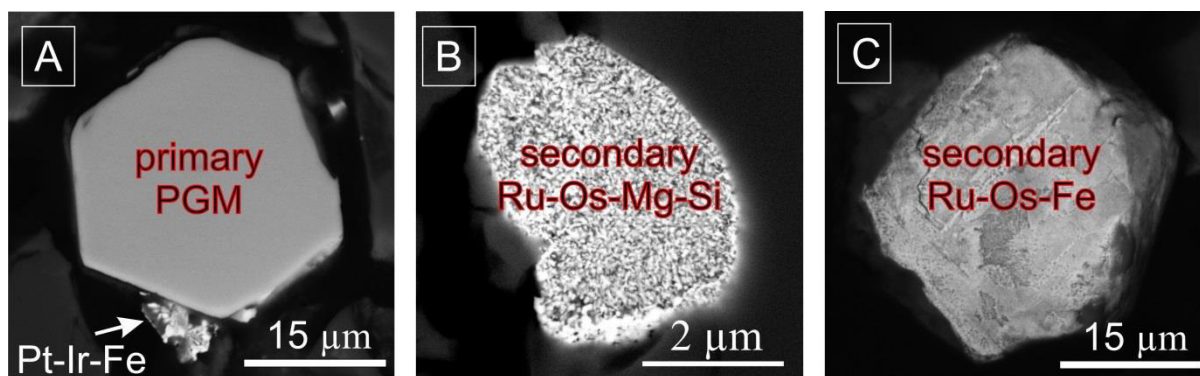


Fig. 8.2. Examples of BSE images of analysed primary PGM (magmatic stage) (A), secondary Ru-Os-Mg-Si (stages of serpentinization) (B) and secondary Ru-Os-Fe grains (stages of lateritization) (C).

8.3. Results

Overall, PGM from the Falcondo Ni laterite yield low $^{187}\text{Os}/^{188}\text{Os}$ ratios typical of mantle PGM. Primary PGM yield $^{187}\text{Os}/^{188}\text{Os}$ ratios between 0.12215 (saprolite; Loma Peguera) and 0.12153 (limonite, Loma Peguera) (Fig. 8.3; Table 8.1). Secondary Ru-Os-Mg-Si PGM show very similar low ratios, varying from 0.11973 to 0.12149. in contrast the Ru-Os-Fe grains, formed at very low temperature in the laterite display systematically higher ratios up to 0.1265 (Fig. 8.3). $^{187}\text{Re}/^{188}\text{Os}$ values are very low for all studied PGM (<0.0015) (Fig. 8.3). The calculated Rhenium-depleted (T_{RD}) model ages for the above described grains set in two groups: primary and secondary Ru-Os-Mg-Si PGM cluster around ~0.9 Ga, whereas Ru-Os-Fe grains cluster around ~0.5 Ga (Fig. 8.4).

No PGM from highest levels in the limonite horizon with textural and chemical evidence suggesting *in-situ* neoformation processes (see chapter 7) have been analysed at this stage of investigation.

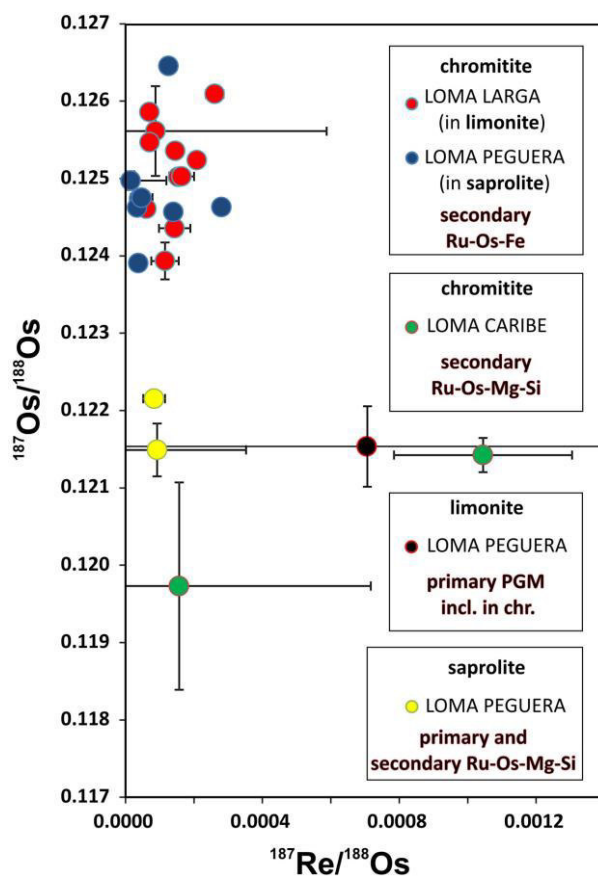


Fig. 8.3. Plot of $^{187}\text{Os}/^{188}\text{Os}$ vs. $^{187}\text{Re}/^{188}\text{Os}$ of primary and secondary PGM from different sample locations within the Falcondo mining area (see chapter 5). Uncertainties are 2σ ; those not shown are smaller than the symbol.

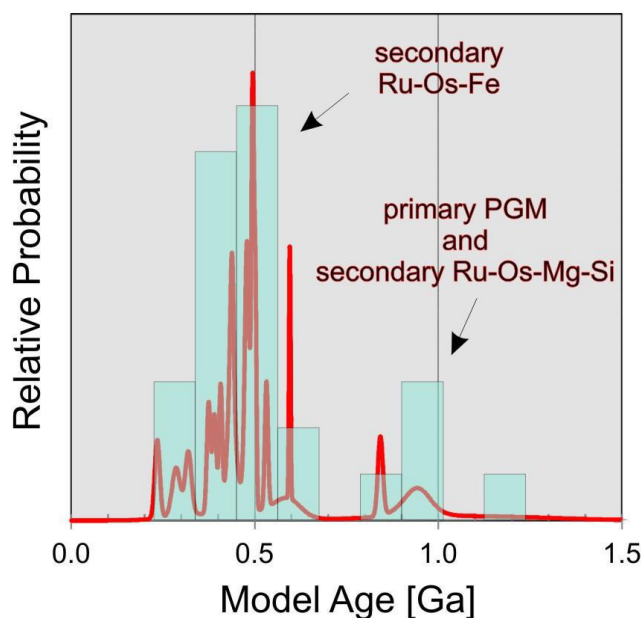


Fig 8.4. Cumulative-probability plots and histograms (shaded bars) of Os model ages (Ga) for investigated PGM.

PGM				$^{187}\text{Os}/^{188}\text{Os}$	2σ	$^{187}\text{Re}/^{188}\text{Os}$	2σ	T_{RD} (Ga)	2σ (Ga)
Loma Peguera									
LP1 <53(C)-PGM1	primary	Os-Ir-Fe	limonite	0.12153	0.00128	0.00068	0.00050	0.93	0.18
LP40-1(4)-PGM1	secondary	Ru-Os-Mg-Si	saprolite	0.12149	0.00034	0.00009	0.00026	0.94	0.05
LP40-1(4)-PGM3	primary	RuS	saprolite	0.12215	0.00005	0.00008	0.00003	0.84	0.01
LP6<53-(5)-PGM1	secondary	Ru-Os-Fe	saprolite	0.12463	0.00003	0.00028	0.00002	0.49	0.00
LP6<53-(3)-PGM1	secondary	Ru-Os-Fe	saprolite	0.12390	0.00001	0.00004	0.00001	0.60	0.00
LP6<53-(H)-PGM1	secondary	Ru-Os-Fe	saprolite	0.12462	0.00002	0.00003	0.00001	0.49	0.00
LP6<53-(H)-PGM2	secondary	Ru-Os-Fe	saprolite	0.12475	0.00005	0.00005	0.00003	0.48	0.01
LP6<53-(G)-PGM1	secondary	Ru-Os-Fe	saprolite	0.12457	0.00002	0.00014	0.00002	0.50	0.00
LP6<53-(F)-PGM1	secondary	Ru-Os-Fe	saprolite	0.12645	0.00005	0.00013	0.00002	0.23	0.01
LP6<53-(F)-PGM2	secondary	Ru-Os-Fe	saprolite	0.12473	0.00003	0.00004	0.00001	0.48	0.00
LP6<53-(M)-PGM1	secondary	Ru-Os-Fe	saprolite	0.12497	0.00012	0.00002	0.00010	0.44	0.02
LP6<53-(M)-PGM1-1	secondary	Ru-Os-Fe	saprolite	0.12504	0.00006	0.00010	0.00001	0.43	0.01
LP6<53-(M)-PGM1-2	secondary	Ru-Os-Fe	saprolite	0.12471	0.00004	0.00006	0.00002	0.48	0.01
Loma Larga									
LL <53 (ML A)- PGM1	secondary	Ru-Os-Fe	limonite	0.12561	0.00058	0.00009	0.00050	0.35	0.08
LL <53 (ML A)- PGM2	secondary	Ru-Os-Fe	limonite	0.12536	0.00004	0.00015	0.00002	0.39	0.01
LL <53 (ML A)- PGM3	secondary	Ru-Os-Fe	limonite	0.12524	0.00003	0.00021	0.00002	0.41	0.00
LL <53 (ML A)- PGM4	secondary	Ru-Os-Fe	limonite	0.12586	0.00006	0.00007	0.00002	0.32	0.01
LL <53 (ML A)- PGM5	secondary	Ru-Os-Fe	limonite	0.12461	0.00003	0.00006	0.00001	0.50	0.00
LL <53 (ML A)- PGM6	secondary	Ru-Os-Fe	limonite	0.12609	0.00008	0.00026	0.00003	0.29	0.01
LL <53 (ML A)- PGM7	secondary	Ru-Os-Fe	limonite	0.12502	0.00003	0.00015	0.00002	0.44	0.00
LL <53 (ML A)- PGM8	secondary	Ru-Os-Fe	limonite	0.12547	0.00003	0.00007	0.00001	0.37	0.00
LL <53 (ML A)- PGM11	secondary	Ru-Os-Fe	limonite	0.12393	0.00024	0.00012	0.00004	0.59	0.03
LL <53 (ML A)- PGM12	secondary	Ru-Os-Fe	limonite	0.12503	0.00008	0.00016	0.00004	0.44	0.01
LL <53 (ML A)- PGM13	secondary	Ru-Os-Fe	limonite	0.12436	0.00003	0.00014	0.00005	0.53	0.00
Loma Caribe									
Chromite 3a-PGM4	secondary	Ru-Os-Mg-Si	chromitite	0.12142	0.00022	0.00104	0.00026	0.94	0.03
Chromite 3a-PGM7	secondary	Ru-Os-Mg-Si	chromitite	0.11973	0.00134	0.00016	0.00056	1.18	0.19

Table 8.1. Os isotopic data of primary, secondary and (trans-)formed PGM from different locations within the Falcondo mining area.

8.4. Discussion

Although additional analyses are required to better evaluate the Os isotope characteristics of PGM found within Ni laterites, following interpretations can be made based on these first observations. All analysed PGM reveal low $^{187}\text{Os}/^{188}\text{Os}$ ratios below the present-day Os isotopic ratio of mantle materials (i.e. 0.1290, see Walker et al., 2002). Furthermore, primary PGM and secondary PGM formed by desulphurization of primary PGM during stages of serpentinization reveal almost identical $^{187}\text{Os}/^{188}\text{Os}$ ratios and Os model ages. This suggests that serpentinization of primary PGM with subsequent

incorporation of Mg silicates does not significantly affect the Re-Os system.

On the contrary, secondary Ru-Os-Fe grains from limonite and saprolite show very distinct Os-isotope compositions, suggesting that disturbance (i.e. opening) of the Re-Os system occurred at very low temperature during stages of lateritization. An opening of the Re-Os isotopic system in Os-rich PGMs was described for the first time in PGM from the metamorphosed chromitites of Bulgaria (González-Jiménez et al., 2012) and it is reported from PGM in the lateritic environment for the first time here. These observations are in frank disagreement with previous studies suggesting that Re-Os system in PGM remains unchanged

even during post-magmatic alteration processes (e.g. Hattori and Hart, 1991).

It is noteworthy, that Malitch et al. (2004) recognized significant higher $^{187}\text{Os}/^{188}\text{Os}$ values of PGM found within the Moho transition zone at Kraubath (Austria) and speculated that this feature could be an evidence of a “radiogenic” crustal component incorporation. Perturbations to the Os isotopic system by alteration processes, characterized by a significant meteoric water component, were reported from metamorphosed iron formations (Ripley et al., 2008). These authors assessed the possible effects on the Re-Os system by Os exchange with Fe in magnetite.

With respect to in this work discussed Ru-Os-Fe grains found in highest levels of the Ni laterite profile, microraman investigation and synchrotron through-the-substrate X-ray micro-diffraction (tts- μXRD) have proved that they consist of Ru rich hexaferrum and oxidized magnetite (see chapter 7). As a consequence it can be speculated, that circulating Fe rich fluids penetrated porous, secondary PGM, resulting in formation of secondary PGM – magnetite compounds. This event has most likely contributed to the observed $^{187}\text{Os}/^{188}\text{Os}$ shift by addition of either radiogenic ^{187}Os or parent ^{187}Re . As shown in chapters 4, 6 and 7, PGE can clearly not be considered immobile and noble elements within Ni laterites. Quantitative element mappings of one Ru-Os-Fe grain reveal higher Fe contents (more oxidized magnetite) precisely at zones with lower Os concentrations (see chapter 6). Thus, gentle but steady mobilization of PGE and subsequent loss of Os is believed to be the

driving factor for gradually higher $^{187}\text{Os}/^{188}\text{Os}$ ratios in the weathering profile. This trend is well observed by comparing average $^{187}\text{Os}/^{188}\text{Os}$ values of secondary Ru-Os-Fe grains found in saprolite (Fe content ~8 wt%) with grains from limonite (Fe content ~17 wt%) (Fig. 8.2).

Extensive addition of either crustal Os or Re to studied PGM has not been observed at this stage of investigation. However, future analyses will show if this also applies to Pt and Ir rich PGM found at highest levels of the Ni laterite and considered to have formed by *in situ* growths (see chapter 7).

8.5. Final remarks

Presented results suggest that serpentinization of the Loma Caribe peridotite has not significantly affected the Re-Os system in Os-rich PGM. This is noted by the fact, that primary PGM formed at magmatic stage and secondary Ru-Os-Mg-Si PGM formed due desulphurization of primary PGM with significant incorporation of Mg silicates, have almost identical Os isotope characteristics, typical of the mantle. However, the Re-Os system can be significantly disturbed during stages of lateritization when porous secondary PGM react with Fe-rich fluids, thus forming hexaferrum and magnetite in the interstices of secondary PGM. Here presented data indicate that more radiogenic $^{187}\text{Os}/^{188}\text{Os}$ ratios in higher levels of the weathering profile are linked to steady mobilization of PGE within secondary PGM resulting in subsequent loss of Os counterbalanced by the incorporation of Fe.

Chapter 9

Summary of conclusions

1. Critical metals (CM; i.e. REE, Sc, PGE) are concentrated in Ni laterites towards the surface in specific zones:
 - (i) REE in clay minerals rich horizons and within zones composed of secondary Mn oxide(s)
 - (ii) Sc within zones rich in secondary Fe and Mn bearing oxide(s)
 - (iii) PGE in zones with high concentrations of residual chromian spinel and secondary Fe and Mn bearing oxide(s) at upper levels of the Ni laterite profile.
2. Concentration factors for CM enrichment involve:
 - (i) residual enrichment by intense weathering
 - (ii) mobilization of CM during changing Eh and pH conditions with subsequent reprecipitation at favourable geochemical barriers
 - (iii) interactions between biosphere and limonitic soils at highest levels of the profile with involved neoformation processes.
3. Total contents of CM in investigated Ni laterites are low when compared with conventional ore deposits but are of economic significance as CM should be seen as cost inexpensive by-products during the Ni (+Co) production. Innovative extraction methods currently under development will boost the significance of Ni laterites as future unconventional CM ore deposits.
4. Ni laterites at Falcondo contain up to 640 ppb total PGE and have to be considered potential unconventional PGE deposits. The observed PGE enrichment is independent of PGE-enriched substratum (e.g. chromitites) and mainly explained by residual accumulation of PGE-bearing mineral phases (e.g. disseminated Cr-spinel).
5. Three different types of PGM are present within the lateritic profiles:
 - (i) primary PGM (magmatic stage)
 - (ii) secondary PGM (alteration of pre-existing PGM)

- (iii) PGM due to *in situ* neoformation after PGE mobilization.
6. Results of this investigation provide morphological and chemical evidence for *in situ* neoformation of PGM within Ni laterites by bioreduction and/or electrochemical accretion.
7. The innovative HS-11 heavy-mineral separation technique has proven to be highly suitable to find minute amounts of PGM and other CM bearing mineral phases within limonite and saprolite samples.
8. “Multistage PGE grains” from highest levels of Ni laterites are good objects to investigate PGM (trans-)formations from hypogene to supergene environments and can be seen as the missing link between competing hypotheses regarding the origin of nuggets found on the surface.
9. The observation of accumulations of most likely biogenic mediated *in situ* growth of Pt rich nanoparticles in supergene environments could help to explain:
- (i) why Pt bearing nuggets are the most abundant PGM found in surface environments (Cabri et al., 1996)
 - (ii) why Pt nuggets from placer deposits generally surpass the grain sizes of Pt grains found in parent rocks by several orders of magnitude (few micrometers vs. several millimeters) (Reith et al., 2014 and reference therein)
 - (iii) how anthropogenic PGE contamination may affect our biosphere.
10. Results of this thesis suggest that serpentinization of the Loma Caribe peridotite has not significantly affected the Re-Os system in Os-rich PGM.
11. The Re-Os system can be significantly disturbed during stages of lateritization when porous secondary PGM react with Fe-rich fluids, thus forming hexaferrum and magnetite in the interstices of secondary PGM.
12. Here presented data indicate that more radiogenic $^{187}\text{Os}/^{188}\text{Os}$ ratios in higher levels of the weathering profile are linked to steady mobilization of PGE within secondary PGM resulting in subsequent loss of Os counterbalanced by the incorporation of Fe.
13. In this investigation presented data clearly states that PGE are neither noble nor inert in surface environments, at least in those related to tropical Ni laterites from the Northern Caribbean.

References

- Ahmad, S., Morris, D.F.C., 1978. Geochemistry of some lateritic nickel-ores with particular reference to the distribution of noble metals. *Mineral. Magazine* 42, 143, M 4-8.
- Aiglsperger, T., Proenza J.A, Zaccarini, F., Labrador, M., Navarro-Ciuriana, D., 2011. Looking for needles in a haystack: how to find PGM in laterites by using hydroseparation techniques. *Macla* 15, 23-24.
- Aiglsperger, T., Proenza, J.A., Lewis, J.F., Longo, F., 2014. Is Microbial Activity Causing PGM Neof ormation in Ni-Laterites? Evidence from Falcondo (Dominican Republic). *Macla* 19, 19-20.
- Aiglsperger, T., Proenza, J.A., Zaccarini, F., Lewis, J.F., Garuti, G., Labrador, M., Longo, F., 2015. Platinum group minerals (PGM) in the Falcondo Ni laterite deposit, Loma Caribe peridotite (Dominican Republic). *Miner. Deposita* 50, 105-123.
- Anders, E., Grevesse, N., 1989. Abundances of the elements: Meteoritic and solar: *Geochim. Cosmochim. Ac.* 53, 197-214.
- Andreu, E., Torró, L., Proenza, J.A., Domenech, C., García-Casco, A., Villanova de Benavent, C., Chavez, C., Espaillet, J., Lewis, J.F., 2015. Weathering profile of the Cerro de Maimón VMS deposit (Dominican Republic): textures, mineralogy, gossan evolution and mobility of gold and silver. *Ore Geol. Rev.* 65, 165-179.
- Arndt, U.W., Wonacott, A.J., 1977. *The Rotation Method in Crystallography*. Amsterdam, North Holland Biomedical Press, Elsevier.
- Audet, M.A., 2009. Le massif du Koniambo, Nouvelle-Calédonie Formation et obduction d'un complexe ophiolitique du type SSZ. Enrichissement en nickel, cobalt et scandium dans les profils résiduels: PhD thesis (in french), 327 p.
- Augé, T., Legendre, O., 1994. Platinum-Group Element oxides from the Pirogues ophiolitic mineralization, New Caledonia: Origin and significance. *Econ. Geol.* 89, 1454-1468.
- Augé, T., Maurizot, P., Breton, J., Eberlé, J.M., Gilles, C., Jézequel, P., Mezière, J., Robert, M., 1995. Magmatic and supergene platinum-group minerals in the New Caledonia Ophiolite. *Chron Rech Min* 520, 3-26.
- Augusthitis, S.S., 1965. Mineralogical and geochemical studies of the platiniferous dunite – birbirite – pyroxenite complex of Yubdo, Birbir, W. Ethiopia. *Chemie der Erde* 24, 159-165.

- Azaroual, M., Romand, B., Freyssinet, P., Disnar, J.R., 2001. Solubility of platinum in aqueous solutions at 25°C and pHs 4 to 10 under oxidizing conditions. *Geochim Cosmochim Acta* 65, 4453-4463.
- Baas Becking, L.G.M., Kaplan, I.R., Moore, D., 1960. Limits of the natural environment in terms of pH and oxidation-reduction potentials. *Jour. Geology* 68, 243-284.
- Babechuk, M.G., Widdowson, M., Kamber, B.S., 2014. Quantifying chemical weathering intensity and trace element release from two contrasting basalt profiles, Deccan Traps, India. *Chem. Geol.* 363, 56–75.
- Ballhaus, C., Bockrath, C., Wohlgemuth- Ueberwasser, C., Laurenz, V., Berndt, J., 2006. Fractionation of the noble metals by physical processes. *Contrib Mineral Petr* 152, 667-684.
- Berger, A., Janots, E., Gnos, E., Frei, R., Bernier, F., 2014. Rare earth element mineralogy and geochemistry in a laterite profile from Madagascar. *Appl. Geochem.* 41, 218–228.
- Bowin, C.O., 1966. Geology of the central Dominican Republic (a case history of part of an island arc). In: Hess, H. (Ed.), *Caribbean Geological Studies. Mem. Geol. Soc. Am.* 98, pp. 11-84.
- Bowles, J.F.W., 1986. The development of platinum-group minerals in laterites. *Econ Geol* 81, 1278-1285.
- Bowles, J.F.W., Gize, A.P., Vaughan, D.J., Norris, S.J., 1994. Development of platinum-group minerals in laterites-initial comparison of organic and inorganic controls. *Transact. Instn. Min. Metall.* 103, B53-B56.
- Brand, N.W., Butt, C.R.M., Elias, M., 1998. Nickel laterites: classification and features. *AGSO J. Aust. Geol. Geophys.* 17, 81–88.
- Branley, S.L., Goldhaber, M.B., Ragnarsdottir, K.V., 2007. Crossing Disciplines and Scales to Understand the Critical Zone. *Elements* 3, 307-314.
- Brantley, S.L., White, T.S., White, A.F., Sparks, D., Richter, D., Pregitzer, K., Derry, L., Chorover, J., Chadwick, O., April, R., Anderson, S., Amundson, R., 2006. *Frontiers in Exploration of the Critical Zone, An NSF sponsored Workshop. National Science Foundation*, 30 pp.
- Braun, J., Pagel, M., Muller, J., Bilong, P., Michard, A., Guillet, B., 1990. Cerium anomalies in lateritic profiles. *Geochim. Cosmochim. Acta* 54, 781-795.
- Brugger, J., Etschmann, B., Grosse, C., Plumridge, C., Kaminski, J., Paterson, D., Shar, S.S., Ta, C., Howard, D.L., de Jonge, M.D., Ball, A.S., Reith, F., 2013. Can biological toxicity drive the contrasting behavior of platinum and gold in surface environments? *Chem. Geol.* 343, 99 – 110.
- Butt, C.R.M., Cluzel, D., 2013. Nickel laterite ore deposits: Weathered serpentinites. *Elements* 9, 123-128.

- Cabral, A.R., Lehmann, B., Tupinambá, M., Schlosser, S., Kwitko-Ribeiro, R., De Abreu, F.R., 2009. The platiniferous Au-Pd belt of Minas Gerais, Brazil, and genesis of its botryoidal Pt-Pd aggregates. *Econ. Geol.* 104, 1265-1276.
- Cabral, A.R., Radtke, M., Munnik, F., Lehmann, B., Reinholz, U., Rieseemeier, H., Tupinambá, M., Kwitko-Ribeiro, R., 2011. Iodine in alluvial platinum-palladium nuggets: Evidence for biogenic precious-metal fixation. *Chem. Geol.* 281, 152-132.
- Cabri, L.J., 2002. The platinum-group minerals. In *The Geology, Geochemistry, Mineralogy and Mineral Beneficiation of Platinum-Group Elements*. Edited by L.J. Cabri. Canadian Institute of Mining, Metallurgy and Petroleum, Special Volume 54, 13-129.
- Cabri, L.J., Harris, D.C., 1975. Zoning in Os-Ir alloys and the relation of the geological and tectonic environment of the source rocks to the bulk Pt: Pt + Ir + Os ratio for placers. *Can Mineral* 13, 266-274.
- Cabri, L.J., Harris, D.C., Weiser, T.W., 1996. The mineralogy and distribution of Platinum Group Mineral (PGM) placer deposits of the world. *Exploration and Mining Geology* 5, 73-167.
- Cabri, L.J., Rudashevsky, N.S., Rudashevsky, V.N., Gorkovetz, V.Y., 2008. Study of native gold from the Luopensulo deposit (Kostomuksha area, Karelia, Russia) using a combination of electric pulse disaggregation (EPD) and hydroseparation (HS). *Miner. Eng.* 21, 463-470.
- Cabri, L.J., Rudashevsky, N.S., Rudashevsky, V.N., Lastra, R., 2006. Hydroseparation: a new development in process mineralogy of platinum-bearing ores. *CIM Bulletin* 99, 1092, 1-7.
- Campbell, S., G., Reith, F., Etschmann, B., Brugger, J., Martinez-Criado, G., Grodon, R.A., Southam, G., 2015. Surface transformations of platinum grains from Fifield, New South Wales, Australia. *Am. Min.* 100, 1236-1243.
- Capobianco, C.J., Drake, M.J., 1990. Partitioning of ruthenium, rhodium, and palladium between spinel and silicate melt and implications for platinum group element fractionation trends. *Geochim. Cosmochim. Ac.* 54, 869-874.
- Chakhmouradian, A.R., Wall, F., 2012. Rare Earth Elements: Rare Earth Elements: Minerals, Mines, Magnets (and More). *Elements* 8, 333-340.
- Chan, T.K., Finch, I.J., 2001. Determination of platinum-group elements and gold by inductively coupled plasma mass spectrometry. In: *Australian Platinum Conference*, Perth, Western Australia, pp. 1-9.
- Chorover, J., Kretzschmar, R., Garcia-Pichel, F., Sparks, D.L., 2007. Soil biogeochemical processes within the critical zone. *Elements* 3, 321-326.

- Chu, H., Chi, G., Bosman, S., Card, C., 2015. Diagenetic and geochemical studies of sandstones from drill core DV10-001 in the Athabasca basin, Canada, and implications for uranium mineralization. *J. Geochem. Explor.* 148, 206-230.
- Colombo, C., Oated, C.J., Monhemius, A.J., Plant, J.A., 2008. Complexation of platinum, palladium and rhodium with inorganic ligands in the environment. *Geochem. Explor. Environ. Anal.* 8, 91-101.
- Cooper, G.R.C., 2002. Oxidation and toxicity of chromium in ultramafic soils in Zimbabwe. *Appl. Geochem.* 17, 981-986.
- Dalvi, A.D., Bacon, W.G., Osborne, R.C., 2004. The past and future of nickel laterites. PDAC 2004, International Convention, Prospectors and Developers Association of Canada, March 7-10, Toronto, Ontario, Canada, pp. 1-27.
- Desborough, G.A., Criddle, A.J., 1984. Bowieite: a new rhodium-iridium-platinum sulfide in platinum-alloy nuggets, Goodnews Bay, Alaska. *Can. Mineral.* 22, 543-552.
- Draper, G., Gutiérrez, G., Lewis, J.F., 1996. Thrust emplacement of the Hispaniola peridotite belt: orogenic expression of the mid Cretaceous Caribbean arc polarity reversal? *Geology* 24, 1143-1146.
- Duzgoren-Aydin, N.S., Aydin, A., Malpas, J., 2002. Distribution of clay minerals along a weathered pyroclastic profile, Hong Kong. *Catena* 50, 17-41.
- EC (European Commission), 2014. Report on critical raw materials for the EU. Report of the ad-hoc Working Group in defining critical raw materials: Brussels, Belgium. Available at http://ec.europa.eu/enterprise/policies/raw-materials/files/docs/crm-report-on-critical-raw-materials_en.pdf. Accessed 25 March 2015.
- Economou-Eliopoulos, M., Eliopoulos, D.G., Apostolikas, A., Maglaras, K., 1997. Precious and rare earth element distribution in Ni-laterite deposits Lokris area, Central Greece. In: Proceedings of the 4th Biennial SGA Meeting, Papunen, H. (Ed.), Turku, Finland, pp. 411-413.
- Eliopoulos, D., Economou, G., Tzifas, I., Papatrechas, C., 2014. The potential of rare earth elements in Greece. ERES 2014, 1st European Rare Earth Resources Conference, September 4-7, Milos, Greece, pp. 308-316.
- Eliopoulos, D.G., Economou-Eliopoulos, M., 2000. Geochemical and mineralogical characteristics of Fe-Ni- and bauxitic-laterite deposits of Greece. *Ore Geol. Rev.* 16, 41-58.
- Escuder Viruete, J., Díaz de Neira, A., Hernaiz Huerta, P.P., Monthel, J., García Senz, J., Joubert, M., Lopera, E., Ullrich, T., Friedman, R., Mortensen, J., Pérez-Estaún, A., 2006.

- Escuder Viruete, J., Pérez-Estaún, A., Contreras, F., Joubert, M., Weis, D., Ullrich, T.D., Spadea, P., 2007. Plume mantle source heterogeneity through time: Insights from the Duarte Complex, Hispaniola, northeastern Caribbean. *J. Geophys. Res.* 112, B04203.
- Fleet, M.E., Crocket, J.H., Liu, M., Stone, W.E., 1999. Laboratory partitioning of platinum-group elements (PGE) and gold with application to magmatic sulfide–PGE deposits. *Lithos* 47, 127-142.
- Fleet, M.E., De Almeida, C.M., Angeli, N., 2002. Botryoidal platinum, palladium and potarite from the Bom Sucesso stream, Minas Gerais, Brazil: compositional zoning and origin. *Can. Mineral.* 40, 341-355.
- Foustoukos, D.I., Bizimis, M., Frisby, C., Shirey, S.B., 2015. Redox controls on Ni–Fe–PGE mineralization and Re/Os fractionation during serpentinization of abyssal peridotite. *Geochim. Cosmochim. Ac.* 150, 11-25.
- Freyssinet, Ph., Butt, C.R.M., Morris, R.C., 2005. Ore-forming processes related to lateritic weathering. *Econ. Geol.* 100th Anniversary Volume, 681-722.
- Froment, F., Tournié, A., Colomban, P., 2008. Raman identification of natural red to yellow pigments: ochre and iron-containing ores. *J. Raman Spectrosc.* 39, 560-568.
- Frost, B.R., Evans, K.A., Swapp, S.M., Beard, J.S., Mothersole, F.E., 2013. The process of serpentinization in dunite from New Caledonia. *Lithos* 178, 24-39.
- Fuchs, A.W., Rose, A.W., 1974. The geochemical behavior of platinum and palladium in the weathering cycle in the Stillwater Complex, Montana. *Econ. Geol.* 69, 332-346.
- Galí, S., Proenza, J.A., Labrador, M., Tauler, E., Melgarejo, J.C., 2007. Numerical modelling of oxide-type Ni laterite deposits: preliminary results. In: Andrew, C.J. et al. (Eds.), *Digging Deeper*, 2. Irish Association of Economic Geology, pp. 1385-1388.
- Garuti, G., Proenza, J.A., Zaccarini, F., 2007. Distribution and mineralogy of platinum-group elements in altered chromitites of the Campo Formoso layered intrusion (Bahia State, Brazil): control by magmatic and hydrothermal processes. *Mineral. Petrol.* 86, 159-188.
- Garuti, G., Pushkarev, E.V., Zaccarini, F., Cabella, R., Anikina, E.V., 2003. Chromite composition and platinum-group mineral assemblage in the Uktus Alaskantype complex (central Urals, Russia). *Mineral. Deposita* 38, 312-326.
- Garuti, G., Zaccarini, F., 1997. In situ alteration of platinum-group minerals at low temperature: evidence from serpentinized and weathered chromitite of the Vourinos complex, Greece. *Can. Mineral.* 35, 611-626.

- Garuti, G., Zaccarini, F., Proenza, J.A., Thalhammer, O.A.R., Angeli, N., 2012. Platinum-group minerals in chromitites of the Niquelândia layered intrusion (Central Goiás, Brazil): Their magmatic origin and low-temperature reworking during serpentinization and lateritic weathering. *Minerals* 2, 365-384.
- Gleeson, S.A., Butt, C.R., Elias, M., 2003. Nickel laterites: a review. *SEG Newsletter* 54, 11–18.
- Golightly, J.P., 1981. Nickeliferous laterite deposits. *Econ. Geol.* 75th Anniversary Vol., 710–735.
- Golightly, J.P., 2010. Progress in understanding the evolution of nickel laterites. *Soc. Econ. Geol. Spec. Publ.* 15, 451-485.
- Golightly, J.P., Plamondon, M., Srivastava, R.M., 2008. 43-101F1 Technical report on the Moa Occidental and Moa Oriental nickel laterite properties in Cuba: Prepared for Sherritt International Corporation, 102 p., accessed March 25, 2015, at <http://www.sedar.com/GetFile.do?lang=EN&docClass=24&issuerNo=00002460&fileName=/csf/sprod/data88/filings/01240793/00000001/f%3A%5Ccrcher%5C12941-0001%5C2007AIF%5C43-101report.pdf>.
- González-Jiménez, J.M., Gervilla, F., Griffin, W.L., Proenza, J.A., Augé, T., O'Reilly, S.Y., Pearson, N.J., 2012. Os-isotope variability within sulfides from podiform chromitites. *Chem. Geol.* 291, 224 – 235.
- González-Jiménez, J.M., Griffin, W.L., Gervilla, F., Proenza, J.A., O'Reilly, S.Y., Pearson, N.J., 2014b. Chromitites in ophiolites: how, where, when, why? Part I. Origin and significance of platinum-group minerals. *Lithos* 189, 127-139.
- González-Jiménez, J.M., Griffin, W.L., Proenza, J.A., Gervilla, F., O'Reilly, S.Y., Akbulut, M., Pearson, N.J., Arai, S., 2014a. Chromitites in ophiolites: How, where, when, why? Part II. The crystallization of chromitites. *Lithos* 189, 140-158.
- Grant, J.A., 1986. The isocon diagram—a simple solution to Gresens' equation for metasomatic alteration. *Econ. Geol.* 81, 1976–1982.
- Grant, J.A., 2005. Isocon analysis: A brief review of the method and applications. *Phys. Chem. Earth* 30, 997–1004.
- Gray, J.D., Schorin, K.H., Butt, C.R.M., 1996. Mineral associations of platinum and palladium in lateritic regolith, Ora Banda Sill, Western Australia. *J. Geochem. Explor.* 57, 245-255.
- Gresens, R.L., 1967. Composition–volume relationships of metasomatism. *Chem. Geol.* 2, 47–55.
- Haldemann, E.G., Buchan, R., Blowes, J.H., Chandler, T., 1979. Geology of lateritic nickel deposits, Dominican Republic. In: Evans, D.J.I., Shoemaker, R.S., Veltman, H. (Eds.), *International Laterite Symposium*, Amer. Inst. Mining, Metal. and Petroleum Engineers, New York, pp. 57-84.

- Hattori, K., Cabri, L.J., 1992. Origin of Platinum-Group-Mineral Nuggets inferred from an Osmium-Isotope Study. *Can. Mineral.* 30, 289-301.
- Hattori, K., Cabri, L.J., Johanson, B., Zientek, M.L., 2004. Origin of placer laurite from Borneo: Se and As contents, and S isotopic compositions. *Min. Mag.* 68, 353-368.
- Hattori, K., Hart, S.R., 1991. Osmium-isotope ratios of platinum-group minerals associated with ultramafic inclusions: Os isotopic evolution of the oceanic mantle. *Earth Planet. Sci. Lett.* 107, 499-514.
- Hein, J.R., Mizell, K., Koschinsky, A., Conrad, T.A., 2013. Deep-ocean mineral deposits as a source of critical metals for high- and green-technology applications: Comparison with land-based resources. *Ore Geol. Rev.* 51, 1-14.
- Hirose, K., Kawamoto, T., 1995. Hydrous partial melting of lherzolite at 1 GPa: the effect of H₂O on the genesis of basaltic magmas. *Earth. Planet. Sci. Lett.* 133, 463-473.
- Irvine, T.N., 1967. Chromian spinel as a petrogenetic indicator. II. Petrologic applications. *Can. J. Earth Sci.* 4, 71-103.
- Iturralde-Vinent, M.A., Díaz Otero, C., Rodríguez Vega, A., Díaz Martínez, R., 2006. Tectonic implications of paleontologic dating of Cretaceous-Danian sections of Eastern Cuba. *Geol. Acta* 4, 89-102.
- Janots, E., Bernier, F., Brunet, F., Muñoz, M., Trcera, N., Berger, A., Lanson, M., 2015. Ce(III) and Ce(IV) (re)distribution and fractionation in a laterite profile from Madagascar: insights from in situ XANES spectroscopy at the Ce LIII-edge, *Geochim. Cosmochim. Ac.* 153, 134-148.
- Jochum, K.P., Weis, U., Stoll, B., Kuzmin, D., Yang, Q., Raczek, I., Jacob, D.E., Stracke, A., Birbaum, K., Frick, D.A., Günther, D., Enzweiler, J., 2011. Determination of Reference Values for NIST SRM 610-617 Glasses Following ISO Guidelines. *Geostand. Geoanal. Res.* 35, 397-429.
- Johnson, D.B., du Plessis, C.A., 2015. Biomining in reverse gear: Using bacteria to extract metals from oxidised ores. *Miner. Eng.* 75, 2-5.
- Kalatha, S., Economou-Eliopoulos, M., 2015. Framboidal pyrite and bacterio-morphic goethite at transitional zones between Fe-Ni laterites and limestones: Evidence from Lokris, Greece. *Ore Geol. Rev.* 65, 413-425.
- Kamenetsky, V.S., Crawford, A.J., Meffre, S., 2001. Factors controlling chemistry of magmatic spinel: an empirical study of associated olivine, Cr-spinel and melt inclusions from primitive rocks. *J. Petrol.* 42, 655-671.
- Koen, G.M., 1964. Rounded platinoid grains in the Witwatersrand banket. *Trans. Geol. Soc. S. Afr.*, 67, 139-147.

- Konishi, Y., Ohno, K., Saitoh, N., Nomura, T., Nagamine, S., Hishida, H., Takahashi, Y., Uruga, T., 2007. Bioreductive deposition of platinum nanoparticles on the bacterium *Shewanella* algae. *J. of Biotech.* 128, 648 – 653.
- Kooijman, E., Berndt, J., Mezger, K., 2012. U-Pb dating of zircon by laser ablation ICP-MS: recent improvements and new insights. *Eur. J. Mineral.* 24, 5-21.
- Laskou, M., Economou-Eliopoulos, M., 2007. The role of microorganisms on the mineralogical and geochemical characteristics of the Parnassos-Ghiona bauxite deposits, Greece. *J. Geochem. Explor.* 93, 67-77.
- Lavaut, W., 1998. Tendencias geológicas del intemperismo de las rocas ultramáficas en Cuba oriental. *Revista Minera y Geología* 15, 9-16.
- Lazarenkov, V.G., Tikhomirov, B., Zhidkov, Ya., Talovina, V., 2005. Platinum Group Metals and Gold in Supergene Nickel Ores of the Moa and Nikaro Deposits (Cuba). *Lithol. Miner. Resour.* 40, 521-527.
- Lázaro, C., Blanco-Quintero, I.F., Rojas-Agramonte, Y., Proenza, J.A., Núñez-Cambra, K., García-Casco, A., 2013. First description of a metamorphic sole related to ophiolite obduction in the northern Caribbean: Geochemistry and petrology of the Güira de Jauco Amphibolite complex (eastern Cuba) and tectonic implications. *Lithos* 179, 193–210.
- Le, L., Tang, J., Ryan, D., Valix, M., 2006. Bioremediation of nickel laterite ores using multi-metal tolerant *Aspergillus foetidus* organism. *Min. Eng.* 19, 1259–1265.
- Leblanc, M., Nicolas, A., 1992. Les chromitites ophiolitiques. *Chronique de la Recherche Minière* 507, 3-25.
- Lewis, J.F., Draper, G., Proenza, J.A., Espaillet, J., Jiménez, J., 2006a. Ophiolite-related ultramafic rocks (serpentinites) in the Caribbean region: a review of their occurrence, composition, origin, emplacement and nickel laterite soils. *Geol. Acta* 4, 237-263.
- Lewis, J.F., Escuder-Viruete, J., Hernaiz-Huerta, P.P., Gutiérrez, G., Draper, G., Pérez-Estaún, A., 2002. Subdivisión geoquímica del arco de Isla Circum-Caribeño, Cordillera Central Dominicana: Implicaciones para la formación, acreción y crecimiento cortical en un ambiente intraoceánico. *Acta Geol. Hisp.* 37, 81-122.
- Lewis, J.F., Jiménez, J.G., 1991. Duarte complex in the La Vega-Jarabacoa-Janico Area, Central Hispaniola: geological and geochemical features of the sea floor during the early stages of arc evolution. In: Mann, P., Draper, G., Lewis, J.F. (Eds.), *Geologic and Tectonic Development of the North America-Caribbean Plate Boundary in Hispaniola*. *Geol. Soc. Am. Spec. Paper* 262, pp. 115–142.

- Lewis, J.F., Proenza, J.A., Jolly, W.T., Lidiak, E.G., 2006b. Monte del Estado (Puerto Rico) and Loma Caribe (Dominican Republic) peridotites: A look at two different Mesozoic mantle sections within northern Caribbean region. *Geophys. Res. Abstr.*, 8, A-08798.
- Lewis, J.F., Proenza, J.A., Melgarejo, J.C., Gervilla, F., 2003. The puzzle of Loma Caribe Chromitite. Taller del Proyecto N° 433 del PICG/UNESCO, *Memorias Geomin 2003* (published in CD, ISBN: 959-7117-11-8).
- Liivamägi, S., Somelar, P., Mahaney, W.C., Kirs, J., Vircava, I., Kirsimäe, K., 2014. Late Neoproterozoic Baltic paleosol: Intense weathering at high latitude? *Geology* 42, 323-326.
- Linchenat, A., Shirakova, I., 1964. Individual characteristics of nickeliferous iron (laterite) deposits of the northeast part of Cuba (Pinares de Mayari, Nicaro and Moa). 24th International Geological Congress, Montreal, Part 14, Section 14, pp. 172-187.
- Lithgow, E.W., 1993. Nickel laterites of central Dominican Republic Part I. Mineralogy and ore dressing. In: Reddy, R.G., Weizenbach, R.N. (Eds.), *The Paul E. Queneau Int. Symposium, Extractive Metallurgy of Copper, Nickel and Cobalt. Volume I: Fundamental Aspects*. The Minerals, Metals and Materials Society, Portland, pp. 403-425.
- Little, B.J., Wagner, P.A., Lewandowski, Z., 1997. Spatial relationships between bacteria and mineral surfaces. In: Banfield, J.F., Nealson, K.H. (Eds.), *Geomicrobiology: Interactions between microbes and minerals*, *Reviews in Mineralogy* 35, 123-159.
- Lorand, J.-P. and Alard, O., 2001. Platinum-group element abundances in the upper mantle: new constraints from in situ and whole-rock analyses of Massif Central xenoliths (France). *Geochimica et Cosmochimica Acta* 65, 2789–2806.
- Lorand, J.P., Luguet, A., Alard, O., 2008. Platinum-group elements: A new set of key tracers for the Earth's interior. *Elements* 4, 247-252.
- Magmatic relationships and ages of Caribbean Island arc tholeiites, boninites and related felsic rocks, Dominican Republic. *Lithos* 90, 161-186.
- Maier, W.D., Barnes, S.-J., Bandyayera, D., Livesey, T., Li, C., Ripley, E., 2008. Early Kibaran rift-related mafic–ultramafic magmatism in western Tanzania and Burundi: Petrogenesis and ore potential of the Kapalagulu and Musongati layered intrusions. *Lithos* 101, 24-53.
- Maksimovic', Z.J., Pantó, G., 1996. Authigenic rare earth minerals in karst-bauxites and karstic nickel deposits. In: Jones, A.P., Wall F., Williams C.T. (Eds.), *Rare Earth Minerals: Chemistry, Origin and Ore Deposits*. Mineralogical Society Series 7, London: Chapman and Hall, pp. 257–279.
- Malitch, K. N., 2004. Osmium isotope constraints on contrasting sources and prolonged melting in the Proterozoic upper mantle: evidence from ophiolitic Ru–Os sulfides and Ru–Os–Ir alloys. *Chem. Geol.* 208: 157– 173.

- Mann, A.W., 1984. Mobility of gold and silver in lateritic weathering profiles: some observations from Western Australia. *Econ. Geol.* 79, 38-49.
- Marchesi, C., Garrido, C.J., Godard, M., Proenza, J.A., Gervilla, F., Blanco-Moreno, J., 2006. Petrogenesis of highly depleted peridotites and gabbroic rocks from the Mayarí-Baracoa Ophiolitic Belt (eastern Cuba). *Contrib. Mineral. Petrol.* 151, 717–736.
- Marchesi, C., Garrido, C.J., Proenza, J.A., Konc, Z., Hidas, K., Lewis, J.F., Lidiak, E., 2012. Mineral and whole rock compositions of peridotites from Loma Caribe (Dominican Republic): insights into the evolution of the oceanic mantle in the Caribbean region. *Geophys. Res. Abstr.* 14, EGU2012–EGU12161.
- Marchesi, C., González-Jiménez, J.M., Gervilla, F., Garrido, C.J., Griffin, W.L., O'Reilly, S.Y., Proenza, J.A., Pearson, N.J., 2011. In situ Re–Os isotopic analysis of platinum-group minerals from the Mayarí–Cristal ophiolitic massif (Mayarí–Baracoa Ophiolitic Belt, eastern Cuba): implications for the origin of Os-isotope heterogeneities in podiform chromitites. *Contributions to Mineralogy and Petrology* 161, 977–990.
- Marsh, E.E., Anderson, E.D., 2011. Ni-Co laterite deposits: U.S. Geological Survey Open-File Report 2011, 1259-1268.
- McDonald, A.M., Proenza, J.A., Zaccarini, Z., Rudashevsky, N.S., Cabri, L.J., Stanley, C.J., Rudashevsky, V.N., Melgarejo, J.C., Lewis, J.F., Longo, F., Bakker, R.J., 2010. Garutiite, (Ni,Fe,Ir), a new hexagonal polymorph of native Ni from Loma Peguera, Dominican Republic. *Eur J Mineral* 22, 293-304.
- Medaris, L.G., Singer, B.S., Dott, Jr., R.H., Naymark, A., Johnson, C.M., Schott, R.C., 2003. Late Paleoproterozoic Climate and Tectonics in Southern Lake Superior Region and Proto-North America: Evidence from Baraboo Interval Quartzites. *J. Geol.* 111, 243-257.
- Meyer, F.M., Happel, U., Hausberg, J., Wiechowski, A., 2002. The geometry and anatomy of the Los Pijiguaos bauxite deposit, Venezuela. *Ore Geol. Rev.* 20, 27-54.
- Mochalov, A.G., Dmitrenko, G.G., Rudashevsky, N.S., Zhernovsky, I.V., Boldyreva, M.M., 1998. Hexaferrum (Fe,Ru),(Fe,Os), (Fe,Ir) – a new mineral. *Zap. Vseross. Mineral. Obshch.* 127, 41–51 (in Russian).
- Mongelli, G., 1997. Ce-anomalies in the textural components of Upper Cretaceous karst bauxites from the Apulian carbonate platform (southern Italy). *Chem. Geol.* 140, 69-79.
- Nahon, D., Colin, F., Boulange, B., 1992. Metallogeny of weathering: an introduction in weathering and soils & paleosols. In: Martini IP, Chesworth W (eds) *Weathering, Soils and Paleosols (Developments in Earth Surface Processes vol. 2)*, Elsevier, Amsterdam, pp 445 – 471.

- Naldrett, A.J., Duke, J.M., 1980. Platinum metals in magmatic sulfide ores. *Science* 208, 1417–1428.
- Ndjigui, P.D., Bilong, P., 2010. Platinum-group elements in the serpentinite lateritic mantles of the Kongo–Nkamouna ultramafic massif (Lomié region, South-East Cameroon). *J. Geochem. Explor.* 107, 63–76.
- Nelson, C.E., Proenza, J.A., Lewis, J.F., López-Kramer, J., 2011. The metallogenic evolution of the Greater Antilles. *Geol. Acta* 9, 229–264.
- Norton, S.A., 1973. Laterite and bauxite formation. *Econ. Geol.* 68, 353–361.
- Nowell, G.M., Pearson, D.G., Parman, S.W., Luguet, A., Hanski, E., 2008. Precise and accurate $^{186}\text{Os}/^{188}\text{Os}$ and $^{187}\text{Os}/^{188}\text{Os}$ measurements by multi-collector plasma ionisation mass spectrometry, Part II: laser ablation and its application to single grain Pt–Os and Re–Os geochronology. *Chemical Geology* 248, 394–426.
- Oberthuer, T., Weiser, T.W., Melcher, F. 2014. Alluvial and Eluvial Platinum-group minerals from the Bushveld Complex, South Africa. *S. Afr. J. Geol.* 117, 255–274.
- Ottemann, J., Augustithis, S.S., 1967. Geochemistry and origin of "platinum-nuggets" in lateritic covers from ultrabasic rocks and birbirités of W. Ethiopia. *Miner. Deposita* 1, 269–277.
- Pagé, P., Bédard, J.H., Schroetter, J.M., Tremblay, A., 2008. Mantle petrology and mineralogy of the Thetford Mines Ophiolite Complex. *Lithos* 100, 255–292.
- Pan, P., Wood, S.A., 1994. Solubility of Pt and Pd sulfides and Au metal in aqueous bisulfide solutions. *Miner. Deposita* 29, 312–326.
- Pearson, N.J., Alard, O., Griffin, W.L., Jackson, S.E., O'Reilly, S.Y., 2002. In situ measurement of Re–Os isotopes in mantle sulfides by laser ablation multicollector–inductively coupled plasma mass spectrometry: analytical methods and preliminary results. *Geochimica et Cosmochimica Acta* 66, 1037–1050.
- Platina Resources, 2015. Excellent testwork results from Owendale Scoping Study. Available at http://www.platinaresources.com.au/files/announcements/2015_01_20_-_PGM_ASX_-_Owendale_Scoping_Study.pdf. Accessed 25 March 2015.
- Pol, A., Barends, T.R.M., Bietl, A., Khadem, A.F., Eygensteyn, J., Jetten, M.S.M., Op den Camp, H.J.M., 2014. Rare earth metals are essential for methanotrophic life in volcanic mudpots. *Environ. Microbiol.* 16, 255–264.
- Proenza, J.A., 2015. Mineralogía y Geoquímica de Ni, Co, EGP, Sc, REE en Yacimientos Lateríticos. *Macla*, 3–9.

- Proenza, J.A., Díaz-Marínez, R., Iriondo, A., Marchesi, C., Melgarejo, J.C., Gervilla, F., Garrido, C.J., Rodríguez-Vega, A., Lozano-Santacruz, R., Blanco-Moreno, J.A., 2006. Primitive Cretaceous island-arc volcanic rocks in eastern Cuba: the Téneme Formation. *Geol. Acta*, 4, 103-121.
- Proenza, J.A., Gervilla, F., Melgarejo, J.C., 1999b. La Moho Transition Zone en el Macizo Ofiolítico Moa-Baracoa: un ejemplo de interacción magma/peridotite. *Revista de la Sociedad Geológica de España* 12, 309-327.
- Proenza, J.A., Gervilla, F., Melgarejo, J.C., Bodinier, J.L., 1999a. Al- and Cr-rich chromitites from the Mayarí-Baracoa Ophiolitic Belt (Eastern Cuba): consequence of interaction between volatile-rich melts and peridotite in suprasubduction mantle. *Econ. Geol.* 94, 547–566.
- Proenza, J.A., Lewis, J.F., Melgarejo, J.C., Gervilla, F., Jackson, T., Jolly, W.T., Lidiak, E.G., 2001. Peridotites and chromitites in eastern Cuba, Jamaica, Hispaniola and Puerto Rico: A comparison of Jurassic-Cretaceous mantle section within Caribbean region. Reunión del Proyecto N° 433 del PICG/UNESCO. *Memorias Geomin 2001* (published in CD, ISBN: 959-7117-10-X).
- Proenza, J.A., Tauler, E., Melgarejo, J.C., Gali, S., Labrador, M., Marrero, N., Perez-Nelo, N., Rojas-Puron, A.L., Blanco-Moreno, J.A., 2007a. Mineralogy of oxide and hydrous silicate Ni laterite profiles in Moa Bay area, northeast Cuba. In: Andrew, C.J. et al. (Eds), *Digging Deeper*, 2. Irish Association of Economic Geology, pp. 1389-1392.
- Proenza, J.A., Zaccarini, F., Escayola, M., Cávana, C., Shalamuk, A., Garuti, G., 2008. Composition and textures of chromite and platinum-group minerals in chromitites of the western ophiolitic belt from Córdoba Pampeans Ranges, Argentina. *Ore Geology Reviews* 33, 32–48.
- Proenza, J.A., Zaccarini, F., Lewis, J., Longo, F., Garuti, G., 2007b. Chromian spinel composition and platinum-group mineral assemblage of PGE-rich Loma Peguera chromitites, Loma Caribe peridotite, Dominican Republic. *Can. Mineral.* 45, 211–228.
- Redwood, S., 2014. Gold surge Mining is booming in the Dominican Republic as investors follow the gold rush. *Mining Journal* 24, 23-27.
- Reith, F., Campbell, S.G., Ball, A.S., Pring, A., Southam, G., 2014. Platinum in Earth surface environments. *Earth-Sc. Rev.* 131, 1-21.
- Reith, F., Stewart, L., Wakelin, S.A., 2012. Supergene gold transformation: Secondary and nano-particulate gold from southern New Zealand. *Chem. Geol.* 320-321, 32-45.
- Righter, K., Cambell, A.J., Humayun, M., Herwig, R.L. 2004. Partitioning of Ru, Rh, Pd, Re, Ir and Au between Cr-bearing spinel, olivine, pyroxene and silicate melts. *Geochim. Cosmochim. Acta* 68, 867–880.

- Ripley, E.M., Shafer, P., Li, C., Hauck, S.A., 2008. Re-Os and O isotopic variations in magnetite from the contact zone of the Duluth Complex and the Biwabik Iron Formation, northeastern Minnesota. *Chem Geol* 249, 213–226.
- Rius, J., Labrador, A., Crespi, A., Frontera, C., Vallcorba, O., Melgarejo, J.C., 2011. Capabilities of through-the-substrate micro-diffraction: application of Patterson-function direct methods to synchrotron data from polished thin sections. *J. Synchrotron Rad* 18, 891–898.
- Rius, J., Vallcorba, O., Frontera, C., Inmaculada, P., Crespi, A., Miravittles, C., 2015. Application of synchrotron through-the-substratemicrodiffraction to crystals in polished thin sections. *IUCrJ* 2: 452–463.
- Roqué-Rosell, J., Mosselmans, J.F.W., Proenza, J.A., Labrador, M., Galí, S., Atkinson, K.D., Quinn, P.D., 2010. Sorption of Ni by “lithiophorite-asbolane” intermediates in Moa Bay lateritic deposits, Eastern Cuba. *Chem. Geol.* 275, 9–18.
- Rösler, H.J., Lange, H., 1972. *Geochemical tables*, Amsterdam, Elsevier, 468 p.
- Rudashevsky, N.S., Burakov, B.E., Lupal, S.D., Thalhammer, O.A.R., Saini-Eidukat, B., 1995. Liberation of accessory minerals from various rock types by electric-pulse disintegration – method and application. *Trans. Inst. Min. Metall., Sec. C Mineral. Proc., Extract. Metall.* 104, C25–C29.
- Rudashevsky, N.S., Garuti, G., Andersen, J.C., Kretser, Yu L., Rudashevsky, V.N., Zaccarini, F., 2002. Separation of accessory minerals from rocks and ores by hydroseparation (HS) technology: method and application to CHR-2 chromitite, Niquelândia intrusion, Brazil. *Trans. Inst. Mining and Metall* 111, B87–B94.
- Rudashevsky, N.S., Lupal, S.D., Rudashevsky, V.N., 2001. The hydraulic classifier. Russia patent N 2165300, Patent Cooperation Treaty PCT/RU01/00123 (Moscow: 20 April 2001; 10 May 2001) (in Russian and English).
- Rudashevsky, N.S., Rudashevsky, V.N., 2006. Patent of Russian Federation #2281808, invention “Hydraulic Classifier”, Moscow, 20 August 2006.
- Rudashevsky, N.S., Rudashevsky, V.N., 2007. Patent of Russian Federation #69418, industrial (useful) model, “Device for separation of solid particles”, Moscow, December 27, 2007.
- Salpeteur, I., Martel-Jantin, B., Rakotomanana, D., 1995. Pt and Pd mobility in ferralitic soils of the Andriamena area (Madagascar). Evidence of a supergene origin of some Pt and Pd minerals. *Chron. Rech. Min.* 520, 27–45.
- Samama, J.C., 1986. *Ore fields and continental weathering*: New York, Van Nostrand Reinhold Co., 326 p.

- Sambridge, M., Lambert, D.D., 1997. Propagating errors in decay equations: examples from the Re–Os isotopic system. *Geochimica et Cosmochimica Acta* 61, 3019–3024.
- Scandium International Mining Corp., 2015. <http://www.scandiummining.com/s/nyngan.asp>., Accessed 19 April 2015.
- Sherritt, 2012. Sherritt international corporation. 2012 annual report. Available at: <http://www.sherritt.com/getattachment/7a7b0634-0dd4-46c4-bcda-19d73042fa9c/2012-Annual-Report>. Accessed 25.03.2015.
- Shi, R., Alard, O., Zhi, X., O'Reilly, S.Y., Pearson, N.J., Griffin, W.L., Zhang, M., Chen, X., 2007. Multiple events in the Neo-Tethyan oceanic upper mantle: evidence from Ru–Os–Ir alloys in the Luobusa and Dongqiao ophiolitic podiform chromitites, Tibet. *Earth and Planetary Science Letters* 261, 33–48.
- Simandl, G.J., 2014. Geology and market-dependent significance of rare earth element resources. *Miner. Deposita* 49, 889-904.
- Stockman, H.W., Hlava, P.F., 1984. Platinum-group minerals in Alpine chromitites from southwestern Oregon. *Econ. Geol.* 79, 491-508.
- Stumpfl, E.F., Tarkian, M., 1976. Platinum Genesis: New Mineralogical Evidence. *Econ. Geol.* 71, 1451-1460.
- Stumpfl, E.F., 1974. The genesis of platinum deposits. Further thoughts. *Min. Sci. Eng.* 6, 120 – 141.
- Swanson, H.E., Fuyat, R.K., Ugrinic, G.M., 1955. Standard X-ray diffraction powder patterns. *Natl. Bur. Stand. (U.S.) Circ.* 539, IV, 8.
- Talovina, I.V., Lazarenkov, V.G., 2001. Distribution and genesis of platinum group minerals in nickel ores of the Sakhara and Elizavet deposits in the Urals. *Lithol. Mineral. Res.* 36, 116-122.
- Tauler, E., Proenza, J.A., Galí, S., Lewis, J.F., Labrador, M., García-Romero, E., Suárez, M., Longo, F., Bloise, G., 2009. Ni-sepiolite–falcondoite in garnierite mineralisation from the Falcondo Ni-laterite deposit, Dominican Republic. *Clay Miner.* 44, 435–454.
- Terekhov, D.S., Nanthakumar, V.E., 2013. Direct extraction of nickel and iron from laterite ores using carbonyl process. *Miner. Engin.* 54, 124-130.
- TOPAS, General Profile and Structure Software for Powder Diffraction Data, V2.1 Bruker AXS Gmbh, Karlsruhe, Germany.
- Traoré, D., Beauvais, A., Augé, T., Parisot, J.C., Colin, F., Cathelineau, M., 2008b. Chemical and physical transfers in an ultramafic rock weathering profile: Part 2. Dissolution vs. accumulation of platinum group minerals. *Am. Mineral.* 93, 31-38.

- Traoré, D., Beauvais, A., Chabaux, F., Peiffert, C., Parisot, J.C., Ambrosi, J.P., Colin, F., 2008a. Chemical and physical transfers in an ultramafic rock weathering profile: Part 1. Supergene dissolution of Pt-bearing chromite. *Am. Mineral.* 93, 22–30.
- Trincal, V., Charpentier, D., Buatier, M.D., Grobety, B., Lacroix, B., Labaume, P., Sizun, J.P., 2014. Quantification of mass transfers and mineralogical transformations in a thrust fault (Monte Perdido thrust unit, southern Pyrenees, Spain). *Mar. Petrol. Geol.* 55, 160-175.
- Tsikouras, B., Karipi, S., Rigopoulos, I., Perraki, M., Pomonis, P., Hatzipanagiotou, K., 2009. Geochemical processes and petrogenetic evolution of rodingite dikes in the ophiolite complex of Othrys (Central Greece). *Lithos* 113, 540-554.
- Urashima, Y., Wakabayashi, T., Masaki, T., Terasaki, Y., 1974. Ruthenium, a new mineral from Horokanai, Hokkaido, Japan. *Mineral. J. (Jpn)*, 7, 438–444.
- USGS, 2013. Mineral commodity summaries 2013. Available at: <http://minerals.usgs.gov/minerals/pubs/mcs/2013/mcs2013.pdf>. Accessed 25.03.2015.
- Uysal, I., Zaccarini, F., Sadiklar, M.B., Bernhardt, H.-J.M., Bigi, S., Garuti, G., 2009. Occurrence of rare Ru–Fe–Os–Ir–oxide and associated Platinum-group minerals (PGM) in the chromitite of Mugla ophiolite, SW-Turkey. *Neues Jahrbuch für Mineralogie (Abhandlungen)* 185, 323–333.
- van Achterbergh, E., Ryan, C.G., Jackson, S.E., Griffin, W.L., 2001. Data reduction software for LA-ICP-MS. In: Sylvester, P., (Ed.), *Laser-ablation-ICPMS in the Earth Sciences: Principles and Applications*. Mineralogical Association of Canada, Short Course, pp. 239-243.
- Villanova-de-Benavent, C., Proenza, J.A., Galí, S., García-Casco, A., Tauler, E., Lewis J.F., Longo, F., 2014. Garnierites and garnierites: Textures, mineralogy and geochemistry of garnierites in the Falcondo Ni laterite deposit, Dominican Republic. *Ore Geol. Rev.* 58, 91-109.
- Vodyanitskii, Y.N., 2010. Iron hydroxides in soils: A review of publications. *Eurasian. Soil Sci.* 43, 1244-1254.
- Vymazalová, A., Laufek, F., Drábek, M., Stanley, C.J., Baker, R.J., Bermejo, R., Garuti, G., Thalhammer, O., Proenza, J.A., Longo, F., 2012. Zaccariniite, RhNiAs, a new platinum-group mineral from Loma Peguera, Dominican Republic. *Can. Minerl.* 50, 1321-1329.
- Wagner, P.A., 1929. *The Platinum Deposits and Mines of South Africa*. Oliver & Boyd, London, U.K., 326 pp.
- Walker, R.J., Brandon, A.D., Bird, J.M., Piccoli, P.M., McDonough, W.F., Ash, R.D., 2005. ^{187}Os – ^{186}Os systematics of Os–Ir–Ru alloy grains from southwestern Oregon. *Earth Planet. Sci. Lett.* 230, 211-226.

- Walker, R.J., Horan, M.F., Morgan, J.W., Becker, H., Grossman, J.N., Rubin, A.E., 2002. Comparative ^{187}Re – ^{187}Os systematics of chondrites: implications regarding early solar system processes. *Geochimica et Cosmochimica Acta* 66, 4187–4201.
- Wang, W., Pranolo, Y., Cheng, C.Y., 2011. Metallurgical processes for scandium recovery from various resources: A review. *Hydrometallurgy* 108, 100-108.
- Westland, A., D., 1981, Inorganic chemistry of the platinum-group elements: Canadian Inst. Mining Metallurgy Spec. Vol. 23, p.5-18.
- Wilde, A., Edwards, A., Yakubchuk, A., 2003. Unconventional deposits of Pt and Pd: A review with implications for exploration. *SEG Newsletter* 52, 1 and 10-18.
- Wood, S.A., 1996. The role of humic substances in the transport and fixation of metals of economic interest (Au, Pt, Pd, U, V). *Ore Geol. Rev.* 11, 1-31.
- Yang, Y., Liu, S., Jin, Z., 2009. Laterization and its control to gold occurrence in Laowanchang gold deposit, Guizhou Province, Southwest of China. *J. Geochem. Explor.* 100, 67-74.
- Zaccarini, F., Bindi, L., Garuti, G., Proenza, J.A., 2014. Ruthenium and magnetite intergrowths from the Loma Peguera chromitite, Dominican Republic, and relevance to the debate over the existence of platinum-group element oxides and hydroxides. *Can. Mineral.* 52, 617–624.
- Zaccarini, F., Proenza, J.A., Ortega, Gutierrez, F., Garuti, G., 2005. Platinum group minerals in ophiolitic chromitites from Tehuitzingo (Acatlan complex, Southern Mexico): implications for post-magmatic modification. *Mineral. Petrol.* 84, 147–168.
- Zaccarini, F., Proenza, J.A., Rudashevsky, N.S., Cabri, L.J., Garuti, G., Rudashevsky, V.N., Melgarejo, J.C., Lewis, J.F., Longo, F., Bakker, R.J., Stanley, C.J., 2009. The Loma Peguera ophiolitic chromitite (Central Dominican Republic): a source of new platinum group minerals (PGM) species. *N. Jb. Miner. Abh.* 185, 335-349.